Morphology-Driven Electrochemistry in Energy Devices: Tin-Halide Perovskite Solar Cells and Microstructured Current Collectors for Solid-State Batteries

Tomás Henrique Campos Ferreira Prior
Master in Engineering Physics
Department of Physics and Astronomy
Faculty of Science of the University of Porto and Faculty of Engineering of the University of Porto
2024/2025

Morphology-Driven Electrochemistry in Energy Devices: Tin-Halide Perovskite Solar Cells and Microstructured Current Collectors for Solid-State Batteries

Tomás Henrique Campos Ferreira Prior

Dissertation carried out as part of the Master in Engineering Physics

Department of Physics and Astronomy

2024/2025

Supervisor
Maria Helena Sousa Soares de Oliveira Braga, Associate Professor with aggregation, Faculty of Engineering of University of Porto

Co-supervisor
Luísa Manuela Madureira Andrade Silva, Auxiliar Professor, Faculty of engineering of University of Porto

Co-supervisor
Hugo Gaspar, PhD Researcher, CENTI

MatΣR
Materials Energy Research

New Generation Storage

"***Study hard what interests you the most in the most undisciplined, irreverent and original manner possible.***" — Richard Feynman

Dedicated to Nani

Acknowledgements

I would like to express my heartfelt gratitude to Professor Helena Braga, my supervisor, for her guidance, patience, and insightful feedback throughout this thesis. More than anything, I am grateful for her belief in my work, her trust in my judgement, and the freedom she gave me to pursue ideas as I envisioned them, as well as for supporting the research grant that made this project possible.

I am equally grateful to my co-supervisor, Professor Luisa Andrade, who welcomed me into her laboratory, trusted me, and provided invaluable feedback in an area where I began as a complete novice. I am indebted to her group: Dr. Vera Duarte, Joana Príncipe, and Andrés Soto. Their patient instruction and generous support in the lab made this work possible. I offer them my deepest thanks and hope to repay their generosity someday. My door will always be open to them!

The same is true of my MatER colleagues, whose knowledge and hard work supported me throughout this journey. In particular, I am most grateful to Ângela Freitas and Beatriz Gomes. Ângela deserves at least half the credit for the assembly and testing of the batteries, and Beatriz helped me enormously with the writing of my first paper. To them, and to all the members of MatER, I extend my warmest thanks.

I am deeply grateful to my family. In special to my mother, who, despite our many arguments, made my life immeasurably easier so I could devote my energy and time to this work. To my father, whose kindness has always sustained me. To Milu, who has always been a mother to me. To my sister Ana, for her guidance and support. And to my brother Rui, for always being there and for indulging in countless conversations about my niche interests.

Finally, I thank my close friends. They get me out of the house, keep me laughing and smiling.

Resumo

Soluções mais simples, localizadas e ambientalmente seguras para a captura e armazenamento de energia são essenciais. Células fotovoltaicas de perovskitas à base de estanho e coletores de corrente de cobre microestruturados para baterias de estado sólido à base de sódio oferecem um caminho viável. Na Parte I deste trabalho, examinámos como a oxidação do precursor SnI_2 governa a formação de fases, a morfologia e o desempenho do dispositivo em perovskitas de halogenetos de estanho, com foco em $CsSnI_3$. Precursores oxidados suprimiram a fase preta e degradaram a qualidade do filme. A purificação removeu SnI_4 e SnO_2 e restaurou $CsSnI_3$ de alta qualidade com grãos maiores. Utilizando SnI_2 de alta pureza, variámos a composição, a arquitetura do dispositivo e o processamento para avaliar a estabilidade. Uma breve exposição intensa ao ar causou alterações óticas menores, enquanto uma exposição branda prolongada produziu nanocristais superficiais consistentes com Cs_2SnI_6. Medições elétricas e de superfície indicaram deslocamentos da função de trabalho e da condutividade induzidos pela oxidação, e a microscopia mostrou crescimento limitado por difusão que favorece curtos-circuitos parasitas (shunting) e baixa tensão de circuito aberto. SnF_2 reduziu a oxidação da “tinta” e melhorou a uniformidade, mas introduziu novas feições superficiais. Em geral, o controlo de oxigénio e a morfologia são os principais constrangimentos, com desalinhamento de bandas induzido por oxidação e shunting impulsionado pela morfologia a limitarem a operação do dispositivo. Na Parte II, avaliámos coletores de corrente de cobre microestruturados em células “pouch” $Zn/Na_{2.99}Ba_{0.005}OCl/Cu$ sem elétrodos. Filmes de cobre sobre parileno-C microestruturado, fabricados por litografia coloidal e gravação reativa por iões, apresentaram cerca de 30% de maior área superficial. O mapeamento por sonda Kelvin revelou deslocamentos do potencial de superfície que acompanharam maior transporte iónico, enquanto a resistividade do cobre permaneceu dentro da gama esperada. O desempenho correlacionou-se mais fortemente com o potencial químico superficial e a concentração de portadores: menor densidade eletrónica resultou em correntes de descarga mais elevadas, maior capacitância interfacial e maior tensão de patamar e capacidade no primeiro ciclo. Estes resultados indicam que a energética interfacial, mais do que a morfologia por si só, governa o comportamento da célula.

Palavras-chave: Células solares de perovskita, Perovskitas à base de estanho, Estabilidade, Oxidação, Morfologia, Baterias de estado sólido de sódio, Coletores de corrente microestruturados, Engenharia interfacial, Células tipo *pouch*, Sem elétrodos

Abstract

Simple, localized, and environmentally safer solutions for energy capture and storage are essential. Perovskite photovoltaics and sodium-based solid-state batteries provide a viable path forward. In particular, replacing toxic lead with tin in halide perovskites offers a more sustainable route for next-generation photovoltaics, while microstructured copper current collectors enable progress in sodium-based solid-state batteries. In Part I of this work, we examined how SnI_2 precursor oxidation governs phase formation, morphology, and device performance in tin halide perovskites, focusing on $CsSnI_3$. Oxidized precursors suppressed the desirable black phase and degraded film quality, while purification to remove SnI_4 and SnO_2 restored high quality $CsSnI_3$ with larger grains. Using high purity SnI_2, we then varied composition, device stack, and processing to assess stability. Short intense air exposure caused only minor optical shift, whereas prolonged mild exposure produced surface nanocrystals consistent with Cs_2SnI_6. Electrical and surface measurements revealed oxidation driven shifts in work function and conductivity, and microscopy showed diffusion limited growth that promotes shunts and low open circuit voltage. SnF_2 reduced ink oxidation and improved uniformity, but introduced new surface features. Overall, oxygen control and morphology remain the primary bottlenecks, with oxidation induced band misalignment and morphology driven shunting limiting device operation. In Part II, we evaluated microstructured copper current collectors in electrodeless $Zn/Na_{2.99}Ba_{0.005}OCl/Cu$ pouch cells. Copper films on microstructured parylene-C made by colloidal lithography and reactive ion etching showed increased roughness and about 30% higher surface area. Kelvin probe mapping revealed surface potential shifts that tracked higher ionic transport and lower bulk resistance, while copper resistivity remained near bulk values and mobilities in the expected range. Performance correlated most strongly with surface chemical potential and carrier concentration: lower electron density yielded higher discharge currents, larger interfacial capacitance, and higher first cycle plateau voltage and capacity. These results indicate that interfacial energetics, rather than morphology alone, govern cell behavior.

Keywords: Perovskite solar cells, Tin-based perovskites, Stability, Oxidation, Morphology, Sodium SSBs, microstructured current collectors, interfacial engineering, pouch-cells, electrode-less

Table of Contents

List of Tables vii

List of Figures viii

List of Abbreviations xvi

Introduction 1

1. Part I – Background and state-of-the-art 6

1.1. General theoretical principles and technological overview 6

1.1.1. Band structure and photovoltaic effect in semiconductors 6

1.1.2. Evolution of photovoltaic cell (PVC) technology 7

1.1.3. Factors limiting efficiency of photovoltaic cells. 8

1.2. Perovskite solar cells 11

1.2.1. OIHPs - Organic Inorganic Halide Perovskites 12

1.2.2. Device architecture 16

1.2.3. Synthesis methods 19

1.2.4. Challenges for perovskite solar cells 22

1.3. Tin-Halide Perovskites 23

1.3.1. Stabilization and enhancement of tin-halide perovskites 24

2. Materials and Methods (Part I) 27

2.1. Materials 27

2.2. Methods 27

2.2.1. SnI_2 purification process 27

2.2.2. Precursor solution preparation 28

2.2.3. Substrate preparation procedure 29

2.2.4. Device fabrication procedure 29

2.2.5. Characterizations 31

3. Results and discussion (Part I) 34

3.1. Effect of Precursor Oxidation and Purification on Perovskite Films 34

3.1.1. First batch of cells 34

3.1.2. Precursor purification study 36
3.2. Studies Using High-Purity SnI_2 Precursor 42
3.2.1. Device Fabrication Attempts 42
3.2.2. Effect of degradation on perovskite film 45
3.2.3. Electrochemical property measurements 48
3.2.4. Morphology of the perovskite crystals and effect of wetting layer 53
3.2.5. Effects of tin fluoride additive on film morphology 58
3.3. Conclusions and future work 61
4. Part II - Background and state-of-the-art 65
4.1. Fundamental principles of electrochemical energy storage 65
4.2. Sodium based Solid state batteries 67
4.3. Microstructuring in batteries 69
4.3.1. Microstructuring methods 70
5. Materials and Methods (Part II) 72
5.1. Fabrication of the Microstructured Copper Current Collectors 72
5.1.1. Parylene-C Deposition 72
5.1.2. Microsphere Deposition 72
5.1.3. Reactive Ion Etching (RIE) 73
5.1.4. Copper Deposition 73
5.2. Characterization of the Microstructured Copper Current Collectors 73
5.2.1. Charge Transport Measurements 73
5.2.2. Topography and Surface Potential Measurements 74
5.2.3. Scanning Electron Microscopy and X-Ray Photoelectron Spectroscopy 76
5.2.4. Separator Preparation and Cell Assembly 76
5.3. Pouch Cell Electrochemical Characterization 77
5.3.1. Electrochemical Impedance Spectroscopy (PEIS) 77
5.3.2. Cyclic Voltammetry (CV) 78
5.3.3. Charge/Discharge Cycles and GITT 78

6. Results and discussion (Part II) 80
6.1. Characterization of the Microstructured Current Collectors 80
6.1.1. Topographical Characterization 80
6.1.2. KPFM Characterization 85
6.1.3. Charge Transport Measurements 88
6.2. Pouch Cell Electrochemical Characterization 90
6.2.1. Potentiostatic Electrochemical Impedance Spectroscopy 90
6.2.2. Cyclic Voltammetry 93
6.2.3. Charge/Discharge Cycles and GITT Stability Tests 94
6.2.4. Comparison of Correlated Parameters 96
6.3. Conclusions and future work 99
Conclusion 101
References 104
Attachments 122
Appendix A.1 122
Appendix A.2 125
Appendix A.3 126
Appendix A.4 128

List of Tables

Table 1 – Summary of strategies, results, and mechanistic explanations from selected studies aimed at improving performance and stability in tin-halide perovskite solar cells. 25

List of Figures

Figure 1 – Evolution of research solar cell's efficiencies over time. This plot is courtesy of the National Renewable Energy Laboratory, Golden, CO.....8
Figure 2 – Representative J–V curves affected by common loss factors. Curves calculated from the illuminated diode model (equations above) using typical solar-cell parameters. The baseline is shown with J_{sc}, OCV, FF, and MPP marked. Variants illustrate the impact of common loss factors on the J-V curve. 11
Figure 3 – Diagram of the general perovskite crystal structure. Reproduced from reference [38]. Used under the terms of CC BY 3.0..... 11
Figure 4 – (a) Formability of 3D lead (red) and tin (blue) halide perovskites as a function of A-site cation and halide anion radii. Solid and dashed lines mark the bounds of the tolerance and octahedral factors, respectively. Adapted from [43] Reproduced with permission under ACS copyrights **(b)** Structural phases of formamidinium- and cesium-based halide perovskites. Reproduced with permission from [44]. Copyright 2021 American Chemical Society. **(c)** On the left: Heating phase diagram for $CsPb(Br_xI_{1-x})_3$ thin films aged in a humid environment for composition, x, between 0 (pure $CsPbI_3$) and 1 (pure $CsPbBr_3$) On the right: Cooling phase diagram for the same $CsPb(Br_xI_{1-x})_3$ thin films as they cool down from a high temperature. [45]. Used under the terms of CC BY 3.0. **(d)** Dependance of tolerance factor on A-site cation effective radius. Adapted from [46]. Used under the terms of CC BY-NC 3.0. **(e)** Summary of phase transition temperatures in halide perovskites reported in the literature collected at ambient pressure as a function of composition. Cubic structures exhibit Pm3m symmetry, tetragonal structures exhibit either I4/mcm or P4/mbm symmetry, and the orthorhombic phase exhibits Pnma symmetry, unless otherwise noted. Green colors indicate phases not represented by the above categories. Adapted from [47]. Used under the terms of CC BY-NC 3.0. 13
Figure 5 – (a-c) Schematic energy levels in AMX_3 perovskites. **(a)** represent trends in changing the halide anions, **(b)** represent trends in changing the metal cations. **(c)** represent trends in changing the A-site cation. Arrows indicate the shift in energy levels upon atom or small molecule substitution. **(d-f)** Orbital contributions to the energy bands of $CsPbI_3$. **(d)** $CsPbI_3$ DOS projected on the Cs, Pb, and I atoms (partial DOS). **(e)** Orbital-resolved COHP; positive (negative) sign indicates bonding (anti-bonding) character. The line colors indicate which atomic orbitals are involved in the bonds (anti-bonds). **(f)** Schematic energy level diagram extracted from the COHP analysis; the energy levels E_1 to E_4 which are relevant for the tight-binding analysis are

marked. Bonding interactions are shaded in yellow, and anti-bonding interactions in pink. (a-f) Adapted from [49]. Used under the CC BY-NC 4.0. **(g)** Calculated electronic band structure of α-$CsPbI_3$ with (black/left) and without (blue/right) spin-orbit coupling interaction. Reproduced from [50]. Used with permission under Copyright © 2013 American Chemical Society. **h)** Schematic illustration of deep and shallow charge carrier traps in perovskites. Based on [54] and [57]..... 15
Figure 6 – (a) Schematics of mesoporous, n–i–p, and p–i–n perovskite solar cell architectures. **(b)** Contact behavior schematics: poor extraction and poor selectivity, good extraction with poor selectivity, and good extraction and good selectivity. **(c)** Typical vacuum referenced energy levels, Evac = 0, for common HTLs, perovskites, ETLs and electrodes. Values taken from: FTO and ITO- [78] ; PTAA-[79], [80], [81] ;PEDOT:PSS-[82], [83], [84]; P3HT- [85], [86], [87]; NiO-[88], [89], [90] ; CuSCN- [91], [92]; CuI- [93], [94]; Perovskites-[95] ;PCBM- [96], [97], [98]; ICBA- [99], [100], [101];C60- [102], [103];SnO2-[104], [105], [106] ;ZnO-[107], [108] ;Au, Ag and Cu-[109]..... 19
Figure 7 – (a) Solvent selection map for perovskite inks: dielectric constant, ε_r, versus Gutmann donor number, DN. Adapted from [129], copyright AAAS, used with permission. **(b-d)** Literature prevalence, log scale counts, of deposition routes for the perovskite absorber, HTL, and ETL layers, from [111]. **(e)** Schematics of solution processed film fabrication: one step and two step spin coating with antisolvent, air knife assisted D bar coating, blade coating, slot die coating, spray coating, and inkjet coating, plus post treatments including annealing and surface passivation. Adapted from Nature Reviews Methods Primers [28], copyright Springer Nature, used with permission. 21
Figure 8 – Schematic representation of the purification process used to clean the oxidized SnI_2 powder..... 28
Figure 9 – Schematic representation of the cells fabricated in this work. 31
Figure 10 – (a) Schematic representation of the layer stacking and experimental setup used to perform SKP measurements. **(b)** Typical absorption spectrum for halide perovskites (in black). Obtained from [168], used under CC BY 4.0..... 32
Figure 11 – (a) filtered perovskite solution prepared with oxidized SnI_2 precursor. **(b)** First FTO/PTAA(PEAI)/CsSnI3/PCBM/BCP/Ag cells fabricated. **(c)** time sequence of pictures of perovskite films crystalizing during thermal annealing. Arrow indicates direction of time. Photographs spaced 5 seconds from each other. **(d)** Pictures showing the degradation of the perovskite films inside the glovebox. **(e)** Pictures showing the degradation of the perovskite films outside the glovebox..... 36
Figure 12 – (a) Picture illustrating the reduction concentration of SnI_4 in the waste toluene for consecutive washes. **(b)** SnI_2 crystals after the purification process. **(c)**

Perovskite precursor solutions, before filtration, prepared with (from left to right) “toluene washed + DMF filtration” precursor, “Toluene wash” precursor, unwashed oxidized precursor. **(d)** The same perovskite solutions shown in **(c)** after filtration. Example of resultant perovskite films synthesized with **(e)** “toluene washed + DMF filtration” precursor **(f)** “Toluene wash” precursor **(g)** unwashed oxidized precursor..... 38
Figure 13 – XRD patterns of perovskite films prepared from different precursor treatments. **(a)** Toluene wash + DMF filtration, **(b)** Toluene wash only, **(c)** unwashed oxidized precursor. Symbols in the XRD spectra identify the phase with highest influence on that peak. Graphs below the spectra show all correlated peaks for the identified phases. Phase identification peaks obtained from: COD database [172] for SnO_2 and CsI peaks; Wang et al. (2022) [173] for γ-$CsSnI_3$ (orthorhombic), Y-$CsSnI_3$ (orthorhombic yellow phase) and Cs_2SnI_6..... 40
Figure 14 – Top-down SEM images of perovskite films prepared from different precursor treatments. **(a, d)** Toluene wash with DMF filtration. **(b, e)** Toluene wash. **(c, f)** Oxidized precursor. **(g)** High-magnification image of toluene wash. **(h)** High-magnification image of oxidized precursor..... 41
Figure 15 – (a) Perovskite solution prepared using 99.999% purity SnI_2 precursor. **(b)** Perovskite film obtained from the solution shown in subfigure **(a)**. **(c)** Cells after thermal deposition of Ag contacts, with partial removal of silver from the left cell using sticky tape. **(d)** Cell after thermal deposition of 20 nm Au contacts. **(e)** Cell after deposition of Ag contacts with a controlled venting process. **(f)** Cell obtained from the final attempt. **(g)** High resolution SEM image of a perovskite film showing glass fragments (highlighted in red). The distinction between glass fragments and other features is visible in the back scattered electron image (highlighted in yellow). **(h)** EDS spectrum acquired from a region containing glass fragments..... 44
Figure 16 – (a) Time evolution of absorption* as a function of photon energy for $CsSnI_3$ films on a glass substrate measured by UV VIS NIR spectrophotometry. Two nominally identical samples, A and B, were recorded repeatedly over about 90 minutes, and successive spectra follow the time order indicated in the inset. Vertical dotted lines mark literature bandgap energies for phases that may be present in the film. The arrow highlights the progressive decrease in apparent absorption during the measurement period. **(b)** Tauc plot of absorption* zoomed on the absorption edge ROI. Straight lines represent the linear fit of the linear absorption edge. Bandgap values determined from X intercept. *Because reflectance was not measured reliably, one minus transmittance is reported in place of absorption..... 45

Figure 17 – Scanning electron microscopy of a $CsSnI_3$ film stored in a nitrogen glovebox for more than one month. Images are shown at two magnifications. Left panels show secondary electron mode. Right panels show backscattered electron mode. Scale bars are 10 μm in the upper panels and 1 μm in the lower panels. 47
Figure 18 – Temperature-dependent dark transport parameters extracted from Hall-effect measurements for two perovskite thin film samples. Left column **(a, c, e, g)** corresponds to sample 1, right column **(b, d, f, h)** corresponds to sample 2. Red symbols indicate the heating cycle, blue symbols indicate the cooling cycle. (a, b) Electrical conductivity as a function of temperature. **(c, d)** Bulk charge carrier concentration (CCC bulk) as a function of temperature, the horizontal dashed line marks zero. **(e, f)** Hall mobility as a function of temperature, plotted on a logarithmic scale. **(g, h)** Average Hall coefficient as a function of temperature, the horizontal dashed line marks zero. 50
Figure 19 – Scanning Kelvin probe (SKP) line scan of surface work function (WF) across a Cu, PTAA, $CsSnI_3$, and PCBM stack. The y axis shows surface WF in eV referenced to vacuum level. The x axis shows the lateral tip position in millimeters. Two independent scans are plotted (1^{st} trial and 2nd trial). Vertical dashed lines mark the approximate lateral boundaries between layers. Horizontal dashed lines indicate literature WF values for PTAA, about 5.15 eV (estimated from known VBM and CBM) [195], $CsSnI_3$, about 4.9 eV [196], and PCBM, about 4.37 eV [198]..... 51
Figure 20 – Estimated energy-level diagram of FTO/PTAA/$CsSnI_3$/PCBM/Ag stack, referenced to vacuum (Evac = 0 at top; energy depth increases downward). Colored bars show approximate band positions. Grey bars indicate contact work functions. Horizontal purple lines are SKP-derived (measured/estimated) work functions; horizontal black dashed lines are literature work-function values. Dotted and dashed green boxes bound three literature ranges (Reference A and Reference B) for the CsSnI3 band edges. **(a)** Expected scenario for full device with minimal oxidation **(b)** Expected scenario for oxidized $CsSnI_3$ surface. References for WF, CBM and VBM values: FTO- [204] ; PTAA- [195]; Ref A-[205], Ref B-[49] ; PCBM- [198] ; Ag- [206]; Cs_2SnI_6-[185]..... 53
Figure 21 – Scanning electron microscopy of a $CsSnI_3$ film. **(a)** Low magnification secondary electron, SE, image showing continuous film coverage, scale bar 200 micrometers. **(b)** Low magnification backscattered electron, BSE, image with comparable large-area morphology, scale bar 200 micrometers. **(c)** Intermediate magnification SE image resolving faceted grains with dendritic ridges, scale bar 50 micrometers. **(d)** Intermediate magnification BSE image of the same morphology, scale bar 50 micrometers. **(e)** High magnification SE image highlighting terrace-like steps

within grains, scale bar 10 micrometers. **(f)** High magnification BSE image of the same region, scale bar 10 micrometers. 56
Figure 22 – Atomic force microscopy of a $CsSnI_3$ perovskite film. **(a)** Area 1 height map shown with the full acquisition range, color bar 0 to 250 nm, scale bar 4 micrometers. **(b)** Same field of view as in (a) displayed with a narrower color range, 80 to 160 nm, to enhance topographic contrast, scale bar 4 micrometers. **(c)** Area 2 height map with the full range, color bar 0 to 200 nm, scale bar 4 micrometers. **(d)** Same field of view as in (c) with a narrower color range, 50 to 120 nm, to enhance contrast, scale bar 4 micrometers. **(e)** Cross sectional image of a FTO/PTAA(PEAI)/$CsSnI_3$/PCBM/BCP stack with measured thicknesses indicated, approximately 565 nm (FTO) and 294 nm (Perovskite). 57
Figure 23 – Schematic of diffusion limited dendritic growth on a {100} facet of $CsSnI_3$. Color code: the yellow square is the crystal nucleus and growing facet; the pink to red background represents the concentration field of growth species in the surrounding medium, darker red indicates higher concentration and lighter pink indicates depletion; red wavy lines depict diffusing species and the effective diffusion path; pale gray rings indicate isoconcentration fronts and depletion zones; black arrows show preferred growth directions and relative rates; thin black lines mark primary and secondary dendrite rims; thick black bands represent coalesced rims where dendrites interlock; blue arrows are annotations only. From left to right the sequence shows nucleation in a region of high concentration, initial growth with long diffusion paths that slow the facet center, faster edge advance as the diffusion path becomes shorter at the rim, formation of secondary dendrites, and two outcomes, either matching dendrites do not interlock and ridges remain, or mismatched dendrites interlock and coalesce, resulting in a smooth facet with no ridges. 57
Figure 24 – Scanning electron microscopy of a $CsSnI_3$ film on PTAA after PCBM and BCP deposition and PCBM sintering. **(a)** Low magnification secondary electron image showing continuous coverage, scale bar 50 micrometers. **(b)** Low magnification backscattered electron image of the same area, scale bar 50 micrometers. **(c)** High magnification secondary electron image resolving faceted grains with terrace like ridges, scale bar 10 micrometers. **(d)** High magnification backscattered electron image of the same region, scale bar 10 micrometers. **(e)** Highest magnification secondary electron image highlighting smoothened grain surfaces and grain boundaries with occasional small particulates, scale bar 1 micrometer. **(f)** Highest magnification backscattered electron image of the same area, scale bar 1 micrometer. 58

Figure 25 – Oxidation and remediation of a $CsSnI_3$ perovskite precursor solution. Left: solution prepared with pure SnI_2. Middle: oxidized solution. Right: solution after addition of SnF_2, which restores the original state. 59
Figure 26 – Scanning electron microscopy of perovskite films prepared with varying SnF_2 content: **(a)** 0 mol% SnF_2, scale bar 200 μm; **(b)** 10 mol% SnF_2, scale bar 200 μm; **(c)** 20 mol% SnF_2, scale bar 80 μm. (values of mol% are in excess relative to SnI_2 molarity in stoichiometrically correct solution). Higher magnifications of panels (a), (b), and (c) are shown in **(d)**, **(e)**, and **(f)**, with scale bars of 50 μm, 50 μm, and 10 μm, respectively. **(g)** Close-up image of a zone with similar crystal formations to the highlighted zone on (d). Panel **(h)** shows the boxed region from (e). 61
Figure 27 – Diagram of the four-step fabrication process for the microstructured copper current collectors. 72
Figure 28 – Examples of electrochemical characterization methods. **(a,b)** Potentiostatic electrochemical impedance spectroscopy, PEIS: **(a)** a Nyquist response with fully resolved features, **(b)** a typical measurement where features merge, which introduces ambiguity in analysis. Adapted from reference [273]. Licensed under CC BY 4.0. **(c)** Cyclic voltammetry. PA indicates the anodic peak (charge), PC indicates the cathodic peak (discharge). Source: Wikimedia Commons – Cyclic Voltammetry. Licensed under CC BY-SA 4.0. (d) Typical discharge profile for a battery with a plateau at the equilibrium potential. 79
Figure 29 – Examples of topography images, obtained via AFM, of the copper current collectors with different etching times: **(a)** 0 min; **(b)** 6 min; **(c)** 9 min; **(d)** 12 min; **(e)** 15 min. The images shown were upscaled to 1024 × 1024 pixels, from the original 256 × 256, for enhanced visual clarity..... 81
Figure 30 – Extracted parameters from topography images: **(a)** root-mean-square (RMS) of topography; **(b)** surface area increase from flat topography (400 μm^2); **(c)** number of particles; **(d)** average distance between 6 nearest neighbors; **(e)** standard deviation of average nearest-neighbor distance. 83
Figure 31 – SEM images of the microstructured copper surfaces. Topographic features such as defects, residue from the patterning process, and grain boundaries are highlighted in red, green, and yellow, respectively. Samples' etching: **(a)** 6 min; **(b)** 9 min. 84
Figure 32 – Atomic number contrast SEM images, obtained with backscattered electrons, for the microstructured copper samples etched for 12 min (left) and 15 min (right), highlighting the increased inhomogeneity resulting from the prolonged etching

process with particles forming bridges, which result in the formation of two phases with not too dissimilar density, likely $Cu^0/Cu^+/Cu^{2+}$ based. 85
Figure 33 – Maps of surface potentials ϕCu, where $\mu Cu - \mu tip = 0 = \mu Cu - \mu tip = e(\phi tip - \phi Cu)$, where the tip is calibrated to be equal to the standard hydrogen electrode $\mu tip = 0 \text{ eV } vs\ SHE = -4.44 \text{ eV vs electrons at rest in vaccum}$, obtained via KPFM, of the copper current collectors with different etching times: **(a)** 0 min; **(b)** 6 min; **(c)** 9 min; **(d)** 12 min; **(e)** 15 min. Areas masked in dark blue represent excluded points where the surface potential dropped below 0 V due to charge accumulation. These areas were not considered for obtaining the average surface potential, as the focus is herein given to the background. 87
Figure 34 – (a) Average surface potential of each KPFM image for different etching durations; **(b)** standard deviation of surface potential of each KPFM image for different etching durations. 87
Figure 35 – Comparison of XPS spectra, near Cu 2p3/2 peaks, obtained for the microstructured copper samples etched for 0 **(left)** and 15 **(right)** minutes. Cu^+ peaks colored in blue, Cu^0 peaks colored in rose, Cu^{2+} peaks colored in green and loss features colored in red. 88
Figure 36 – Electrical properties of copper current collectors for each etching duration (0, 6, 9, 12, and 15 min): **(a)** temperature-dependent resistivity measurements for each etching duration; **(b)** comparison between the resistivity at room temperature (RT) and 40 °C for each etching duration; **(c)** temperature-dependent charge carrier mobility for each etching duration; **(d)** comparison between the mobility at RT and 40 °C for each etching duration; **(e)** temperature dependence of calculated bulk charge carrier concentration (CCCbulk) across etching durations; **(f)** CCCbulk at RT and 40 °C for each etching duration. Solid and dashed lines in (b), (d), and (f) represent data at RT and 40 °C, respectively. Note: negative values of the mobility and CCCbulk correspond to negative charges, which are electrons in this case. 89
Figure 37 – Two equivalent circuits used for modeling the PEIS. CPE: Constant Phase Element, Ma: modified restricted diffusion element. Suffixes: HF (high frequency), MF (mid-frequency), LF (low frequency). 91
Figure 38 – (a) Plots of selected PEIS cycles for different $Zn/Na_{2.99}Ba_{0.005}OCl$/microstructured Cu cells; **(b–f)** average values of different PEIS parameters for cells with each current collector type at RT and 40 °C, pre- and post-CV; **(b)** resistance in series R_{series}; **(c)** $1/R_{HF}$; **(d)** C_{HF}; **(e)** $1/R_{MF}$; **(f)** C_{MF}; **(g)** $1/R_{LF}$; **(h)** C_{LF}. The low-frequency semicircle was not present on 0 min cells at RT. Most cells did not show a post-CV LF semicircle; therefore, this data was excluded from the comparison. 92

Figure 39 – (a) Selected CV curves for Zn/$Na_{2.99}Ba_{0.005}OCl$/microstructured Cu cells with each current collector type; **(b)** comparison across etching duration of maximum discharge current (red) and maximum charging current (black) at RT and 40 °C. Note: effective surface area = 6.25 cm^2..... 94
Figure 40 – Charge/discharge cycle plots of all Zn/$Na_{2.99}Ba_{0.005}OCl$/microstructured Cu cells: **(a)** Comparison between all batches and etching times. Discharge was performed through a 26.4 kΩ or 21.7 kΩ external material resistor. **(b)** Cells from batch 2; **(c)** cells from batch 1; **(d)** cells from batch 3. 95
Figure 41 – GITT performance of selected Zn/$Na_{2.99}Ba_{0.005}OCl$/microstructured Cu cells with different etching durations: **(a)** 0 min; **(b)** 9 min (140 h); **(c)** zoom between 110 h and 140 h; **(d)** 12 min; **(e)** 15 min; and **(f)** zoom of 15 min between 110 and 125 h. ... 96
Figure 42 – Comparison across etching durations of selected parameters (average values) for the Zn/$Na_{2.99}Ba_{0.005}OCl$/microstructured Cu cells (left axis) and microstructured Cu current collector parameters (right axis): **(a)** $1/R_{HF}$ at RT and 40 °C and surface potential vs. etching time; **(b)** pre-CV C_{LF} at RT and 40 °C, Max $I_{discharge}$ at RT and 40 °C, and CCCbulk (electrons) at RT and 40 °C. 98
Figure 43 – Correlation between maximum cyclic voltammetry (CV) currents and R_{HF}: **(a)** Maximum charging current vs. R_{HF}. **(b)** Maximum discharging current vs. R_{HF}. The red dashed line indicates the $1/R_{HF}$ trend line; R^2 denotes the corresponding coefficient of determination. 98

List of Abbreviations

(P)EIS	(POTENTIOSTATIC) ELECTROCHEMICAL IMPEDANCE SPECTROCOPY
3-THMAI	3-THIENYL-METHACRYLIC ACID-IODIDE
AC	ALTERNATE CURRENT
AFM	ATOMIC FORCE MICROSCOPE
BAI	N-BUTYLAMMONIUM IODIDE
BSE	BACKSCATTERED ELECTRON
CB	CHLOROBENZENE
CBM	CONDUCTION BAND MINIMUM
CC	CURRENT COLLECTOR
CCC	CHARGE CARRIER CONCENTRATION
CIGS	COPPER INDIUM GALLIUM SELENIDE
CIS	SCANNING KELVIN PROBE
CIS	COPPER INDIUM SELENIDE
COHP	CRYSTAL ORBITAL HAMILTON POPULATION
CV	CYCLIC VOLTAMETRY
CVD	CHEMICAL VAPOUR DEPOSITION
DMF	DIMETHYLFORMAMIDE
DMSO	DIMETHYLSULFOXIDE
DOS	DENSITY OF STATES
DSSC	DYE SENSITIZED SOLAR CELLS
EC	EQUIVALENT CIRCUIT
EDAI	ETHANE-1,2-DIAMMONIUM IODIDE
EDLC	ELECTRIC DOUBLE LAYER CAPACITOR
EDS	ENERGY DISPERSIVE SPECTROSCOPY
ERE	EXTERNAL RADIATIVE EFFICIENCY
ETL	ELECTRON TRANSPORT LAYER
FCUP	FACULTY OF SCIENCES OF THE UNIVERSITY OF PORTO
FEUP	FACULTY OF ENGINEERING OF THE UNIVERSITY OF PORTO
FF	FILL FACTOR
FOEI	PENTAFLUOROPHEN-OXYETHYLAMMONIUM IODIDE
FTO	FLURINE-DOPED TIN OXIDE
GB	GLOVEBOX

GBL	GAMMA-BUTYROLACTONE
GDP	GROSS DOMESTIC PRODUCT
GITT	GALVANOSTATIC INTERMITTENT TITRATION TECHNIQUE
HTL	HOLE TRANSPORT LAYER
ICBA	INDENE-C60 BISADDUCT
IQR	INTERQUARTILE RANGE
ITO	INDIUM-DOPED TIN OXIDE
IV	CURRENT-VOLTAGE
JSC	SHORT CIRCUIT CURRENT DENSITY
KPFM	KELVIN PROVE FORCE MICROSCOPY
KSCN	POTASSIUM THIOCYANATE
LB	LANGMUIR–BLODGETT
LED	LIGHT EMITTING DIODE
MPP	MAXIMUM POWER POINT
MW	MOLECULAR WEIGHT
NASICON	NA+ SUPERIONIC CONDUCTOR
NGS	NEW GENERATION STORAGE
NIR	NEAR INFRA RED
NMP	N-METHYL-2-PYRROLIDONE
NTP	NORMAL TEMPERATURE AND PRESSURE
OCV	OPEN CIRCUIT VOLTAGE
OIHP	ORGANIC-INORGANIC HALIDE PEROVSKITE
PAI	PROPYLAMMONIUM IODIDE
PCBM	PHENYL-C61-BUTYRIC ACID METHYL ESTER
PCE	POWER CONVERSION EFFICIENCY
PEAI	PHENETHYLAMMONIUM IODIDE
PEDOT:PSS	POLY(3,4-ETHYLENEDIOXYTHIOPHENE) POLYSTYRENE SULFONATE
PEN	POLYETHYLENE NAPHTHALATE
PEO	POLYETHYLENE OXIDE
PMMA	POLY(METHYL METHACRYLATE)
PNG	PORTABLE NETWORK GRAPHICS
PSC	PEROVSKITE SOLAR CELL
PTAA	POLY(TRIARYLAMINE)
PTFE	POLYTETRAFLUOROETHYLENE

PTM	PHTHALAMIDE
PV	PHOTOVOLTAIC
PVAC	POLYVINYL ACETATE
PVC	PHOTOVOLTAIC CELL
REACH	REGISTRATION, EVALUATION, AUTHORISATION AND RESTRICTION OF CHEMICALS
RIE	REACTIVE ION ETCHING
RMS	ROOT MEAN SQUARE
ROI	REGION OF INTEREST
RT	ROOM TEMPERATURE
S-Q	SHOCKLEY–QUEISSER
SE	SECONDARY EMISSION
SEI	SOLID ELECTROLYTE INTERFACE
SEM	SCANNING ELECTRON MICROSCOPE
SHE	STANDARD HYDROGEN ELECTRODE
SKP	SCANNING KELVIN PROBE
SKPM	SCANNING KELVIN PROBE MICROSCOPY
SOC	SPIN ORBIT COUPLING
SSB	SOLID STATE BATTERY
TCO	TRANSPARENT CONDUCTIVE OXIDE
TSC	THIOSEMICARBAZIDE
UP	UNIVERSITY OF PORTO
UV	ULTRA-VIOLET
VBM	VALENCE BAND MAXMIMUM
WF	WORK FUNCTION
XPS	X-RAY PHOTOELECTRON SPECTROSCOPY
XRD	X-RAY DIFFRACTION

Introduction

Context

It is very common to refer to the ages of history by the materials and tools humans mastered. From the stone-age to the silicon age. Yet an equally important narrative focuses on our ability to channel the constraints of the laws of thermodynamics into providing useful energy; *work*. From fire for food, gravity for water to steam for turbines. This capacity has propelled us from the early days of evolution to the empires of history, and now it propels our modern economic system [1]. However, the same laws that allow this evolution are also causing its byproducts to stifle it. This phenomenon is commonly referred to as human-induced climate change, which is a result of the emission of greenhouse gases as a byproduct of burning fossil fuels [2] to produce *work*. The international monetary fund estimates that the accumulated cost of climate change will be 23% of annual global gross domestic product (GDP) by 2100 [3]. Meanwhile the same estimate indicates that an investment of 2% of annual GDP would be enough to support sufficient mitigation and adaptation efforts, which include, among others, the restructuring of our energy system into sustainable sources.

In practice, the transition also involves a shift in scale: centralized plants give way to distributed microgeneration, including rooftops, facades, and community systems, whose rapid growth is already evident and policy-relevant [4] [5]. Because output is variable, mixed capture and storage architectures, for example PV combined with batteries, align supply with demand, reduce curtailment, and improve resilience [6]. Any viable solution must be simple, cost-effective, and environmentally responsible, and it should be guided by life-cycle assessment to avoid burden shifting as deployment scales [7].

Motivation

Conventional batteries impose weight and volume penalties. In electric vehicles they force the use of lightweight structures that add cost [8]. On-site storage often needs large space, and future space missions will depend on renewable systems, increasing demand for lightweight, high-energy storage [9], [10].

Solid-state batteries address many of these issues. They enable faster charging, improve safety by eliminating flammable components, resist dendrites, reduce thermal runaway and oxygen release, and operate over wider temperatures. Their higher electrolyte density suits applications where weight and volume are constrained, including electric vehicles and aerospace [11].

Shaping current-collector and electrode topography may further improve performance. Microstructured electrodes increase surface area and boost double-layer capacitance in supercapacitors [12], [13]. In batteries, three-dimensional architectures enhance interface stability and adhesion and help suppress dendrites, improving safety and cycle life [14], [15], [16]. Pseudocapacitors also benefit because their surface-confined reactions are sensitive to current-collector geometry and morphology [17].

Lithium solid-state batteries perform well but face safety and cost concerns due to lithium scarcity and extraction challenges [18]. Sodium offers a cheaper, more abundant alternative with better sustainability [19], though its larger ionic radius lowers energy density. Embedding storage into structural components mitigates weight and space limits [20]. Coaxial structural batteries with sodium solid electrolytes combine cost and safety advantages with load bearing [21]. Braga's group uses $Na_{2.99}Ba_{0.005}OCl$, with ionic conductivity of 10^{-2} S cm^{-1} and a pyroelectric coefficient of 5.37 C m^{-2} $°C^{-1}$, attributed to ferroionic behavior [22],[23]. In an anode-less configuration, dissimilar current collectors set a chemical potential difference that drives sodium plating and stripping during charge and discharge [24]. Performance depends on plating efficiency and fully reversible sodium deposition [25], [26].

In parallel, solar energy capture using photovoltaic cells has attracted growing research and commercial interest. Most commercially available solar cells rely on monocrystalline or polycrystalline silicon, which are costly and energy intensive to manufacture [27]. The combination of high manufacturing energy demand, stringent processing requirements, substantial material costs, and only modest efficiencies has motivated the search for photovoltaic materials and device architectures that can improve performance while being cheaper to manufacture and more environmentally friendly to produce and decommission.

Perovskite solar cells (PSCs) have emerged as a leading candidate. Perovskites denote a crystal structure with the general formula ABX_3. PSCs commonly employ Organic-Inorganic Halide Perovskites (OIHPs), composed of an organic or inorganic A-site cation, a group XIV metal, typically Pb, and a halide at the X site, most often iodide. Perovskite films combine strong optical absorption, efficient charge transport, and notable defect tolerance, which together yield high performance in lab-scale devices [28]. Still, their reliance on lead, which is highly toxic, represents a significant concern [29]. To address this, tin-based perovskite solar cells have been proposed and studied for several years. Theoretical calculations indicate that these materials may even exceed the performance of their lead-based counterparts [30]. However, realizing this potential requires resolving

issues in fabrication, compatibility with materials originally developed for lead-based PSCs, and severe stability challenges [31].

Taken together, the energy capture and storage systems examined in this work constitute realistic alternatives to the mainstream approaches in these fields. Beyond their scientific and technological interest, they offer tangible routes to simplify manufacturing and improve the safety and performance of next generation energy capture and storage systems.

Objectives

This work is organized in two parts. Part I examines tin-based perovskite solar cells. Part II investigates microstructured copper current collectors for sodium-based solid-state batteries.

The work on tin-based perovskite solar cells had an initial goal of development and optimization of functional lab-scale devices, followed by a gradual introduction of semi-transparency in the cells for their utilization in agrivoltaics. From the beginning we understood these goals were extremely ambitious, especially considering that tin-based perovskite solar cells were a novelty in the context of this laboratory. Early results showed that the original targets were not attainable within the available timeframe and resources, so we redirected the study toward degradation mechanisms in tin-based perovskite solar cells and toward a pragmatic route to obtain functional devices using the materials and equipment at hand. We then defined the following specific objectives: (i) study oxidation and degradation in tin-based perovskite solar cells, (ii) assess the viability of purification methods for low-grade partially oxidized precursors (iii) evaluate the effect of modifying perovskite composition through cation exchange or additives, (iv) fabricate functional devices using high-grade precursors, and (v) compare the performance of devices made from purified precursors with those made from high-grade precursors.

On the other hand, the work on microstructured copper current collectors for sodium-based solid-state batteries was conducted in collaboration with New Generation Storage project partners from CENIMAT|i3N-NOVA, who fabricated the microstructured copper collectors. Our goals were to characterize the morphology and electrochemistry of these collectors, integrate them into sodium-based solid-state pouch cells, and relate collector properties to device performance. We investigated the following variables: (i) surface geometry and morphology of the collectors, (ii) electrochemical characteristics of the copper surface, (iii) charge transport characteristics of the collectors, (iv) the

electrochemical nature of the interface between the electrolyte and the current collector, (v) overall pouch cell performance, including impedance, cycling behavior, and stability, and (vi) correlations between pouch cell performance metrics and collector characterization parameters.

Contributions

This thesis was developed under Agenda “NGS—New Generation Storage”, ref. no. C644936001-00000045, investment project no. 58, under the Incentive System “Agendas for Business Innovation”, funded by the PRR—Recovery and Resilience Plan and the European Union’s NextGenerationEU funds. However, the views and opinions expressed herein are solely those of the author(s) and do not necessarily reflect the views and opinions of the European Union or the European Commission. Neither the European Union nor the European Commission can be held responsible for them.

During this period, beyond the work reported in this thesis, I contributed to the fabrication and testing of coaxial structural batteries within the NGS project. In parallel, I developed Python scripts to automate data collection and analysis for several instruments, including Asylum Research AFM, Biologic SKP, Linseis Hall effect, and Gamry and Biologic potentiostats. After refactoring, these scripts will be released for public use through a GitHub repository.

Portions of this work were presented at the Integrity-Reliability-Failure 2025 (IRF 2025) and the Doctoral Congress in Engineering 2025 (DCE 2025), both held at FEUP.

The collaborative work under the NGS project led to the publication of “Surface Morphology and Electrochemical Behavior of Microstructured Cu Electrodes in All-Solid-State Sodium Batteries,” (Molecules 2025, 30(17), 3493; 10.3390/molecules30173493) for which I was first author. My roles included conceptualization, methodology, software, formal analysis, investigation, data curation, visualization, and original draft preparation.

Finally, during this master’s thesis I also served as co-first author of the review article “Ferroelectric and Ferroionic Multifunctional Quantum Sensors: Incursion into Applications,” which is currently under review. My primary contribution was a section on the ferroionic properties of organic-inorganic halide perovskites, and I also contributed extensively to the research, writing and reviewing of other sections.

1. Part I – Background and state-of-the-art

This chapter covers the theoretical and technological background of the work about perovskite solar cells. It begins with an overview of general photovoltaic principles and technologies, followed by a detailed discussion of the fundamental aspects of perovskite solar cells, including their chemistry, physics, device architectures, synthesis approaches and associated challenges. Finally, the chapter examines the distinctive properties of tin-based perovskites, synthesizing key findings from relevant research in this emerging area.

1.1. General theoretical principles and technological overview

The physics of photovoltaic devices presented in this section are largely adapted from the book: Würfel & Würfel - *Physics of Solar Cells: From Basic Principles to Advanced Concepts* [32].

1.1.1. Band structure and photovoltaic effect in semiconductors

In crystalline solids, the periodicity of the lattice imposes a periodic potential, so electrons energies form a standing-wave whose discrete levels broaden into nearly continuous energy bands. As with sound waves, interference creates ranges of forbidden states, the band gaps. Solids contain multiple gaps at different energies. States below the Fermi level are largely filled, so electronic conduction requires electrons with energies near or above it. This means the gap nearest the Fermi level most strongly governs the optoelectronic behavior of a material. Bands below and above the Fermi level are termed valence and conduction bands, respectively. On a vacuum-referenced scale (E = 0 eV), the higher energy valence band maximum (VBM) corresponds to the ionization energy, the lower energy conduction band minimum (CBM) corresponds to the electron affinity, and the Fermi level corresponds to the work function at the surface.

This band picture explains conductivity classes. In metals, bands cross or lie very near the Fermi level, so carriers are readily available and conductivity is high. In insulators, a wide gap separates valence and conduction bands at the Fermi level, so promoting carriers is energetically costly and conductivity is low. Semiconductors resemble insulators but with much smaller gaps, typically a few eV, matching near-infrared, visible, and near-ultraviolet photon energies. Photovoltaic action relies on promoting an electron from the valence to the conduction band by photon absorption. Because energy levels are tied to electron crystal momentum, any change of state must conserve both energy and total momentum. When a transition requires a change in momentum, a phonon from the lattice must be created or absorbed to balance the momentum. If the conduction

band minimum and valence band maximum share the same momentum, the gap is direct; if they do not, it is indirect. Direct gaps allow phonon-less transitions with much higher transition probability, leading to a higher absorption coefficient. These materials are therefore more efficient photovoltaic absorbers.

When an electron is excited to the conduction band, it leaves an unfilled state in the valence band that behaves as a quasi-particle called a hole. Because charge neutrality must be maintained, the electron-hole pair has two outcomes. They either recombine, so the electron does not contribute to current, or they are separated which is how charge moves through the device. Thus, maximizing photovoltaic current requires efficient separation. In traditional semiconductors, separation is achieved by a p-n junction. A region with higher donor (electron) concentration meets a region with higher acceptor (hole) concentration, which creates a depletion zone and an internal electric field across it. That field drives electrons and holes apart while diffusion moves the charges away from the junction, where their concentration is highest. Many thin film photovoltaic devices rely on a slightly different picture. Separation occurs through diffusion driven by carrier concentration gradients and by drift due to the electric field across the absorber. The concentration gradient arises when electrons are removed at one side by a contact with slightly higher electron affinity and holes are removed at the other side by a contact with slightly lower ionization energy. Equalization of electrochemical potentials, that is, Fermi levels, creates an electric field across the absorber. This field is often weaker than that of a p-n junction, such as in 3D perovskites, so these devices often require very long diffusion lengths to separate pairs before recombination [33].

1.1.2. Evolution of photovoltaic cell (PVC) technology

The evolution of solar cell material technology is conventionally divided into three main generations based on their maturity and design principles [34], whose PCE time evolution is shown in **Figure 1**:

1. The first generation uses high grade semiconductor materials like Silicon (Si) or Gallium Arsenide (GaAs) to create large monocrystalline or polycrystalline structures. These are the most well studied and widely available for commercial applications. Despite their decent efficiencies they use large amounts of high-grade materials, and their fabrication involves energy intensive and wasteful processes.
2. The second generation focuses on reducing the production cost of solar cells by requiring less strict material specifications and using simpler fabrication techniques. This is generally achieved using thin films, at the cost of efficiency

and longevity. The materials used include amorphous silicon (a-Si), Cadmium Telluride (CdTe) and Copper Indium (Gallium) Selenide (CIS/CIGS).

3. The third generation marks a shift in PVC's by introducing several novel materials, architectures and concepts to the photovoltaic landscape. These include concentrated photovoltaic cells, organic and hybrid cells, multi-junction cells, Dye-Sensitized cells, Quantum dots and Perovskites. The latter of which will be in focus on this work.

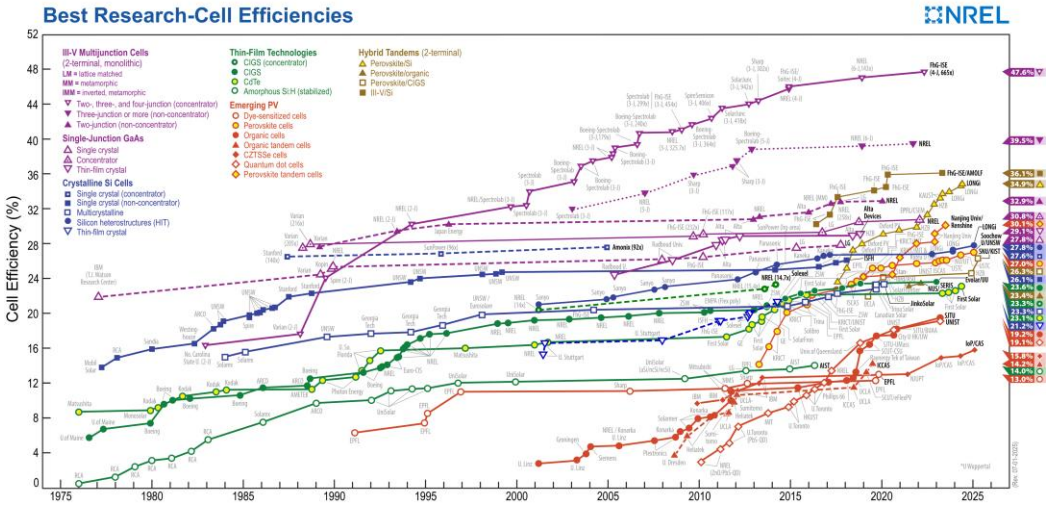


Figure 1 – Evolution of research solar cell's efficiencies over time. This plot is courtesy of the National Renewable Energy Laboratory, Golden, CO

1.1.3. Factors limiting efficiency of photovoltaic cells.

The current density-voltage (*J-V*) characteristic describes how a solar cell converts light into electrical power. Under illumination, the total current results from the superposition of the photogenerated current and the diode current that the device exhibits in the dark, with additional effects from practical parasitic resistances such as series and shunt resistance.

A compact and widely used representation of this behavior is given by:

$$J(V) = J_{ph} - J_0 \left[exp\left(\frac{q\,(V + JR_s)}{n\,\mathrm{k_B T}} \right) - 1 \right] - \frac{V + JR_s}{R_{sh}}$$

In this expression, J_{ph} is the light-generated current density determined by the absorbed photon flux and the efficiency of carrier collection. J_0 is the dark saturation current density that aggregates all recombination pathways; smaller values indicate lower recombination. The ideality factor n is typically near 1 for radiative recombination and near 2 for trap-assisted Shockley Read Hall recombination in depletion or defect rich regions. The resistance in series, R_s, arising from contacts and transport layers, reducing

the effective voltage at high current, pulling the curve downward at low voltages. the shunt resistance, R_{sh}, provides a leakage current near short circuit. The constants q, k_B, are the electron charge and Boltzmann constant, and the variable T is the temperature. In qualitative terms, an increase in J_0 shifts the curve toward lower voltages, a large R_s flattens the knee of the curve, and a small R_{sh} pulls the curve downward.

Key figures of merit follow directly from this model:

- **Short-circuit current density, $J_{SC} = J(V = 0)$.** When R_{sh} is large and J_0 is small, $J_{SC} \approx J_{ph}$. Under these conditions, optics and charge collection primarily limit J_{SC}.
- **Open-circuit voltage, OCV**: $V_{OC} \approx \frac{n k_B T}{q} \ln\left(\frac{J_{ph}}{J_0} + 1\right)$. It's the reverse bias voltage at which J = 0, neglecting parasitic resistances. This relation shows that reducing J_0 increases OCV logarithmically.
- **Fill factor, $FF = \frac{V_{mpp} J_{mpp}}{V_{OC} J_{SC}}$**. FF captures the squareness of the J-V curve, based on the maximum power point (mpp). It is primarily degraded by R_s and R_{sh}, with a secondary dependence on recombination through its influence on curvature.
- **Power conversion efficiency, PCE: $\eta = \frac{V_{OC} J_{SC} FF}{P_{in}}$**, where P_{in} is the incident optical power density.

This framework separates the main performance levers in a clear way. Optical absorption and carrier collection set J_{SC}, recombination determines J_0 and therefore OCV, and parasitic resistances largely govern FF.

Within the Shockley–Queisser (S-Q) detailed balance framework, which assumes a single junction under one sun illumination (1 kW m^{-2}), an ideal step function absorptivity above the band edge, and radiative recombination as the sole loss mechanism, the maximum theoretical efficiency is approximately 33% at a bandgap of approximately 1.34 eV. This limit reflects a fundamental trade off with bandgap: increasing E_g suppresses the radiative dark saturation current, which raises OCV, but it also truncates the usable spectrum and lowers J_{SC}.

In the radiative limit, the dark saturation current density follows $J_{0,\mathrm{rad}}(E_g, T) \propto exp\left(-\frac{E_g}{k_B T}\right)$ and the short circuit current density equals the integrated solar photon flux above the band edge, $J_{SC}(E_g) \propto \int_{E_g}^{\infty} \Phi_{\odot}(E)\, dE$. Thus, J_0 decreases exponentially with increasing E_g, while J_{SC} is set by the cumulative photon flux above the band edge and therefore diminishes as E_g increases.

A convenient scalar to quantify voltage loss is the open circuit voltage deficit, defined as the difference between the bandgap voltage and the measured open circuit voltage:

$$\Delta V_{OC} \equiv \frac{E_g}{q} - V_{OC} = \underbrace{\left(\frac{E_g}{q} - V_{OC}^{\mathrm{rad}}\right)}_{\text{thermodynamic and optical limit}} + \underbrace{\left(\Delta V_{OC}^{\mathrm{nonrad}}\right)}_{\text{nonradiative loss}}$$

The nonradiative component can be written in terms of the external radiative efficiency, ERE, which is the quantum efficiency under forward bias:

$$\Delta V_{OC}^{\mathrm{nonrad}} = \frac{k_B T}{q} \ln\left(\frac{1}{\mathrm{ERE}}\right).$$

Improving ERE through bulk and interface passivation, cleaner surfaces, and lower defect densities directly increases OCV by reducing ΔV_{OC}^{nonrad}.

Optical losses, which influence J_{SC} and V_{OC}^{rad}, arise from reflection, parasitic absorption in contacts and transport layers, incomplete absorption in thin or weakly absorbing films, and sub bandgap transmission.

Transport and resistive losses primarily affect the fill factor. A large series resistance R_s, caused by limited conductivity or contact resistance, reduces the effective voltage at high current and flattens the J-V knee. A small shunt resistance R_{sh} increases leakage near short circuit and pulls the curve downward. These effects usually have a modest influence on OCV but can cause several absolute percent losses in efficiency through the fill factor.

Collection losses occur when photogenerated carriers fail to reach the contacts. Limited mobility lifetime product $\mu \cdot \tau$, interfacial band misalignment, and space charge can depress J_{SC} and, in some cases, produce an S shaped J-V characteristic. Together, these considerations provide a clear map from physical loss mechanisms to their signatures in J_{SC}, OCV , and FF, and they guide strategies to recover voltage and current in device optimization. These losses are summarized on **Figure 2**.

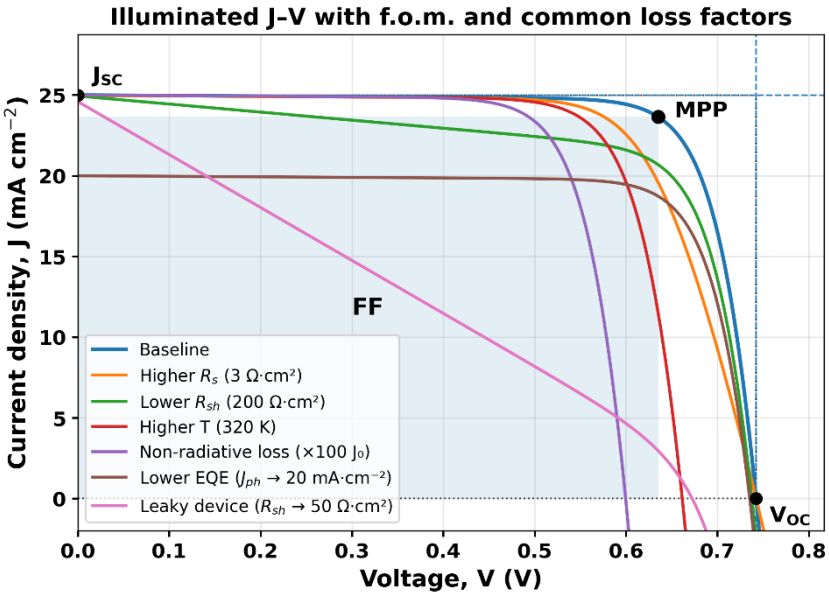


Figure 2 – Representative J–V curves affected by common loss factors. Curves calculated from the illuminated diode model (equations above) using typical solar-cell parameters. The baseline is shown with J_{sc}, OCV, FF, and MPP marked. Variants illustrate the impact of common loss factors on the J-V curve.

1.2. Perovskite solar cells

Perovskite solar cells (PSCs) are an emerging technology that aims to solve some of the problems related to traditional silicon cells by reducing cost and improving efficiency [28]. Perovskites are a class of compounds which have the general chemical formula $A^{2+}B^{4+}(X^{2-})_3$, derived from the original perovskite mineral Calcium Titanate ($CaTiO_3$). The fact that the crystal structure includes 3 ions of different sizes allows for a wide variety of formulations and properties, ranging from ferroelectric materials like Lead Zirconate Titanate (PZT – $Pb(Zr_xTi_{1-x})O_3$) [35], to semiconductor materials like halide perovskites (ABX_3, where X = I, Br, Cl). This last group is of highest importance for optoelectronic applications, such as solar cells or light emitting diodes (LED's) [36], due to their optimal bandgaps, high optical absorption, efficient emission and strong charge mobility [37].

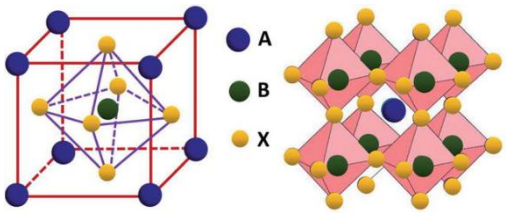


Figure 3 – Diagram of the general perovskite crystal structure. Reproduced from reference [38]. Used under the terms of CC BY 3.0.

1.2.1. OIHPs - Organic Inorganic Halide Perovskites

In organic-inorganic halide perovskites (OIHPs), three halide ions are paired with a group XIV metal cation (Ge^{2+}, Sn^{2+}, Pb^{2+}) at the B-site and with a large A-site cation, which can be either an inorganic group I ion (Cs^+, Rb^+) or an organic molecule such as methylammonium ($CH_3NH_3^+$, MA^+) or formamidinium ($CH_5N_2^+$, FA^+). The introduction of organic cations was driven by the need to stabilize the ideal cubic perovskite structure, which is fully symmetric and particularly suitable for optoelectronic applications [39]. The structural stability of a perovskite can be quantified using the Goldschmidt tolerance factor (*t*):

$$t = \frac{r_A + r_X}{\sqrt{2}(r_B + r_X)}$$

where r_A, r_B, r_X are the effective ionic radii of the A, B and X-site ion, respectively [40]. The most common inorganic A-site cation, Cs^+, has an ionic radius of 1.88 Å [41]. For $CsPbI_3$, a widely studied inorganic perovskite, the tolerance factor is 0.81. The optimal range for halide perovskites is around 0.9, meaning that a larger A-site cation is required to achieve a stable cubic phase. Organic cations such as MA^+ (2.17 Å) and FA^+ (2.53 Å) [42] yield tolerance factors closer to 0.9, improving the structural stability of the cubic phase, as shown on **Figure 4**.

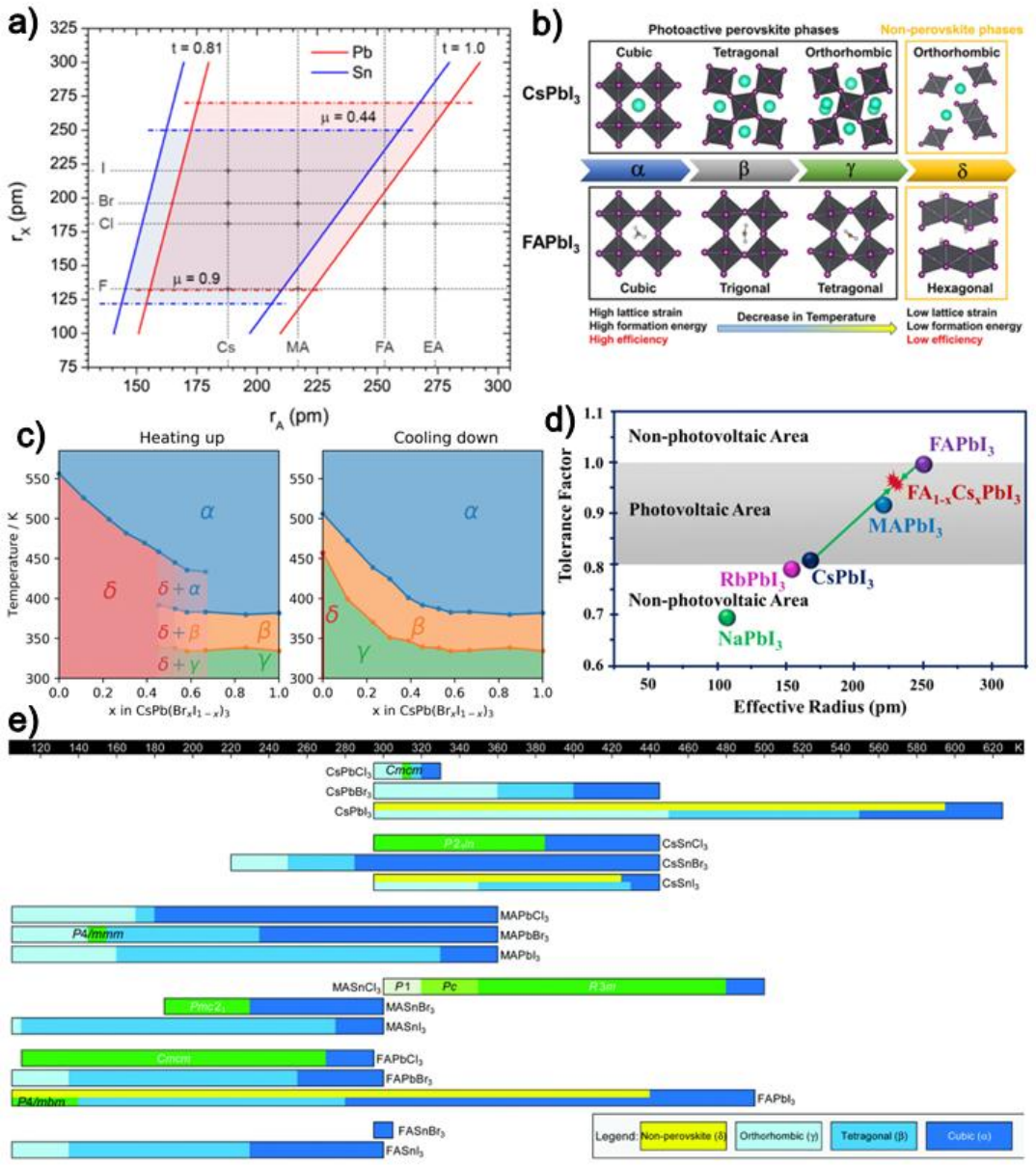


Figure 4 – (a) Formability of 3D lead (red) and tin (blue) halide perovskites as a function of A-site cation and halide anion radii. Solid and dashed lines mark the bounds of the tolerance and octahedral factors, respectively. Adapted from [43] Reproduced with permission under ACS copyrights **(b)** Structural phases of formamidinium- and cesium- based halide perovskites. Reproduced with permission from [44]. Copyright 2021 American Chemical Society. **(c)** On the left: Heating phase diagram for $CsPb(Br_xI_{1-x})_3$ thin films aged in a humid environment for composition, x, between 0 (pure $CsPbI_3$) and 1 (pure $CsPbBr_3$) On the right: Cooling phase diagram for the same $CsPb(Br_xI_{1-x})_3$ thin films as they cool down from a high temperature. [45]. Used under the terms of CC BY 3.0. **(d)** Dependance of tolerance factor on A-site cation effective radius. Adapted from [46]. Used under the terms of CC BY-NC 3.0. **(e)** Summary of phase transition temperatures in halide perovskites reported in the literature collected at ambient pressure as a function of composition. Cubic structures exhibit Pm3m symmetry, tetragonal structures exhibit either I4/mcm or P4/mbm symmetry, and the orthorhombic phase exhibits Pnma symmetry, unless otherwise noted. Green colors indicate phases not represented by the above categories. Adapted from [47]. Used under the terms of CC BY-NC 3.0.

Besides the typical perovskite polymorphs (commonly called “black phases” and denoted as α, β, and γ), iodide-based metal halide perovskites can also adopt a non-perovskite polymorph (commonly called the “yellow phase” and denoted as δ or Y), which is a photo-inactive insulator [44]. In many compositions, particularly all-inorganic and

formamidinium-based iodide perovskites, the black phases are only meta-stable under normal temperature and pressure (NTP) conditions, with the yellow δ-phase being the thermodynamic ground state. Although δ-phase formation can occur spontaneously at ambient conditions, it is often accelerated by external factors such as exposure to moisture, oxygen, elevated temperature, or prolonged illumination [44], [47].

The energy levels of ion orbitals are crucial in determining the band structure of semiconductor perovskites (**Figure 5a-f**). Their strong optical absorption, on the order of 10^5 cm^{-1}, arises from their small direct band gap [43]. The VBM is primarily determined by the p orbital energy level of the X-site anion. Larger anions (Cl < Br < I) have higher energy p orbitals, which raise the VBM [48]. The CBM energy depends on the interaction between the B-site cation and the X-site anion. This interaction involves an antibonding configuration of their p orbitals, which have strong overlap due to the large size of group XIV metals and halides [49]. Additionally, spin-orbit coupling (SOC) lifts the degeneracy of states close to the CBM, particularly in PbX_3 perovskites; as Pb is larger than Ge and Sn; leading to a lower CBM [50].

The A-site cation does not directly contribute to the band structure but influences it indirectly by modifying the lattice size, which alters the B-X orbital overlap. A reduction in the B-X-B bond angle from the ideal 180º of the cubic phase (caused by increased octahedral tilting) reduces orbital overlap, narrows the electronic bands, and typically increases the band gap [49]. A-site cations can also cause charge imbalance. Dipolar cations, such as methylammonium or formamidinium, introduce slight lattice polarization. In halide perovskites, this dielectric moment reduces the ionization potential, raising the VBM and lowering the band gap [51]. The dielectric nature of organic cations paired with the soft, deformable nature of the perovskite lattice can reduce the exciton binding energy, which is inversely proportional to the square of the dielectric constant (dielectric screening) [52]. Furthermore, the strong B-X orbital overlap results in small effective masses for electrons and holes. This leads to both smaller binding energy and higher charge carrier mobility, contributing to more efficient charge extraction and less output voltage loss [43].

OIHPs are also known for their defect tolerance. Because the band structure depends mainly on the B and X-site ions, defects associated with them are most relevant to optoelectronic performance [48]. The antibonding configuration of the B-X orbitals that create the conduction band, result in reduced electron density between them. Defects in such a configuration typically occur near the band edges and are highly charge selective, acting as unipolar shallow traps rather than efficient recombination centers (**Figure 5h**).

This contributes to the resilience of OIHPs against defect-induced performance losses [53],[54].

One final advantage of OIHP's is their tunability. By mixing different cations and anions a mixed perovskite structure can be created. The fine tuning of properties such as tolerance factor, bandgap and stability can be easily achieved by changing the stoichiometric ratios of the ions in the material. This confers a degree of adaptability and versatility that is unique to OIHP's, making them especially suitable for tandem devices (devices with more than one active layer) [55], [56].

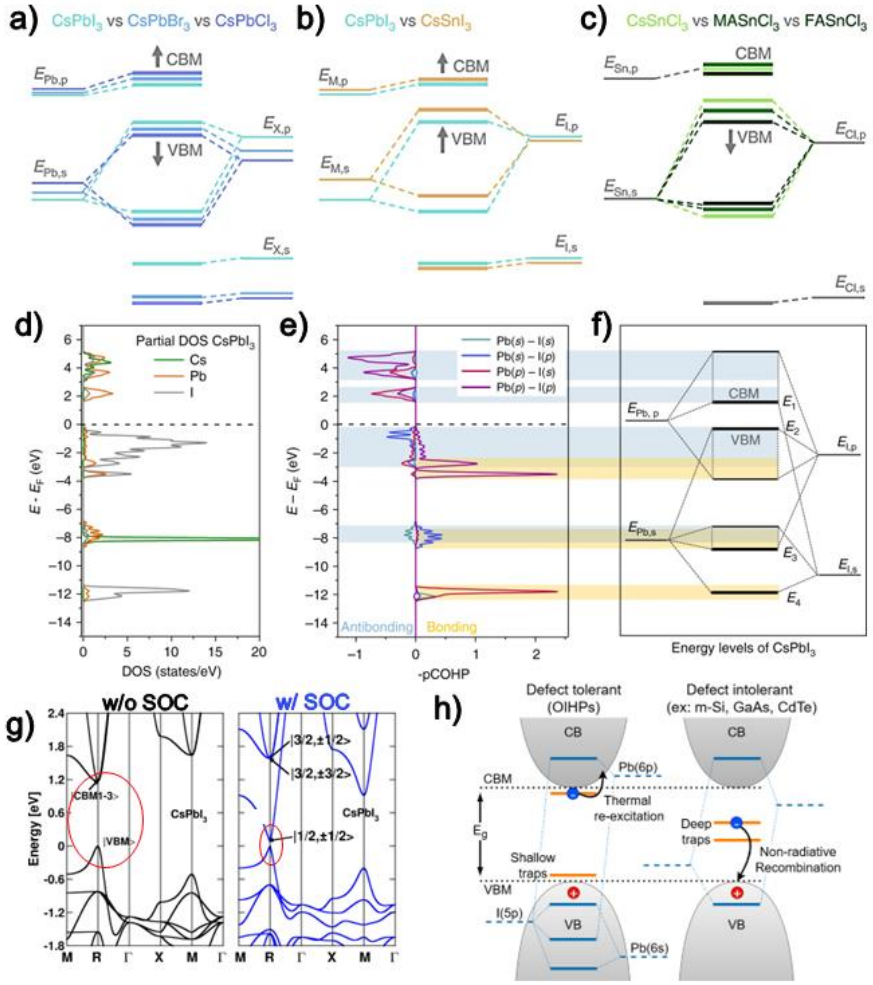


Figure 5 – (a-c) Schematic energy levels in AMX_3 perovskites. **(a)** represent trends in changing the halide anions, **(b)** represent trends in changing the metal cations. **(c)** represent trends in changing the A-site cation. Arrows indicate the shift in energy levels upon atom or small molecule substitution. **(d-f)** Orbital contributions to the energy bands of $CsPbI_3$. **(d)** $CsPbI_3$ DOS projected on the Cs, Pb, and I atoms (partial DOS). **(e)** Orbital-resolved COHP; positive (negative) sign indicates bonding (anti-bonding) character. The line colors indicate which atomic orbitals are involved in the bonds (anti-bonds). **(f)** Schematic energy level diagram extracted from the COHP analysis; the energy levels E_1 to E_4 which are relevant for the tight-binding analysis are marked. Bonding interactions are shaded in yellow, and anti-bonding interactions in pink. (a-f) Adapted from [49]. Used under the CC BY-NC 4.0. **(g)** Calculated electronic band structure of α-$CsPbI_3$ with (black/left) and without (blue/right) spin-orbit coupling interaction. Reproduced from [50]. Used with permission under Copyright © 2013 American Chemical Society. **h)** Schematic illustration of deep and shallow charge carrier traps in perovskites. Based on [54] and [57].

1.2.2. Device architecture

Traditional silicon based solar cells typically rely on a homojunction between n and p doped silicon slabs for charge separation. This requires expensive and energy intensive doping techniques [58]. Furthermore, their limited optical absorption requires the use of thick absorption layers, in the order of hundreds of micrometers [34]. PSCs' high optical absorption allows the use of thin films, with thicknesses on the order of hundreds of nanometers [59]. This fact significantly reduces the amount of material used, lowering cost and ecological footprint. Furthermore, it facilitates the use of a wider range of synthesis methods such as spin coating, spray coating, inkjet and slot-die coating [60].

Perovskite solar cells originated from dye-sensitized solar cells (DSSCs), where a mesoporous TiO_2 scaffold was infiltrated with a light-absorbing dye to generate photocurrent. In 2009, Miyasaka and co-workers replaced the dye with halide perovskites, demonstrating much higher photocurrents but limited stability [61]. While mesoporous devices were crucial in establishing the high efficiency potential of perovskite photovoltaics, research has since moved toward planar architectures that are more scalable and stable due to their fully solid-state architecture [59], [62].

In full planar architectures, the intrinsic perovskite semiconductor is "sandwiched" between two thin films: a P-type and an N-type semiconductor, the so-called charge transport layers. These layers allow for the selective extraction of charges, efficiently un-binding excitons and leading to lower recombination rates [54]. The selective extraction of charges can only occur if the energy levels of the transport layers are correctly aligned with the energy levels of the perovskite as seen in **Figure 6b**, which can be achieved by doping or compositional engineering [63].

Planar structures can be divided into two groups. Normal architecture or N-I-P (N-type – Intrinsic – P-type), when the ETL contacts the transparent (front) electrode, and inverted architecture or P-I-N (P-type – Intrinsic – N-type), when the HTL contacts the transparent electrode [28]. The former architecture was the first adopted, as it was carried over from the mesoporous architecture, and since then achieved the highest certified efficiency for non-tandem PCS's of 26% as of 2025 (Figure 1). When contrasted with mesoporous structures, N-I-P designs show several additional advantages. Planar architectures accommodate complex perovskite compositions more effectively than mesoporous scaffolds and simplify optical design by reducing scattering and parasitic absorption [63]. Planar interfaces are easier to engineer, enabling control of band alignment and defect passivation that improves reproducibility and stability [63]. However, because this architecture evolved from mesoporous designs, it retains drawbacks such as

degradation pathways, scaling challenges, hysteresis, and costly hole transport layers [64].

The planar p–i–n architecture offers significant advantages due to its compatibility with low-temperature processing. Organic ETLs such as PCBM, or solution-processed oxides like ZnO and SnO_2, can be deposited at temperatures below 150 °C, enabling fabrication on flexible substrates and integration with tandem devices on silicon, CIGS, or polymers. This lower temperature makes the structure highly scalable and well suited to roll-to-roll manufacturing of large-area modules [54],[65].

Inverted devices also exhibit improved operational stability and reduced hysteresis compared to N–i–P cells. The absence of TiO_2 eliminates UV-induced photocatalytic degradation, while fullerene-based ETLs effectively passivate trap states at the perovskite interface. These features suppress ion migration and interfacial recombination, leading to longer lifetimes, more reliable performance measurements, and greater reproducibility [66]. Its natural compatibility with semi-transparent top contacts also makes it the preferred choice for perovskite/silicon tandem solar cells, which represent one of the most commercially promising applications [67].

A central limitation of the p–i–n architecture lies in the choice of hole transport layers. Common options include PEDOT:PSS, PTAA, and NiO_x, but each presents challenges. PEDOT:PSS is hydrophilic, which promotes good adhesion and uniform perovskite film growth, yet this same property makes it hygroscopic and accelerates device degradation by trapping moisture [65]. PTAA, in contrast, is hydrophobic, which improves stability but prevents direct wetting of the perovskite precursor solution and therefore requires an additional interfacial layer, typically PEAI, to enable proper film formation [68]. NiO_x offers improved stability but often contains defects that demand careful passivation [69]. Electron transport layers also impose constraints. Fullerene derivatives such as PCBM and C_{60} remain the most widely used, but they suffer from inherently low conductivity, which restricts fill factors, and they are relatively expensive and prone to long-term instability. To achieve competitive performance, they typically require supplementary passivation strategies or additional interlayers [66].

The back contact in perovskite solar cells functions as the electrode for charge collection, extracting holes in N–i–P devices and electrons in p–i–n devices. Its primary role is to ensure efficient carrier extraction and transport, form an ohmic contact with the adjacent transport layer, and maintain minimal energy barriers. Depending on the device design, it may also serve optical functions, acting as a reflective electrode in single-junction

opaque cells or as a semi-transparent electrode in tandem and bifacial configurations [70].

A significant challenge in organic–inorganic halide perovskites (OIHPs) is ion migration from the back contact, particularly the diffusion of halides into metal electrodes [71]. This process leads to the formation of compounds such as AuI or AgI, which compromise electrical conductivity and accelerate device degradation. To mitigate this problem, ultrathin buffer layers can be introduced between the transport layer and the electrode to act as protective interfacial barriers [72]. Furthermore, they improve energy level alignment between the metal contact and the adjacent transport layer, lowering injection barriers and enhancing carrier extraction. Buffer layers, such as BCP, also protect the other layers during metal electrode deposition, which could otherwise cause damage, thereby enhancing both operational stability and device lifetime [73].

The front contact is the light-entry side of a perovskite solar cell. Key requirements include high transparency in the visible range (400–800 nm), low sheet resistance to reduce ohmic losses, and a smooth, chemically stable surface that supports uniform deposition of subsequent layers [74]. Thermal stability is also important, as some fabrication steps, particularly with TiO_2 ETLs, involve high temperatures [75].

The substrate, typically soda-lime glass or a flexible polymer, provides mechanical support and protection [75],[76]. These are coated with a transparent conducting oxide (TCO). Fluorine-doped tin oxide (FTO) is favored in N–i–P devices for its robustness, while indium tin oxide (ITO) is preferred in p–i–n structures due to its higher transparency and smoother surface, despite higher cost and lower thermal stability [75]. Alternatives such as Al-doped ZnO (AZO) or In–Zn–O (IZO) are being explored but remain less developed [75]. Surface treatments such as UV-ozone or O_2-plasma improve wettability and film formation [77].

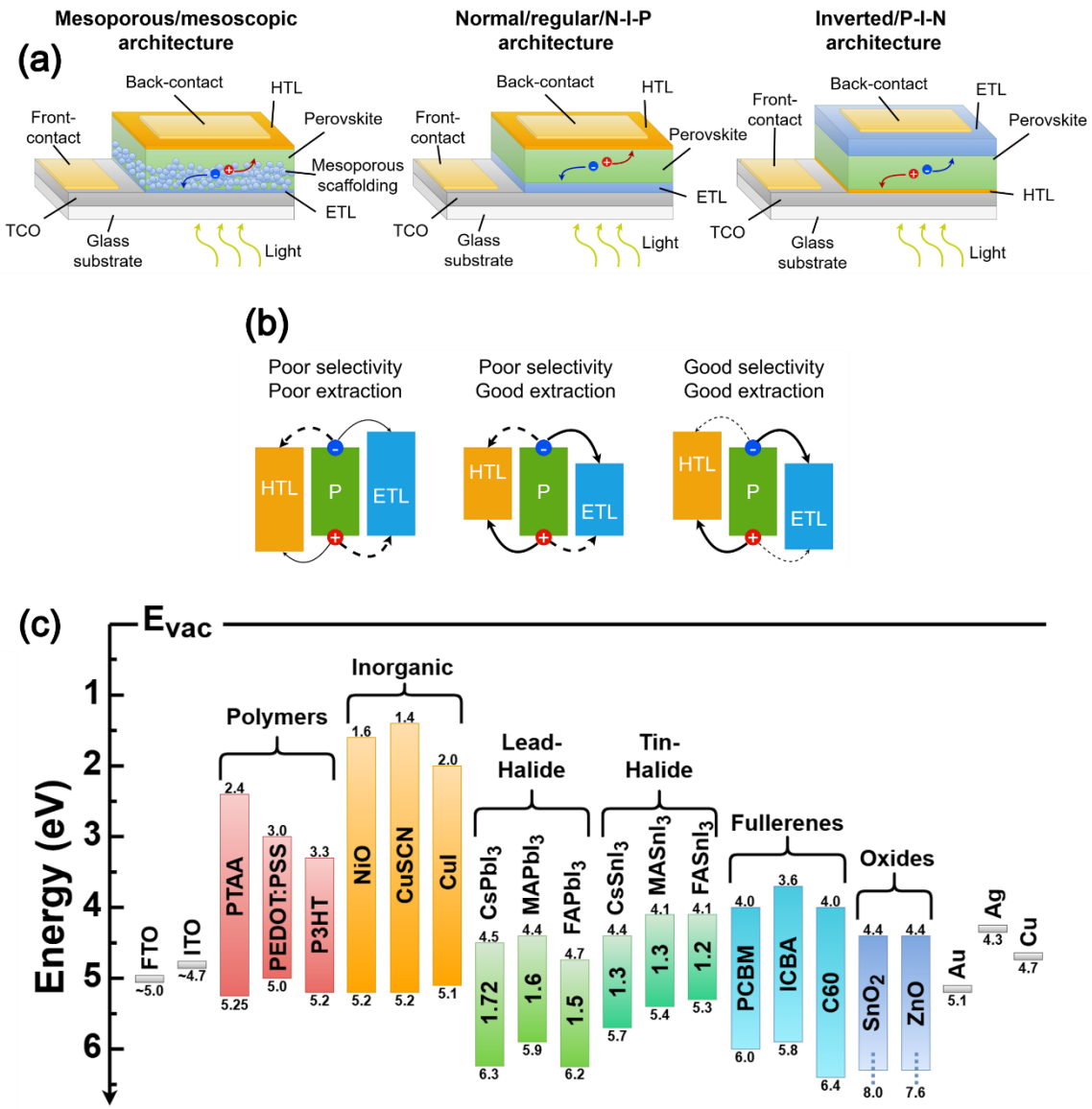


Figure 6 – (a) Schematics of mesoporous, n–i–p, and p–i–n perovskite solar cell architectures. **(b)** Contact behavior schematics: poor extraction and poor selectivity, good extraction with poor selectivity, and good extraction and good selectivity. **(c)** Typical vacuum referenced energy levels, Evac = 0, for common HTLs, perovskites, ETLs and electrodes. Values taken from: FTO and ITO- [78] ; PTAA-[79], [80], [81] ;PEDOT:PSS- [82], [83], [84]; P3HT-[85], [86], [87]; NiO-[88], [89], [90] ; CuSCN- [91], [92]; CuI- [93], [94]; Perovskites-[95] ;PCBM- [96], [97], [98]; ICBA- [99], [100], [101];C60- [102], [103];SnO2-[104], [105], [106] ;ZnO-[107], [108] ;Au, Ag and Cu-[109]

1.2.3. Synthesis methods

The choice of perovskite film formation route strongly influences microstructure, grain size and texture, defect density, and device metrics such as OCV and fill factor, which justifies a dedicated discussion [28]. A broad toolbox exists, including dry, vacuum-based routes such as co-evaporation, thermal evaporation and chemical vapor deposition, and solution-based, scalable coatings such as blade coating, slot-die coating, inkjet printing, and spray coating, each with distinct trade-offs in control, throughput, and materials use [110]. In the lab-scale PSC literature, solution processing has historically dominated, with

spin coating frequently reported for small-area devices, and recent database-driven text mining [111] and community reviews [112] indicate it remains common in 2024 to 2025, even as scalable methods gain momentum (**Figure 7b-d**).

In solution synthesis, perovskite precursors are typically dissolved in polar, aprotic solvents, most commonly DMF, DMSO, NMP, or GBL, which provide high halide solubility and drying profiles conducive to uniform films [113]. These solvents act as strong Lewis bases, coordinating to Pb^{2+} and Sn^{2+} to form transient solvate adduct intermediates, for example PbI_2·DMSO, that delay nucleation, slow crystallization, and yield smoother, denser films once the adduct is displaced during antisolvent quenching and annealing [114]. In practice, mixed systems such as DMF:DMSO balance volatility and viscosity with coordination strength, yet efficient removal of strongly coordinating components is essential to avoid residual complexes and defect formation [113].

Spin coating translates ink rheology and drying kinetics into film thickness and uniformity through centrifugal thinning and solvent evaporation. Classic models show that higher viscosity and higher solute concentration produce thicker films, whereas higher rotation speed and longer spin time thin the layer. The acceleration phase governs the early hydrodynamic regime and sets the timing window for nucleation control [115]. Practical variables include dispense volume and method, whether static or dynamic, the rotation profile, including speed, acceleration, and duration, the substrate temperature, and the ambient composition. All of these parameters interact with solvent coordination strength to set coverage, grain size, and defect density [116]

During spin coating, a nonpolar antisolvent is dispensed to rapidly extract DMF and DMSO, drive the wet film into supersaturation, and convert solvate intermediates into the perovskite phase, which improves coverage and grain uniformity when timed correctly [117],[118]. Common choices include toluene, chlorobenzene, diethyl ether, and increasingly green options such as ethyl acetate or mixtures of ethyl acetate and isopropyl alcohol, which reduce toxicity while preserving control over nucleation [119]. Application rate and timing are critical, because slower, well controlled dosing can yield more uniform crystallization and fewer defects [120]. Antisolvents can also deliver passivating and speciation control additives, for example PEAI for surface and 2D capping, or KSCN to tune growth kinetics in ethyl acetate [121], [122].

Post deposition annealing removes residual solvent, promotes ionic motion and grain growth, converts coordinative intermediates such as PbI_2·DMSO into the perovskite phase, and helps set the target polymorph or phase [117], [123]. Atmosphere control refines these kinetics: solvent vapor annealing slows evaporation to enable more uniform

nucleation and coarsening, for example mixed DMF and chlorobenzene vapor at room temperature, whereas inert environments minimize the effects of moisture and oxygen [124], [125]. Beyond hot plate single temperature anneals, process variables include temperature ramps, dwell time, and ambient composition, as well as gas quenching, directed N_2 to trigger fast intermediate to perovskite conversion, pulsed infrared or intense pulsed light annealing for millisecond crystallization, and hot casting using preheated substrates to drive rapid solvent removal and large grain films [126],[127],[128].

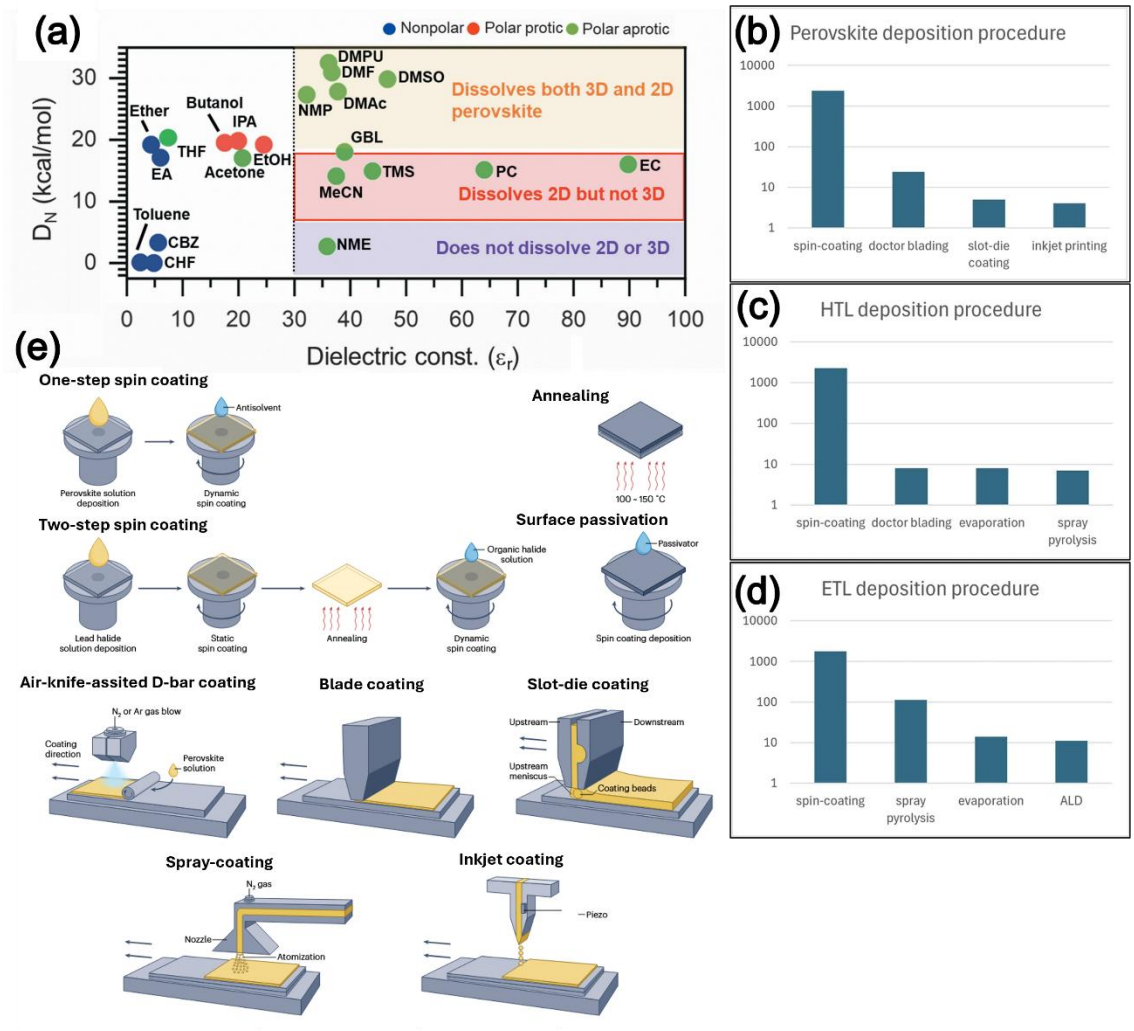


Figure 7 – (a) Solvent selection map for perovskite inks: dielectric constant, ε_r, versus Gutmann donor number, DN. Adapted from [129], copyright AAAS, used with permission. **(b-d)** Literature prevalence, log scale counts, of deposition routes for the perovskite absorber, HTL, and ETL layers, from [111]. **(e)** Schematics of solution processed film fabrication: one step and two step spin coating with antisolvent, air knife assisted D bar coating, blade coating, slot die coating, spray coating, and inkjet coating, plus post treatments including annealing and surface passivation. Adapted from Nature Reviews Methods Primers [28], copyright Springer Nature, used with permission.

1.2.4. Challenges for perovskite solar cells

Despite rapid efficiency gains and intense research activity, the commercialization of perovskite solar cells remains constrained by three major barriers: operational stability, manufacturability at scale, and environmental/regulatory risks linked to lead [130].

Durability is primarily limited by light accelerated drift of mobile ions, halides and A site cations, which distort internal fields and accumulate at interfaces where they can react with contacts and interlayers, for example Ag to AgI, increasing resistance and reducing OCV and fill factor [131], [132]. Moisture and oxygen, together with heat, further drive decomposition through superoxide reactions, especially in MA and FA systems [133]. In ambient air without encapsulation, devices often fail within hours to days, rapidly at relative humidity of 80% or higher, although interface engineered outliers have operated for more than 1000h in dry air at 10 to 20% relative humidity [134],[135]. With encapsulation, cells now retain approximately 98% after 1000h at 85ºC and 85% relative humidity, and carbon based mini modules keep more than 92% after 3000h under the same stress [136], [137]. For context, crystalline silicon modules typically degrade by about 0.5 to 0.6% per year, with about 80% power warranted at 25 years [138].

Translating lab recipes to manufacturing requires replacing spin coating with scalable methods such as slot die, blade, or roll to roll coating, and formulating antisolvent free, ambient processable inks that still deliver uniform films and controlled phase formation [139],[140]. A parallel push toward green solvent systems provides selection frameworks and practical routes that avoid DMF while preserving crystallization control [141]. At the module level, fully roll to roll lines have reported about 11% PCE for serially interconnected modules [142]. At cm^2 scale, hybrid meniscus coated sub-modules reach about 16.1% PCE [143]. While near m^2 panels have been certified at about 15.0% PCE, showing rapid progress but a remaining gap from pilot to mass production [144].

Environmentally, Pb is persistent and bioaccumulative, and perovskite derived Pb has been detected in plants, which underscores the need for containment and robust end of life logistics [29]. Still, operational Pb release from intact, well encapsulated modules can be kept very low, and containment can be reinforced with lead sequestration interlayers and encapsulants [145], [146]. The larger risks lie upstream and downstream: in the supply chain, where mining, refining, and transport of Pb bearing precursors pose pollution and spill hazards; in manufacturing, where worker exposure and waste handling require stringent controls; and at end of life, where improper decommissioning can lead to toxic Pb release. Encouragingly, aqueous, closed loop recycling now demonstrates near complete recovery of device constituents, easing end of life concerns [147]. In the

European Union, photovoltaic modules are presently outside RoHS limits, and workplace and process exposures fall under REACH. However, both frameworks are periodically revised and may tighten over time if risk assessments shift [148].

1.3. Tin-Halide Perovskites

The large-scale implementation of lead-halide perovskites, while less concerning than previously thought, still poses challenges related to waste management during synthesis and decommissioning, as well as potential environmental contamination risks. A widely proposed solution is to replace the B-site cation, lead (Pb), with tin (Sn), an element in the same group (Group 14) of the periodic table. Tin has a smaller atomic number (Z = 50) compared to lead (Z = 82), resulting in a smaller atomic radius and a distinct electronic configuration. This difference in electron distribution affects their chemical and optoelectronic properties [49]. Despite these differences, tin retains similar structural and electronic characteristics to lead, making it a promising alternative for reducing environmental and toxicity concerns [149].

Furthermore, tin-based perovskites such as $FaSnI_3$, $MASnI_3$ and $CsSnI_3$ have bandgaps between 1.2-1.4eV [37], [49] which is closer to the ideal S-Q value than their Pb based counterparts. Additionally, charge carrier mobilities in polycrystalline tin-based perovskite films are typically higher, around 10^2 cm^2 V^{-1} s^{-1}, while their lead-based counterparts typically exhibit mobilities around 10^1 cm^2 V^{-1} s^{-1} [150]. Nevertheless, tin-halide perovskites are not without drawbacks. Three primary challenges arise from the electronic properties of tin, which impact the performance of tin-based perovskites [31].

The first issue is the higher energy levels (lower relative to vacuum on an absolute scale) of tin perovskites. While the structural similarity between lead (Pb) and tin (Sn) results in analogous perovskite frameworks, their distinct orbital configurations lead to significant differences in band energy levels [31], [49]. In tin perovskites, the higher energy levels of the 5s and 5p atomic orbitals of Sn result in elevated absolute band energies compared to their lead-based counterparts. This shift in energy levels can lead to poor band alignment between the perovskite absorber and the charge transport layers developed for Pb-based PSCs, resulting in losses of open-circuit voltage and fill factor [31], [151].

Another critical challenge in tin-halide perovskites is the oxidation of Sn^{2+} to Sn^{4+}. Unlike the relatively inert $6s^2$ electron pair in lead, the higher energy $5s^2$ electrons in tin are more reactive, making Sn^{2+} prone to oxidation. This introduces additional complexity during synthesis, as the oxidation of the SnI_2 precursor into SnI_4 will degrade the quality of the perovskite structure, resulting in a heavily p-type material [152], [153].

Furthermore, the high energy levels contribute to weaker Sn-I bonds, making the perovskite more susceptible to reactions with H_20 and O_2, potentially inducing undesirable phase transitions to the non-perovskite yellow phase or to the double perovskite A_2SnI_6 [154].

Finally, a related issue is the higher Lewis acidity of Sn^{2+}, which stems from the higher energy of the 5p orbital. This leads to a faster crystallization rate compared to lead-based perovskites. The rapid crystallization often results in small, randomly oriented crystals and a low formation energy of Sn vacancies [153]. These vacancies create shallow defects that act as recombination centers, significantly impacting the material's performance. Additionally, these surface vacancies act as initiating sites for moisture induced de-composition [154]. Finally, Sn vacancies act as p-dopants within the perovskite structure [153]. As a result, hole concentrations in tin-halide perovskites are generally higher, ranging from 10^{17} to 10^{20} cm^{-3}, compared to lead-based perovskites, which typically exhibit hole concentrations around 10^{16} cm^{-3} [30].

In fact, the carrier transport properties of tin-halide perovskites are heavily influenced by their defect chemistry, which plays a dominant role in determining their performance. Defect formation in tin-halide perovskites is not only ubiquitous but also challenging to study due to difficulties in reproducibility. These challenges, which are not limited to tin-halide perovskites, arise from variations in precursors, synthesis conditions, and measurement environments, leading to significant discrepancies in reported optoelectronic metrics such as charge carrier densities, lifetimes, mobilities, and diffusion lengths [149].

Despite this, tin-halide perovskites exhibit other advantageous properties, including lower binding energies, smaller effective masses, and higher electrical conductivity compared to their lead-based counterparts [150], [155]. Moreover, studies have demonstrated that suppressing defects in tin-halide perovskites can significantly reduce hole carrier densities while simultaneously increasing carrier lifetimes and diffusion lengths to values comparable to or even exceeding those of lead-based perovskites [155]. These findings highlight the potential of defect engineering as a pathway to optimizing the performance of tin-halide perovskites for optoelectronic applications. The next subsection synthesizes various routes of optimization reported in literature.

1.3.1. Stabilization and enhancement of tin-halide perovskites

For tin-halide perovskite solar cells to become a viable alternative to lead-based PSCs, their critical stability issues must be resolved. However, it is equally important that any solution remains simple, cost-effective, and does not introduce new environmental

concerns. To this end, there are several routes that have been explored. A summary of relevant studies that employ unique strategies to target the major challenges of tin-based PSC's are displayed in table 1.

Table 1 – Summary of strategies, results, and mechanistic explanations from selected studies aimed at improving performance and stability in tin-halide perovskite solar cells.

Cell stack	Route tested	Results observed	Mechanistic explanation	REF
ITO/PEDOT:PSS/ **$FASnI_3$**/ PCBM/BCP/Ag	**SnF_2** (~15 mol% vs SnI_2) **in solution**	Fewer pinholes and better stability	SnF_2 retards oxidation and V_Sn formation; segregates at the HTL interface, forming an ultrathin SnS (S−Sulfur from PEDOT:PSS) interlayer that alters the interfacial chemistry.	[156]
ITO/PEDOT:PSS/ **$FASnI_3$**/ C60/BCP/Ag	**$EDAI_2$** (1 mol%) **+ BAI** (organic salts) **in solution**	PCE rose from 7.4% to 8.9% after ~1400 h storage in GB (no encapsulation);	$EDAI_2$ slowly passivates surface defects and suppresses oxidation; "slow crystal relaxation" improves film order over time.	[157]
ITO/PEDOT:PSS/ **$FASnI_3$**/ PCBM/Ag	**Hydroxybenzene-sulfonic acid + excess $SnCl_2$ in solution**	~80% PCE retained after 500 h air exposure (no encapsulation)	hydroxybenzene group acts as an antioxidant, scavenging O_2 radicals; $SnCl_2$-sulfonate complexes coat grain boundaries, blocking oxidation pathways.	[158]
ITO/PEDOT:PSS/ **$FASnI_3$**/ C60/BCP/Ag	**FOEI** (organic salt) **in solution**	10.16% PCE certified; longer carrier lifetimes; smoother films	FOEI lowers solution surface energy leading to smooth (100)-oriented growth, reduced trap density and recombination.	[159]
ITO/PEDOT:PSS/ **$FASnI_3$**/ C60/BCP/Ag	**PAI** (organic salt) **in chloroform pretreatment before annealing**	Preferential (100) growth; 11.22% PCE certified; >1000h of MPP stability reported.	PAI aggregates at nucleation centers inducing templated growth by reconstruction of the intermediate phase, which reduces trap density and stability.	[160]
ITO/PEDOT:PSS/ **$FASnI_3$**/ ICBA/BCP/Ag	**Trimethylthiourea (3T) additive in solution**	Certified PCE ≈14%, long carrier lifetimes; notably smoother, thicker films.	The formation of H-bonds with iodide leads to 3T staying in the film during preparation and improving adhesion to the underlayer. 3T is also a Lewis base which controls growth kinetics.	[161]
ITO/**$FASnI_3$**/ PCBM/BCP/Ag **(HTL-free)**	**Eliminate degradation related to PEDOT:PSS**	HTL-free devices retained 20% more PCE than devices w/PEDOT:PSS.	PEDOT:PSS degrades with light exposure and contributes to oxidation of tin perovskites. Band-bending guarantees correct energy alignment between $FASnI_3$ and the ITO.	[162]
ITO/PEDOT:PSS/ **$FASnI_3$**/ C60/BCP/Ag	**Lewis base anti-solvent (PMMA) and post-annealing recrystallization in DMSO vapor**	Vertical Sn concentration gradient; Ultra-stable devices retained +13% PCE after 1000h in 1-sun operation.	The Sn gradient (Sn-rich near ETL) shifts the WF in the perovskite significantly increases built-in field, reducing recombination; The Sn rich region protects the bulk perovskite from oxygen and light induced degradation.	[163]
ITO/PEDOT:PSS/ **$CsSnI_3$**/ ICBA/BCP/Ag	**Phthalimide (PTM)** molecular additive **in solution**	High PCE of 10.1% in B-γ-CsSnI3; Improved thermal/light stability	The lone electron pairs of NH and two CO functional groups in the PTM enhance the electron density around the Sn^{2+} within the $CsSnI_3$ and protect it from oxidation to Sn^{4+}	[164]
ITO/PEDOT:PSS/ **$CsSnI_3$**/ ICBA/BCP/Ag	**3-ThMAI solution post-treatment (spin-coating and annealing)**	High PCE of 12% with improved reproducibility.	The 3-ThMAI act as bifunctional polar modifiers. The sulfur coordinates with un-coordinated Sn^{2+} on the surface and passivate defect states. A stronger electric field at the modified Perovskite/ETL interface improves electron extraction.	[165]

ITO/PEDOT:PSS **$CsSnI_3$**/ C60/BCP/Cu	**Thiosemicarbazide (TSC)** passivator (vapor deposition synthesis)	90% PCE retention after 500h of continuous illumination.	S=C-N functional groups strongly coordinate with defects, leading to increased vacancy formation energies and better light stability	[166]

Collectively, these studies on tin-based perovskites point to several similar mechanisms and general trends. Sulfur-containing additives coordinate undercoordinated Sn through Sn-S bonding, which suppresses oxidation of Sn^{2+} to Sn^{4+}, improving stability. Increasing the electron density around Sn^{2+} further reduces its oxidation propensity and correlates with higher PCE. Performance can also be improved by two complementary approaches: reducing defect and trap densities via passivating additives or post treatments, and strengthening the built-in electric field through interfacial or compositional engineering to promote charge separation and extraction. Careful control of crystallization kinetics yields improved film morphology, including larger grains and fewer grain-boundary defects, which translates into better stability and efficiency. Finally, the literature remains concentrated on formamidinium based perovskites, while cesium-based analogues have received comparatively little attention since 2024, indicating a gap that merits systematic study.

2. Materials and Methods (Part I)

In this section, the materials, equipment and procedures adopted during this work are going to be laid out.

2.1. Materials

During this work, the following materials were used:

Substrate: Fluorine-doped Tin Oxide (FTO) glass substrates (TEC 7 Ω/sq, Greatcell solar),

Solid precursors: Bathocuproine 99.99 % (BCP, Sigma-Aldrich), Cesium iodide 99.9 % (CsI, Honeywell), Formamidinium iodide (FAI, Greatcell solar), Lead (II) iodide 98 % (PbI2, TCI), [6,6]-Phenyl C61 butyric acid methyl ester > 99 % (PCBM, Ossila), Poly[bis(4-phenyl)(2,4,6-trimethylphenyl)amine] (MW = 13) (PTAA, Ossila), 2-(4-Fluorophenyl) ethylamine Hydroiodide (F-PEAI, TCI); Phenethylamine hydriodide (PEAI, Greatcell solar), Tin(II) iodide 99+% (SnI_2, ThermoFisher Scientific), Tin(II) iodide ultra dry 99.999% metals basis (SnI_2, AlfaAesar), Tin(II) Fluoride 99% (SnF_2, Thermofisher Scientific)

Solvents: Chlorobenzene anhydrous 99.8 % (CB, Sigma-Aldrich), Isopropanol anhydrous (2-propanol, Sigma-Aldrich), Dimethyl sulfoxide anhydrous ≥ 99.9 % (DMSO, Sigma-Aldrich), N,N-Dimethylformamide anhydrous 99.8 % (DMF, Sigma-Aldrich), Toluene anhydrous (Sigma-Aldrich), analytical-grade Toluene (Merck).

2.2. Methods

2.2.1. SnI_2 purification process

To remove SnI_4 formed by oxidation of the degraded SnI_2 precursor (99 %, AlfaAesar), a purification method adapted from Zeng *et al.* [167] was employed. The procedure involved adding anhydrous toluene to the oxidized SnI_2 powder. Since SnI_4 is soluble in toluene while SnI_2 is not, this allows selective extraction of the SnI_4 into the solvent phase, thereby reducing its concentration in the remaining SnI_2 powder. The washing step was repeated until the waste solution became clear, indicating effective removal of SnI_4.

If analytical-grade toluene is used, a partial hydrolysis of SnI_2 and the formation of SnO_2 occur. To address this, a secondary purification step was introduced. The washed SnI_2 powder, now containing SnO_2, was dissolved in anhydrous DMF. As SnO_2 is insoluble in DMF, it remained suspended and was subsequently removed by filtration through a 2

µm PTFE filter. The purified SnI_2 was then recrystallized by evaporating the DMF solvent. All steps of the purification process, as illustrated in **Figure 8**, were conducted inside an N_2-filled glovebox.

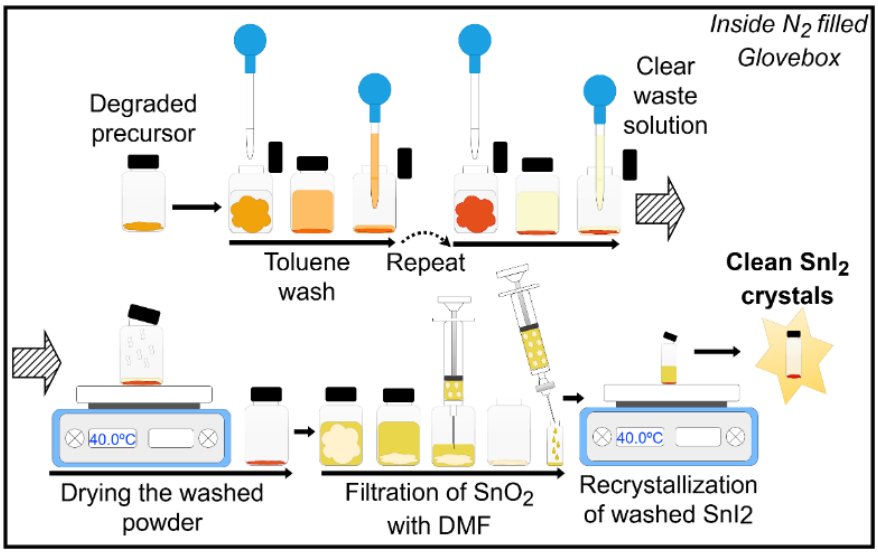


Figure 8 – Schematic representation of the purification process used to clean the oxidized SnI_2 powder.

2.2.2. Precursor solution preparation

All solids were added to unused vials inside an N_2-filled glovebox. After the target mass was reached, the corresponding solvents were added using a micropipette. The CsI, FAI, and SnI_2 precursors were weighed in a different glovebox and transported to the fabrication glovebox in sealed vials.

The following stock solutions were prepared and stored within the glovebox: PTAA in toluene (1.5 mg/mL); PEAI in DMF (5 mg/mL); F-PEAI in DMF (5 mg/mL); PCBM in CB (20 mg/mL); BCP in 2-propanol (0.5 mg/mL). These stock solutions were used as needed and discarded one month after preparation.

Perovskite ink solutions ($CsSnI_3$, $FASnI_3$, $CsPbI_3$) were prepared by weighing the required amounts of the iodide salt (CsI or FAI) and metal iodide (SnI_2 or PbI_2) into a single vial. DMF and DMSO solvents were then added to achieve a 0.8 M solution with a solvent ratio of DMF:DMSO = 4:1, following the protocol described in reference [164]. The mixtures were stirred at room temperature within the glovebox until complete dissolution. Mixed-cation perovskite inks were prepared by combining appropriate volumes of the single-cation perovskite solutions to achieve the desired cation ratio. For example: $Cs_{0.5}FA_{0.5}SnI_3$ = 0.5 mL of $CsSnI_3$ + 0.5 mL of $FASnI_3$.

SnF_2 was incorporated into the perovskite inks only after complete dissolution of the iodide salts and metal iodide components. A calculated volume of perovskite ink was transferred into a vial containing the required amount of SnF_2, based on the target stoichiometry. The mixture was stirred until homogeneous and ready for deposition.

2.2.3. Substrate preparation procedure

The FTO-coated glass substrates were labeled using a Versa Laser engraving system to identify individual cells. A laser scribing process (P1 scribe) was then performed to electrically isolate the front-contact from the back-contact by cutting the FTO. The substrates were then manually cut into pieces of approximately 250 x 150 mm. Then, substrates were washed using a 10 % aqueous Hellmanex solution and a soft brush. After, substrates were sequentially submitted to ultrasonication in distilled water, acetone, 2-propanol, and ethanol for 10 minutes each. The substrates were then dried under a nitrogen flow. Immediately before the deposition process, the substrates were treated with oxygen plasma at 100 mW for 10 minutes and subsequently transferred to a N2-filled glovebox.

For the spectrophotometry and charge transport tests, a thin glass slide was used instead of the conductive substrates. The cleaning procedure and plasma treatment were the same.

2.2.4. Device fabrication procedure

The device fabrication process, except for the deposition of the back contacts, was carried out entirely within an N_2-filled glovebox to prevent exposure to moisture and oxygen. All layers were deposited via spin coating. Prior to each deposition, surface contaminants were removed from the substrates using a directed N_2 flow. Precursor inks were dispensed onto each substrate using a micropipette, ensuring complete surface coverage, and the spin coating program was initiated immediately afterward. Following spin coating, substrates were transferred to a hot plate set to the target temperature, which was manually controlled using a thermocouple. After annealing, substrates were cooled in plastic Petri dishes. The cells were allowed to cool for at least 10 minutes before deposition of the subsequent layer. The cells were handled with stainless-steel tweezers, taking care not to scratch the deposited layers, although minor scratching occasionally occurred.

The specific spin-coating and annealing process parameters for each layer, performed in the same order as in text, was as follows: **HTL –** 50μL of filtered PTAA ink were spin-coated at 2000rpm for 40s then annealed at 100ºC for 10 min. **Wetting layer –** 100μL of

PEAI (or F-PEAI) ink were spin-coated at 4000rpm for 30s, no annealing was performed. **Perovskite layer –** 60μL of filtered perovskite ink were deposited using a two step spin coating process, first at 1000rpm for 10s then at 5000rpm for 45s. After 15 s into the second step, 100 mL of CB was applied in a single, continuous jet to avoid droplet formation. This was followed by annealing at the target temperature, typically 75ºC for 10 minutes. **ETL –** 50μL of PCBM ink were spin-coated at 2000rpm for 30s then annealed at 100ºC for 10 min. **Buffer layer –** 80μL of BCP ink were spin-coated at 4000rpm for 30s. No annealing was performed.

Before their deposition, the PTAA and Perovskite inks were filtered using a 2μm PTFE filter.

After the spin-coating of all layers, the front-contact area of the stack was cleaned using a bistoury knife to remove most solid residues, followed by gentle wiping with acetonitrile-soaked cotton swabs to remove any remaining material. This ensured that the front-contact was defined solely by the exposed FTO. After this step, the substrates were kept inside the glovebox for at least 12 h before the back-contact deposition.

The deposition of the back contacts was performed in a bench-top high-vacuum thermal evaporator (VapourStation, Oxford Vacuum Science Limited). The cells were loaded onto a custom metallic support, which incorporated a deposition mask, inside the glovebox. The support was then transferred to the vacuum chamber, limiting air exposure to approximately 5 minutes before the chamber pressure reached vacuum conditions. The system required at least one hour to reach the target pressure of ~3 nbar. Once this pressure was reached, thermal evaporation of the silver back-contacts was initiated. The deposition rate was gradually ramped from 0.1 Å/s to 1.5 Å/s to ensure uniform film formation and strong adhesion of the metal to the underlying layers Deposition was stopped when a thickness of approximately 80 nm was reached.

Initially, the vacuum chamber was backfilled with ambient air immediately after the thermal evaporation, and the devices were promptly removed for characterization. However, to minimize device degradation, this procedure was revised: the devices were allowed to cool under high vacuum for at least 30 minutes prior to removal, and the vacuum chamber was backfilled with nitrogen instead of ambient air. A schematic representation of the resulting devices is shown in **Figure 9**.

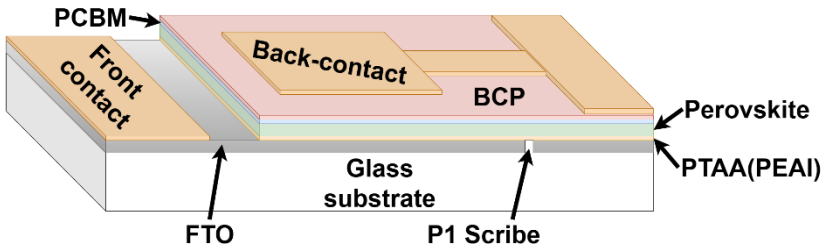


Figure 9 – Schematic representation of the cells fabricated in this work.

2.2.5. Characterizations

The **current density–voltage (J-V)** characteristics of the inverted PSCs were recorded by applying an external potential load and measuring the generated photocurrent using a Zennium workstation (Zahner Elektrik, Germany) controlled by the Thales XT 5.1.4 software package. Measurements were performed under AM 1.5G irradiation at 100 mW cm^{-2} (1 sun) using a solar simulator (150 W Oriel class A). Devices were characterized immediately after preparation at room temperature in ambient air. The active area was defined by a black shadow mask with an aperture of 0.196 cm^2.

Spectrophotometry was used to record the absorption spectrum of the perovskite films. A typical absorption graph for halide perovskites is shown in **Figure 10b**. The spectral features reflect the optoelectronic properties which are tied to the crystalline phases present, enabling assessment of perovskite degradation. The optical bandgap of a semiconductor can also be estimated from the absorption edge using a Tauc analysis.

This characterization was performed on a Shimadzu UV-3600i Plus UV-Vis-NIR spectrophotometer with an ISR-1503 integrating sphere. Calibration for reflectance and transmittance was performed in air over a wavelength range of 300 to 1100 nm.

Scanning electron microscopy (SEM) was used to access the surface morphology of the perovskite films, revealing the presence of grain coalescence, grain density, grain size and undesired features such as pinholes.

SEM was performed on two instruments: a desktop Phenom X SEM and a FEI QUANTA 400 FEG ESEM. Chemical composition analysis was conducted with an EDAX Genesis X4M energy-dispersive X-ray spectrometer.

X-ray Diffraction (XRD) was used to determine the crystalline composition of the perovskite thin film and identify secondary phases.

Measurements were performed in air at 25 °C using a Malvern Panalytical Empyrean multipurpose diffractometer. Continuous scanning was conducted over a 2θ range of 10°

to 60° with a step size of 0.026°, using Cu Kα radiation (λ = 1.54060 Å). Data was analyzed using the Match! Software

Atomic Force Microscopy (AFM) was used to determine the scale of topological features in the perovskite film, allowing the quantification of surface roughness.

Measurements were performed under ambient conditions on an MFP-3D Infinity (Asylum Research) with an ASYELEC-01-R2 silicon tip featuring a reflective Ti/Ir coating. The tip had a resonant frequency of ~75 kHz and a spring constant of 2.8 N/m. Topography was acquired in tapping mode and analyzed using a custom Python script.

Scanning Kelvin probe (SKP) measurements were used to map the surface work function of each layer in the device stack. The WF is the energy difference between the vacuum level and the Fermi level at the surface, so spatial variations in WF reveal local electrostatic potential and band bending. When combined with independently measured bandgaps and an assumed vacuum level alignment at clean interfaces, the WF can be used to estimate the positions of the valence and conduction band edges for each layer.

SKP was performed in a dry box using a Biologic SKP-M470 system equipped with U-SKP-370/1 tips. To isolate the WF of each layer individually, an alternative stack configuration was employed, as illustrated in **Figure 10a**. The FTO substrate ensured a common ground reference.

Charge transport characteristics were assessed using Hall effect measurements on a Linseis HCS 1 system equipped with two neodymium magnetic circuits on a movable sled. Gold-coated probes contacted the perovskite thin film in a van der Pauw geometry. A film thickness of 300 nm was assumed based on prior cross-section analysis. Measurements were conducted during both heating and cooling cycles in a nitrogen-purged chamber.

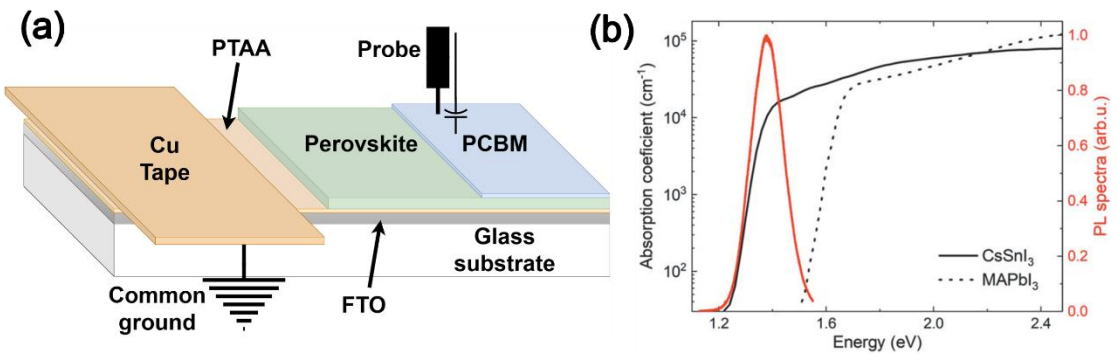


Figure 10 – (a) Schematic representation of the layer stacking and experimental setup used to perform SKP measurements. **(b)** Typical absorption spectrum for halide perovskites (in black). Obtained from [168], used under CC BY 4.0.

3. Results and discussion (Part I)

This section is divided into two parts. The first examines how precursor oxidation impacts perovskite films and evaluates a method for obtaining an oxidation-free precursor. The second focuses on optimizing the perovskite derived from a new 99.999% pure precursor to obtain functional solar cells. Finally, the section concludes with a discussion of the key findings from these studies and explores several potential directions for further improvement.

3.1. Effect of Precursor Oxidation and Purification on Perovskite Films

3.1.1. First batch of cells

The initial batch of devices employed an FTO/PTAA/$CsSnI_3$/PCBM/BCP/Ag structure. When preparing the first perovskite precursor solution (CsI + SnI_2 in DMF:DMSO), the mixture immediately developed a deep dark red color (**Figure 11a**), rather than the expected clear light yellow [167]. This indicated severe oxidation of the SnI_2 precursor. While some degree of oxidation was anticipated due to the precursor's limited purity (99%), the extent observed was unusually high. The SnI_2 precursor powder seemed to be heavily oxidized, posing a significant challenge given that it was the only available source of SnI_2. With no immediate alternatives, the decision was made to continue using this precursor in order to investigate the effects of oxidation, while simultaneously exploring potential solutions reported in the literature.

The fabricated cells showed an OCV of 0V when tested with 1-sun illumination. Measurements with a multimeter revealed very low resistance, although the devices were not short-circuited (which would cause an OCV of 0V). Visually, the perovskite layer seemed to become transparent with a dark neutral/yellow taint, in contrast to the dark opaque orange/brown observed during fabrication inside the GB. In addition, signs of corrosion were visible on the silver contacts (**Figure 11b**). The observed color change and loss of opacity suggest that exposure to air, both during transfer to the thermal deposition chamber and after venting the chamber, caused the perovskite to transition to its yellow phase through oxidation. Furthermore, the combination of heat and oxygen during venting likely initiated a reaction with the silver, leading to corrosion and ultimately the degradation of the perovskite layer.

A-site cation mix and stability tests

To better understand the role of the A-site cation in the formation and stability of the black-phase, perovskite films with three formulations ($CsSnI_3$, $FASnI_3$ and $Cs_{0.5}FA_{0.5}SnI_3$)

were synthesized with sequentially increasing annealing temperatures, from 60ºC to around 125ºC.

The $FASnI_3$ perovskite did not form the black-phase at any temperature. Instead, the films remained dark orange, with those annealed at higher temperatures gradually turning light orange after some minutes. Subsequent studies have shown that black-phase $FASnI_3$ can form at around 70ºC. This indicates that the presence of SnI_4 in the precursor solution prevents the formation of black-phase for tin perovskites with FA cation. This was not the case for $CsSnI_3$ and the mixed $Cs_{0.5}FA_{0.5}SnI_3$ perovskites, which formed the black phase at all tested temperatures (**Figure 11c**). Based on these results, $CsSnI_3$ was selected for subsequent studies, as it enabled reliable black-phase formation even when using a lower-quality precursor.

Stability tests were conducted by storing some perovskite films inside the glovebox and others under ambient conditions. Since the oxidation state of these materials can be readily inferred from their color, the test focused on monitoring visible changes over time. The results are shown in **Figure 11d-e**. Degradation inside the glovebox seems to be minimal with films maintaining their color after 40h. As expected, degradation outside the glovebox is considerable after 20 hours of air exposure with all films having turned into the Y-phase. Noticeably, after 2 hours the inorganic $CsSnI_3$ perovskites have fully transitioned into their Y-phase, while the mixed $Cs_{0.5}FA_{0.5}SnI_3$ still hold some dark brown color, indicating that the black-phase is still present. This is in agreement with the expected higher stability of FA-based perovskites [169].

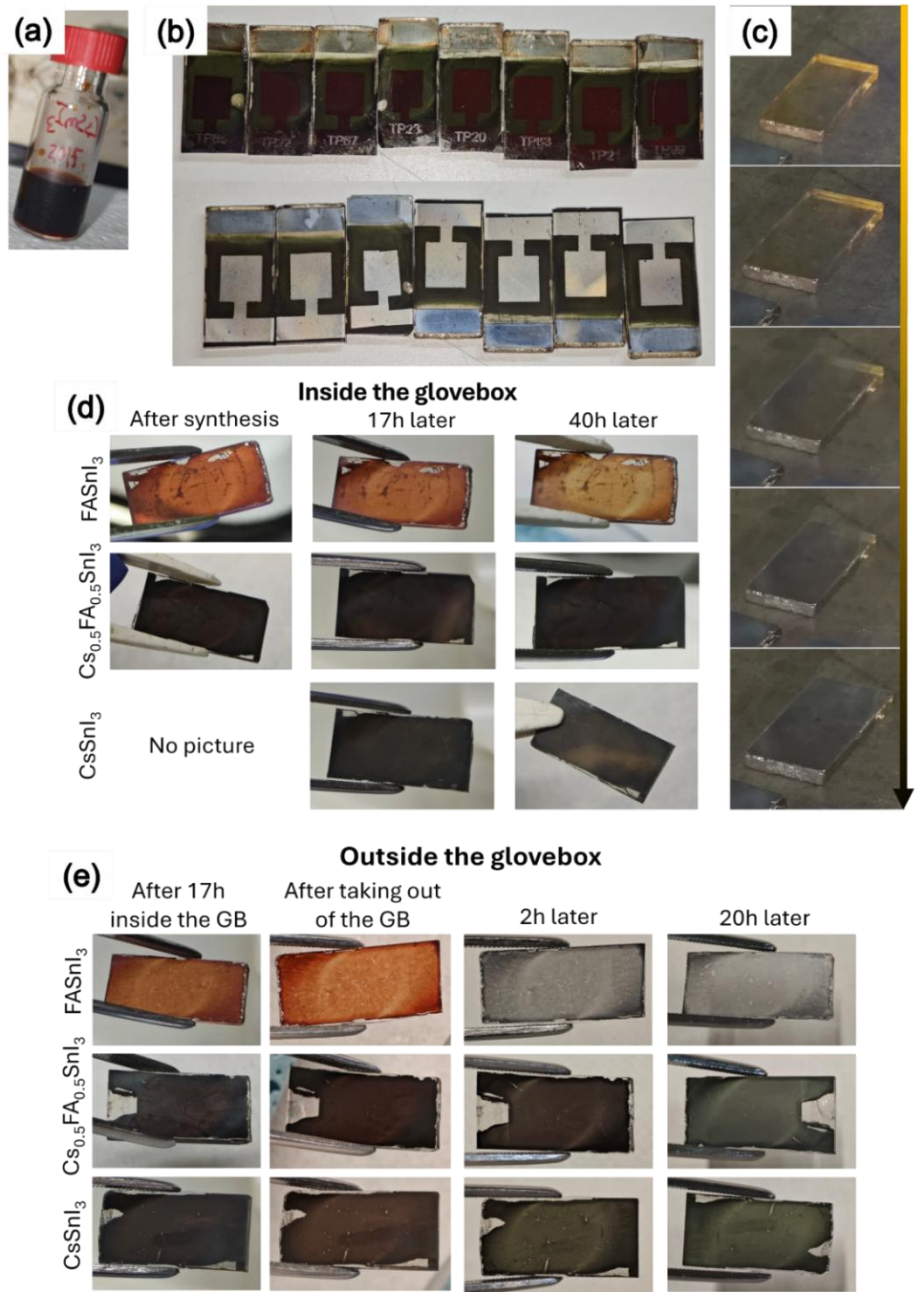


Figure 11 – (a) filtered perovskite solution prepared with oxidized SnI_2 precursor. **(b)** First FTO/PTAA(PEAI)/CsSnI3/PCBM/BCP/Ag cells fabricated. **(c)** time sequence of pictures of perovskite films crystalizing during thermal annealing. Arrow indicates direction of time. Photographs spaced 5 seconds from each other. **(d)** Pictures showing the degradation of the perovskite films inside the glovebox. **(e)** Pictures showing the degradation of the perovskite films outside the glovebox.

3.1.2. Precursor purification study

The detrimental effects of oxidation on the perovskite films were evident. The darkened precursor solution indicated severe oxidation, while the films themselves appeared dark brown rather than the expected dark red [170], suggesting a widened bandgap and the presence of the Y-phase. Since the precursor in its initial state could not produce acceptable films, a purification method adapted from Zeng et al. [167] was employed. As

described in the methods section, this procedure involves repeatedly washing the degraded precursor with toluene until the solution becomes clear (**Figure 12a**). The process relies on the insolubility of the polar ionic SnI_2 in the nonpolar solvent toluene, in contrast to the oxidized SnI_4, which is nonpolar and highly soluble. Consequently, undissolved SnI_2 can be separated from the dissolved SnI_4. A limitation of this method is the hydrolysis of SnI_x compounds into SnO_2 in the presence of water in non-anhydrous solvents. Since the procedure requires about 40 mL of toluene per 100 mg of precursor, analysis-grade toluene was used instead of the more costly anhydrous toluene, leading to the formation of significant amounts of SnO_2. Fortunately, SnO_2 is less detrimental than SnI_4, as it is insoluble in DMF and DMSO, which are the solvents used for perovskite solution preparation, and can therefore be largely removed by filtration (this is evident by the reduction in turbidity of the solutions). However, the relatively high amount of SnO_2 remaining in the washed powder makes it impossible to weigh the material accurately and achieve the correct stoichiometric ratio in the perovskite solution. To address this, an extra step was introduced: the washed powder was dissolved in DMF, the insoluble SnO_2 filtered out, and the SnI_2 recovered by drying and recrystallization. This yielded large, intensely red crystals (**Figure 12b**), consistent with purified SnI_2 [167]. The mass yield of the procedure was around 60%, though this value does not account for the SnI_4 and SnO_2 already present in the initial powder, meaning that true SnI_2 recovery is higher.

It is important to note that the purification process had several limitations. First, the washing step showed poor selectivity, as some SnI_2 remained suspended in the solvent and was removed together with the soluble SnI_4. Second, unwanted irreversible side reactions occurred, notably the hydrolysis of SnI_2 to SnO_2.Third, the method generated a large amount of toxic solvent waste, since toluene was required in significant quantities to dissolve SnI_4. These limitations were a result of the available materials and equipment. However, each of these issues can be addressed by modifying the procedure. For instance, using a centrifuge to force the suspended SnI_2 into a pellet would increase selectivity of the wash, improving yield. Using high purity anhydrous toluene would limit the formation of SnO_2 and eliminate the need for the additional DMF-based filtration step. Finally, recovering and recycling the wasted toluene by distillation and dehydration would significantly reduce the solvent waste. In addition, the extracted SnI_4 could potentially be chemically reduced back to SnI_2, using metallic tin powder [171], further improving the efficiency of the process.

To assess the quality of the perovskite films and the effect of the washing process, three solutions, seen in **Figure 12c,d** were prepared: one using the degraded SnI_2 powder, another using the toluene-washed SnI_2 (with SnO_2) and a third using the clean SnI_2

crystals (SnO_2 filtered out). The resultant perovskite films (**Figure 12e-g**), prepared using the standard procedure described in the methods section, were analyzed in XRD and SEM.

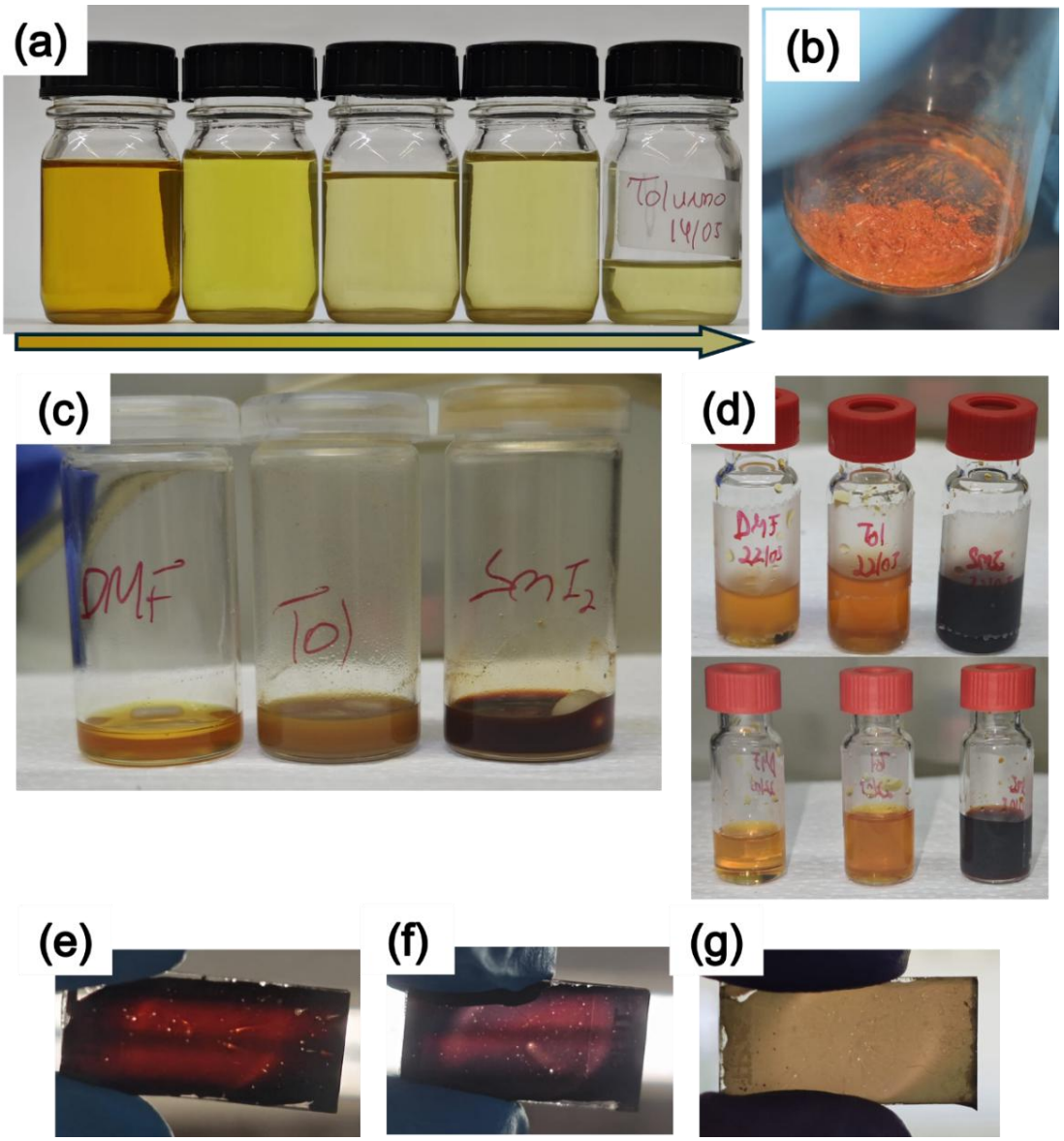


Figure 12 – (a) Picture illustrating the reduction concentration of SnI_4 in the waste toluene for consecutive washes. **(b)** SnI_2 crystals after the purification process. **(c)** Perovskite precursor solutions, before filtration, prepared with (from left to right) "toluene washed + DMF filtration" precursor, "Toluene wash" precursor, unwashed oxidized precursor. **(d)** The same perovskite solutions shown in **(c)** after filtration. Example of resultant perovskite films synthesized with **(e)** "toluene washed + DMF filtration" precursor **(f)** "Toluene wash" precursor **(g)** unwashed oxidized precursor.

X-ray diffraction analysis

To access the compositional differences between perovskite films prepared from each precursor solution, XRD analysis was employed. Representative spectra for each type of perovskite film is shown in **Figure 13**. Before discussing the results, a caveat must be mentioned: the "toluene washed + DMF filtered" samples degraded during

transportation. Unfortunately, due to time constraints, it was impossible to repeat this analysis with pristine samples. Thus, direct quantitative comparison between spectra is not feasible. Still, a broader qualitative analysis remains possible and provides valuable insights for this study.

Comparing the samples prepared with oxidized and toluene-washed precursors (**Figure 13 b** and **c** respectively) we see that the major difference is the absence of yellow-phase $CsSnI_3$ in the "toluene washed" sample. This confirms the visual identification of this phase and shows that the purification process has significantly improved the perovskite film. Even so, peaks related to an independent CsI phase are still present which is likely a result of excess CsI due to the incorrect stoichiometric ratio. This interpretation is supported by the absence of this phase in the "toluene wash + DMF filtration" sample (**Figure 13a**). The "toluene-washed" sample shows a significant B-γ-$CsSnI_3$ peak at 26.5º. This peak is less prominent in the "toluene wash + DMF filtration" sample. Given the observed film color and subsequent analyses of other samples, the reduced presence of black-phase $CsSnI_3$ is most likely attributable to degradation that occurred during transportation rather than an intrinsic limitation of the purification method.

In all samples, SnO_2 peaks remain prominent. These are most likely attributed to the fluorine-doped SnO_2 substrate, FTO, rather than SnO_2 within the perovskite film. Even so, the presence of Cs_2SnI_6 suggests that some SnO_2 may also be present at the surface, since SnO_2 is a byproduct of the Cs_2SnI_6 degradation pathway: $2\,CsSnI_3 + O_2 \rightarrow Cs_2SnI_6 + SnO_2$ [154]. Furthermore, the low intensity of Cs_2SnI_6 peaks indicate that it is only present as a thin layer in the surface. It is noteworthy that the degradation pathway often cited in literature, in which SnI_2 oxidizes to SnI_4 and yields the yellow phase, is not evident here, since the degraded sample shows no yellow phase. In fact, the presence of the Y-phase was not visually observed in any sample.

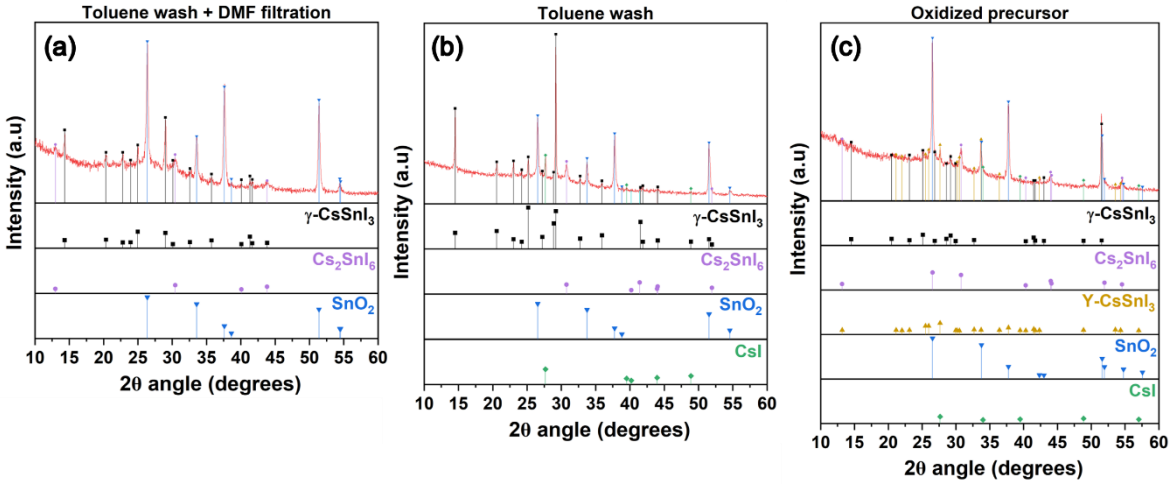


Figure 13 – XRD patterns of perovskite films prepared from different precursor treatments. **(a)** Toluene wash + DMF filtration, **(b)** Toluene wash only, **(c)** unwashed oxidized precursor. Symbols in the XRD spectra identify the phase with highest influence on that peak. Graphs below the spectra show all correlated peaks for the identified phases. Phase identification peaks obtained from: COD database [172] for SnO_2 and CsI peaks; Wang et al. (2022) [173] for γ-$CsSnI_3$ (orthorhombic), Y-$CsSnI_3$ (orthorhombic yellow phase) and Cs_2SnI_6.

Scanning electron microcopy

Having confirmed the presence of black phase, it is important to assess the quality of the perovskite film via SEM. The efficiency of PSCs is heavily dependent on homogeneity and absence of defects in the perovskite film. Defects such as pinholes, gaps between crystals and irregular crystal formation increase charge carrier recombination and can even create short-circuits between the extraction layers, which significantly reduce OCV. The presence of such defects is typically assessed with SEM imaging.

Selected SEM images of the perovskite films are shown in **Figure 14**. Overall, these images show some clear trends. Crystal size increased substantially from approximately 1µm or less in **Figure 14 e** and **f**, to large crystals with diameters in the order of several tens of micrometers. Furthermore, there is also a significant reduction in the gap between crystals, with grain boundaries being better defined in the "Toluene wash + DMF filtration" sample than in the others. Finally, homogeneity also seems to improve with the washing process, specifically when compared with the sample prepared with the unwashed precursor. The latter shows irregular crystal formations (**Figure 14h**). This irregular morphology can be attributed to local depletion of Sn-I caused by the oxidation of SnI_2 to SnI_4 before and during nucleation. The resulting low local supersaturation shifts the crystal growth into a diffusion-limited regime [174], where protruding tips intercept most of the diffusing species and advance rapidly, while neighboring regions are starved [175], [176]. This produces star-shaped, skeletal islands (bright arms) bordered by darker, recessed valleys where coalescence stalled. In short, the dendrites mark zones that captured the available constituents, whereas the surrounding areas lacked sufficient Sn^{2+} and I^- to complete the crystal network, due to the general oxidation into SnI_4. Similar features can be seen in **Figure 14d** for the sample with the purified precursor, although they likely have a different root cause, which will be discussed in later sections. Looking at images for the "toluene wash" sample (**Figure 14e**) we see that there is no dendritic formation, supporting the conclusion that those dendrites are due to SnI_4 oxidation. Furthermore, the size of grains and homogeneity is increased. However, the grain boundary gaps are still quite significant, as seen in **Figure 14g**. This might be a result of the Sn-depleted content of the perovskite solution. Compounds such as SnI_2 or PbI_2 form adducts (intermediary structures in the solution) with DMSO, such as $SnI_2(DMSO)_4$. These adducts are typically beneficial as they promote higher nucleation rates,

homogeneous film formation and stronger coalescence of domains [177], [178]. However, in Sn-poor conditions the higher nucleation rates lead to quick Sn^{2+} starvation, limiting crystal growth and leaving significant gaps between crystals [179]. This idea is supported by the presence of an independent CsI phase in the XRD spectra on the samples that were out of stoichiometric ratio, likely to be located at crystal interfaces where Sn depletion is strongest.

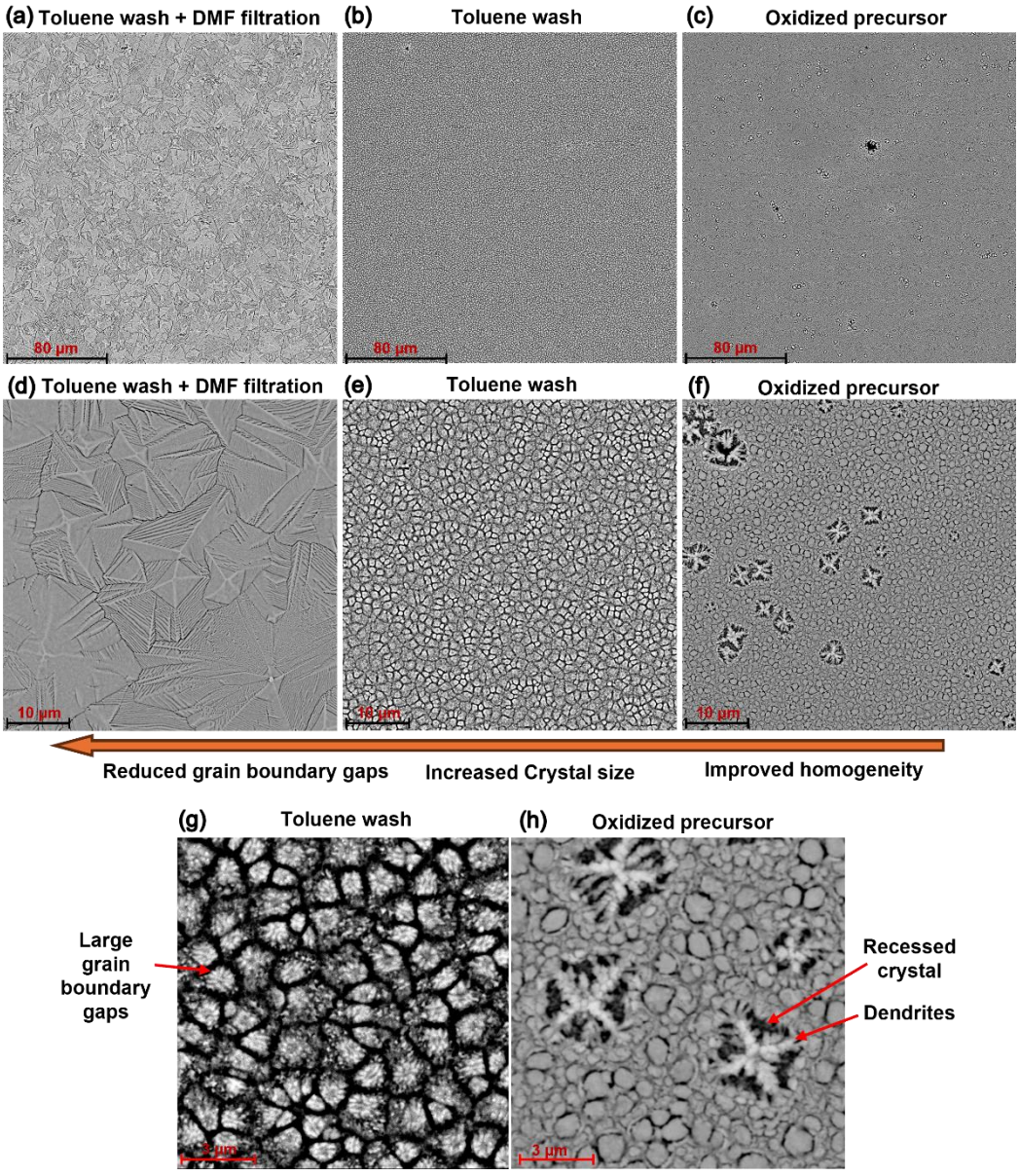


Figure 14 – Top-down SEM images of perovskite films prepared from different precursor treatments. **(a, d)** Toluene wash with DMF filtration. **(b, e)** Toluene wash. **(c, f)** Oxidized precursor. **(g)** High-magnification image of toluene wash. **(h)** High-magnification image of oxidized precursor.

3.2. Studies Using High-Purity SnI_2 Precursor

Given the time-consuming and resource-intensive nature of the purification process, it was not feasible to proceed with the optimization of prototype solar cells using the SnI_2 precursor obtained through this route. Instead, a commercially available SnI_2 precursor with 99.999% purity was acquired, allowing the fabrication of devices without an additional purification step. This approach was intended both to streamline the continuation of the study and to provide a reference for comparison with the purified precursor. However, the difficulty in producing fully functional cells soon became a major obstacle, ultimately preventing the intended comparative analysis. Consequently, the focus of the work shifted toward identifying strategies to achieve operational devices within the constraints of the available materials, equipment, and time.

In this section, the different attempts to fabricate a functional cell are briefly outlined. This is followed by an examination of possible factors contributing to the poor device performance, informed by XRD, SEM/EDS, AFM, SKP, spectrophotometry, and Hall-effect measurements. Finally, potential directions for future work are discussed.

3.2.1. Device Fabrication Attempts

The first attempted fabrication of a full device with the new SnI_2 precursor was based on the same FTO/PTAA(PEAI)/$CsSnI_3$/PCBM/BCP/Ag configuration. The CsI+SnI_2 in DMF:DMSO precursor solution showed a clear yellow with a slight orange tint color (**Figure 15a**), indicating less oxidation than solutions prepared with the purified precursor. The resulting perovskite film (example in **Figure 15b**) had strong dark red color, indicating the formation of the black-phase. After thermal evaporation of the silver contacts the devices' OCV was measured under illumination, showing no OCV. This time the perovskite film under the area of Ag deposition seemed to have disappeared, as seen on **Figure 15c**. Interestingly, and unlike previous tests, the rest of the film was visually intact, indicating that a reaction with Ag was the problem, not the stability of the perovskite during the thermal deposition process. It is unlikely that the mere presence of silver induced such a quick degradation of the perovskite film during the deposition process, which lasts only a few minutes. Instead, the main problem could be the venting step, where the vacuum chamber is refilled with air, while the cells are still warm. The presence of silver likely acted as a catalyst for the reaction with oxygen, leading to the degradation of the zones in contact with silver. The reactivity of silver with halide perovskite is well established, as described in section 1.2.2, especially with the heat and vacuum of thermal deposition.

With this hypothesis in mind, the next batch of cells was prepared with gold contacts, which are typically more stable than silver [65]. Thermal deposition of gold requires a high source temperature that can heat and damage the cells. To limit thermal stress, we deposited the film in multiple short steps with cooling intervals and restricted the thickness to 20 nm. An example of a resulting cell is shown in **Figure 15d**. Although the perovskite layer did not degrade during processing, the devices still exhibited no measurable OCV under illumination. The device shown in **Figure 15d** likely failed due to a short-circuit between the FTO and the Au contact caused by a visible hole in the film. However, other cells showed no apparent holes in the contact region, and multimeter tests detected no short circuits, even though the measured resistance was low.

One uncontrolled step in the deposition workflow was venting the vacuum chamber. In earlier runs, the chamber was vented immediately after deposition by backfilling with ambient air. The combination of residual heat and low-pressure oxygen during venting, together with the catalytic activity of Ag/Au, may have promoted perovskite degradation, even if it was not immediately observable. To prevent oxygen ingress during venting, a nitrogen line was connected to the chamber's vent valve to allow O_2-free backfilling. To further minimize exposure, cells were loaded under a directed N_2 stream, and the chamber was prefilled with nitrogen before initiating the pump-down sequence. An example of a resulting cell is shown in **Figure 15e**. For the first time, all cells exhibited a non-zero open-circuit voltage: ~10 mV without the shading mask and ~4 mV with it. However, the measured I-V curves were linear, consistent with devices showing very low OCV. All subsequent attempts followed this procedure.

Further attempts to fabricate functional devices involved adding lead iodide to form $CsSn_{0.5}Pb_{0.5}I_3$. These cells had difficulty transitioning to the black phase, even after annealing at 140ºC, and ultimately did no function. Other attempts included adding SnF_2 to improve stability and changing the wetting layer from PEAI to F-PEAI. All of them resulted in similar OCVs of 10mV.

At a later stage of the procedures, high resolution SEM/EDS images were obtained for different perovskite films. Among other observations, which will be discussed in the following sections, the images revealed micrometer sized fragments of glass (**Figure 15g,h**). These fragments were most likely introduced when metal tweezers were used to handle the substrates inside the glovebox. Although a nitrogen jet was applied to clean the surface after each step, the fragments were probably deposited during transfer from the spin coater to the hot plate, when the solution had already been spun, making it

impossible to clean the surface again. To address this issue, a final attempt was made using plastic tweezers that did not scratch the glass. The resulting cells, one of which is shown in **Figure 15f**, displayed no improvement, despite exhibiting a visually clean and hole free surface.

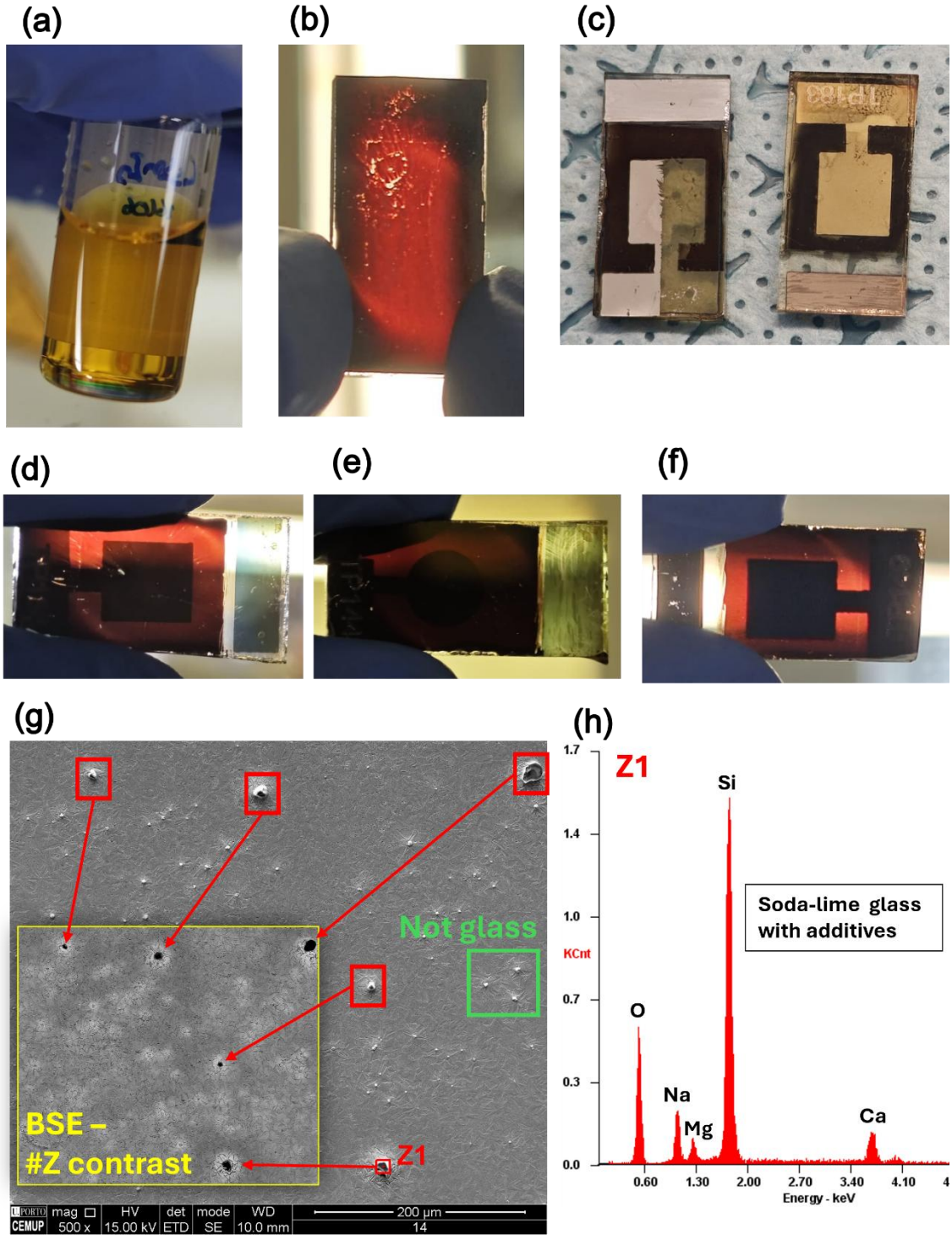


Figure 15 – (a) Perovskite solution prepared using 99.999% purity SnI_2 precursor. **(b)** Perovskite film obtained from the solution shown in subfigure **(a)**. **(c)** Cells after thermal deposition of Ag contacts, with partial removal of silver from the left cell using sticky tape. **(d)** Cell after thermal deposition of 20 nm Au contacts. **(e)** Cell after deposition of Ag contacts with a controlled venting process. **(f)** Cell obtained from the final attempt. **(g)** High resolution SEM image of a perovskite film

showing glass fragments (highlighted in red). The distinction between glass fragments and other features is visible in the back scattered electron image (highlighted in yellow). **(h)** EDS spectrum acquired from a region containing glass fragments.

3.2.2. Effect of degradation on perovskite film

As described in previous sections, the primary limitation of tin-based perovskite solar cells is their instability in air. This effect was evident during fabrication: when the chamber was backfilled with nitrogen, the devices delivered a measurable open-circuit voltage, whereas under air they produced no OCV. These observations indicate that air-induced degradation directly compromises device operation.

An important caveat is that the reflectivity measurement was not done correctly (reflectivity was too high at longer wavelengths). This meant that we could not use it to calculate absorbance, thus 1-transmittance is shown. The transmittance (t) of the perovskite film was calculated as: $t_{film} = \frac{t_{stack}}{t_{glass}}$.

To probe this behavior, we used UV-VIS-NIR spectrophotometry to track changes in the optical response of the perovskite. Because the Y-phase has a wider bandgap than the black phase, air exposure is expected to reduce absorption at longer wavelengths. We therefore measured the transmittance of two identical $CsSnI_3$ films on glass at several time points over 90 minutes of continuous air exposure. The results are shown in **Figure 16**.

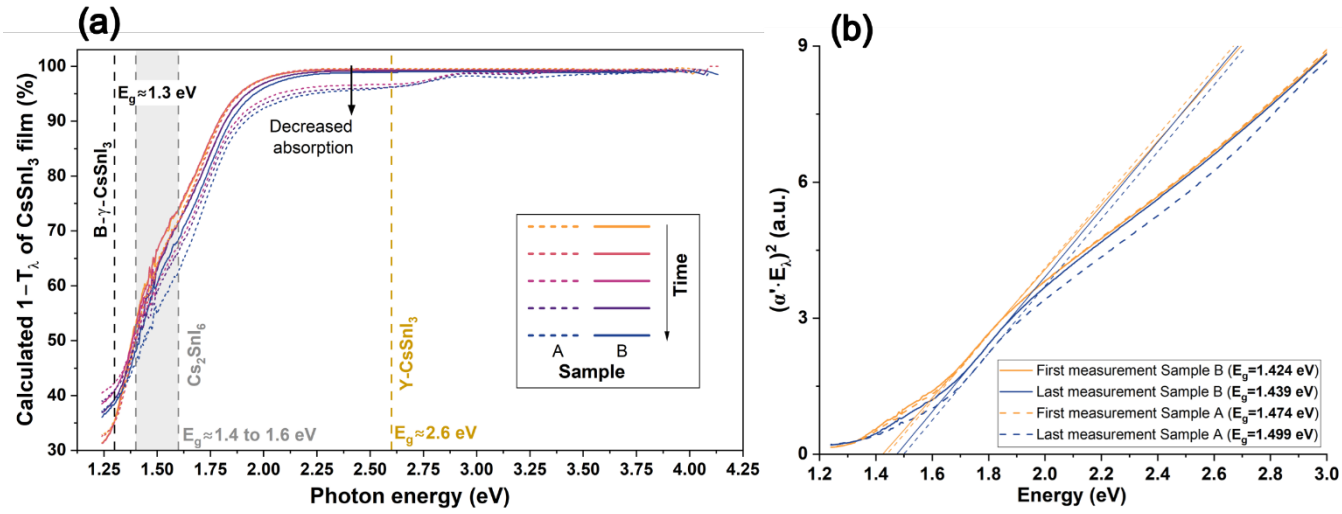


Figure 16 – (a) Time evolution of absorption* as a function of photon energy for $CsSnI_3$ films on a glass substrate measured by UV VIS NIR spectrophotometry. Two nominally identical samples, A and B, were recorded repeatedly over about 90 minutes, and successive spectra follow the time order indicated in the inset. Vertical dotted lines mark literature bandgap energies for phases that may be present in the film. The arrow highlights the progressive decrease in apparent absorption during the measurement period. **(b)** Tauc plot of absorption* zoomed on the absorption edge ROI. Straight lines represent the linear fit of the linear absorption edge. Bandgap values determined from X intercept. *Because reflectance was not measured reliably, one minus transmittance is reported in place of absorption.

The expected decrease in absorption as the film degrades is observed. Sample A shows an interesting behavior on the 2.7eV zone, where an absorption edge seems to be created upon the third measurement. This is close to the expected yellow phase band gap which might be an indication that this phase has formed during the degradation process. The increase in the effective optical bandgap of the film is verified by the Tauc analysis [180], which showed an increase of 25meV and 15meV for samples A and B, respectively. The value of the optical bandgap calculated on the first measurement was around 1.43eV for both samples. This value lies at the lower end of those reported for Cs_2SnI_6 but is higher than most reports for B-γ-$CsSnI_3$ [181],[182],[183],[184],[185]. However, the fact that the bandgap increases with air exposure time indicates that the film is transitioning into the higher bandgap Cs_2SnI_6 phase from the lower bandgap B-γ-$CsSnI_3$. Furthermore, the presence of a double slope (the first slope between 1.3eV and 1.5eV the second slope between 1.5eV and 1.75eV) could be a result of the presence of two distinct phases. The fact that the slopes progressively merge with time may support this idea. Despite these changes, the overall absorption reduction is around 10% over 90 minutes of measurement, indicating that only minor degradation occurred during this period. This observation aligns with the visual signs of degradation observed for almost all films prepared in this work.

To directly observe the effects of mild degradation on the perovskite film, a $CsSnI_3$ film was analyzed in SEM after being left for more than a month inside the glovebox. The resulting images are shown in **Figure 17**.

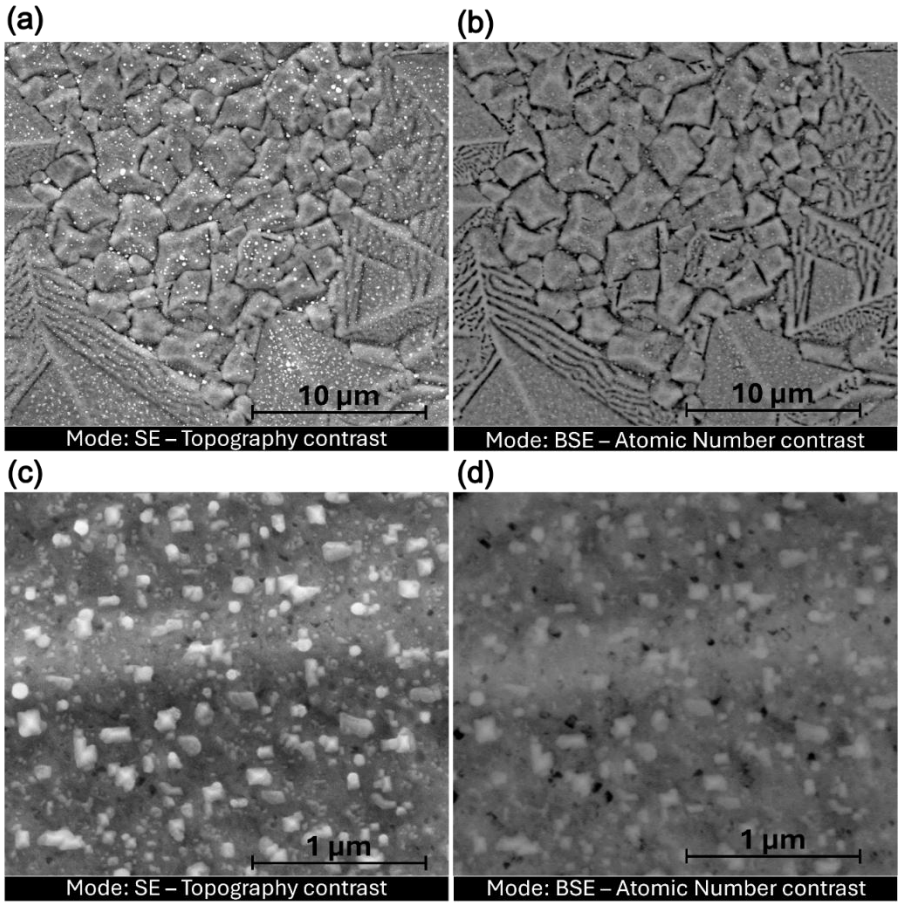


Figure 17 – Scanning electron microscopy of a $CsSnI_3$ film stored in a nitrogen glovebox for more than one month. Images are shown at two magnifications. Left panels show secondary electron mode. Right panels show backscattered electron mode. Scale bars are 10 µm in the upper panels and 1 µm in the lower panels.

Bright spots in **Figure 17a** are distributed across the entire sample. Fresh films, such as those shown previously, sometimes display similar features, but at much lower density, typically one or two in a 50x50 µm area. This comparison suggests that the bright spots are associated with perovskite degradation. The close-up topography in **Figure 17c** shows that each bright spot is a highly faceted protrusion emerging from the surface of a larger crystal. In **Figure 17d**, these protrusions appear brighter than the surrounding crystal. Backscattered electron (BSE) imaging is primarily sensitive to the average atomic number, and although topography can also influence contrast, at nanometer scale and at 15 kV, the topographic contribution is strongly reduced. We therefore interpret the higher BSE intensity of the protrusions as evidence that they have higher average atomic number relative to the host crystal. If they arise from air-induced degradation, a plausible assignment is Cs_2SnI_6, which has a higher average atomic number than $CsSnI_3$ and is reported to form at film surfaces as nanocrystals during oxidative conversion [184], [186], [187]. Focusing the beam to acquire EDS data burned these small crystals, which prevented reliable compositional analysis.

Another feature evident in the close-up images is the presence of small dark spots that appear in both secondary electron and backscattered electron images, indicating that they are holes or voids within the crystal. These features are commonly associated with degradation [187]. Oxidation of Sn(II) to Sn(IV) can generate tin- and iodide-related defects at the surface and, with time, these defects may drive localized restructuring that forms pinholes, producing the observed dark topographic contrast.

Overall, stability tests indicate that even trace amounts of oxygen and water promote degradation of the black phase into more stable products, like Cs_2SnI_6. The transformation initiates at the surface and proceeds at small length scales. Nevertheless, brief air exposure, on the order of 1 hour, has a relatively low impact on the film's optical characteristics.

3.2.3. Electrochemical property measurements

The morphology of perovskite films strongly influences solar cell performance. Defects, pinholes, and high surface roughness degrade device operation and reduce PCE. Electrochemical properties are equally critical because they govern charge generation, transport, and interfacial kinetics. Measurements of charge transport and electrochemical potentials provide information that morphology alone cannot capture.

Charge transport measurements shown in **Figure 18** were performed in a van der Pauw (VdP) Hall geometry on a perovskite film deposited on an insulating glass substrate. Four gold probes contacted the film surface near the perimeter. This configuration is suboptimal because the perovskite-gold interface likely forms a non-ohmic contact that adds contact resistance and charge accumulation. Such contacts can introduce artifacts, including hysteresis and mixed ionic and electronic conduction, which distort the measured conductivity, carrier concentration, mobility, and Hall coefficient. Additionally, the setup probes lateral charge transport, whereas current flow in an operating solar cell is predominantly vertical. Thus, these measurements may not accurately reflect the transport characteristics of the perovskite film under device operation.

Electrical conductivity is a key metric for perovskite films. If conductivity is too low, series resistance increases and the fill factor decreases. If it is too high, it may indicate an elevated carrier concentration caused by self-doping, particularly in tin-based PSCs, which is undesirable because the same defects that drive self-doping also introduce non-radiative recombination losses. The measured conductivities (**Figure 18a,b**) fluctuate around 100 S/cm and 30 S/cm for samples 1 and 2, respectively. These values are high for perovskite films but typical for $CsSnI_3$ films [188], [189]. Charge carrier density (**Figure 18c,d**) is on the order of 10^{19} and 10^{18} cm^{-3} for samples 1 and 2, consistent with

prior reports for $CsSnI_3$ [55], [189]. Measured mobilities (**Figure 18e,f**) range from approximately 10^1 to 10^3 cm^2 V^{-1} s^{-1} in both samples and increase with temperature. These values are on the higher side of the ranges typically reported in the literature [55], [150], [189].

However, at most measurement points, the Hall coefficient is negative, and the Hall-derived mobility and carrier concentration indicate n-type conduction. The literature generally describes $CsSnI_3$ as p-type, attributed to tin vacancies formed as Sn^{2+} oxidizes to Sn^{4+}. In contrast, Cs_2SnI_6 is strongly n-type. The observed n-type response could arise from partial surface conversion of $CsSnI_3$ to Cs_2SnI_6. Given the brief air exposure, any Cs_2SnI_6 should be confined to a thin surface layer on bulk $CsSnI_3$, which would be unlikely to dominate transport across the entire film. Moreover, the measured absolute values of conductivity and carrier density are consistent with self-doped $CsSnI_3$, but significantly higher than values reported for Cs_2SnI_6 thin films [182], [183], [185].

The oscillations between predominantly positive and predominantly negative charge carriers could be a result of ion migration during the measurement. Furthermore, the positive temperature dependence of mobility is atypical for halide perovskites, where mobility usually decreases as temperature rises due to stronger electron-phonon interactions [190]. The observed trend suggests a significant contribution from ionic motion to the transport signal, since ionic conductivity increases with temperature [191]. Taken together, these results suggest that the negative Hall sign does not necessarily originate from extensive phase conversion to Cs_2SnI_6 and may instead reflect surface or interfacial conduction, mixed pathways, or measurement artifacts.

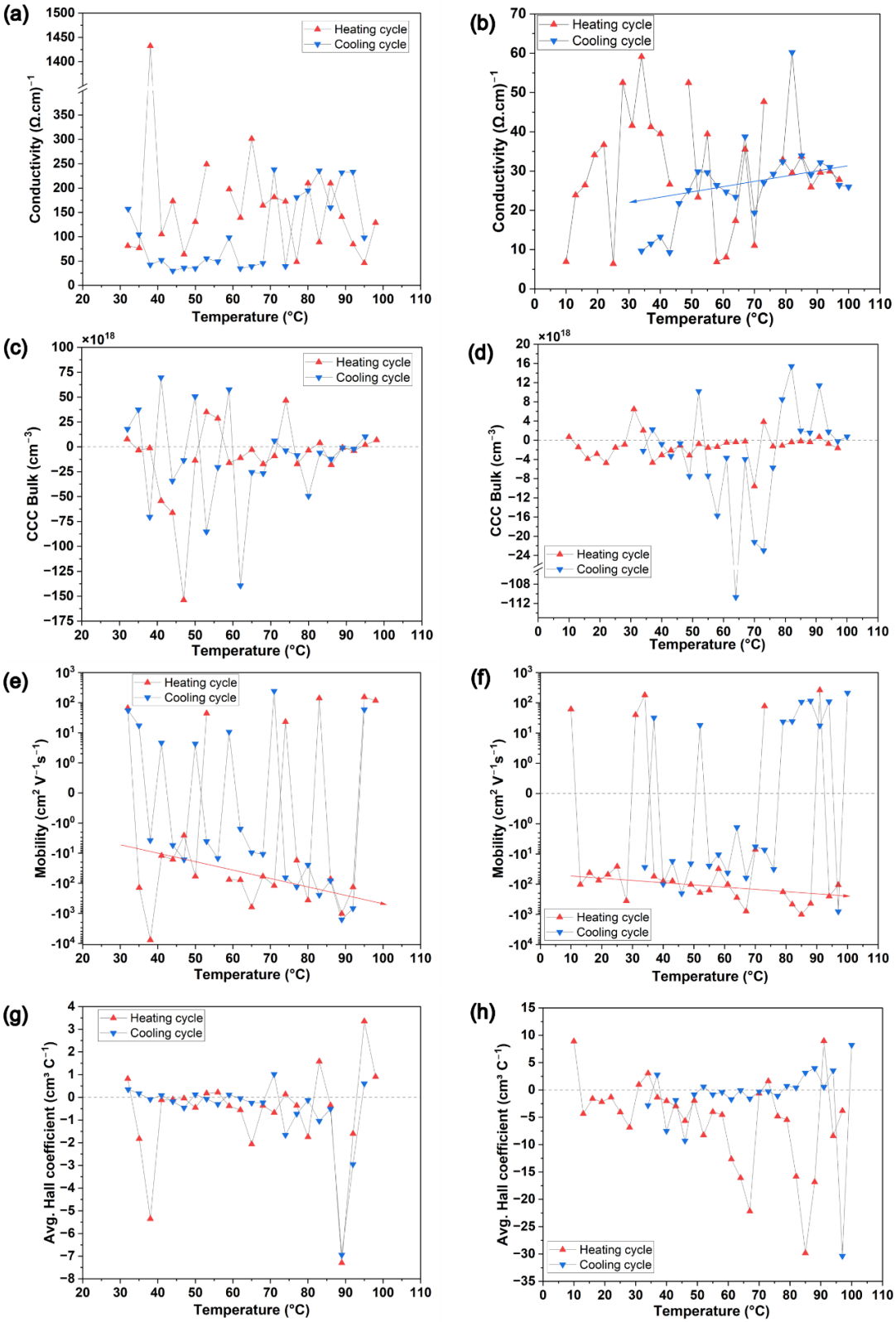


Figure 18 – Temperature-dependent dark transport parameters extracted from Hall-effect measurements for two perovskite thin film samples. Left column **(a, c, e, g)** corresponds to sample 1, right column **(b, d, f, h)** corresponds to sample 2. Red symbols indicate the heating cycle, blue symbols indicate the cooling cycle. (a, b) Electrical conductivity as a function of temperature. **(c, d)** Bulk charge carrier concentration (CCC bulk) as a function of temperature, the horizontal dashed line marks zero. **(e, f)** Hall mobility as a function of temperature, plotted on a logarithmic scale. **(g, h)** Average Hall coefficient as a function of temperature, the horizontal dashed line marks zero.

Scanning kelvin probe measurements allow for the inference of the surface work function of each layer in a cell, which corresponds to the fermi level of the material. The placement of the fermi level in the bandgap depends on the charge carrier concentration and sign. N-type materials have a fermi level closer to the conduction band while p-type materials have a fermi level closer to the valence band. Section 1.2.2 highlighted that proper energy level alignment across the device stack is critical for device performance. Estimating the surface work function enables assessment of the alignment between layers. However, SKP measurement probes the surface potential, which can differ from bulk energy levels because it is sensitive to internal band bending [192] and to external influences such as oxidation, interfacial dipoles, and charge accumulation [193].

The results from the SKP measurement are shown on Erro! A origem da referência não f oi encontrada.. The PTAA work function is slightly lower than expected. However, the PEAI wetting layer can lower the surface potential through interfacial dipoles [194]. Thus, the measured plateau at about 5.05 eV is close to the expected value of 5.15 eV [195].

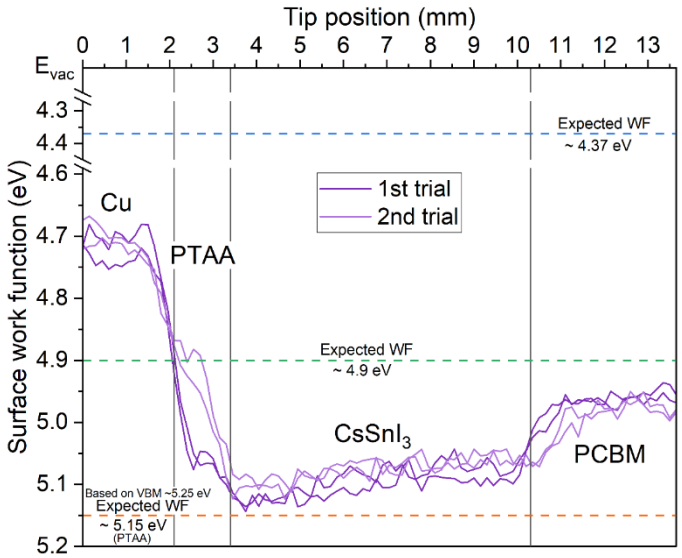


Figure 19 – Scanning Kelvin probe (SKP) line scan of surface work function (WF) across a Cu, PTAA, $CsSnI_3$, and PCBM stack. The y axis shows surface WF in eV referenced to vacuum level. The x axis shows the lateral tip position in millimeters. Two independent scans are plotted (1st trial and 2nd trial). Vertical dashed lines mark the approximate lateral boundaries between layers. Horizontal dashed lines indicate literature WF values for PTAA, about 5.15 eV (estimated from known VBM and CBM) [195], $CsSnI_3$, about 4.9 eV [196], and PCBM, about 4.37 eV [198].

For the perovskite, the average surface work function is about 5.1 eV, which is higher than the expected 4.9 eV [196]. Because the measurement was performed in air, surface oxidation is expected. This creates room for two scenarios: In the first, commonly cited in the literature as the Y-phase degradation pathway, the oxidation of Sn^{2+} to Sn^{4+} increases donor defects, enhancing the p-type character and consequently raising the WF near the surface. The other scenario involves the degradation to Cs_2SnI_6, which

happens in dry air and is accelerated by light exposure [154]. Cs_2SnI_6 is a double-perovskite n-type material with a WF ≈ 4.9 to 5.1eV [185], [186]. Both cases could lead to an increase in the WF to values closer to the measured 5.1eV. However, they could lead to very different scenarios in what concerns band alignment. $CsSnI_3$ self-doping does not significantly change the position of the CBM or VBM [197]. On the other hand, the presence of a Cs_2SnI_6 surface layer would create a potential well in the conduction band, increasing recombination at the interface between the perovskite and the ETL as shown on **Figure 20b**.

Still, it is expected that the WF of the perovskite near the PTAA interface to be lower, closer to the expected 4.9 eV. In a p type semiconductor, the Fermi level lies closer to the valence band maximum. Taking the $CsSnI_3$ bandgap to be 1.3 eV [49], we estimate the VBM to be ~0.4 eV below the Fermi level near the PTAA/Perovskite interface. Assuming a perovskite WF of 5.0 eV at that interface, the corresponding ionization energy is approximately 5.4 eV. The PTAA's VBM is ~5.25 eV relative to the vacuum level [195], which implies an uphill offset for hole extraction of about 0.2 eV, which provides efficient hole extraction without significant voltage loss.

Looking at the other interface, the PCBM layer shows a WF plateau around 5.0 eV. This value is higher than the expected 4.37 eV [198]. Two considerations help explain this difference. First, PCBM is sensitive to oxygen and light, which, similar to the perovskite, can increase the WF [199],[200]. Second, the PCBM thickness is approximately 10 to 20 nm. At this thickness, the underlying layer can still influence the measured surface potential because the film may not fully screen interfacial charge, particularly when the thickness is comparable to the Debye length [201]. Given that the layer beneath PCBM has a higher WF, this coupling would raise the measured WF of PCBM. Both effects likely contribute to the high value. Even so, the PCBM layer has a lower WF than the perovskite, as expected. The CBM of PCBM is near 4.0 eV [198]. Using the previous assumptions for $CsSnI_3$, with WF equal to 5.0 eV and the Fermi level 0.4 eV above the VBM, the VBM is at 5.4 eV (VBM = WF + dE_{VBM} = 5.0 + 0.4), and the perovskite CBM is at 4.1 eV (CBM = VBM − Eg = 5.4 − 1.3). This yields a small uphill offset of about 0.1 eV for electron extraction into PCBM. This modest misalignment is a known incompatibility between halide-perovskites and common electron transport layers, although it should not prevent device operation [202].

Finally, a significant shift in the work function is measured across the X axis for perovskite. WF values start slightly above 5.1eV near the PTAA interface and end below

5.1eV near the PCBM interface. This may be an indication of band bending due to the built-in electric field [192], [203].

Overall, the differences between our measured values and those reported in the literature can be explained by oxidation since the SKP measurements were taken after more than 30 minutes of air exposure. Such prolonged exposure does not occur during fabrication (after the protocol revision), so oxidation is weaker and has limited depth, as we have seen in the SEM images of pristine films. In addition, the completed stack is covered by BCP, which reduces direct contact with air. Taken together, these factors indicate that the bulk energy levels in the devices should remain close to the intended values, and severe band misalignment is not expected, as shown in **Figure 20a**.

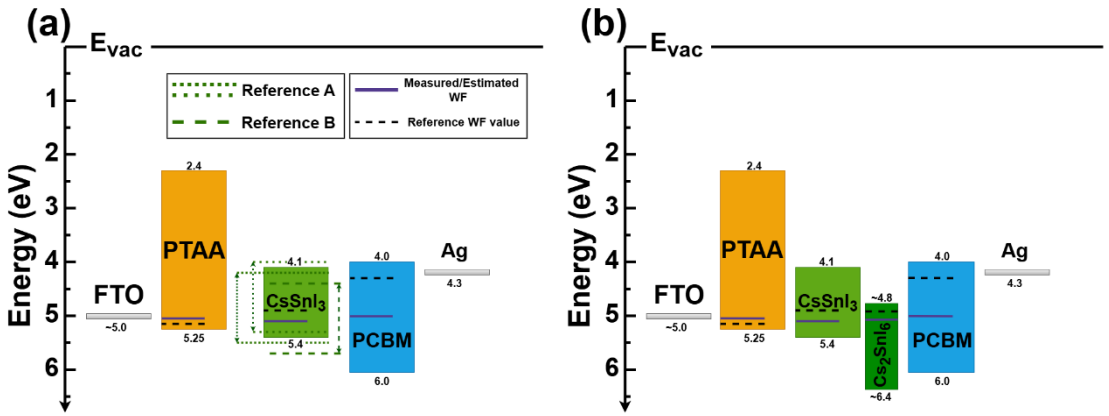


Figure 20 – Estimated energy-level diagram of FTO/PTAA/$CsSnI_3$/PCBM/Ag stack, referenced to vacuum (Evac = 0 at top; energy depth increases downward). Colored bars show approximate band positions. Grey bars indicate contact work functions. Horizontal purple lines are SKP-derived (measured/estimated) work functions; horizontal black dashed lines are literature work-function values. Dotted and dashed green boxes bound three literature ranges (Reference A and Reference B) for the CsSnI3 band edges. **(a)** Expected scenario for full device with minimal oxidation **(b)** Expected scenario for oxidized $CsSnI_3$ surface. References for WF, CBM and VBM values: FTO- [204] ; PTAA- [195]; Ref A-[205], Ref B-[49] ; PCBM- [198] ; Ag- [206]; Cs_2SnI_6-[185].

Overall, the electrochemical properties of the perovskite film and device layer stack are within the expected bounds, considering the suboptimal experimental setup. While the measured transport characteristics are not ideal, they should not prove to be a total barrier for the device functioning.

3.2.4. Morphology of the perovskite crystals and effect of wetting layer

To compare the morphology of the perovskite obtained with the new high purity precursor, SEM images are compiled in **Figure 21**. Overall the films seem relatively uniform. However, there are some features that should be inspected more carefully.

The SEM images in **Figure 21c,d** show cruciform, needle-like dendrites that originate from single nuclei and extend from the grain center toward the corners. Whether the outer grain boundary is square faceted or shows spherulitic or chevron-like serrations,

the interior cruciform consistently runs from center to corners along the same in-plane <110> set. The persistent 45º alignment relative to the center point indicates a common kinetic origin tied to edge propagation, rather than post-growth cracking. AFM images (**Figure 22a,b,c,d**) shows that the arms are raised ridges bordered by shallow depressed plateaus, with a typical height difference of approximately 40 to 60 nm. The bright lines in SEM therefore arise primarily from topographic secondary-electron contrast, not composition contrast.

These features are related to Hopper/diffusion limited growth, which is the result of high supersaturation and slow diffusion speed, reported broadly, for example in NaCl [207] or metal alloys [208], and also in halide perovskites [175], [176], [209], [210],[211],[212],[188].

The crystallization of solution-processed films typically involves two coupled kinetic processes [179]. First, when local supersaturation is reached, solute species precipitate and react to assemble the crystal lattice. This step is governed by molecular-scale thermodynamics and reaction pathways that determine how precursors dissociate and recombine. The reverse process, dissolution back into the liquid, can also occur but becomes less significant as solvent evaporates during annealing. Second, mass transport must replenish reactants at the growth front through concentration gradients and diffusion. Overall growth is limited by whichever step is slower. If precipitation and incorporation are slow, or if dissolution is significant, the regime is reaction-controlled, also called reaction-limited. If the diffusive flux to the interface cannot keep pace with precipitation, the regime is diffusion-controlled, which can result either from low diffusivity, for example due to high solution viscosity, or from very rapid precipitation under high supersaturation. In halide perovskites, reaction-limited growth is generally preferred because it ties crystal evolution to intrinsic molecular interactions of the precursors and solvents, whereas diffusion-limited growth often produces spatially inhomogeneous concentrations and poor morphology. In practical terms, rapid antisolvent exposure and fast solvent evaporation create steep concentration and viscosity gradients. A nucleus can deplete local precursors faster than diffusion can replenish them, so edges and tips outrun faces under flux-limited growth. Thus, reducing the volume of anti-solvent, limiting the initial evaporation of solvents or slowing the crystallization reaction could improve film morphology, although this was not tested.

Another relevant characteristic is the presence of ridges at 45º to the main dendritic formations, which form terrace like steps propagating from the center of the crystal on the faceted faces. We first tested whether the facet ridges and terraces were stress-relief

features imposed by the wetting layer. This was plausible because the two underlayers behaved very differently during spin coating: on PEAI the ink spread readily, whereas on F-PEAI spreading was visibly hindered. If underlayer-driven stress were responsible, such a clear change in spreading and adhesion should have altered the ridge pattern. However, the SEM morphologies were essentially the same on both underlayers, and ridge spacing, straightness, and grain-locked alignment were unchanged, so the wetting-layer stress hypothesis is not supported by the images.

A more consistent interpretation is again the kinetically driven dendritic, hopper-type growth, as schematized on **Figure 23**. Secondary branches can run along the sides of the square, that is, along <100>, which are rotated by 45º relative to the main <110> directions. Where neighboring side branches meet and coalesce, the valley closes and the surface appears flatter; where they do not meet, a linear gap or ridge remains between dendrites.

These morphological features create high roughness in the film, which is even visually apparent during the fabrication process as they do not seem like polished mirror-like surface often described in literature [164], [213]. AFM characterization (**Figure 22a,b,c,d**) shows roughness on the order of the measured film thickness, roughly 300nm (**Figure 22e**). Considering the features presented earlier, it is likely they contribute to the formation of short-circuiting paths between layers, significantly hindering device performance. This hypothesis is supported by the measured series resistance of fully assembled cells, which was around 20Ω in dark and 3Ω under illumination based on the linear J-V characteristics. when typical resistances are on the order of kΩ [214], [215].

Finally, the morphology of the films after PCBM and BCP deposition and the subsequent thermal treatments were examined (**Figure 24**). The PCBM anneal was carried out at 100ºC, which is higher than the perovskite annealing temperature. Even so, films with and without the PCBM layer show largely similar morphology. The topographic contrast is only slightly reduced across the sample, which suggests a largely conformal PCBM coating. After BCP deposition, no additional changes are evident. In some regions, small surface smudges are visible on the perovskite (**Figure 24c,d,e,f**), but they are limited in extent.

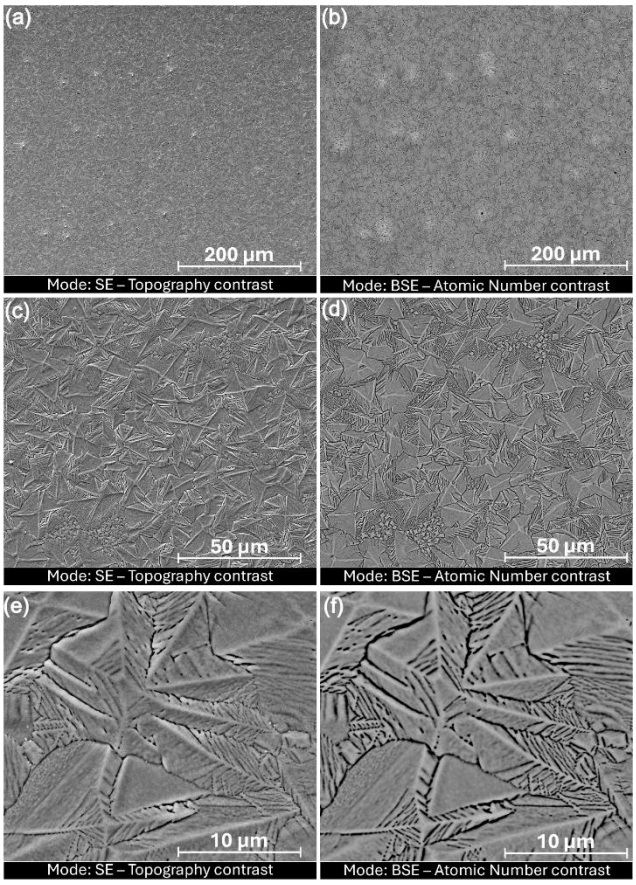


Figure 21 – Scanning electron microscopy of a $CsSnI_3$ film. **(a)** Low magnification secondary electron, SE, image showing continuous film coverage, scale bar 200 micrometers. **(b)** Low magnification backscattered electron, BSE, image with comparable large-area morphology, scale bar 200 micrometers. **(c)** Intermediate magnification SE image resolving faceted grains with dendritic ridges, scale bar 50 micrometers. **(d)** Intermediate magnification BSE image of the same morphology, scale bar 50 micrometers. **(e)** High magnification SE image highlighting terrace-like steps within grains, scale bar 10 micrometers. **(f)** High magnification BSE image of the same region, scale bar 10 micrometers.

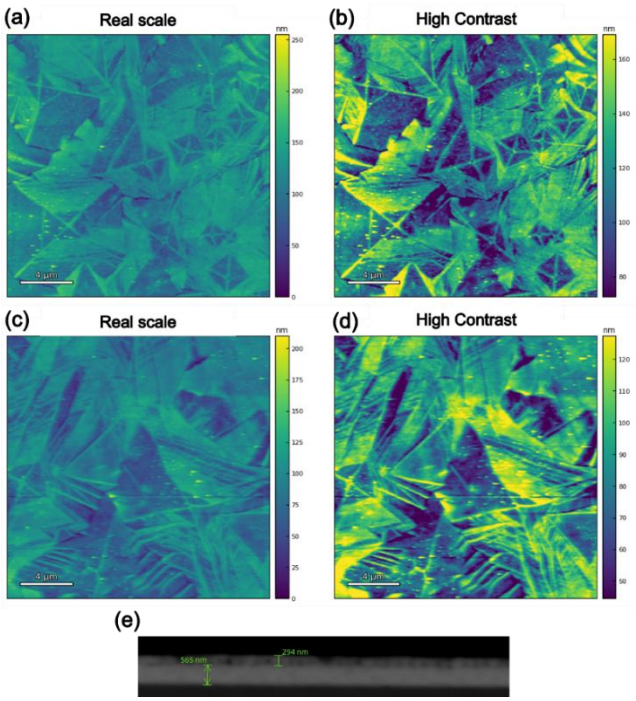


Figure 22 – Atomic force microscopy of a $CsSnI_3$ perovskite film. **(a)** Area 1 height map shown with the full acquisition range, color bar 0 to 250 nm, scale bar 4 micrometers. **(b)** Same field of view as in (a) displayed with a narrower color range, 80 to 160 nm, to enhance topographic contrast, scale bar 4 micrometers. **(c)** Area 2 height map with the full range, color bar 0 to 200 nm, scale bar 4 micrometers. **(d)** Same field of view as in (c) with a narrower color range, 50 to 120 nm, to enhance contrast, scale bar 4 micrometers. **(e)** Cross sectional image of a FTO/PTAA(PEAI)/$CsSnI_3$/PCBM/BCP stack with measured thicknesses indicated, approximately 565 nm (FTO) and 294 nm (Perovskite).

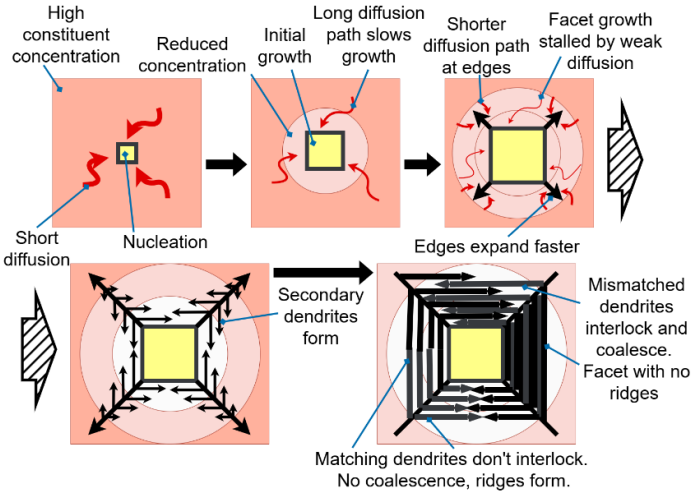


Figure 23 – Schematic of diffusion limited dendritic growth on a {100} facet of $CsSnI_3$. Color code: the yellow square is the crystal nucleus and growing facet; the pink to red background represents the concentration field of growth species in the surrounding medium, darker red indicates higher concentration and lighter pink indicates depletion; red wavy lines depict diffusing species and the effective diffusion path; pale gray rings indicate isoconcentration fronts and depletion zones; black arrows show preferred growth directions and relative rates; thin black lines mark primary and secondary dendrite rims; thick black bands represent coalesced rims where dendrites interlock; blue arrows are annotations only. From left to right the sequence shows nucleation in a region of high concentration, initial growth with long diffusion paths that slow the facet center, faster edge advance as the diffusion path becomes shorter at the rim, formation of secondary dendrites, and two outcomes, either matching dendrites do not interlock and ridges remain, or mismatched dendrites interlock and coalesce, resulting in a smooth facet with no ridges.

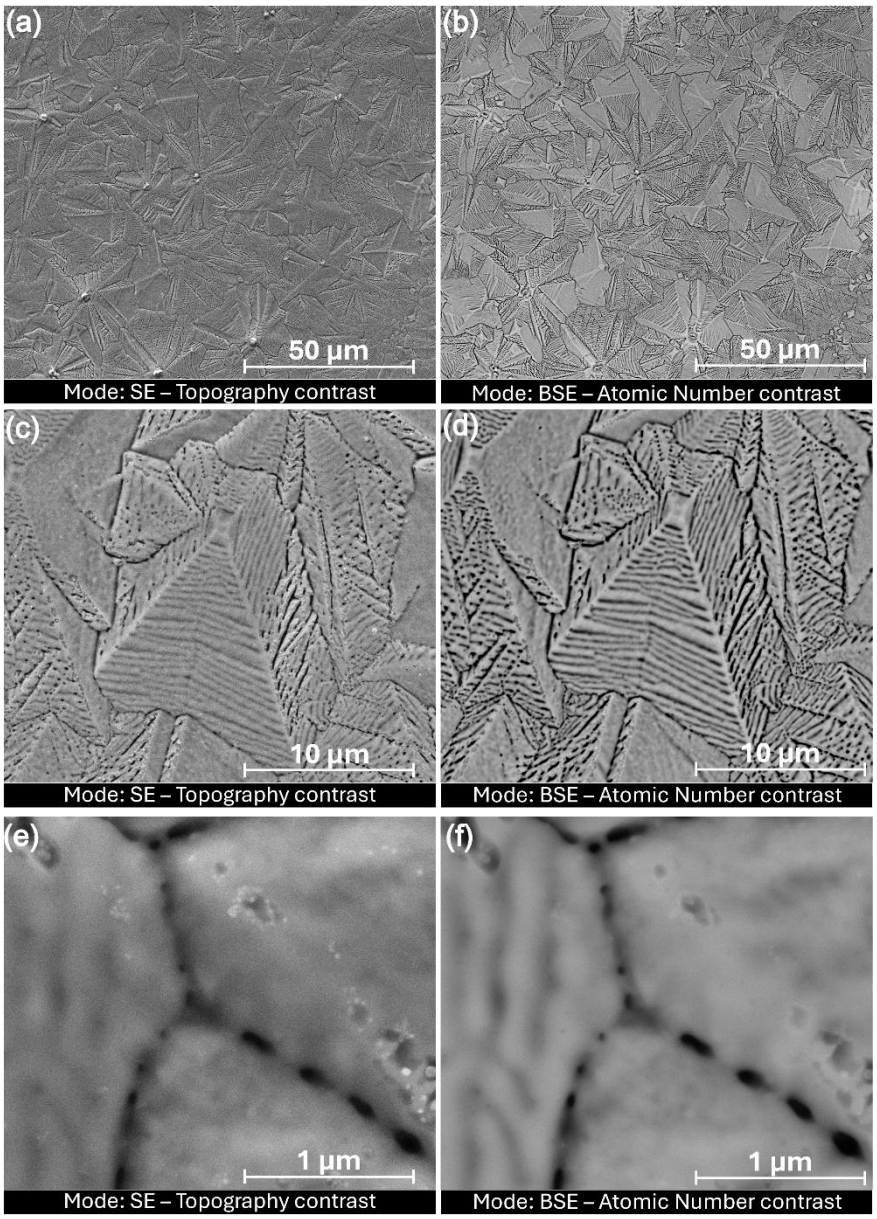


Figure 24 – Scanning electron microscopy of a $CsSnI_3$ film on PTAA after PCBM and BCP deposition and PCBM sintering. **(a)** Low magnification secondary electron image showing continuous coverage, scale bar 50 micrometers. **(b)** Low magnification backscattered electron image of the same area, scale bar 50 micrometers. **(c)** High magnification secondary electron image resolving faceted grains with terrace like ridges, scale bar 10 micrometers. **(d)** High magnification backscattered electron image of the same region, scale bar 10 micrometers. **(e)** Highest magnification secondary electron image highlighting smoothened grain surfaces and grain boundaries with occasional small particulates, scale bar 1 micrometer. **(f)** Highest magnification backscattered electron image of the same area, scale bar 1 micrometer.

3.2.5. Effects of tin fluoride additive on film morphology

The use of tin fluoride (SnF_2) is established in literature as the best way to prevent oxidation of the perovskite precursor solution, ensuring that the deposited film is oxidation free, by reacting with the oxidized SnI_4 to form SnF_4 and SnI_2 [216]. Although fresh high purity SnI_2 shows minimal oxidation in solution, DMSO promotes oxidation [178]. In addition, the precursor gradually degrades even under inert storage.

Consequently, adding SnF_2 is necessary to preserve the quality of the perovskite ink. The effects on film morphology are also generally accepted to be beneficial. SnF_4 can act to slow down the crystallization kinetics of the perovskite, passivate defects on grain boundaries and reduces the formation of pinholes leading to improved film continuity [155], [156].

The addition of SnF_2 to the perovskite solutions showed an almost immediate change in color from light orange to clear yellow, indicating the quick effect of the sacrificial agent as shown on **Figure 25**.

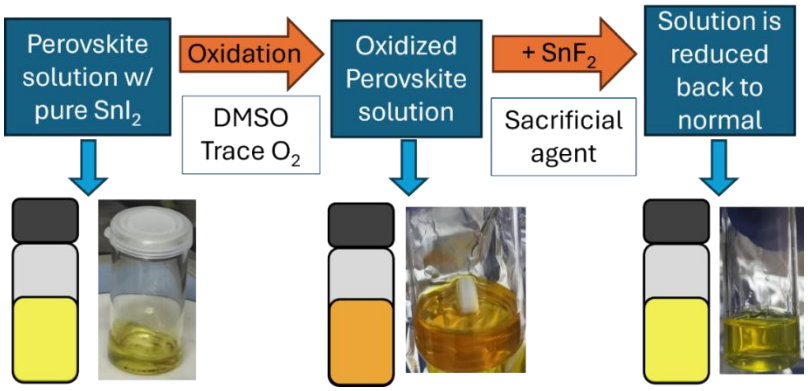


Figure 25 – Oxidation and remediation of a $CsSnI_3$ perovskite precursor solution. Left: solution prepared with pure SnI_2. Middle: oxidized solution. Right: solution after addition of SnF_2, which restores the original state.

In **Figure 26** are shown SEM images of perovskite films prepared with different concentrations of SnF_2. The sample with 20 mol% SnF_2 exhibits the most pronounced change in crystallization behavior. Nucleation is abundant, but grains remain very small and coalescence is minimal. At 20 mol% excess (mol% in excess relative to SnI_2 molarity in a stoichiometrically correct solution), the perovskite ink is strongly tin rich. A modest tin excess is often reported to improve film quality by suppressing oxidation and vacancy formation [217], but an extreme imbalance could limit crystal growth by depleting other constituents which suppresses grain growth and coalescence.

All films display two domain types with distinct crystal morphologies. The prevalent domain contains few large crystals with diameters of tens of micrometers. The less common domain comprises many small crystals with diameters of a few micrometers (**Figure 26g**). The addition of SnF_2 seems to reduce the discrepancy between these regions. The size of the larger crystals is reduced while nucleation is higher and the overall homogeneity of the film seems to be improved. Additionally, the frequency of the small crystal domains is reduced.

Additionally, irregular dome-like protrusions are sometimes observed at the centers of individual crystals. To the best of our knowledge, similar features have not been reported. Given that the morphology of these films already differs markedly from most literature examples, this previously unreported feature may reflect an interplay between the overall film morphology and the presence of the fluoride additive. Prior studies of fluoride additives in tin halide perovskites describe reaction-limited crystallization, in which fluoride-bearing species derived from SnF_2 and SnF_4 are excluded from the perovskite lattice and redistributed to interfaces and grain boundaries, where they seal pinholes and passivate defects [156], [179]. In contrast, the films examined here appear to grow under diffusion-limited conditions. Under these kinetics, mass transport may be insufficient to carry fluoride species away from early nuclei, leading to their accumulation at nucleation sites and persistence during subsequent growth. This localized enrichment could produce irregular dome-like protrusions at crystal centers.

One final important observation is that adding SnF_2 did not change the measured open-circuit voltage. In principle, this suggests that oxidation during fabrication is not the primary cause of band misalignment, because SnF_2 is expected to suppress oxidation during this stage. Therefore, if band misalignment is present, it is unlikely to arise from perovskite oxidation during fabrication under the conditions employed in this work.

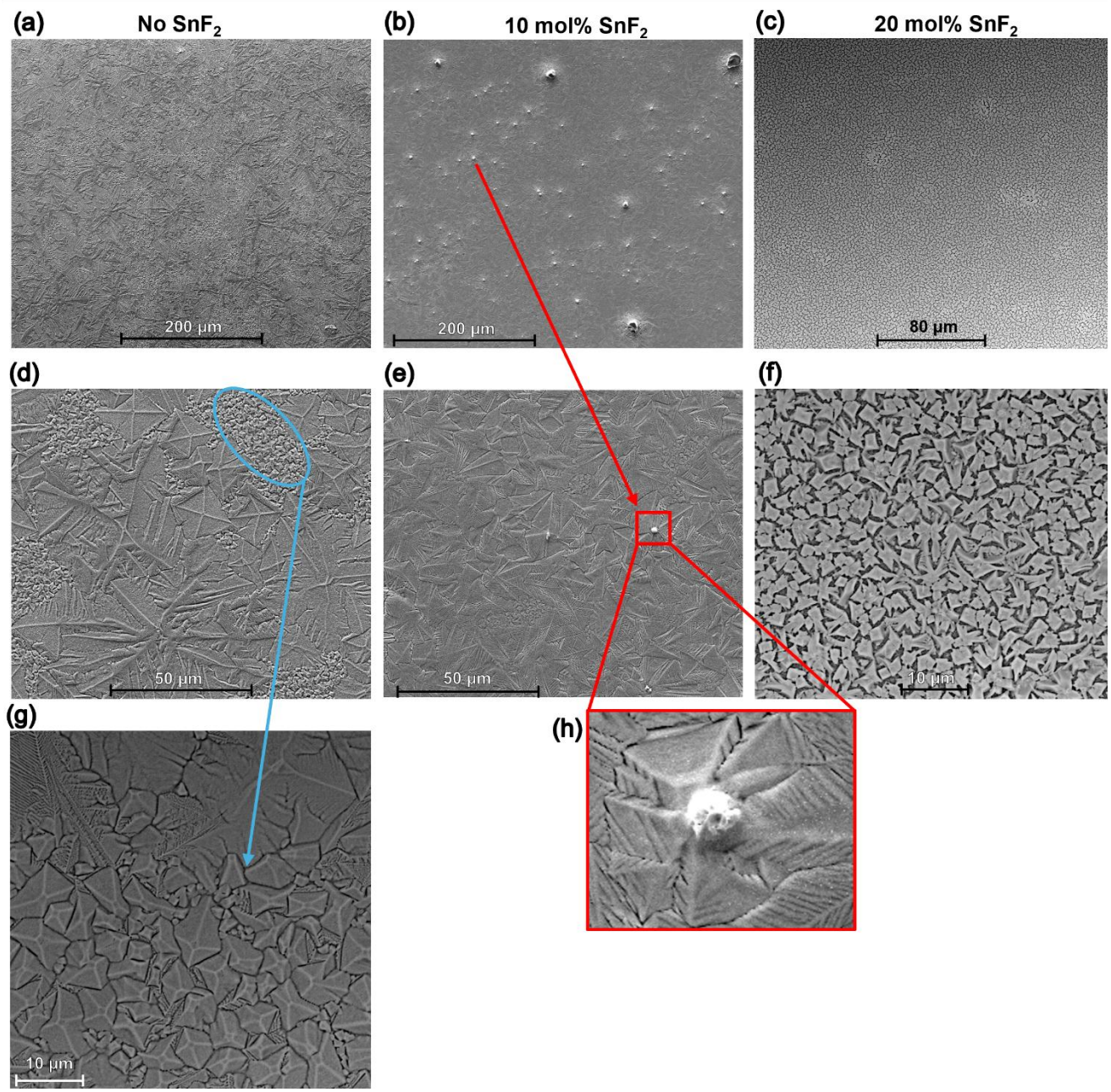


Figure 26 – Scanning electron microscopy of perovskite films prepared with varying SnF_2 content: **(a)** 0 mol% SnF_2, scale bar 200 µm; **(b)** 10 mol% SnF_2, scale bar 200 µm; **(c)** 20 mol% SnF_2, scale bar 80 µm. (values of mol% are in excess relative to SnI_2 molarity in stoichiometrically correct solution). Higher magnifications of panels (a), (b), and (c) are shown in **(d)**, **(e)**, and **(f)**, with scale bars of 50 µm, 50 µm, and 10 µm, respectively. **(g)** Close-up image of a zone with similar crystal formations to the highlighted zone on (d). Panel **(h)** shows the boxed region from (e).

3.3. Conclusions and future work

This work initially focused on systematically investigating how precursor oxidation influences the morphology and device-relevant properties of $CsSnI_3$ thin films. It was demosntrated that an oxidized SnI_2 precursor inhibits the formation of the black-phase in $FASnI_3$ perovskites and severely compromises the morphology of $CsSnI_3$ perovskite films. To address this, a purification protocol was employed to removed SnI_4 and SnO_2

from the oxidized precursor. The resulting oxidation-free SnI_2 crystals enabled the production of $CsSnI_3$ films with larger, well-defined crystals.

In the second part of the study, a commercially available high purity SnI_2 precursor was used, and several modifications were introduced to the perovskite film, device architecture and fabrication process. To assess the stability of tin perovskites, brief, high-intensity oxygen exposure was compared with prolonged, mild exposure. Spectrophotometry indicated that oxidation introduces new phases in the perovskite film, consistent with prior reports, although these effects were minor for approximately one hour of air exposure. Under prolonged, mild exposure inside a glovebox, surface nanocrystals consistent with a Cs_2SnI_6 phase formation were observed.

Electrochemical characterization was conducted using Hall effect and scanning Kelvin probe (SKP) measurements. Hall effect measurements yielded conductivities of 30 to 100 S/cm, broadly consistent with literature values given the limitations of our measurement setup. SKP measurements revealed surface work functions of $CsSnI_3$ and PCBM that were higher than expected, likely due to strong surface oxidation from air exposure. The morphology of $CsSnI_3$ perovskite films was studied using scanning electron microscopy and atomic force microscopy. Both techniques revealed a rough topography dominated by cruciform dendritic growth, characteristic of diffusion-limited crystallization. This growth is likely induced by the antisolvent step or by solvent evaporation. The resulting surface roughness can promote shunting between layers, contributing to the very low open circuit voltages in the fabricated devices. The introduction of SnF_2 reduced precursor oxidation and produced more homogeneous films with a narrower crystal size distribution. However, the additive also produced unwanted surface features, likely due to the accumulation of fluorine-containing byproducts at nucleation sites.

Despite repeated fabrication attempts, all devices showed very small open-circuit voltages (OCVs) and near-linear *J-V* curves. Measurable OCVs only appeared when oxygen exposure was minimized, particularly during vacuum backfilling, suggesting that oxidation-induced band misalignment is a key loss pathway preventing functional operation. Even so, the observed film morphology likely accounts for most of the OCV loss by creating shunt connections between layers.

Based on the problems identified and the improvement avenues discussed, we propose the following directions for future work:

Morphology improvements

- Implement a two-step annealing protocol: first, a brief low-temperature anneal to promote uniform nucleation and ionic diffusion during early growth, then a higher-temperature anneal to ensure crystallization into the black phase and complete solvent evaporation. [218],[219].
- Reduce the total antisolvent volume to soften the quench and limit dendritic growth; alternatively use a finer antisolvent mist to improve spatial uniformity.
- Perform the annealing in a controlled solvent vapor atmosphere to allow a higher peak temperature while moderating crystal reorganization, which should improve film uniformity.
- Systematically vary the perovskite ink concentration to tune nucleation density and grain size.
- Evaluate the effect of additives such as PTM, $EDAI_2$ and sulfur containing compounds.

Stack compatibility and electrochemical alignment

- Study the effect of precursor stoichiometry beyond simple Sn:Cs ratios, including halide mixing (I/Br) to tune bandgap and stability.
- Introduce ultrathin interlayers (e.g., 2D perovskites, self-assembled monolayers) to passivate defects and optimize energy alignment.
- Optimize the PCBM annealing temperature to balance surface smoothing with interfacial stability and energy level alignment.
- Try alternative hole transport layers such as PEDOT:PSS to improve wetting and band alignment.

Oxidation control

- Carry out the back contact deposition on an inert atmosphere, to remove oxygen exposure before this sensitive process.

Although this study yielded several relevant conclusions, including some potentially novel observations, it also has limitations that warrant further investigation. A more systematic investigation of degradation is recommended. Perovskite films should be subjected to accelerated degradation by direct air exposure at controlled relative humidity for defined durations (10 min, 30 min, 60 min, 2 h). After exposure, samples should be stored in an inert environment before characterization. Subsequent compositional analysis by XRD, morphological analysis by SEM and AFM, surface

energetics by SKP, and electrical characterization by Hall effect should then be performed under controlled conditions. The same protocol should be applied to films within complete stacks composed of PTAA, perovskite, PCBM, and BCP to assess the influence of the transport and buffer layers. In addition, device-level characterization (*J-V* curves, SEM, AFM, SKP) should be repeated after thermal deposition to determine the impact of this process. Together with a parallel optimization of perovskite film morphology as outlined above, this workflow should provide a robust path toward fabricating fully functional devices in the laboratory and potentially reveal new strategies to improve their performance.

4. Part II - Background and state-of-the-art

Section 1.1.1 described how the crystal structure of a material determines its electronic properties through the position of the band gap relative to the Fermi level. It was explained that electronically connected materials must balance their electrochemical potential (Fermi level). To this end, charge redistributes until a common electrochemical potential is reached, which establishes an interfacial electric field. In this section, we examine how this interaction underpins electrochemical energy storage devices, with a focus on batteries. We then discuss the role of the active species, the design of solid-state electrolytes, and how microstructuring of electrodes and interfaces influences ion transport, reaction kinetics, and overall device performance.

4.1. Fundamental principles of electrochemical energy storage

The concepts presented in this subsection are based on the original ideas and work **Braga et al.** [220], and well synthesized in ref. [221].

Let's consider the situation where two materials (electrodes) with a different electrochemical potential ($\bar{\mu}_i$ and $\bar{\mu}_j$) are placed into electrical contact via a third material (a separator) which has its own electrochemical potential ($\bar{\mu}_s$). In this situation two scenarios can arise depending on the properties of the separator material.

First, if the separator is a good electron conductor, electrons can move freely between the electrodes, provided the electrodes are also conductive. A transient electric field forms at the separator interfaces and then dissipates as charge redistributes by electron transfer, equalizing the electrochemical potentials. The governing relation is:

$$\bar{\mu}_i - \bar{\mu}_j = \mu_j - \mu_i + z_i e\phi_i - z_j e\phi_j$$

Where $\bar{\mu}$ is the electrochemical potential (fermi energy), μ is the chemical potential, z is the charge of the mobile charges and ϕ is the electric potential of the material. In the first scenario, difference in electrochemical potentials is balanced by electron exchange which changes the chemical potentials of each material.

Second, if the separator is an electronic insulator that blocks electron exchange, the chemical potentials of the electrodes remain unchanged. Equilibrium is then achieved by establishing a static potential difference $\Delta V_{i;j}$ (i.e. an electric field).

If the separator is an inert material with no mobile charges and a high dielectric constant, the imbalance in electrochemical potential will lead to the formation of an electric field across the separator. This is the basic principle of a capacitor, which will

work even if the electrodes are the same material, because the imbalance is created by applying a potential difference (voltage) across the device. In this case, the energy stored is given by $E = (CV^2)/2$, where V is the electronic potential and C is the capacitance. For a flat geometry $C \propto \varepsilon A/d$ where ε is the dielectric constant of the separator, A is surface area and d is the distance between each side of the capacitor. Thus, increasing the dielectric constant or the area will increase the stored energy at a given voltage.

However, If the separator contains mobile charges, that is, an electrolyte, the potential imbalance drives these charges to the interfaces, where they accumulate and form an electric double layer capacitor (EDLC). The equilibrium open circuit voltage of the system is sustained across this double layer. The separation between interfacial electrons in the electrode and counter ions in the electrolyte is on the order of angstroms, which makes electron tunneling into the electrolyte possible. When tunneling occurs, electrons reduce the active ionic species to a neutral form, for example $Li^+ + e^- \rightarrow Li^0$. The neutral species typically nucleates on the electrode as plating or contributes to the growth of a solid electrolyte interface (SEI). Nonetheless, at thermodynamic equilibrium, the reverse oxidation reaction proceeds at the same rate at each interface, so no sustained redox reaction takes place.

In such a device, the electrode with the highest electrochemical potential, referenced to vacuum with μ<0), or equivalently the smallest work function, is the negative electrode and, during discharge, the anode, where oxidation occurs. The opposite electrode, which has the lowest electrochemical potential, is the positive electrode or cathode, where reduction occurs during discharge. The opposite electrode, which has the lowest electrochemical potential, is the negative electrode or cathode because it's where reduction reaction occurs during discharge.

Thus when a negative voltage is applied at the negative electrode (positive voltage on the positive electrode) the electrochemical imbalance is amplified, and the materials can exchange electrons with the external circuit. The resulting overpotential favors reduction at the negative electrode and oxidation at the positive electrode. Plating or intercalation occurs at the negative electrode and energy is stored in the device.

We can utilize the energy stored in the system by connecting the electrodes through an external circuit. The electrodes can then exchange electrons while the coupled interfacial reactions proceed. At the anode, active species are oxidized and enter the electrolyte. At the cathode, electrons from the circuit reduce the active species. Discharge continues

until the electrochemical potentials re-equilibrate under load or the inventory of active species is exhausted.

As reactive species are consumed at the interfaces, they must be replenished by ion migration. Otherwise, the interfacial reactions become transport limited and the current declines. Therefore, the electrolyte should have high ionic conductivity (σ) to sustain supply at the interfaces. Once the electrochemical potentials are balanced again, or the available reactive species are depleted, the redox reactions stop and, at open circuit, the device relaxes to its new OCV.

In the simplest case, where the electrodes are inert metals and therefore provide no active species, the number of participants in the reaction is limited by the electrolyte. Thus, the overall energy stored will be limited since $E \propto QV$, where Q is the total charge taking place in the redox reaction.

More complex systems, including those with alkali metal anodes and/or intercalation cathodes for example, incorporate active species within both electrodes. Consequently, the total capacity, which is proportional to the amount of redox active species participating in the reactions, increases substantially [222],[223].

4.2. Sodium based Solid state batteries

Conventional Li ion and Na ion cells use organic liquid electrolytes because these solvents deliver high room temperature ionic conductivity, about 10^{-3} to 10^{-2} S cm^{-1}, readily wet and conform to porous composite electrodes without applied pressure, and are manufacturable at scale through established coating and impregnation steps. These attributes minimize interfacial impedance, support fast charge transport through tortuous electrodes, and enable robust high rate performance. The drawbacks are equally clear: flammability and thermal runaway risks, solvent oxidation at high voltage, parasitic reactions at reactive anodes that drive SEI formation and growth, and concentration polarization arising from cation transference numbers well below unity. Together, these limitations cap practical voltage windows, complicate fast charging, and constrain the use of metal anodes [18], [221], [224].

Solid electrolytes are electronically insulating, ion conducting solids that include ceramics such as oxides, sulfides and halides, polymer (such as PEO) based systems, and their composites. A solid-state battery typically consists of a composite cathode (active material, solid electrolyte and a conductive additive), a solid electrolyte separator, and either an alkali metal or an insertion anode. To function effectively, the composite cathode must provide co-percolation of ions, electrons, and active material. Unlike

liquids, solid-solid contact and the chemistry of the interface dominate impedance and cycling behavior [225],[226].

The field builds on fast ion conductors such as AgI and beta alumina and on Armand's late 1970s proposal of polymer electrolytes. Sodium β''-alumina enabled commercial high temperature Na-S and Na-$NiCl_2$ cells [227]. Interest accelerated in the 2010s with ceramics that reach the millisiemens range and with improved polymer and composite strategies, which reframed Li and Na solid state batteries as credible routes to safer systems with higher energy [228],[225],[229].

Across Na-ion solid electrolytes, oxide ceramics remain important. NASICON, $Na_{1+x}Zr_2Si_xP_{3-x}O_{12}$, is a benchmark Na conductor that can reach about 10^{-3} S cm^{-1} in well processed pellets, is chemically robust, and is widely used to study Na and solid electrolyte interfaces. Although thermodynamics predict some reducibility against Na-metal, stable cycling is achievable when the interphase is engineered, for example by creating phosphate rich layers or using thin metals or alloys. [230], [231]. β''-alumina also provides very high Na mobility with proven durability, historically at elevated temperature, while room temperature use is limited by interfacial contact issues and by high temperature sintering requirements during processing [227].

Sulfide electrolytes offer complementary traits. Na_3PS_4 and derivatives are soft, readily densified solids with conductivities around 10^{-4} to 10^{-3} S cm^{-1}, and halogen or dopant tuning can further enhance transport [232]. Direct Na contact, however, often forms mixed conducting interphases such as Na_2S and Na_3P, so ultrathin protective or deliberately reactive interlayers are typically required. [233], [234]. Na_3SbS_4, including tungsten doped variants, reaches some of the highest conductivities among Na sulfides, greater than 10^{-2} S cm^{-1} in some reports, yet it shares the tendency toward Na-reduction, so interphase engineering is again essential [235].

Halide and oxyhalide electrolytes are another choice. Amorphous or defect rich and complex halides, for example $NaTaCl_6$ type, $LaCl_3$ based, and Na_2ZrCl_6 family compositions, now report millisiemens class conductivities together with superior oxidative stability and deformability. These attributes are attractive for pairing with high voltage cathodes and for creating compliant interfaces. Processing windows based on cold pressing and low temperature treatments are improving, which positions halides as strong Na solid state battery candidates where cathode stability is critical. [236],[237],[238].

Polymers and polymer ceramic composites complement these families. Classic PEO:Na-salt systems are simple and mechanically compliant but show modest room temperature conductivity, about 10^{-5} to 10^{-4} S cm^{-1}, and often require elevated temperature, plasticizers, or nanoscale ceramic fillers. Single ion polymers can mitigate concentration polarization and improve fast charge behavior [239]. Hybridizing polymers with ceramic particles or thin film oxides helps to balance the trade off between conductivity and mechanics [240],[229].

The absence of volatile solvents in solid electrolytes directly mitigates flammability and thermal runaway risks, which is a central driver for both electric vehicles and stationary storage. Many solid electrolytes conduct predominantly the cation, which reduces concentration gradients during fast charging and in principle supports stable alkali metal anodes that could raise energy density [239]. Several oxide and especially halide or oxyhalide electrolytes also show wider oxidative stability, improving compatibility with high voltage cathodes that are relevant for Na based systems. Even so, solid state batteries are not automatically dendrite free or low impedance, since contact loss, interphase formation, and pressure dependent kinetics can still cause shorting or high overpotentials, which has been demonstrated even in Na and NASICON cells, so interfacial engineering remains the primary challenge [225], [241], [242]. Additionally, composite cathodes and scalable manufacturing are equally challenging. Because solids do not self-wet porous electrodes, practical cathodes must manage active material, solid electrolyte, and electronic conduction, with stable contact across large interfacial areas. Processing adds further constraints: oxides often require high temperature densification without grain boundary blocking phases, sulfides and halides are moisture sensitive, and polymer and ceramic hybrids trade conductivity for mechanics at room temperature [225],[243].

4.3. Microstructuring in batteries

Besides compositional advancements in battery technology, other areas have been gaining traction as a potential way to improve performance. One such area is the topology of the interfaces and more specifically, how the tailoring of topology can beneficially influence the performance. This is typically performed by creating micron sized or nano sized structures or features in the relevant interfaces of the device such as the anode, cathode and current collectors.

Micro and nanostructuring can improve electrochemical performance through several coupled mechanisms. At small overpotentials, the interfacial Faradaic resistance follows

$R_{ct} = \frac{RT}{nFi_0A_{eff}}$, where n is the number of active species in the reaction and F is the Faraday constant. Increasing the true contact area A_{eff} or the local exchange current i_0 through engineered microtexture lowers R_{ct}. This is the standard linearized Butler-Volmer and EIS result used to explain how roughness or porosity reduces activation energy. [244].

In solid-state batteries, particularly at interfaces where intrinsic charge transfer is fast, the dominant loss often arises from constriction resistance caused by a limited number of true contact spots. Interface-aware designs such as microtexturing, compliant or three-dimensional current collectors, and pressure-assisted contact increase the true contact area and homogenize current paths, which sharply lowers interfacial impedance and raises the critical current [245] [246],[247]. The hierarchical arrangement of micro and nanostructures can also strengthen both electronic and ionic transport by addressing interfacial phenomena across multiple length scales [14], [248], [249], [250]. These structures may further reduce the alkali-metal nucleation overpotential [145].

The shape of the micro and nanostructures is critical. Architectures that form straight or graded pores with low tortuosity raise effective ionic conductivity and diffusion, which mitigates concentration polarization at high rates [251], [252], [253].

Engineered topography can also improve stability by guiding and limiting dendrite growth. Suitable surface patterning steers dendrites laterally or at a shallow angle, which extends battery lifetime by limiting penetration into the opposite electrode [254]. Nanostructuring can tailor local electric fields, which can lower dendrite height [255]. It also reduces structural stress in the deposited metal during alkali-metal plating, helping to prevent cracks that undermine anode stability [256].

Finally, nanostructured architectures such as one-dimensional or porous particles, combined with engineered binders or designed void space, accommodate the large volume changes that occur during normal operation. This limits cracking and pulverization, preserves electrical pathways, and maintains active interfacial area over cycling [257],[258].

4.3.1. Microstructuring methods

Ultrafast, short pulse laser texturing uses femtosecond to nanosecond beams to form micro and nano grooves, cones, or laser induced periodic surface structures on aluminum and copper [259]. Merits include direct patterning without masks, tunable roughness, and compatibility with foil collectors. Key challenges are capital cost, beam

throughput on wide foils, thermal effects on thin substrates, and integration with roll to roll lines [260].

Mechanical embossing, roll forming, and electroforming can create periodic microgrooves or pillars on aluminum with good line compatibility. Tooling wear, pattern fidelity at high web speeds, and alignment are common issues for embossing and roll forming [261]. Electroforming adds bath chemistry control, thickness uniformity across width, and waste handling as scale up concerns [262].

Clean room methods such as photolithography, deep reactive ion etching, and nanoimprint lithography offer precise, repeatable geometries and extreme area enhancement. They also bring high capital and operating costs, resist and mask logistics, and yield sensitivity. Among these, imprint lithography is noted for higher throughput potential [263].

Electrochemical dealloying starts from a copper zinc alloy on copper and selectively removes zinc to produce a bicontinuous porous copper network. Advantages are conformal porosity and good metal adhesion. Rate control, structural fragility at very high porosity, and process time are typical limitations [264], [265].

Colloidal templating yields ordered three dimensional current collectors after electrodeposition and template removal. The method provides regular pore size and periodicity but can suffer from template cracking, defect propagation, and additional steps for complete template removal [266],[267].

Carbon nanotube and graphene films, either grown by chemical vapor deposition or transferred, provide ultralight, conformal current collectors or interlayers. Benefits include low mass and surface passivation of aluminum for aqueous binder use. Cost of high quality films, transfer induced defects, and contact resistance variability remain important barriers [268], [269].

Metal assisted chemical etching is a wet chemistry route to dense silicon nanowire forests or porous pillars on silicon or metal supports with modest equipment needs. Chemical handling, uniformity across large areas, and surface damage that can raise resistive losses are common concerns [270].

Despite clear electrochemical benefits, extensive micro and nanostructuring remains uncommon in large format commercial cells because manufacturing cost and throughput dominate technology selection [14].

5. Materials and Methods (Part II)

The fabrication of the microstructured copper current collectors was performed by the project partners at CENIMAT/i3N – NOVA. However, it is still relevant to this work.

5.1. Fabrication of the Microstructured Copper Current Collectors

The fabrication of microstructured copper current collectors was based on a bottom-up templating approach combining parylene-C coating, colloidal microsphere assembly, reactive ion etching, and electron-beam evaporation (**Figure 27**).

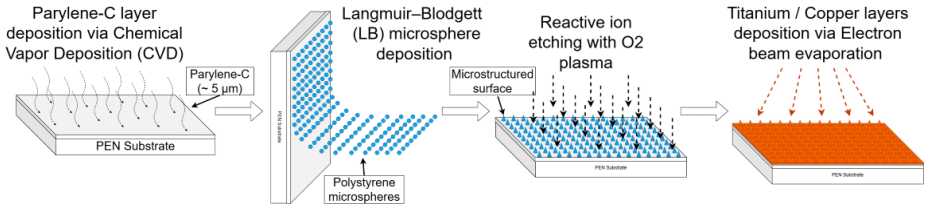


Figure 27 – Diagram of the four-step fabrication process for the microstructured copper current collectors.

5.1.1. Parylene-C Deposition

As a base layer, parylene-C was deposited onto polyethylene naphthalate (PEN) substrates, which served as flexible supports for subsequent microstructuring. Prior to deposition, the PEN substrates were cleaned with isopropanol followed by deionized water. Parylene-C deposition was performed via chemical vapor deposition (CVD) using a PDS-2010 Labcoater 2 system (Specialty Coating Systems), following procedures described in Ref. [271].

The final film thickness was controlled by the mass of the parylene-C dimer precursor and verified using a profilometer. A dimer mass of ~8 g yielded films with thicknesses ranging from 4 to 5 µm. The parylene-C precursor (chloro-para-xylylene dimer) was sourced from SCS (Specialty Coating Systems).

5.1.2. Microsphere Deposition

To create a self-assembled etching mask, polystyrene microspheres were deposited onto the parylene-coated substrates via the Langmuir–Blodgett (LB) technique, as described in Ref. [272]. A colloidal suspension was prepared by diluting a 10% microsphere solution (1.30 ± 0.03 µm diameter, Microparticles GmbH, Berlin, Germany) at a 1:1 volume ratio with a diacetone-based solution containing 1% styrene and 0.1% sulfuric acid.

Before deposition, the LB trough (Biolin Scientific KSV NIMA, Gothenburg, Sweeden) was cleaned with deionized water, followed by ethanol. The tank was then overfilled with 700 mL of deionized water to stabilize the air-liquid interface. A total of 400 µL of the colloidal solution was gently added to the interface using a microsyringe. The system's barriers were closed at 5 mm/min, facilitating self-assembly of the micro-spheres into a close-packed hexagonal monolayer. This monolayer was then transferred onto the parylene-coated substrate by vertically withdrawing the substrate from the water surface at the same speed (5 mm/min).

5.1.3. Reactive Ion Etching (RIE)

To modify the geometry of the polystyrene spheres and, thus, tailor the resulting surface microstructure, oxygen plasma etching was conducted using a Trion Phantom 3 RIE system. The etching conditions were fixed at 50 W power, 20 mTorr O_2 pressure, and 100 sccm gas flow, with the etch durations varied at 0, 6, 9, 12, and 15 min to systematically control the final feature morphology. After RIE, the remaining microspheres were removed by sequential ultrasonic cleaning in toluene and isopropanol.

5.1.4. Copper Deposition

Final metallization was performed by electron-beam evaporation in a custom-built vacuum system. Prior to deposition, the chamber was evacuated to a base pressure of (1–2) × 10^{-6} mbar. A 20 nm titanium adhesion layer was first deposited, followed by 250 nm of copper. Both metals were deposited using separate crucibles containing high-purity pellets. Film thickness was monitored in real time using a quartz crystal microbalance.

This sequence yielded microstructured Cu current collectors with tunable surface morphology, suitable for interface engineering in solid-state battery configurations.

5.2. Characterization of the Microstructured Copper Current Collectors

5.2.1. Charge Transport Measurements

The sheet resistivity of the copper current collector samples was measured using the van der Pauw method, employing a Linseis HCS 1 Hall-effect measurement system. Each sample was prepared with four collinear electrical contacts placed along the edges. A constant current of 3 mA was applied between two adjacent contacts, and the resulting voltage was measured between the remaining two contacts. This configuration allowed for the calculation of resistivity using standard van der Pauw equations. Charge carrier

density and mobility were measured using the same setup and equipment, while applying a 3 mA current for the Hall-effect measurement. Measurements were performed as a function of temperature, from 25 °C up to 70 °C, in controlled inert conditions. Each temperature was equilibrated. The chamber was initially evacuated to 10^{-2} bar and then purged continuously with high-purity nitrogen at 4–5 L/min. This minimized spurious surface reactions, stabilized the thermal conditions, and reduced electrical noise during measurements.

5.2.2. Topography and Surface Potential Measurements

Atomic Force Microscopy (AFM) was used to perform topographical and surface potential analyses of the copper current collectors using an MFP-3D Infinity AFM (Asylum Research). A minimum of eight regions were imaged per sample (2 × 2 cm), using Ti/Ir-coated silicon tips (radius 25 nm ± 10 nm). Images were captured in tapping mode over 20 × 20 μm^2 areas (256 × 256 pixels). Scan rates were adjusted individually to minimize imaging artifacts such as parachuting.

To enhance visual clarity for publication, raw 256 × 256 topography maps obtained from AFM were upscaled to 1024 × 1024 pixels using cubic interpolation (skimage.transform.resize, order = 3) with anti-aliasing enabled. This processing was carried out solely for visualization purposes; all quantitative analysis was performed on the original-resolution data. Color scaling, scale bars, and labels were applied programmatically to maintain consistency across images. The processed images were saved as high-resolution PNG files (300 dpi) using custom Python scripts written in Jupyter Notebooks.

For each AFM image (minimum of eight per sample type), various quantitative parameters were extracted to statistically characterize the surface roughness, structure density, and spatial uniformity:

- Root-Mean-Square Roughness (RMS): Automatically calculated using Igor Pro 6 (Asylum Research). RMS quantifies the average deviation in height across the scanned area and serves as a standard metric for surface roughness. A higher RMS value indicates a rougher and more topographically varied surface.
- Surface Area Increase (%): Also obtained via Igor Pro. This parameter reflects the percentage increase in total surface area compared to an ideal flat 2D surface (20 × 20 μm = 400 μm^2). It captures the increased electrochemically active area made available by the 3D structuring.
- Number of Particles: Computed via Python 3.11.9 using local maxima detection (skimage.morphology.h_maxima) with a height prominence threshold of 20 nm

to isolate individual topographical features (cone-like structures). This metric provides insight into structural density and inter-sample or intra-sample consistency. A uniform particle count across zones indicates good fabrication repeatability.

- Average Distance to Six Nearest Neighbors (D_{6NN}): Using the particle centroids identified above, the average distance to each particle's six closest neighbors was calculated. The particles tend to form hexagonal arrangements, and this metric captures the characteristic spacing between them. This is relevant to understanding how the electrolyte penetrates between structures, as well as where sodium deposition may preferentially occur.
- Standard Deviation of Nearest-Neighbor Distance (σ_{DNN}): For each particle, the distance to its single closest neighbor was computed, and the standard deviation of these distances across each image was used to quantify local ordering. Lower values of σ_{DNN} indicate high spatial uniformity (ordered structure), while higher values suggest disorder or irregular spacing. These parameters were computed individually for each AFM frame, allowing for statistical comparison across etching conditions using box plots.

All non-native analyses were conducted using custom Python scripts in Jupyter Notebooks.

Surface potential measurements were obtained via KPFM using the same scan parameters as AFM (20 × 20 µm, 256 × 256 pixels). Due to occasional tip–sample disconnection events, observable as abrupt potential drops, data points with values below 0 V vs. SHE were masked and excluded from the quantitative analysis. These masked zones typically represent areas where negative charge accumulated and where there was subsequently a breakdown. To ensure accurate surface potential statistics (mean and standard deviation), a custom Python script applied a threshold-based mask ($V_z < 0$ V) to the raw data before calculating these parameters. For visualization, masked regions were overlaid with a semi-transparent dark blue layer, and the upscaled (1024 × 1024) voltage maps were saved as high-resolution PNGs. Color bars were dynamically scaled to valid data ranges, with appropriate unit labels (V or mV).

Quantitative surface potential analysis (SKPM) followed the masking for surface potential < 0 V from each SKPM image. Using custom Python code, the average surface voltage was calculated as the arithmetic mean of all unmasked pixel values. This parameter represents the average local surface potential of the sample relative to the conductive AFM tip and provides insight into the average electronic environment at the sample

surface. These parameters were calculated for each SKPM image individually. With multiple regions analyzed per sample, statistical comparisons between etching conditions were carried out using box plots to capture variability within and across samples. Dual-pass KPFM is used to minimize crosstalk from topography effects. The first pass acquires topography in tapping mode, and the second pass rescans the conducting tip at a constant relative height above the surface.

5.2.3. Scanning Electron Microscopy and X-Ray Photoelectron Spectroscopy

An FEI QUANTA 400 FEG ESEM scanning electron microscope was used. The chemical composition analysis was performed with an EDAX Genesis X4M energy-dispersive X-ray spectrometer. Magnifications of 1000× and 25,000× were used with an energy of 15 keV in both backscattered electron detection and secondary electron detection. To perform the X-Ray Photoelectron Spectroscopy analysis, a Kratos Axis Ultra HSA system was employed. The primary goal was to detect the presence of oxidized copper (Cu^{2+}, Cu^{+}, Cu^{0}) and residue from the fabrication process.

5.2.4. Separator Preparation and Cell Assembly

The electrolyte used in this study was $Na_{2.99}Ba_{0.005}OCl$, a glassy ferroelectric solid-state conductor synthesized via aqueous solvation, following the procedure described by Braga et al. [21],[25]. The synthesis utilized NaCl (99.0%), NaOH (anhydrous, 99%), and $Ba(OH)_2$ (anhydrous, 94–98%) as precursor materials.

Following synthesis and thorough drying, the solid electrolyte powder was mechanically processed using a FRITSCH Planetary Mono Mill PULVERISETTE 6. Milling was performed in a sealed agate vessel containing five agate balls (20 mm diameter), operated at 300 rpm for 40 min to achieve uniform particle size reduction under controlled inert conditions.

The milled electrolyte was subsequently blended with the polyvinyl acetate (PVAc) binder with a weight ratio of 80:20 ($Na_{2.99}Ba_{0.005}OCl$:PVAc). This composite mixture was then re-milled using the same planetary ball-mill configuration to ensure homogeneity and cohesive powder formation.

To fabricate the separator membrane, the composite powder was dispersed in ethanol to form a viscous, homogeneous slurry, which was impregnated onto 3 × 3 cm cellulose sheets serving as mechanical supports. These coated sheets were subsequently placed in a vacuum oven at 40 °C and −500 mbar (relative to atmospheric pressure) for a minimum of 24 h, ensuring complete solvent removal and solidification of the membrane.

Zinc current collectors measuring 25 × 25 mm^2 were cut from a high-purity zinc sheet (99.98%) and used as the negative metal electrode in the assembled cells.

Cell assembly was carried out under ambient conditions, outside a glovebox. The prepared separator was manually positioned between the zinc and copper current collectors, ensuring that no direct electrical contact occurred between the electrodes. Teflon tape was applied around the perimeter to mechanically secure the assembly and maintain alignment.

Finally, the cells were vacuum-sealed using a pilot-scale packaging line. An aluminum-laminated pouch was first formed using a pouch case-forming machine. Subsequently, the top and one side of the pouch were sealed using a top-and-side heat-sealing machine. The partially sealed pouch was placed into a vacuum pre-sealing chamber, where air was evacuated. The final seal was then applied to the remaining side, completing the encapsulation and ensuring environmental isolation of the cell components.

5.3. Pouch Cell Electrochemical Characterization

To assess the electrochemical performance of the Zn/$Na_{2.99}Ba_{0.005}OCl$/structured Cu solid-state cells, potentiostatic electrochemical impedance spectroscopy (PEIS) and cyclic voltammetry (CV) measurements were performed using a Biologic VMP-300 potentiostat. The cells were tested at both room temperature and 40 °C. The cells were heated up to 40 °C inside a thermostat-controlled sand bath, where they were maintained for at least 2 h before being tested.

5.3.1. Electrochemical Impedance Spectroscopy (EIS)

The principle of EIS is straightforward: applying a voltage and measuring the resulting current using a potentiostat connected to the electrochemical system's terminals. However, using an AC voltage necessitates considering the response of reactive elements like capacitive or inductive elements. This leads to adopting the more comprehensive concept of impedance (Z) instead of pure resistance. It takes advantage of the different responses of capacitive, inductive, and resistive elements to various frequencies. Importantly, it's non-destructive because it uses small amplitude signals, from 1 to 10 mV, across a wide frequency range, generally form 1mHz to 1Mhz. Using small amplitude signals is crucial not only to maintain the system's integrity but also to ensure a pseudo-linear electrical response. Complex electrochemical systems do not have a linear response to input signals; for example, doubling the input voltage will not necessarily double the current, like it would in a resistor. The response of a non-linear

system cannot be simplified as the weighted sum of the responses of it's constituents, making analysis challenging. Furthermore, non-linear systems tend to exhibit complex harmonic signals resulting from higher degree excitations. These harmonics will interfere with the measurement, which ideally should be the response at a single frequency. However, if the input signal is small enough, the response of the system can be approximated as linear which mitigates both non-linearity problems. One of the most common methods for analyzing EIS data is fitting it to an equivalent electrical circuit model composed of elements with known impedance. This model should represent the capacitive, inductive, and resistive properties of the physical system. The usefulness of these models is often limited by the physical meaning they have. It is then crucial for each component of the circuit to have a physical basis in the electrochemical system. For instance, the accumulation of charges can be depicted by including a capacitor and resistor [273],[274].

PEIS measurements were conducted at open-circuit voltage by applying a 10 mV AC perturbation across a broad frequency range from 7 MHz down to 100 mHz. The resulting spectra were analyzed by equivalent circuit fitting, using EC-Lab V11.61.

5.3.2. Cyclic Voltammetry (CV)

Cyclic voltammetry applies a controlled voltage sweep to an assembled cell at a defined scan rate, while recording the resulting current. The onset and shape of the current response indicate where the electrodes begin their intended redox reactions, where parasitic processes at solid electrolyte interfaces arise, and whether alkali metal plating and stripping are reversible. These traces are then used to estimate a practical stability window for the solid electrolyte, assess electrode-electrolyte compatibility, and set cut-off voltages or justify protective layers for later cycling tests [225], [275]. The CV cycles were performed at a scan rate of 5 $mV.s^{-1}$, and the experiment was repeated five times to assess cycle-to-cycle reproducibility. The voltage window for each cycle was set between −0.3 V (discharge limit) and +2.1 V (charge limit).

This testing protocol enabled identification of any irreversible processes or degradation over the initial cycles, as well as insight into how surface structuring of the current collector may influence redox kinetics and interfacial stability.

5.3.3. Charge/Discharge Cycles and GITT

Galvanostatic charge and discharge cycling evaluates solid-state cell performance under a controlled current by tracking delivered capacity, Coulombic efficiency, and voltage hysteresis over repeated cycles. Trends in these metrics diagnose rate capability and

reveal progressive resistance growth caused by interfacial reactions or contact loss. The galvanostatic intermittent titration technique (GITT) complements these tests by applying small current pulses separated by relaxation periods, from which the quasi-equilibrium voltage profile can be obtained.

Charge/discharge cycles were conducted with an external material resistance (either 26.4 kΩ or 21.7 kΩ) connected in parallel to each cell. The charging voltage was set to 2.1V. The GITT measurements were carried out using a Neware CT-4008Tn-5V-20mA battery tester (Montclair, CA, USA). Each test cycle consisted of charging the cell at 1 µA for 100 s, followed by a 1 h rest period.

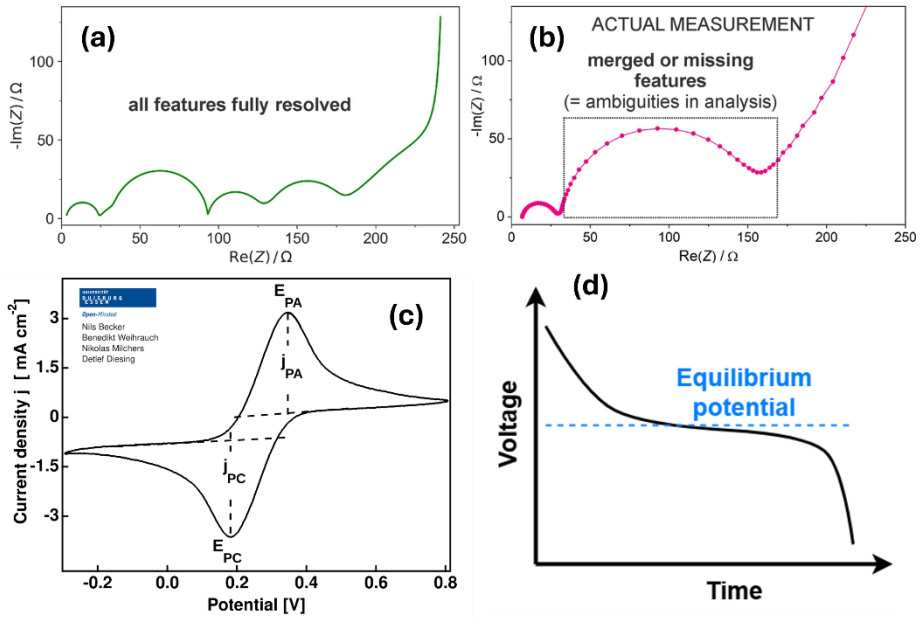


Figure 28 – Examples of electrochemical characterization methods. **(a,b)** Potentiostatic electrochemical impedance spectroscopy, PEIS: **(a)** a Nyquist response with fully resolved features, **(b)** a typical measurement where features merge, which introduces ambiguity in analysis. Adapted from reference [273]. Licensed under CC BY 4.0. **(c)** Cyclic voltammetry. PA indicates the anodic peak (charge), PC indicates the cathodic peak (discharge). Source: Wikimedia Commons – Cyclic Voltammetry. Licensed under CC BY-SA 4.0. (d) Typical discharge profile for a battery with a plateau at the equilibrium potential.

6. Results and discussion (Part II)

This section is organized into two subsections: The first presents the results obtained from the characterization of the microstructured copper current collectors. The second focuses on the electrochemical performance of pouch cells incorporating these microstructured current collectors. Given the extensive range of characterizations conducted, the data have been consolidated into a series of graphs that summarize key parameters relevant to the analysis.

6.1. Characterization of the Microstructured Current Collectors

The characterization of the copper current collectors is an important step in understanding their effect on battery behavior. Topographic features change the nature of electrochemical interfaces between the current collector and the electrolyte. Micro–nanoscale structures were identified and quantified with the use of Atomic Force Microscopy, while Scanning Electron Microscopy and Energy Dispersive X-Ray Spectroscopy were used to assess the presence of surface defects resulting from the fabrication process. Kelvin Probe Force Microscopy complements the topographic analysis by measuring surface potential, which again can affect interfacial phenomena. X-Ray Photoelectron Spectroscopy substantiates the KPFM analysis with compositional surface analysis of the samples. Finally, the sheet resistance of the samples was analyzed using the van der Pauw method [276], while charge carrier concentration and mobility were determined by Hall-effect measurements [277].

6.1.1. Topographical Characterization

The topographical AFM characterization of the copper samples was performed in multiple randomly chosen spots for each sample. **Figure 29** shows that the patterning process creates a honeycomb-like pattern of cone-shaped “particles”. The well-structured distribution of the particles, observed for current collectors with 6 (**Figure 29b**) and 9 min (**Figure 29c**) of etching time, is gradually lost at higher etching times (**Figure 29d,e**). This trend is expected, as etching durations beyond 9-12 min can lead to the complete removal of the PS spheres, which serve as the mask for the parylene-C etching. Once the mask is gone, the subsequent etching becomes more irregular and uncontrolled.

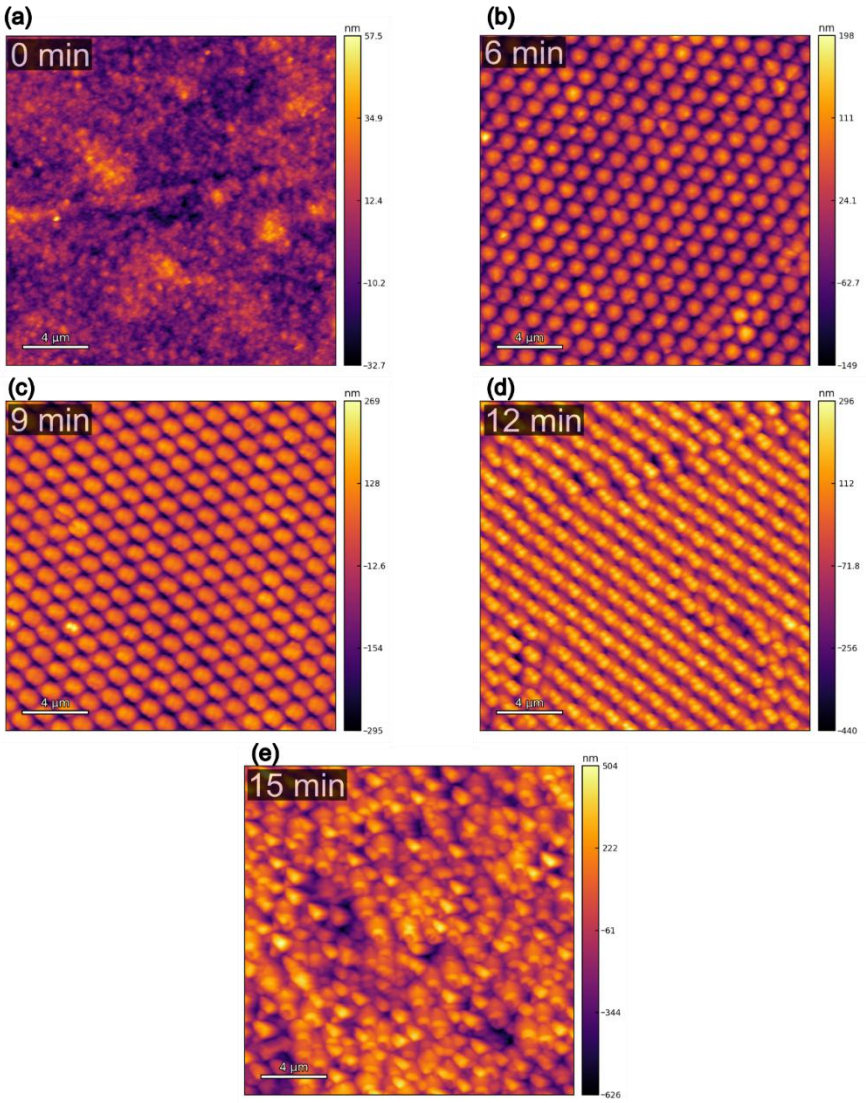


Figure 29 – Examples of topography images, obtained via AFM, of the copper current collectors with different etching times: **(a)** 0 min; **(b)** 6 min; **(c)** 9 min; **(d)** 12 min; **(e)** 15 min. The images shown were upscaled to 1024 × 1024 pixels, from the original 256 × 256, for enhanced visual clarity

To quantitatively evaluate the impact of plasma etching time on the surface morphology of the microstructured copper current collectors, five key topographical parameters were extracted from the AFM images: (1) RMS roughness, (2) relative surface area increase, (3) number of particles, (4) average six-nearest-neighbors distance (D_{6NN}), and (5) standard deviation of nearest-neighbor distances (σ_{DNN}). These parameters were derived from multiple AFM images for each etching condition, and the resulting distributions were analyzed using box plots to capture both inter-sample trends (e.g., how the mean value evolves with etching time) and intra-sample variability (e.g., interquartile range and the presence of outliers) (**Figure 30**).

RMS Roughness: A systematic increase in RMS roughness was observed with longer etching times, confirming that extended O_2 plasma exposure enhances the surface relief.

This behavior is consistent with the expected deepening of surface features as more parylene-C-masked material is selectively removed. Notably, the interquartile range (IQR) narrows at higher etching durations, suggesting that the roughness not only grows but also becomes more spatially homogeneous across the surface (**Figure 30a**).

Surface Area Increase: The evolution of surface area follows a similar trend, increasing steadily with etching time in tandem with RMS roughness, up to an average in-crease of 28.8 ± 1.17% for the 15 min sample. This is expected, as the development of deeper or taller topographical features increases the actual surface area relative to the projected 2D footprint. The reduced IQR at higher etching times also points toward a more uniform topographic landscape, which may enhance the consistency of the elec-trochemical interface (**Figure 30b**).

Number of Particles: Across most etching times, the average number of detectable topographic features remains relatively constant, indicating that the lateral pattern fidelity established by Langmuir–Blodgett deposition of polystyrene (PS) spheres is preserved. This suggests that O_2 plasma etching modifies vertical dimensions without substantially affecting the in-plane distribution of features, at least up to 12 min. At 15 min, however, the appearance of a small number of outliers suggests the onset of local defects or dislocations in the particle lattice, pointing to a possible etching threshold beyond which structural integrity begins to degrade (**Figure 30c**).

Average Six-Nearest-Neighbor Distance (D_{6NN}): The average D_{6NN} remains nearly constant (~1.44–1.47 μm) across all etching durations, indicating that the in-plane periodicity governed by the initial PS sphere array is maintained throughout the etching process. This implies that the etching procedure does not significantly perturb the global spatial arrangement of the features. However, the presence of more outliers at extended etching times may reflect localized pattern distortions resulting from the long etching process (**Figure 30d**).

Standard Deviation of Nearest-Neighbor Distance (σ_{DNN}): In contrast to D_{6NN}, σ_{DNN} exhibits a clear increasing trend with etching time. This indicates growing variability in local feature spacing, which suggests a gradual degradation of short-range order in the feature array. While the global lattice symmetry remains intact, local periodicity becomes less regular, potentially influencing surface potential uniformity and leading to uneven ion nucleation during subsequent sodium plating. This degradation in spatial order complements the observed changes in particle count and D_{6NN}, emphasizing that although the layout is nominally preserved, longer etching introduces disorder at the micro–nanoscale (**Figure 30e**). It is noteworthy highlight that longer etching corresponds

to lower information and, therefore, increased entropy. However, **Figure 30e** shows that the sample with lowest average σ_{DNN} is the one etched for 9 min, while the sample showing the lowest average σ_{DNN} values is the one etched for 12 min, which will later correspond to the current collectors/electrodes of the best-performing cells.

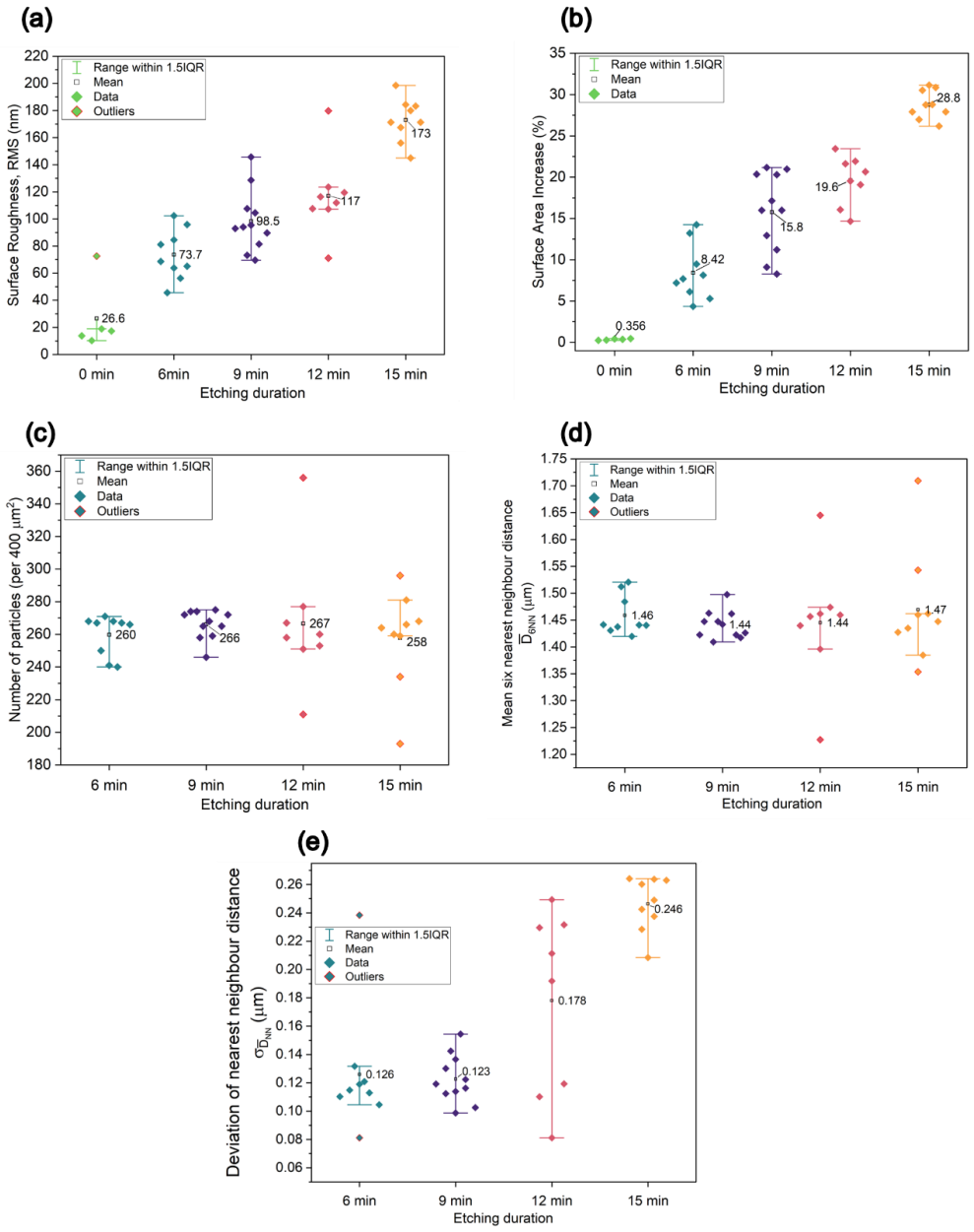


Figure 30 – Extracted parameters from topography images: **(a)** root-mean-square (RMS) of topography; **(b)** surface area increase from flat topography (400 μm^2); **(c)** number of particles; **(d)** average distance between 6 nearest neighbors; **(e)** standard deviation of average nearest-neighbor distance.

Microscale SEM images (**Figure A6**) highlight some features that are less perceptible by AFM. Defects such as unmasked areas and particle grain boundaries, although common in all samples, as highlighted in **Figure 31**, comprise a small part of the total

area. Atomic number contrast images (**Figure A6**, right-hand column) and EDS (**Figure A7**) show that, in most cases, copper was still deposited in those areas.

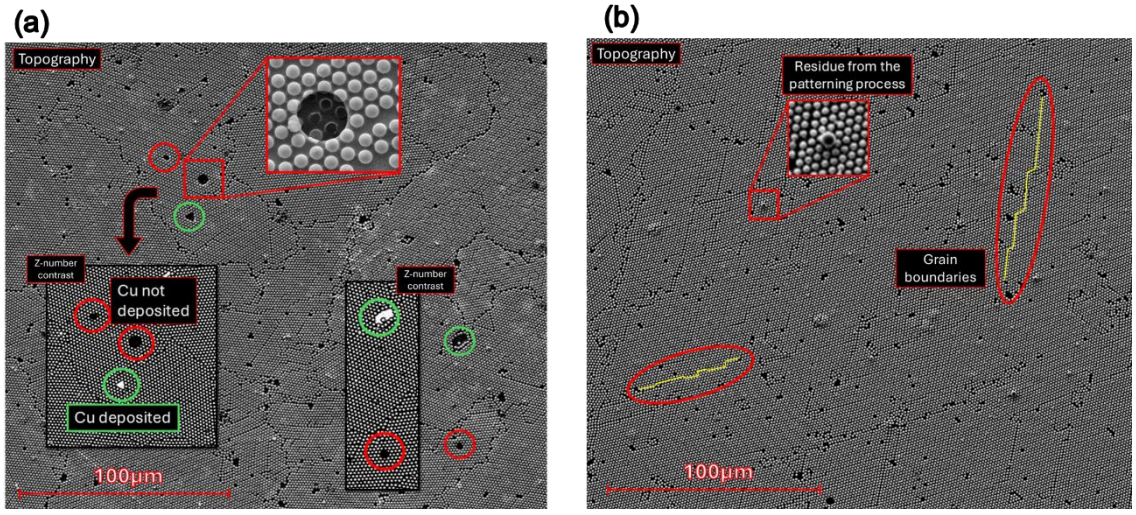


Figure 31 – SEM images of the microstructured copper surfaces. Topographic features such as defects, residue from the patterning process, and grain boundaries are highlighted in red, green, and yellow, respectively. Samples' etching: **(a)** 6 min; **(b)** 9 min.

Additionally, SEM images of the sample etched for 15 min (**Figure 32**) show a less homogeneous surface because of the long etching process. This effect contributes to the increased surface area by creating deeper topographic features besides the cone-like structures highlighted in AFM. Some "bridges" are observed connecting the cones in **Figure A6i**. Where these bridges are more frequent, a brighter phase is found, likely meaning that charge carriers are exchanged and confined in denser, brighter areas (**Figure 32**-right). Finally, the obtained wide XPS spectra (**Figure A8**) shows small Cl 2s peaks (from the parylene-C substrate) and no Ti 2p peaks, indicating that copper was deposited across the entire surface without significant defects or residue.

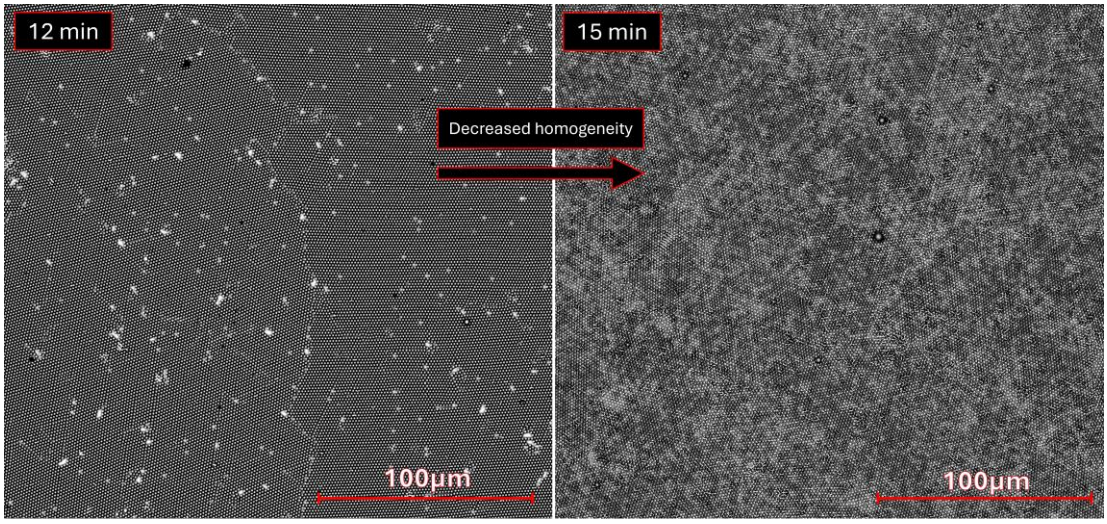


Figure 32 – Atomic number contrast SEM images, obtained with backscattered electrons, for the microstructured copper samples etched for 12 min (left) and 15 min (right), highlighting the increased inhomogeneity resulting from the prolonged etching process with particles forming bridges, which result in the formation of two phases with not too dissimilar density, likely $Cu^0/Cu^+/Cu^{2+}$ based.

6.1.2. KPFM Characterization

The surface potential ϕ of a sample is characterized using Kelvin Probe Force Microscopy (KPFM). The electrochemical potential of the probe aligns with the electrochemical potential of the material $\bar{\mu} = \mu + ze\phi$, where μ is the chemical potential of the material or species, z is the valency of the mobile ion, and e is the elementary charge. It depends on the sum of $e\phi$ and the chemical potential μ of the material or species, if $z = 1$. The work function of a material is WF = $-\bar{\mu}$, accounting for both the chemical potential and the surface potential; in other words, it accounts for bulk and surface phenomena. If the material is electrically insulated and shows no ϕ, then WF = $-\mu$. The work function of the current collector is a relevant parameter, as it influences the performance of the cell, including the solid-state electrolyte's ionic conductivity, charge transfer, and deposition behavior [278]. It is also an indicator of the level of oxidation on the copper surface.

Figure 34a show the average surface potential for the different copper samples, all measured relative to the tungsten WF ≈ 4.44 eV ($\mu = -4.44\,eV$) of the calibrated tip, corresponding to 0 V vs. SHE (standard hydrogen electrode). The 0 min sample exhibits a surface potential in the range of +0.45 V vs. SHE, which aligns with the expected values for clean, metallic copper surfaces (typically +0.34 V $Cu^{2+}/Cu(s)$ vs. SHE and +0.52 V $Cu^{+}/Cu(s)$ vs. SHE) [279], suggesting minimal surface oxidation. In contrast, the microstructured samples show systematically lower average surface potentials, indicating a decrease in work function relative to the flat vacuum reference. Two

competing effects may explain this trend: First, the cone-like surface topography introduced by etching can lead to local charge redistribution. Electrostatic field concentration at the sharper valleys may promote electron accumulation, thereby decreasing the work function, while increasing the local surface potential. The planar top regions between these valleys may exhibit lower electron density, effectively increasing the local work function. This effect is directly observed in the raw KPFM images, where the tips of the cones show higher surface potential vs. SHE than the surrounding valleys. In structured samples, this would lead to lower average surface potential compared to the unstructured sample. This is also noticeable in **Figure 34b**, with structured samples having higher deviation in surface potential. A second important effect is oxidation, which becomes more significant for microstructured surfaces due to their increased surface area. The formation of CuO (with Cu^{2+}) would decrease the work function of the material, thereby lowering the measured surface potential vs. SHE. This oxidation effect likely contributes to the reduced potential observed even at the cone tips, which do not reach the same values as the unstructured, presumably cleaner, flat sample. This idea is substantiated by the XPS Cu 2p ROI spectra (**Figure A9**, left column), which show intense CuO peaks for the 0 and 15 min samples, as shown in **Figure 35**. Still, in all samples, the Cu LMM Auger ROI (**Figure A9**, right column) show a strong Cu_2O peak, indicating general surface oxidation. The 6 min samples show a higher relative amount of Cu^0, and the 15 min samples show almost similar relative distribution of $Cu^{2+}/Cu^{+}/Cu^0$. Native oxidation layers are typically in the order of a few nanometers, which is around the depth of measurement of XPS, while KPFM can be influenced by charge accumulation from the unoxidized underlayer. Thus, XPS only measures the native oxidation layer, while KPFM is influenced by the bulk. This effect is more pronounced on the flat 0 min sample, given that topological effects are reduced. The latter is also corroborated by the surface chemical potential of the 0 min sample being the highest (0.45 V, SHE), corresponding to more Cu^{+}/Cu^0 (0.52 V, SHE) than Cu^{2+}/Cu^0 (0.34 V, SHE), more pronounced than in the other samples showing lowest chemical potentials vs. SHE.

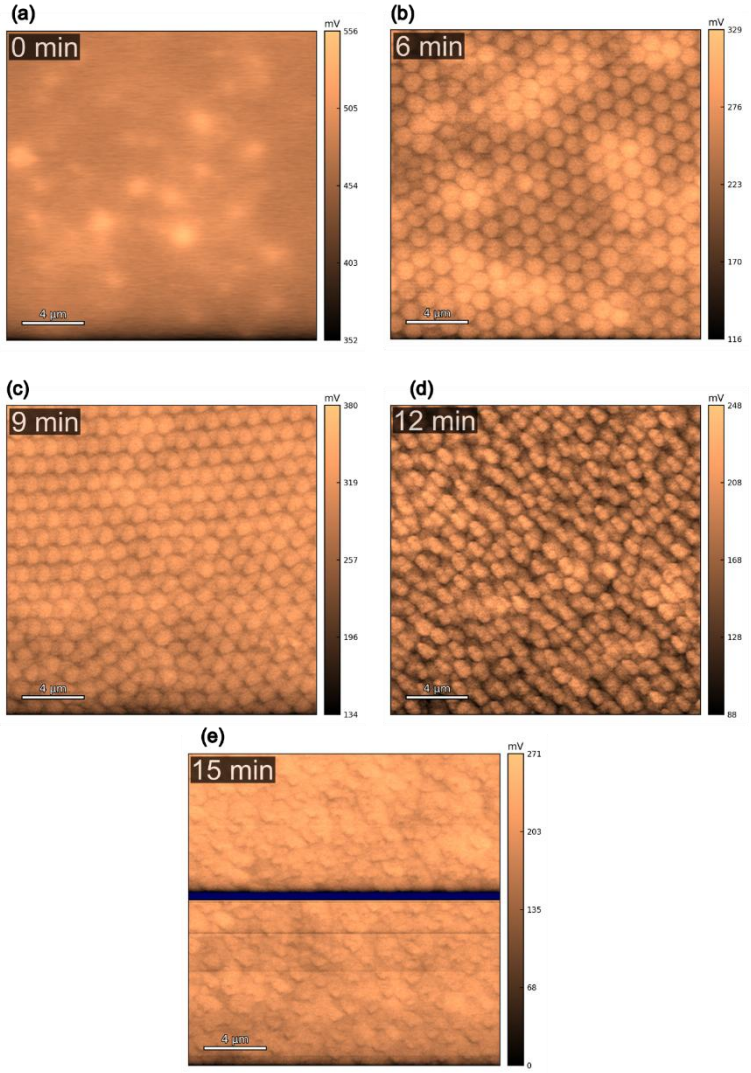


Figure 33 – Maps of surface potentials ϕ_{Cu}, where $\bar{\mu}_{Cu} - \bar{\mu}_{tip} = 0 = \mu_{Cu} - \mu_{tip} = e(\phi_{tip} - \phi_{Cu})$, where the tip is calibrated to be equal to the standard hydrogen electrode $\mu_{tip} = 0$ eV $vs\ SHE = -4.44$ eV vs electrons at rest in vaccum, obtained via KPFM, of the copper current collectors with different etching times: **(a)** 0 min; **(b)** 6 min; **(c)** 9 min; **(d)** 12 min; **(e)** 15 min. Areas masked in dark blue represent excluded points where the surface potential dropped below 0 V due to charge accumulation. These areas were not considered for obtaining the average surface potential, as the focus is herein given to the background.

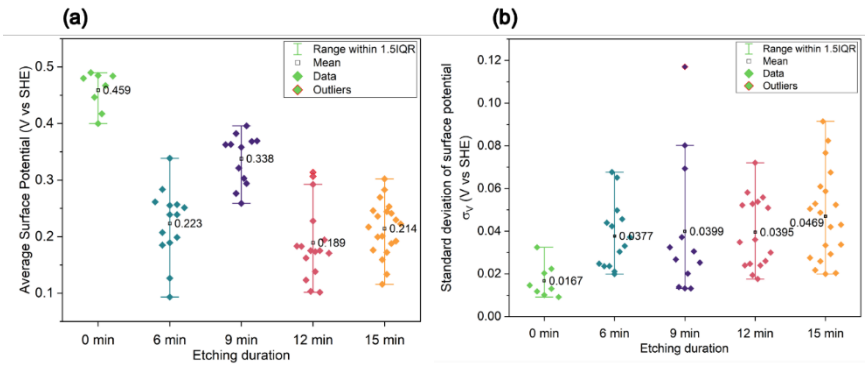


Figure 34 – (a) Average surface potential of each KPFM image for different etching durations; **(b)** standard deviation of surface potential of each KPFM image for different etching durations.

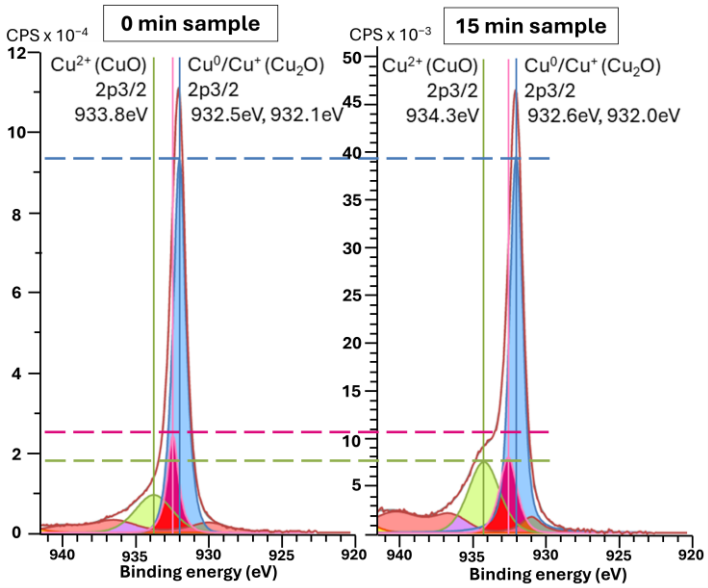


Figure 35 – Comparison of XPS spectra, near Cu 2p3/2 peaks, obtained for the microstructured copper samples etched for 0 **(left)** and 15 **(right)** minutes. Cu^{+} peaks colored in blue, Cu^{0} peaks colored in rose, Cu^{2+} peaks colored in green and loss features colored in red.

6.1.3. Charge Transport Measurements

Given that the current collectors were fabricated by copper deposition, it is important to assess whether this process, along with microstructuring, affects the resistance of the samples and, consequently, the internal resistance of the battery. To investigate this, we performed four-point probe sheet resistance and Hall-effect measurements, as shown in **Figure 36**. The results in **Figure 36a,b** display the expected trend of increasing resistivity with temperature, which is typical of metallic conductors. The values of the correspondent resistivity at 40 °C fall within the range reported in the literature [280], [281], generally between 2 and 4.5 μΩ.cm. These findings suggest that using copper as a thin film does not significantly increase the resistivity of the current collectors, especially when compared to bulk copper, which has a resistivity of approximately 1.68 μΩ.cm [279]. At 25 °C, the 0 min and 6 min samples showed similar resistivity values of approximately 1.96 μΩ.cm, increasing slightly to approximately 2.06 μΩ.cm at 40 °C. The 12 and 15 min samples also exhibited similar behavior, with resistivity values of 2.57 μΩ cm and 2.69 μΩ cm at 25 °C, and 2.68 μΩ.cm and 2.80 μΩ.cm at 40 °C, respectively. The 9 min sample stood out with the highest resistivity, measuring 4.44 μΩ.cm at 25 °C and 4.60 μΩ.cm at 40 °C. Overall, these results indicate that microstructuring shows no optimal collector based on the resistivity of the copper layers. Conversely, it shows that the 9 min sample is the worst in terms of resistivity.

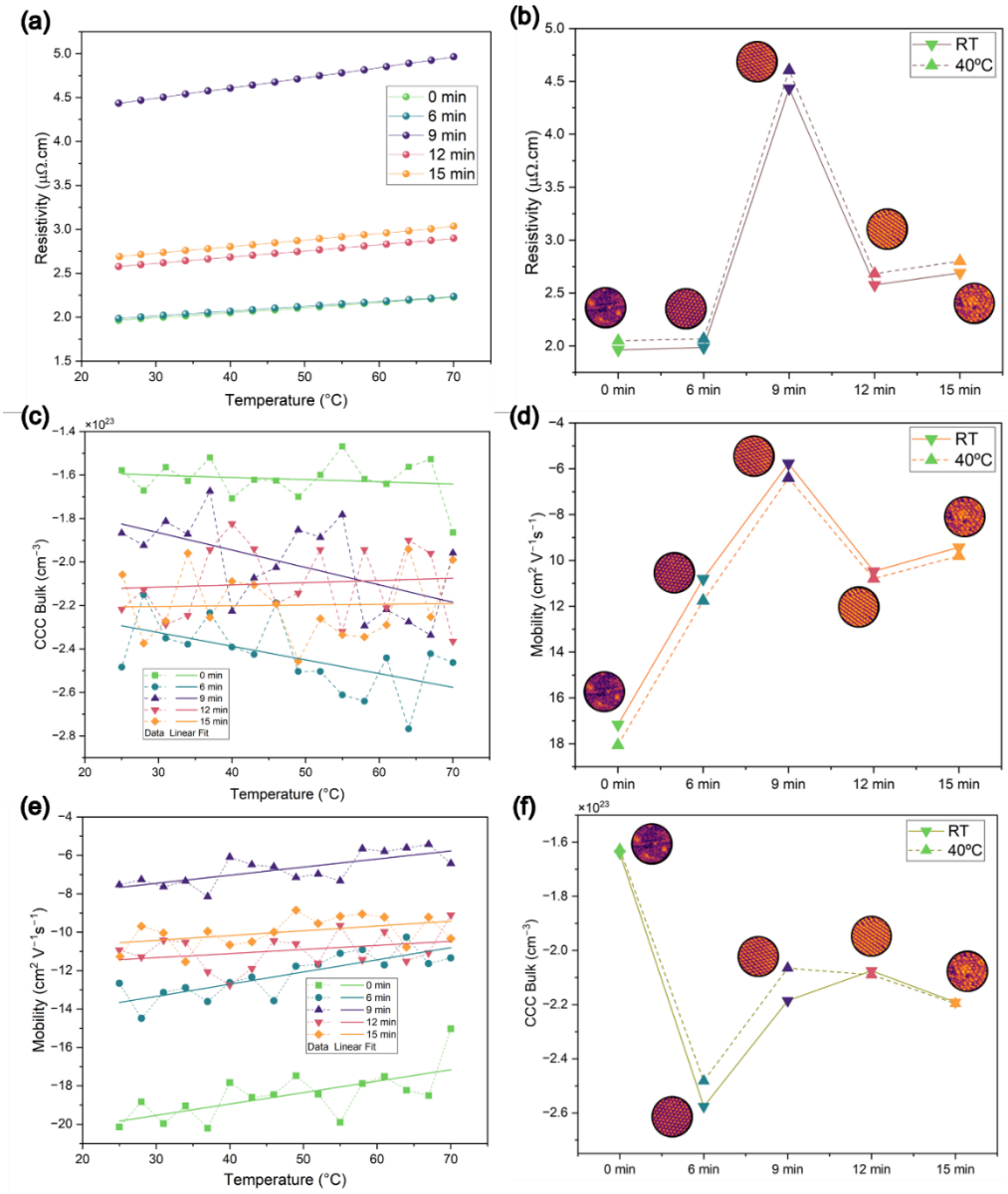


Figure 36 – Electrical properties of copper current collectors for each etching duration (0, 6, 9, 12, and 15 min): **(a)** temperature-dependent resistivity measurements for each etching duration; **(b)** comparison between the resistivity at room temperature (RT) and 40 °C for each etching duration; **(c)** temperature-dependent charge carrier mobility for each etching duration; **(d)** comparison between the mobility at RT and 40 °C for each etching duration; **(e)** temperature dependence of calculated bulk charge carrier concentration (CCCbulk) across etching durations; **(f)** CCCbulk at RT and 40 °C for each etching duration. Solid and dashed lines in (b), (d), and (f) represent data at RT and 40 °C, respectively. Note: negative values of the mobility and CCCbulk correspond to negative charges, which are electrons in this case.

Hall-effect measurements show electron mobility between 6 and 18 $cm^2.V^{-1}.s^{-1}$, which is lower than typical values for copper (~43 $cm^2.V^{-1}.s^{-1}$) [282], with the highest value being for the non-structured sample. This indicates that the microstructuring process influenced electron mobility. Surface roughness exceeding the 250 nm film thickness introduces local thickness variations, creating an inhomogeneous current path. Nevertheless, even the unstructured reference sample displays a mobility below the bulk value, in agreement with earlier reports that thermally evaporated copper films develop

a high density of grain boundaries, which enhance carrier scattering and, thus, lower mobility [283]. The grain boundaries for the microstructured samples are well observed herein in the SEM images (**Figure 31**). The charge carrier concentration (CCCBulk) is approximately 1023 cm^{-3}, close to typical values for copper [284]. Overall, the microstructuring has had some impact on the electrical properties of the samples, with structured samples having higher charge carrier concentrations and lower electron mobility, as compared to the non-structured sample.

6.2. Pouch Cell Electrochemical Characterization

A total of 15 pouch cells were manually assembled, consisting of three cells for each Cu current collector type, in the configuration Zn/$Na_{2.99}Ba_{0.005}OCl$/Cu (Sections 5.2 and 5.3). The cells were identified by the copper current collector etching duration (0, 6, 9, 12, and 15 min) and by batch number (three batches in total). After assembly, all pouch cells showed an open-circuit voltage of approximately 1.1 V. Electrochemical characterization consisted of a sequence of pre-CV PEIS, CV, and post-CV PEIS (Sections 5.2 and 5.3). The cell corresponding to the 15 min etching duration, batch 2, degraded after the first PEIS, and its data were excluded from the analysis. All cells were tested first at RT and then at 40 °C. RT was not controlled, but it was generally around 25 °C for the days in question. Charge/discharge cycles were performed at RT after the batteries has undergone a long period of rest (>30 days) (Sections 5.2 and 5.3). The Galvanostatic Intermittent Titration Technique (GITT) was performed at RT after more than 30 days of the charge/discharge cycles.

6.2.1. Potentiostatic Electrochemical Impedance Spectroscopy

The results obtained from PEIS were analyzed using equivalent circuit fitting (EC fit). Two distinct equivalent circuits, as shown in **Figure 37**, were used in the analysis. The circuit EC2 was preferentially used. Circuit EC1 was used if a third, low-frequency semicircle was present. This analysis allowed for the extraction of key parameters, including the resistance in series (R_{series}), high-frequency capacitance (C_{HF}), and resistance (R_{HF}) corresponding to the left-most semicircle, as well as the mid-frequency capacitance (C_{MF}) and resistance (R_{MF}) corresponding to the intermediate semicircle. Pseudo-capacitances ($C_{HF;MF;LF}$) were calculated from the respective CPE and R elements via:

$$C = Q^{(1/\alpha)} \cdot R^{(1-\alpha)/\alpha}$$

where Q is the resulting capacitance of the CPE, R is the associated resistance and α is the non-ideality factor.

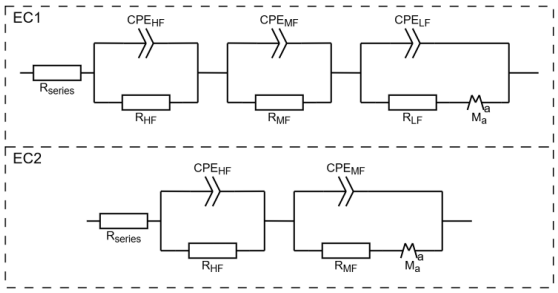


Figure 37 – Two equivalent circuits used for modeling the PEIS. CPE: Constant Phase Element, Ma: modified restricted diffusion element. Suffixes: HF (high frequency), MF (mid-frequency), LF (low frequency).

The extracted parameters for each cell are displayed in **Figures A2–A4**. From these parameters, the mean values were calculated for comparison across etching durations.

The resistance in series R_{series} (**Figure 38a**) is influenced by multiple factors, including the electrolyte, electrode materials, and contact resistance. Given the microstructured thin-film nature of the current collectors used in this study, R_{series} is a particularly relevant parameter for comparison. The samples etched for 0 min, which feature a flat surface, exhibit R_{series} values comparable to those of the microstructured samples, indicating that the structuring process has minimal impact on this parameter. The pouch cells etched for 9 min display a slightly higher average R_{series}, which aligns with the elevated resistivity observed using the vdP method (**Figure 36b**). The values shown in **Figure 38b** are consistent with the results previous studies employing bulk copper sheet electrodes [25], indicating that the use of thin films does not significantly alter R_{series}.

The high-frequency (HF) semicircle is primarily associated with electrolyte bulk phenomena, although grain boundary effects may also influence this region [285], [286]. C_{HF}, the ideal capacitor of thickness d and surface area A, in principle is not affected by the electrodes' surface except by the bias created by the difference in chemical potential, which is responsible for the driving force: the electric field that pulls the cations towards the interfaces while cycling. These bulk cations Na^+ face a resistance, where ρ is the

$$\mathrm{R_{HF}} = \rho \frac{d}{A}$$

ionic resistivity $1/\rho = \sigma$, and σ is the ionic conductivity of the electrolyte.

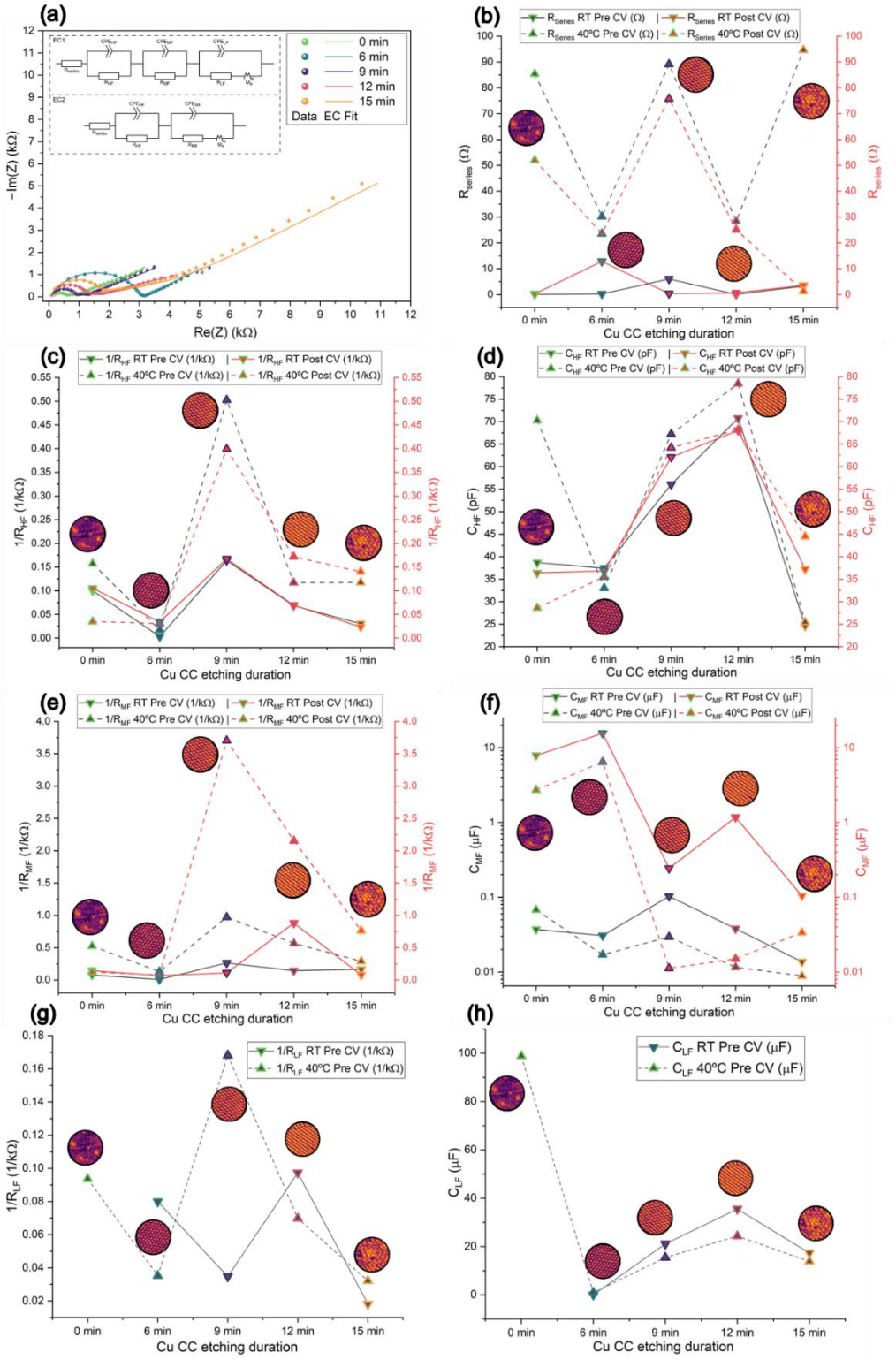


Figure 38 – (a) Plots of selected PEIS cycles for different Zn/$Na_{2.99}Ba_{0.005}OCl$/microstructured Cu cells; **(b–f)** average values of different PEIS parameters for cells with each current collector type at RT and 40 °C, pre- and post-CV; **(b)** resistance in series R_{series}; **(c)** $1/R_{HF}$; **(d)** C_{HF}; **(e)** $1/R_{MF}$; **(f)** C_{MF}; **(g)** $1/R_{LF}$; **(h)** C_{LF}. The low-frequency semicircle was not present on 0 min cells at RT. Most cells did not show a post-CV LF semicircle; therefore, this data was excluded from the comparison.

The corresponding capacitance C_{HF} and resistance R_{HF} values from the HF RC equivalent circuits are presented in **Figure 38c,d**. The capacitances at HF range from 0.01 to 0.1 nF, which are typical for bulk processes in solid-state devices; $1/R_{HF}$ is in the order of 10^{-4} Ω^{-1} and exhibits an optimal value 0.5×10^{-3} Ω^{-1}. Notably, the samples etched for 9 and 12 min show higher capacitance and $1/R_{HF}$.

The mid-frequency and low-frequency semicircles are associated with interfacial processes, including double-layer capacitance and charge-transfer resistance [285], [286]. The corresponding capacitance C_{MF} and resistance $1/R_{MF}$ from the MF RC equivalent circuits are shown in **Figure 38e,f**. The capacitances fall within the range of 10 nF to 10 µF, consistent with typical double-layer capacitor behavior; $1/R_{MF}$ is in the order of 10^{-4} to 4.6×10^{-3} Ω^{-1}, and again, $1/R_{MF}$ shows a maximum for 9 min etching. The C_{MF} varies significantly between pre- and post-CV, unlike the HF parameters, as expected, and does not show any clear trend. This tendency is even more pronounced for the LF parameters, where most cells did not show a LF semicircle after the CV, at both RT and 40 °C. C_{LF} (**Figure 38h**) is 2 to 3 orders of magnitude higher than C_{MF}. Similarly, C_{HF} is 2 to 3 orders of magnitude higher than C_{MF}. All $\frac{1}{R} \propto \frac{1}{\rho} = \sigma$, where σ is the ionic conductivity of Na^+ in the electrolyte: $1/R_{HF}$, $1/R_{MF}$, and $1/R_{LF}$ are similar, with an optimal value for the samples etched for 9 min. Curiously the R_{series} is maximum for the samples etched for 9 min, similar to the resistivity previously shown for the current collectors (**Figure 36a,b**). This indicates that this etching is beneficial for the mobility of the ions in the bulk electrolyte (**Figure 38c,e,g**) within the pouch cell and detrimental to the mobility of electrons in the Cu current collectors (**Figure 36c,d** and **Figure 38b**).

Overall, the use of thin films significantly affects the battery's performance. **Figure A1** shows the PEIS for a $Zn/Na_{2.99}Ba_{0.005}OCl/Cu$ cell that used a 0.125 mm copper sheet as the positive current collector. This cell exhibited impedances in the same order of magnitude as those using copper thin films.

6.2.2. Cyclic Voltammetry

From the CV, the peak charging and discharging currents for each cycle at RT and 40°C were extracted and are displayed in **Figure 39**. This parameter reflects expected battery performance, with higher absolute values corresponding to better cell performance.

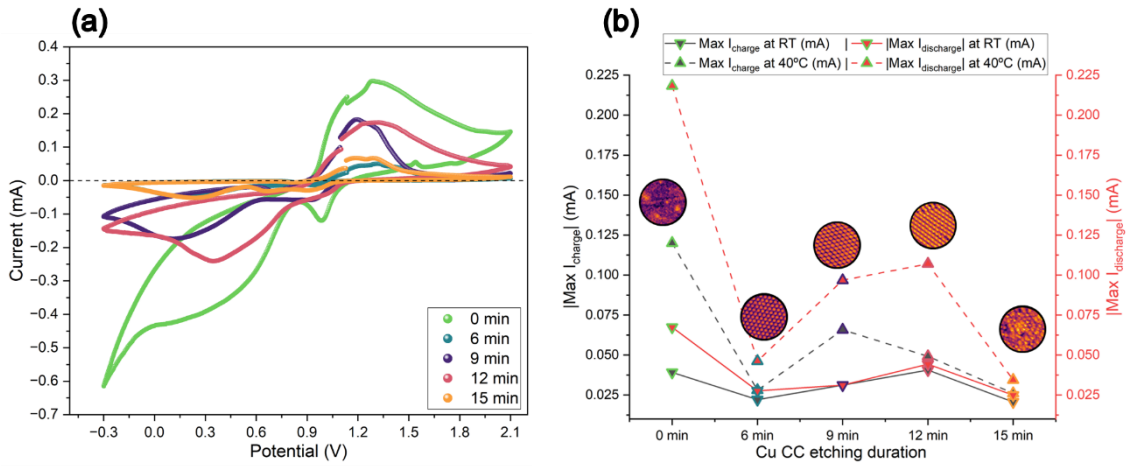


Figure 39 – (a) Selected CV curves for Zn/$Na_{2.99}Ba_{0.005}OCl$/microstructured Cu cells with each current collector type; **(b)** comparison across etching duration of maximum discharge current (red) and maximum charging current (black) at RT and 40 °C. Note: effective surface area = 6.25 cm^2.

The CV data shows peak charging currents of 0.35 mA and discharging currents of 0.85 mA (**Figure A5**). Similar to the trend observed for the PEIS, samples etched for 9 and 12 min show slightly higher peak currents, particularly at 40 °C.

6.2.3. Charge/Discharge Cycles and GITT Stability Tests

The effect shown previously for the CV maximum charge and discharge currents is also observed when the Zn/$Na_{2.99}Ba_{0.005}OCl$/microstructured Cu cells for each collector type are set to charge for three minutes (180 s) and discharge for 24 h (86,400 s) with a 26.4 kΩ or 21.7 kΩ external material resistor (**Figure 40**). The effective surface area of the cells is 6.25 cm^2. The maximum discharge current was 0.038 mA, corresponding to a maximum discharge capacity of 0.56 mAh for the 24 h obtained with the samples etched for 12 min. It is noteworthy that these cells have no capacity, as there are only current collectors. The mobile ions that plate on the copper collector upon discharge have their origin in the electrolyte. The electrolyte is the only source of capacity, and its maximum capacity is ≈660 $mAh.g^{-1}$. However, as the ions plate on both interfaces while cycling, it is not expected that the maximum capacity of the electrolyte will be reached. The cycling voltage plateau and capacities for the three batches of cells with different etch times are in agreement with the C_{LF}, Max $I_{discharge}$, and CCCbulk (for the balance of holes): two features of the cells and one of the individual copper current collectors related to the available number of charge carriers (herein Cu^{2+}/Cu^{+}). The two 15 min cells show self-charge, with arrows pointing up. This is a feature commonly observed with ferroionics of the family $A_{3-2x}M_xOCl$ (A = Li, Na, K; and M = Mg, Ca, Sr, Ba) [287],[288].

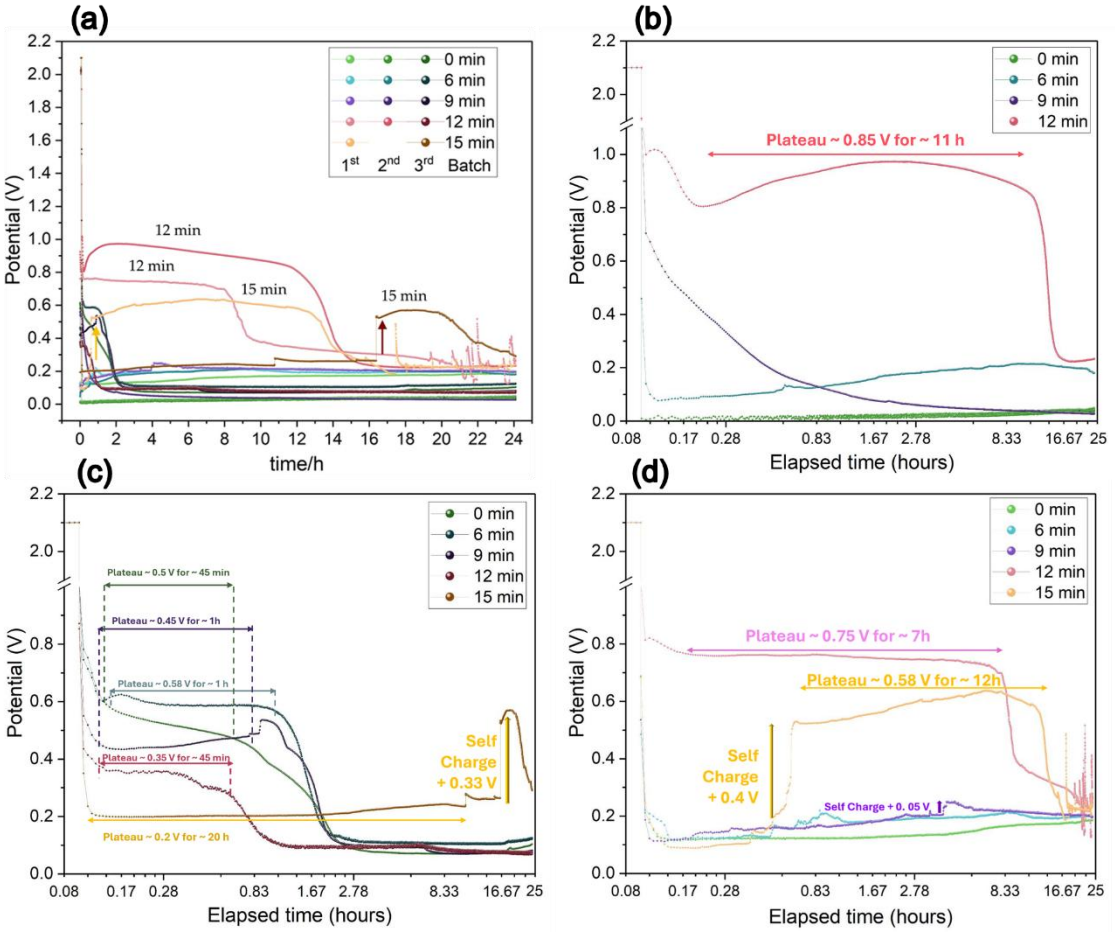


Figure 40 – Charge/discharge cycle plots of all Zn/$Na_{2.99}Ba_{0.005}OCl$/microstructured Cu cells: **(a)** Comparison between all batches and etching times. Discharge was performed through a 26.4 kΩ or 21.7 kΩ external material resistor. **(b)** Cells from batch 2; **(c)** cells from batch 1; **(d)** cells from batch 3.

The GITT data (**Figure 41** and **Figure A10**) indicate improved OCV after cycling, demonstrating that these cells can maintain stable performance over several days, particularly those with 9 min to 15 min etching. The reduced charging current of 1 μA and time of 100 s were intentionally left unaltered to allow direct comparison between all of the cells.

The less response upon charging with a small current, the better, as it shows that the sample is stable and will support higher charge and discharge currents.

Conversely, these cells polarize immediately under the current collectors' potential bias due to the ferroelectric electrolyte, which may indicate that the cells do not support extra charge. We would have to discharge them for many hours or use a higher discharge current before proceeding with the GITT analyses to allow the cells to charge more. However, we wanted to show the response for all of the cells with similar electrochemical "history". The 0 min cell charges to about 4 V, which denotes that it does not hold more

charge and is more unstable, showing an OCV of ~1.5 V. The 9 min cell charges to a maximum of 1.8 V, with a clear charging trend as well as self-cycling, as shown previously by the present family of electrolytes studied by the authors. The 12 min cell shows itself to be very stable when charging between 1.1 and 1.2 V, which is approximately the regular OCV of these cells. The 15 min cell starts by charging immediately to ~5 V, which is in accordance with the immediate discharge shown in **Figure 40** and **Figure 41e**; however, it becomes more stable, with a lower potential difference amplitude after 100 h, when it also starts to self-charge, with self-charging steps at approximately 114, 136, and 159 h. After turning to OCV, the 15 min cell shows a self-charge trend during ~1 h OCV, unlike the 0–12 min samples.

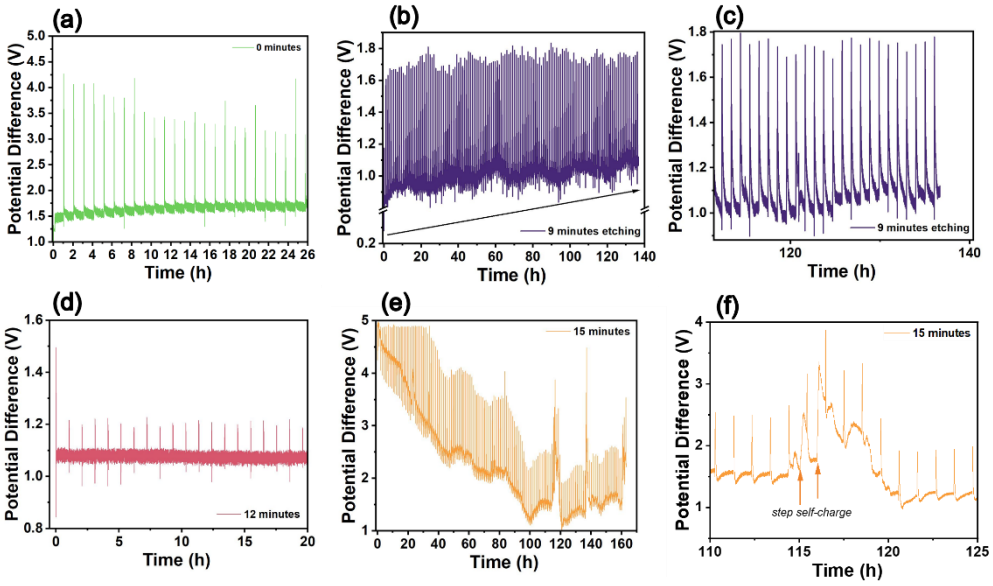


Figure 41 – GITT performance of selected Zn/$Na_{2.99}Ba_{0.005}OCl$/microstructured Cu cells with different etching durations: **(a)** 0 min; **(b)** 9 min (140 h); **(c)** zoom between 110 h and 140 h; **(d)** 12 min; **(e)** 15 min; and **(f)** zoom of 15 min between 110 and 125 h.

6.2.4. Comparison of Correlated Parameters

Although in most cases the relationships between etching duration and measured cell parameters must be taken carefully, similar trends observed between current collector parameters and cell parameters across etching times can help identify the factors underlying the cells' behavior.

Figure 38c shows that the electrolyte conductivity (represented as $1/R_{HF}$) reaches its highest value after 9 min of etching. When the etching time is extended to 12 min, a sharp decrease in conductivity is observed. Based on these results, the 9 min etching condition would be expected to produce a higher maximum current in cyclic voltammetry (CV) and lead to better overall electrochemical performance during cycling. However,

this trend is not confirmed by the data in **Figure 39** and **Figure 40**. In **Figure 39**, the highest current is observed for the unetched (0 min) collector, even though its electrochemical cycling performance was the poorest. The next highest CV currents occurred for the 9 min and 12 min etched samples. Interestingly, when analyzing the charge–discharge cycling in **Figure 40**, the best performance is achieved with the 12 min etched cell. The enhanced performance of the 12 min compared to the 9 min sample collector can be attributed to the increased surface area (as shown in **Figure 30b**), which provides more nucleation sites for sodium metal deposition on the current collector upon cycling, improving the battery performance.

Figure 42a shows a comparison between the average $1/R_{HF}$ and surface potential across all etching durations. Both parameters exhibit similar trends, indicating that higher surface potential generally corresponds to higher $1/\mathrm{R_{HF}} \propto \sigma_{Na^+}$; in other words, the difference in chemical potentials between the Zn (−0.76 V, SHE) and Cu current collectors (+0.34 V, SHE for 9-min) $\Delta V = \frac{-\mu(Zn,SHE)+\mu(Cu,SHE)}{e} = 1.10$ V controls the driving force (electric field inside the cell) that influences the ionic conductivity. As previously discussed, the force acting on charge carriers within the cell is primarily determined by the difference in chemical potential between the opposing current collectors/electrodes. A lower surface potential of the copper current collector (higher in the SHE scale used herein) increases its potential difference relative to the zinc current collector, effectively enhancing charge carrier mobility (Na^+) across the cell and reducing the cell's bulk resistance.

Figure 42b presents the average values of C_{LF}, Max $I_{discharge}$, and CCCbulk (for electrons). In this case, increased C_{LF} correlates with higher discharge currents. A similar trend is observed for CCCbulk (for holes or Cu^{2+} and Cu^+): lower charge carrier concentrations of electrons correspond to higher C_{LF} and Max $I_{discharge}$. This suggests that the Cu/electrolyte interface influences performance through changes in capacitance, which are linked to charge concentrations at the interfaces. All of the latter are correlated with the dynamic tendency to align the Fermi levels (electrochemical potentials $\bar{\mu}$) between the electrolyte and the Cu current collector/positive electrode.

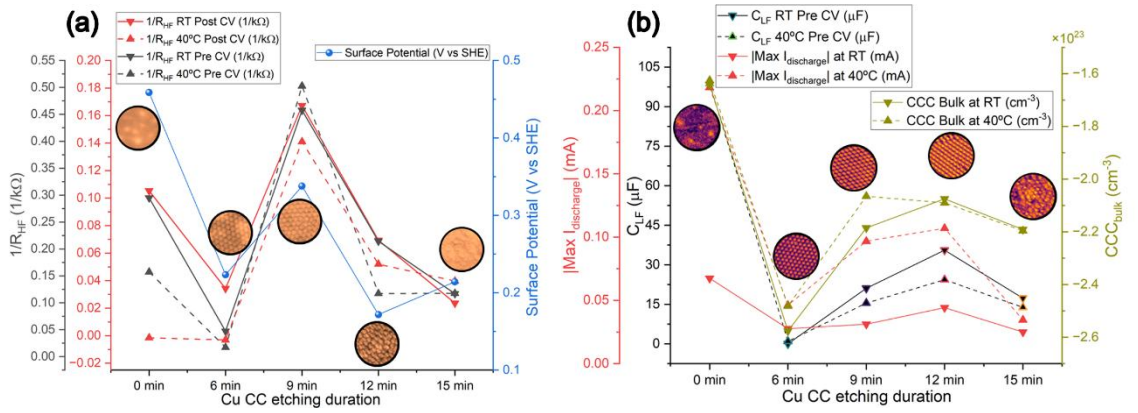


Figure 42 – Comparison across etching durations of selected parameters (average values) for the $Zn/Na_{2.99}Ba_{0.005}OCl$/microstructured Cu cells (left axis) and microstructured Cu current collector parameters (right axis): **(a)** $1/R_{HF}$ at RT and 40 °C and surface potential vs. etching time; **(b)** pre-CV C_{LF} at RT and 40 °C, Max $I_{discharge}$ at RT and 40 °C, and CCCbulk (electrons) at RT and 40 °C.

The bulk resistance of the cell generally makes up a significant portion of the total resistance. The relationship between bulk resistance (R_{HF}) and maximum charge and discharge currents is shown in **Figure 43**. Overall, lower bulk resistance correlates with higher peak currents. This correlation highlights the importance of enhancing charge mobility within the electrolyte by reducing overall resistance, either by increasing the potential difference across the current collectors or by adjusting the electrolyte composition and morphology.

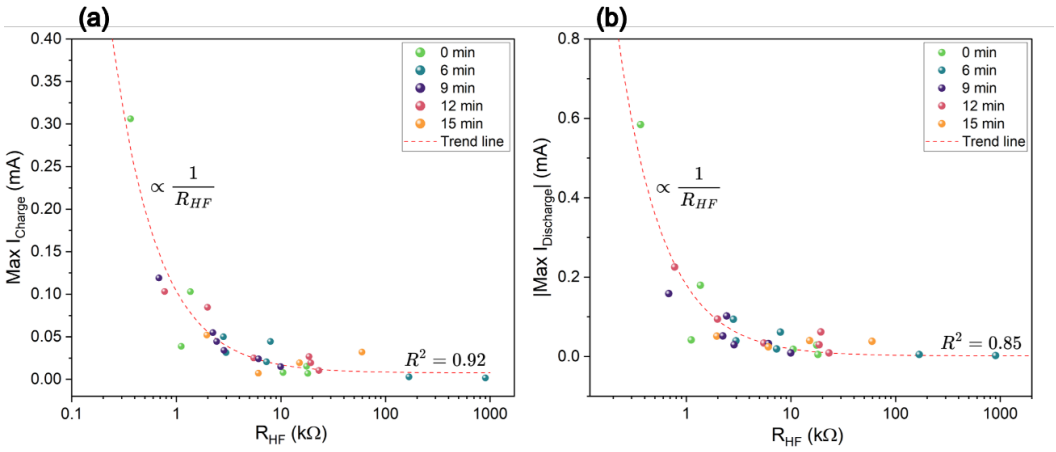


Figure 43 – Correlation between maximum cyclic voltammetry (CV) currents and R_{HF}: **(a)** Maximum charging current vs. R_{HF}. **(b)** Maximum discharging current vs. R_{HF}. The red dashed line indicates the $1/R_{HF}$ trend line; R^2 denotes the corresponding coefficient of determination.

Taken together, these observations highlight the interconnected role of the current collector surface potential, charge carrier concentration, and capacitance in governing cell performance. While etching time alone does not directly determine cell behavior, its influence on current collector properties indirectly shapes critical parameters such as

resistance and maximum discharge current. Understanding how modifications at the Cu/electrolyte interface alter charge transport mechanisms offers a practical pathway to optimizing cell design and improving overall efficiency.

6.3. Conclusions and future work

In this study, we investigated the influence of microstructured copper current collectors on the electrochemical performance of Zn/$Na_{2.99}Ba_{0.005}ClO$/Cu solid-state batteries. By employing a bottom–up colloidal lithography approach followed by reactive ion etching, we systematically varied the surface topography of copper films deposited on flexible parylene-C-coated PEN substrates. Surface characterization revealed that etching times of up to 15 min led to an increase in surface area of approximately 30%, accompanied by progressively rougher and irregular topographies. KPFM measurements showed average surface chemical potential values between 189 mV and 459 mV, comparable to clean or mildly oxidized copper. The microstructured samples had lower surface potential, likely resulting from mixed effects of oxidation and topography. However, the variation in the surface potential matches the variation in the inverse of the bulk resistance in the pouch related to the ionic conductivity in the bulk electrolyte. Charge transport characterization demonstrated that the resistivity of the thin-film copper layers remained within the range of ~1.96 to 4.5 μΩ.cm, close to the values of bulk copper. On the other hand, charge carrier density and mobility seemed to be affected by the microstructuring, with structured samples showing higher charge carrier density (electrons), in the order of 10^{23} cm^{-3}, but lower electron mobility, between 6 and 18 $cm^2.V^{-1}.s^{-1}$. We highlight that a higher concentration of electrons corresponds to lower C_{LF}, Max $I_{discharge}$, and CCC_{bulk} (holes or Cu^{2+}, Cu^{+}). Electrochemical characterization of the assembled Zn/$Na_{2.99}Ba_{0.005}OCl$/microstructured Cu pouch cells showed that, of all of the cells, the ones showing higher average deviation of nearest neighbors (σ_{DNN}) were the best performing (12 and 15 min). However, SEM analyses actually showed that the samples showing the lowest absolute σ_{DNN} (9 and 12 min) seemed to show fewer grain boundaries and spurious defects. The 15 min sample appears very ordered with secondary low magnification, but with backscattered electrons it shows two slightly different phases enabled by “bridges” that form with etching. These cells, showing average surface potential of +0.214 V vs. SHE, also show similar relative concentrations of CuO (Cu^{2+})/Cu_2O (Cu^{+})/Cu^0. Overall, the electrochemical characterization revealed a strong connection with the electrochemical characteristics of the Cu current collectors. Higher surface potential of the copper current collector correlates with increased Na^+ ionic conductivity, as shown by the parallel trends between surface potential and $1/R_{HF}$. This indicates that the potential difference between the Zn and Cu collectors, governed

by their chemical potential, directly affects the driving force for ion transport and helps reduce the cell's bulk resistance. Additionally, higher low-frequency capacitance was correlated with increased discharge currents, while lower charge carrier concentrations (electrons) in the copper current collector also corresponded to higher capacitance and discharge currents. These trends indicate that the Cu/electrolyte interface affects cell performance through variations in interfacial capacitance linked to charge concentrations and the alignment of electrochemical potentials. Order (information) parameters are also likely related to the performance of the cell or, even more likely, the increased surface area at the copper current collector/electrode.

Future work will examine microstructures produced by scalable routes, for example the use of high roughness and flexible stone paper as a substrate, which removes the need for a separate structuring step. Additional electrolyte fabrication methods will be assessed to further improve contact and interface formation. These studies will include measurements on dummy cells that use a single type current collector and the acquisition of cross-sectional imaging. The integration of structured current collectors into structural batteries will also be investigated as a way to improve performance, guided by trends observed in pouch cells. Finally, the application of these current collectors in solid state anode-less pouch cells with a cathode containing active species will be explored to evaluate their effect in a more complex electrochemical system.

General Conclusion

The direct conclusions from the results of Part I and Part II, have already been discussed in sections 3.3 and 6.3, respectively. In this section, I will provide a more holistic overview of the work developed and lessons learned during this thesis.

From the onset, the objectives were ambitious, and pursuing both research topics required sustained effort and careful planning. A key challenge was learning the fabrication process of perovskite solar cells, which involves many steps with strict timing requirements, all while working under limited access to a shared glovebox. Despite these constraints, most of the initial objectives were successfully accomplished.

As outlined in the introduction, this thesis was motivated by the need for simple, low cost and environmentally safer solutions for energy capture and storage. Although it does not present field ready prototypes, it tackles concept level questions that are essential to device performance and remain insufficiently studied. In tin based perovskite solar cells, oxidation is well documented, but its effects on film morphology and on energy level alignment across device layers are less explored. This work clarifies those links and reports observations not widely described in the literature. In sodium based solid state batteries, studies that integrate microstructured copper current collectors into complete cells are scarce. Here, their integration is detailed and the interplay between collector morphology and device electrochemistry is established.

In Part I, we were unable to obtain a fully functional device. Although a very small but detectable OCV was measured, the *J-V* curves remained linear. The oxidation and morphology studies point to band misalignment and parasitic short-circuiting paths as the most likely causes of this behavior. Despite this outcome, the work established a practical foundation for future development in the laboratory, providing a basis on which subsequent efforts can build and improve.

In Part II, we achieved all proposed objectives. Electrochemical and morphological characterization of the copper current collectors and of the assembled pouch cells revealed a strong coupling between interfacial energetics, discharge current, and bulk resistance, primarily linked to the copper electrode work function and charge concentration.

Taken together, the results from both parts reveal several optimization paths that could advance each technology toward commercial viability in a growing energy sector. Combining tin halide perovskite photovoltaics with sodium solid state batteries appears well suited to applications where safety and low cost are more critical than peak

efficiency. Agriculture is one such context. Many farms operate far from reliable grid access, which limits pumped irrigation and other automation. Systems based on the materials studied here could provide local energy generation and storage at lower cost, supporting water management and helping to mitigate yield losses under increasing drought pressure.

Still, this work had some shortcomings that are worth mentioning.

Related to Part I, XRD was difficult to use systematically because samples had to be transported to Aveiro and often degraded in transit, which compromised data. Without consistent integrity between preparation and measurement, we used XRD sparingly rather than as a routine tool, a setback for tracking phase evolution and degradation with statistical confidence.

My experimental organization slowed iteration. I fabricated 12 to 14 cells per batch, altering one variable in half, and a single variable study took about a week from preparation through characterization. Combined with work on the batteries project and article writing, this cadence limited iterations. Early glovebox work was slow and tracking multiple changes across substrates risked confusion, so I kept designs simple. With the experience gained, I am confident a more efficient plan would deliver substantially greater progress.

Time pressure reduced the depth of my analysis. Weekly reviews were shallow, and I leaned on first interpretations without checking enough literature. While writing the thesis I revisited datasets, repeated analyses, and aligned interpretations with prior work, which clarified my understanding. The clearest case is perovskite morphology: initial SEM looked acceptable, so I did not probe further, but higher resolution SEM and closer reading of crystal growth studies revealed inconsistencies. I then revised the morphology discussion, linking observations to growth modes and film formation. Earlier critical review might have prompted different process changes and addressed persistent issues sooner.

In Part II, several aspects could have been improved. First, due to the publication timeline we did not perform post-mortem analysis of the pouch cells and current collectors. Such analysis would have clarified how the microstructure accommodated mechanical stress at the electrolyte interface and how contact evolved during cycling. Cross-sectional imaging would also have been informative.

Second, electrolyte consistency varied more than desired. We produced several batches to limit deviations, yet differences in thickness and surface smoothness still introduced

cell-to-cell variability and added scatter to the data. A dedicated study of the electrolyte fabrication method is needed to define a protocol that yields reproducible thickness, tighter tolerances, and smoother surfaces.

Overall, the study addressed the major variables that influence this system and produced a coherent picture. Even so, tighter process control would reduce sample-to-sample variability and enable stronger conclusions, particularly because the dataset contained only three samples per condition, which prevented meaningful statistical analysis.

On a personal note, this thesis period was one of strong character building and growth. I feel different from a year ago, with a clearer view of how science progresses, how to do it well, and where my strengths and limits lie. The main lesson is that ambitious objectives are worthwhile. Even when specific targets are not met, the process deepens capability and understanding, because the problems and failures faced are learning opportunities that would not arise under safer choices.

References

[1] D. I. Stern, “The role of energy in economic growth,” *Ann. N. Y. Acad. Sci.*, vol. 1219, no. 1, pp. 26–51, Feb. 2011, doi: 10.1111/j.1749-6632.2010.05921.x.
[2] P. Friedlingstein *et al.*, “Global Carbon Budget 2024,” *Earth Syst. Sci. Data*, vol. 17, no. 3, pp. 965–1039, Mar. 2025, doi: 10.5194/essd-17-965-2025.
[3] P. Mitra *et al.*, “Integrating Climate Change into Macroeconomic Analysis: A Review of Impact Channels, Data, Models, and Scenarios,” *IMF Work. Pap.*, vol. 2025, no. 170, p. 1, Aug. 2025, doi: 10.5089/9798229021890.001.
[4] Intergovernmental Panel On Climate Change (Ipcc), Ed., *Climate Change 2022 - Mitigation of Climate Change: Working Group III Contribution to the Sixth Assessment Report of the Intergovernmental Panel on Climate Change*, 1st ed. Cambridge University Press, 2023. doi: 10.1017/9781009157926.
[5] Z. Lin, Q. Zhou, Z. Wang, C. Wang, D. B. Bookhart, and M. Leung-Shea, “A high-resolution three-year dataset supporting rooftop photovoltaics (PV) generation analytics,” *Sci. Data*, vol. 12, no. 1, p. 63, Jan. 2025, doi: 10.1038/s41597-025-04397-y.
[6] M. Arbabzadeh, R. Sioshansi, J. X. Johnson, and G. A. Keoleian, “The role of energy storage in deep decarbonization of electricity production,” *Nat. Commun.*, vol. 10, no. 1, p. 3413, July 2019, doi: 10.1038/s41467-019-11161-5.
[7] J. Fernández-González, M. Rumayor, A. Domínguez-Ramos, A. Irabien, and I. Ortiz, “The Relevance of Life Cycle Assessment Tools in the Development of Emerging Decarbonization Technologies,” *JACS Au*, vol. 3, no. 10, pp. 2631–2639, Oct. 2023, doi: 10.1021/jacsau.3c00276.
[8] O. Ahmadzadeh, R. Rodriguez, J. Getz, S. Panneerselvam, and D. Soudbakhsh, “The impact of lightweighting and battery technologies on the sustainability of electric vehicles: A comprehensive life cycle assessment,” *Environ. Impact Assess. Rev.*, vol. 110, p. 107668, Jan. 2025, doi: 10.1016/j.eiar.2024.107668.
[9] J. Guo, Y. Jing, W. Hou, T. Wang, S. Ma, and G. He, “Demands and challenges of energy storage technology for future power system,” *Energy Internet*, vol. 1, no. 2, pp. 116–122, Nov. 2024, doi: 10.1049/ein2.12017.
[10] A. Pandey, K. Rawat, P. Phogat, Shreya, R. Jha, and S. Singh, “Next-generation energy storage: A deep dive into experimental and emerging battery technologies,” *J. Alloys Compd.*, vol. 1014, p. 178781, Feb. 2025, doi: 10.1016/j.jallcom.2025.178781.
[11] P. U. Nzereogu *et al.*, “Solid-State lithium-ion battery electrolytes: Revolutionizing energy density and safety,” *Hybrid Adv.*, vol. 8, p. 100339, Mar. 2025, doi: 10.1016/j.hybadv.2024.100339.
[12] Z. S. Iro, C. Subramani, and S. S. Dash, “A Brief Review on Electrode Materials for Supercapacitor,” *Int. J. Electrochem. Sci.*, vol. 11, no. 12, pp. 10628–10643, Dec. 2016, doi: 10.20964/2016.12.50.
[13] Z. Yu, L. Tetard, L. Zhai, and J. Thomas, “Supercapacitor electrode materials: nanostructures from 0 to 3 dimensions,” *Energy Environ. Sci.*, vol. 8, no. 3, pp. 702–730, 2015, doi: 10.1039/C4EE03229B.
[14] R. Jain *et al.*, “Nanostructuring versus microstructuring in battery electrodes,” *Nat. Rev. Mater.*, vol. 7, no. 9, pp. 736–746, June 2022, doi: 10.1038/s41578-022-00454-9.
[15] I. Yang, J. Jeong, J. Y. Seok, and S. Kim, “Structurally Tailored Hierarchical Cu Current Collector with Selective Inward Growth of Lithium for High-Performance Lithium Metal Batteries,” *Adv. Energy Mater.*, vol. 13, no. 2, p. 2202321, Jan. 2023, doi: 10.1002/aenm.202202321.
[16] Y. Zhang *et al.*, “Developments, Novel Concepts, and Challenges of Current Collectors: From Conventional Lithium Batteries to All-Solid-State Batteries,”

ChemElectroChem, vol. 11, no. 14, p. e202300739, July 2024, doi: 10.1002/celc.202300739.

[17] L. Liu, H. Zhao, and Y. Lei, "Review on Nanoarchitectured Current Collectors for Pseudocapacitors," *Small Methods*, vol. 3, no. 8, p. 1800341, Aug. 2019, doi: 10.1002/smtd.201800341.

[18] J. Wen, Y. Yu, and C. Chen, "A Review on Lithium-Ion Batteries Safety Issues: Existing Problems and Possible Solutions," *Mater. Express*, vol. 2, no. 3, pp. 197–212, Sept. 2012, doi: 10.1166/mex.2012.1075.

[19] H. Si, J. Ma, X. Xia, Q. Wang, S. Geng, and L. Fu, "Solid-State Sodium-Ion Batteries: Theories, Challenges and Perspectives," *Chem. – Eur. J.*, vol. 31, no. 5, p. e202403247, Jan. 2025, doi: 10.1002/chem.202403247.

[20] T. Jin, G. Singer, K. Liang, and Y. Yang, "Structural batteries: Advances, challenges and perspectives," *Mater. Today*, vol. 62, pp. 151–167, Jan. 2023, doi: 10.1016/j.mattod.2022.12.001.

[21] F. Danzi, P. P. Camanho, and M. H. Braga, "An All-Solid-State Coaxial Structural Battery Using Sodium-Based Electrolyte," *Molecules*, vol. 26, no. 17, p. 5226, Aug. 2021, doi: 10.3390/molecules26175226.

[22] M. H. Braga, J. A. Ferreira, A. J. Murchison, and J. B. Goodenough, "Electric Dipoles and Ionic Conductivity in a Na^+ Glass Electrolyte," *J. Electrochem. Soc.*, vol. 164, no. 2, pp. A207–A213, 2017, doi: 10.1149/2.0691702jes.

[23] M. Carvalho Baptista, H. Khalifa, A. Araújo, B. A. Maia, M. Souto, and M. H. Braga, "Giant Polarization in Quasi-Adiabatic Ferroelectric Na^+ Electrolyte for Solid-State Energy Harvesting and Storage," *Adv. Funct. Mater.*, vol. 33, no. 10, p. 2212344, Mar. 2023, doi: 10.1002/adfm.202212344.

[24] F. Danzi, M. Valente, S. Terlicka, and M. H. Braga, "Sodium and potassium ion rich ferroelectric solid electrolytes for traditional and electrode-less structural batteries," *APL Mater.*, vol. 10, no. 3, p. 031111, Mar. 2022, doi: 10.1063/5.0080054.

[25] Â. Freitas, M. C. Baptista, and M. H. Braga, "Sustainable Solid-State Sodium-Ion Batteries Featuring Ferroelectric Electrolytes," *Int. J. Mol. Sci.*, vol. 25, no. 23, p. 12694, Nov. 2024, doi: 10.3390/ijms252312694.

[26] M. C. Baptista *et al.*, "Conditioning Solid-State Anode-Less Cells for the Next Generation of Batteries," *Batteries*, vol. 9, no. 8, p. 402, Aug. 2023, doi: 10.3390/batteries9080402.

[27] V. Fthenakis and E. Leccisi, "Updated sustainability status of crystalline silicon-based photovoltaic systems: Life-cycle energy and environmental impact reduction trends," *Prog. Photovolt. Res. Appl.*, vol. 29, no. 10, pp. 1068–1077, Oct. 2021, doi: 10.1002/pip.3441.

[28] J. Han *et al.*, "Perovskite solar cells," *Nat. Rev. Methods Primer*, vol. 5, no. 1, p. 3, Jan. 2025, doi: 10.1038/s43586-024-00373-9.

[29] J. Li *et al.*, "Biological impact of lead from halide perovskites reveals the risk of introducing a safe threshold," *Nat. Commun.*, vol. 11, no. 1, p. 310, Jan. 2020, doi: 10.1038/s41467-019-13910-y.

[30] M. Pitaro, E. K. Tekelenburg, S. Shao, and M. A. Loi, "Tin Halide Perovskites: From Fundamental Properties to Solar Cells," *Adv. Mater.*, vol. 34, no. 1, p. 2105844, Jan. 2022, doi: 10.1002/adma.202105844.

[31] N. Sun *et al.*, "Architecture of p-i-n Sn-Based Perovskite Solar Cells: Characteristics, Advances, and Perspectives," *ACS Energy Lett.*, vol. 6, no. 8, pp. 2863–2875, Aug. 2021, doi: 10.1021/acsenergylett.1c01170.

[32] P. Würfel and U. Würfel, *Physics of solar cells: from basic principles to advanced concepts*, 3rd edition. in MyiLibrary. Weinheim: Wiley-VCH Verlag GmbH & Co. KGaA, 2016.

[33] S. Akel, A. Kulkarni, U. Rau, and T. Kirchartz, "Relevance of Long Diffusion Lengths for Efficient Halide Perovskite Solar Cells," *PRX Energy*, vol. 2, no. 1, p. 013004, Mar. 2023, doi: 10.1103/PRXEnergy.2.013004.

[34] J. A. Luceño-Sánchez, A. M. Díez-Pascual, and R. Peña Capilla, “Materials for Photovoltaics: State of Art and Recent Developments,” *Int. J. Mol. Sci.*, vol. 20, no. 4, p. 976, Feb. 2019, doi: 10.3390/ijms20040976.
[35] E. Venkatragavaraj, B. Satish, P. R. Vinod, and M. S. Vijaya, “Piezoelectric properties of ferroelectric PZT-polymer composites,” *J. Phys. Appl. Phys.*, vol. 34, no. 4, pp. 487–492, Feb. 2001, doi: 10.1088/0022-3727/34/4/308.
[36] C. He and X. Liu, “The rise of halide perovskite semiconductors,” *Light Sci. Appl.*, vol. 12, no. 1, p. 15, Jan. 2023, doi: 10.1038/s41377-022-01010-4.
[37] C. C. Stoumpos, C. D. Malliakas, and M. G. Kanatzidis, “Semiconducting Tin and Lead Iodide Perovskites with Organic Cations: Phase Transitions, High Mobilities, and Near-Infrared Photoluminescent Properties,” *Inorg. Chem.*, vol. 52, no. 15, pp. 9019–9038, Aug. 2013, doi: 10.1021/ic401215x.
[38] M. Aslam, T. Mahmood, and A. Naeem, “Organic Inorganic Perovskites: A Low-Cost-Efficient Photovoltaic Material,” in *Perovskite and Piezoelectric Materials*, S. Pola, N. Panwar, and I. Coondoo, Eds., IntechOpen, 2021. doi: 10.5772/intechopen.94104.
[39] J.-W. Lee, S. Tan, S. I. Seok, Y. Yang, and N.-G. Park, “Rethinking the A cation in halide perovskites,” *Science*, vol. 375, no. 6583, p. eabj1186, Feb. 2022, doi: 10.1126/science.abj1186.
[40] J. W. Turnley, S. Agarwal, and R. Agrawal, “Rethinking tolerance factor analysis for chalcogenide perovskites,” *Mater. Horiz.*, vol. 11, no. 19, pp. 4802–4808, 2024, doi: 10.1039/D4MH00689E.
[41] R. D. Shannon, “Revised effective ionic radii and systematic studies of interatomic distances in halides and chalcogenides,” *Acta Crystallogr. Sect. A*, vol. 32, no. 5, pp. 751–767, Sept. 1976, doi: 10.1107/S0567739476001551.
[42] G. Kieslich, S. Sun, and A. K. Cheetham, “Solid-state principles applied to organic–inorganic perovskites: new tricks for an old dog,” *Chem Sci*, vol. 5, no. 12, pp. 4712–4715, 2014, doi: 10.1039/C4SC02211D.
[43] J. S. Manser, J. A. Christians, and P. V. Kamat, “Intriguing Optoelectronic Properties of Metal Halide Perovskites,” *Chem. Rev.*, vol. 116, no. 21, pp. 12956–13008, Nov. 2016, doi: 10.1021/acs.chemrev.6b00136.
[44] Y. An *et al.*, “Structural Stability of Formamidinium- and Cesium-Based Halide Perovskites,” *ACS Energy Lett.*, vol. 6, no. 5, pp. 1942–1969, May 2021, doi: 10.1021/acsenergylett.1c00354.
[45] H. Näsström *et al.*, “Dependence of phase transitions on halide ratio in inorganic $CsPb(Br_x I_{1-x})_3$ perovskite thin films obtained from high-throughput experimentation,” *J. Mater. Chem. A*, vol. 8, no. 43, pp. 22626–22631, 2020, doi: 10.1039/D0TA08067E.
[46] Md. H. Miah *et al.*, “Lead-free alternatives and toxicity mitigation strategies for sustainable perovskite solar cells: a critical review,” *Mater. Adv.*, vol. 6, no. 9, pp. 2718–2752, 2025, doi: 10.1039/D5MA00010F.
[47] A. Alaei, A. Circelli, Y. Yuan, Y. Yang, and S. S. Lee, “Polymorphism in metal halide perovskites,” *Mater. Adv.*, vol. 2, no. 1, pp. 47–63, 2021, doi: 10.1039/D0MA00643B.
[48] A. Buin, R. Comin, J. Xu, A. H. Ip, and E. H. Sargent, “Halide-Dependent Electronic Structure of Organolead Perovskite Materials,” *Chem. Mater.*, vol. 27, no. 12, pp. 4405–4412, June 2015, doi: 10.1021/acs.chemmater.5b01909.
[49] S. Tao *et al.*, “Absolute energy level positions in tin- and lead-based halide perovskites,” *Nat. Commun.*, vol. 10, no. 1, p. 2560, June 2019, doi: 10.1038/s41467-019-10468-7.
[50] J. Even, L. Pedesseau, J.-M. Jancu, and C. Katan, “Importance of Spin–Orbit Coupling in Hybrid Organic/Inorganic Perovskites for Photovoltaic Applications,” *J. Phys. Chem. Lett.*, vol. 4, no. 17, pp. 2999–3005, Sept. 2013, doi: 10.1021/jz401532q.
[51] L. Canil *et al.*, “Tuning halide perovskite energy levels,” *Energy Environ. Sci.*, vol. 14, no. 3, pp. 1429–1438, 2021, doi: 10.1039/D0EE02216K.

[52] R. Su *et al.*, "Dielectric screening in perovskite photovoltaics," *Nat. Commun.*, vol. 12, no. 1, p. 2479, Apr. 2021, doi: 10.1038/s41467-021-22783-z.
[53] R. E. Brandt *et al.*, "Searching for 'Defect-Tolerant' Photovoltaic Materials: Combined Theoretical and Experimental Screening," *Chem. Mater.*, vol. 29, no. 11, pp. 4667–4674, June 2017, doi: 10.1021/acs.chemmater.6b05496.
[54] P. Chen *et al.*, "The Promise and Challenges of Inverted Perovskite Solar Cells," *Chem. Rev.*, vol. 124, no. 19, pp. 10623–10700, Oct. 2024, doi: 10.1021/acs.chemrev.4c00073.
[55] K. J. Savill, A. M. Ulatowski, and L. M. Herz, "Optoelectronic Properties of Tin–Lead Halide Perovskites," *ACS Energy Lett.*, vol. 6, no. 7, pp. 2413–2426, July 2021, doi: 10.1021/acsenergylett.1c00776.
[56] H. F. Zarick, N. Soetan, W. R. Erwin, and R. Bardhan, "Mixed halide hybrid perovskites: a paradigm shift in photovoltaics," *J. Mater. Chem. A*, vol. 6, no. 14, pp. 5507–5537, 2018, doi: 10.1039/C7TA09122B.
[57] H. Bhatia, B. Ghosh, and E. Debroye, "Colloidal $FAPbBr_3$ perovskite nanocrystals for light emission: what's going on?," *J. Mater. Chem. C*, vol. 10, no. 37, pp. 13437–13461, 2022, doi: 10.1039/D2TC01373H.
[58] C. Ballif, F.-J. Haug, M. Boccard, P. J. Verlinden, and G. Hahn, "Status and perspectives of crystalline silicon photovoltaics in research and industry," *Nat. Rev. Mater.*, vol. 7, no. 8, pp. 597–616, Mar. 2022, doi: 10.1038/s41578-022-00423-2.
[59] I. Mesquita, L. Andrade, and A. Mendes, "Perovskite solar cells: Materials, configurations and stability," *Renew. Sustain. Energy Rev.*, vol. 82, pp. 2471–2489, Feb. 2018, doi: 10.1016/j.rser.2017.09.011.
[60] S. L. Hamukwaya *et al.*, "A Review of Recent Developments in Preparation Methods for Large-Area Perovskite Solar Cells," *Coatings*, vol. 12, no. 2, p. 252, Feb. 2022, doi: 10.3390/coatings12020252.
[61] A. Kojima, K. Teshima, Y. Shirai, and T. Miyasaka, "Organometal Halide Perovskites as Visible-Light Sensitizers for Photovoltaic Cells," *J. Am. Chem. Soc.*, vol. 131, no. 17, pp. 6050–6051, May 2009, doi: 10.1021/ja809598r.
[62] Y. Rong, L. Liu, A. Mei, X. Li, and H. Han, "Beyond Efficiency: the Challenge of Stability in Mesoscopic Perovskite Solar Cells," *Adv. Energy Mater.*, vol. 5, no. 20, p. 1501066, Oct. 2015, doi: 10.1002/aenm.201501066.
[63] H. Xiang, P. Liu, W. Wang, R. Ran, W. Zhou, and Z. Shao, "Towards highly stable and efficient planar perovskite solar cells: Materials development, defect control and interfacial engineering," *Chem. Eng. J.*, vol. 420, p. 127599, Sept. 2021, doi: 10.1016/j.cej.2020.127599.
[64] Y. Rong, L. Liu, A. Mei, X. Li, and H. Han, "Beyond Efficiency: the Challenge of Stability in Mesoscopic Perovskite Solar Cells," *Adv. Energy Mater.*, vol. 5, no. 20, p. 1501066, Oct. 2015, doi: 10.1002/aenm.201501066.
[65] J. Príncipe, V. C. M. Duarte, and L. Andrade, "Inverted Perovskite Solar Cells: The Emergence of a Highly Stable and Efficient Architecture," *Energy Technol.*, vol. 10, no. 4, p. 2100952, Apr. 2022, doi: 10.1002/ente.202100952.
[66] H. Pan *et al.*, "Advances in design engineering and merits of electron transporting layers in perovskite solar cells," *Mater. Horiz.*, vol. 7, no. 9, pp. 2276–2291, 2020, doi: 10.1039/D0MH00586J.
[67] J. Huang and L. Mao, "A Review on Perovskite/Silicon Tandem Solar Cells: Current Status and Future Challenges," *Energies*, vol. 18, no. 16, p. 4327, Aug. 2025, doi: 10.3390/en18164327.
[68] Y. Wang *et al.*, "PTAA as Efficient Hole Transport Materials in Perovskite Solar Cells: A Review," *Sol. RRL*, vol. 6, no. 8, p. 2200234, Aug. 2022, doi: 10.1002/solr.202200234.
[69] G. M. Arumugam *et al.*, "Inorganic hole transport layers in inverted perovskite solar cells: A review," *Nano Sel.*, vol. 2, no. 6, pp. 1081–1116, June 2021, doi: 10.1002/nano.202000200.

[70]Z. Yang *et al.*, "Device physics of back-contact perovskite solar cells," *Energy Environ. Sci.*, vol. 13, no. 6, pp. 1753–1765, 2020, doi: 10.1039/C9EE04203B.
[71]H. Zai, Y. Ma, Q. Chen, and H. Zhou, "Ion migration in halide perovskite solar cells: Mechanism, characterization, impact and suppression," *J. Energy Chem.*, vol. 63, pp. 528–549, Dec. 2021, doi: 10.1016/j.jechem.2021.08.006.
[72]S. P. Dunfield *et al.*, "From Defects to Degradation: A Mechanistic Understanding of Degradation in Perovskite Solar Cell Devices and Modules," *Adv. Energy Mater.*, vol. 10, no. 26, p. 1904054, July 2020, doi: 10.1002/aenm.201904054.
[73]J. Zhuang, J. Wang, and F. Yan, "Review on Chemical Stability of Lead Halide Perovskite Solar Cells," *Nano-Micro Lett.*, vol. 15, no. 1, p. 84, Dec. 2023, doi: 10.1007/s40820-023-01046-0.
[74]E. Fortunato, D. Ginley, H. Hosono, and D. C. Paine, "Transparent Conducting Oxides for Photovoltaics," *MRS Bull.*, vol. 32, no. 3, pp. 242–247, Mar. 2007, doi: 10.1557/mrs2007.29.
[75]G. T. Chavan *et al.*, "A Brief Review of Transparent Conducting Oxides (TCO): The Influence of Different Deposition Techniques on the Efficiency of Solar Cells," *Nanomaterials*, vol. 13, no. 7, p. 1226, Mar. 2023, doi: 10.3390/nano13071226.
[76]H. S. Jung, G. S. Han, N.-G. Park, and M. J. Ko, "Flexible Perovskite Solar Cells," *Joule*, vol. 3, no. 8, pp. 1850–1880, Aug. 2019, doi: 10.1016/j.joule.2019.07.023.
[77]R. Guo *et al.*, "Refining the Substrate Surface Morphology for Achieving Efficient Inverted Perovskite Solar Cells," *Adv. Energy Mater.*, vol. 13, no. 43, p. 2302280, Nov. 2023, doi: 10.1002/aenm.202302280.
[78]A. Klein *et al.*, "Transparent Conducting Oxides for Photovoltaics: Manipulation of Fermi Level, Work Function and Energy Band Alignment," *Materials*, vol. 3, no. 11, pp. 4892–4914, Nov. 2010, doi: 10.3390/ma3114892.
[79]J. Endres *et al.*, "Electronic structure of the CsPbBr3/polytriarylamine (PTAA) system," *J. Appl. Phys.*, vol. 121, no. 3, p. 035304, Jan. 2017, doi: 10.1063/1.4974471.
[80]N. Tzoganakis *et al.*, "Ultrathin PTAA interlayer in conjunction with azulene derivatives for the fabrication of inverted perovskite solar cells," *J. Mater. Chem. C*, vol. 9, no. 41, pp. 14709–14719, 2021, doi: 10.1039/D1TC02726C.
[81]A. Intaniwet, C. A. Mills, P. J. Sellin, M. Shkunov, and J. L. Keddie, "Achieving a Stable Time Response in Polymeric Radiation Sensors under Charge Injection by X-rays," *ACS Appl. Mater. Interfaces*, vol. 2, no. 6, pp. 1692–1699, June 2010, doi: 10.1021/am100220y.
[82]J. Hwang, F. Amy, and A. Kahn, "Spectroscopic study on sputtered PEDOT·PSS: Role of surface PSS layer," *Org. Electron.*, vol. 7, no. 5, pp. 387–396, Oct. 2006, doi: 10.1016/j.orgel.2006.04.005.
[83]M. R. Lenze, N. M. Kronenberg, F. Würthner, and K. Meerholz, "In-situ modification of PEDOT:PSS work function using alkyl alcohols as secondary processing solvents and their impact on merocyanine based bulk heterojunction solar cells," *Org. Electron.*, vol. 21, pp. 171–176, June 2015, doi: 10.1016/j.orgel.2015.03.008.
[84]S. Jäckle *et al.*, "Potential of PEDOT:PSS as a hole selective front contact for silicon heterojunction solar cells," *Sci. Rep.*, vol. 7, no. 1, p. 2170, May 2017, doi: 10.1038/s41598-017-01946-3.
[85]K. Bruchlos *et al.*, "Poly(3-hexylthiophene) revisited – Influence of film deposition on the electrochemical behaviour and energy levels," *Electrochimica Acta*, vol. 269, pp. 299–311, Apr. 2018, doi: 10.1016/j.electacta.2018.02.126.
[86]Z. Xu, L.-M. Chen, M.-H. Chen, G. Li, and Y. Yang, "Energy level alignment of poly(3-hexylthiophene): [6,6]-phenyl C61 butyric acid methyl ester bulk heterojunction," *Appl. Phys. Lett.*, vol. 95, no. 1, p. 013301, July 2009, doi: 10.1063/1.3163056.
[87]R. Gironda *et al.*, "Functional Π-conjugated polymers based on maleimide for photovoltaic applications," *Org. Photonics Photovolt.*, vol. 1, Jan. 2013, doi: 10.2478/oph-2013-0004.

[88] Md. B. Islam, M. Yanagida, Y. Shirai, Y. Nabetani, and K. Miyano, "NiO $_x$ Hole Transport Layer for Perovskite Solar Cells with Improved Stability and Reproducibility," *ACS Omega*, vol. 2, no. 5, pp. 2291–2299, May 2017, doi: 10.1021/acsomega.7b00538.

[89] E. Thimsen, A. B. F. Martinson, J. W. Elam, and M. J. Pellin, "Energy Levels, Electronic Properties, and Rectification in Ultrathin p-NiO Films Synthesized by Atomic Layer Deposition," *J. Phys. Chem. C*, vol. 116, no. 32, pp. 16830–16840, Aug. 2012, doi: 10.1021/jp302008k.

[90] C. C. Boyd *et al.*, "Overcoming Redox Reactions at Perovskite-Nickel Oxide Interfaces to Boost Voltages in Perovskite Solar Cells," *Joule*, vol. 4, no. 8, pp. 1759–1775, Aug. 2020, doi: 10.1016/j.joule.2020.06.004.

[91] K. Zhao, R. Munir, B. Yan, Y. Yang, T. Kim, and A. Amassian, "Solution-processed inorganic copper(Ⅰ) thiocyanate (CuSCN) hole transporting layers for efficient p–i–n perovskite solar cells," *J. Mater. Chem. A*, vol. 3, no. 41, pp. 20554–20559, 2015, doi: 10.1039/C5TA04028K.

[92] H. Niu *et al.*, "Solvent-Induced Copper Vacancy in CuSCN Layer: A Strategy to Boost Conductivity and Optimize Energy Levels for Efficient Organic Solar Cells," *Adv. Funct. Mater.*, vol. 35, no. 2, p. 2413167, Jan. 2025, doi: 10.1002/adfm.202413167.

[93] M. Jamshidi and J. M. Gardner, "Copper(I) Iodide Thin Films: Deposition Methods and Hole-Transporting Performance," *Molecules*, vol. 29, no. 8, p. 1723, Apr. 2024, doi: 10.3390/molecules29081723.

[94] A. Liu, H. Zhu, M. Kim, J. Kim, and Y. Noh, "Engineering Copper Iodide (CuI) for Multifunctional p-Type Transparent Semiconductors and Conductors," *Adv. Sci.*, vol. 8, no. 14, p. 2100546, July 2021, doi: 10.1002/advs.202100546.

[95] S. Tao *et al.*, "Absolute energy level positions in tin- and lead-based halide perovskites," *Nat. Commun.*, vol. 10, no. 1, p. 2560, June 2019, doi: 10.1038/s41467-019-10468-7.

[96] J. Maibach, E. Mankel, T. Mayer, and W. Jaegermann, "The band energy diagram of PCBM–DH6T bulk heterojunction solar cells: synchrotron-induced photoelectron spectroscopy on solution processed DH6T:PCBM blends and in situ prepared PCBM/DH6T interfaces," *J. Mater. Chem. C*, vol. 1, no. 45, p. 7635, 2013, doi: 10.1039/c3tc31745e.

[97] K. Akaike *et al.*, "Ultraviolet photoelectron spectroscopy and inverse photoemission spectroscopy of [6,6]-phenyl-C61-butyric acid methyl ester in gas and solid phases," *J. Appl. Phys.*, vol. 104, no. 2, p. 023710, July 2008, doi: 10.1063/1.2957588.

[98] Z. Xu, L.-M. Chen, M.-H. Chen, G. Li, and Y. Yang, "Energy level alignment of poly(3-hexylthiophene): [6,6]-phenyl C61 butyric acid methyl ester bulk heterojunction," *Appl. Phys. Lett.*, vol. 95, no. 1, p. 013301, July 2009, doi: 10.1063/1.3163056.

[99] Y. Li, "Fullerene-Bisadduct Acceptors for Polymer Solar Cells," *Chem. – Asian J.*, vol. 8, no. 10, pp. 2316–2328, Oct. 2013, doi: 10.1002/asia.201300600.

[100] Z.-L. Guan, J. Bok Kim, Y.-L. Loo, and A. Kahn, "Electronic structure of the poly(3-hexylthiophene):indene-C60 bisadduct bulk heterojunction," *J. Appl. Phys.*, vol. 110, no. 4, p. 043719, Aug. 2011, doi: 10.1063/1.3626938.

[101] Y. He, H.-Y. Chen, J. Hou, and Y. Li, "Indene−C_{60} Bisadduct: A New Acceptor for High-Performance Polymer Solar Cells," *J. Am. Chem. Soc.*, vol. 132, no. 4, pp. 1377–1382, Feb. 2010, doi: 10.1021/ja908602j.

[102] M. Lo, Z. Guan, T. Ng, C. Chan, and C. Lee, "Electronic Structures and Photoconversion Mechanism in Perovskite/Fullerene Heterojunctions," *Adv. Funct. Mater.*, vol. 25, no. 8, pp. 1213–1218, Feb. 2015, doi: 10.1002/adfm.201402692.

[103] P. Schulz, L. L. Whittaker-Brooks, B. A. MacLeod, D. C. Olson, Y. Loo, and A. Kahn, "Electronic Level Alignment in Inverted Organometal Perovskite Solar Cells," *Adv. Mater. Interfaces*, vol. 2, no. 7, p. 1400532, May 2015, doi: 10.1002/admi.201400532.

[104] A. M. Ganose and D. O. Scanlon, “Band gap and work function tailoring of SnO_2 for improved transparent conducting ability in photovoltaics,” *J. Mater. Chem. C*, vol. 4, no. 7, pp. 1467–1475, 2016, doi: 10.1039/C5TC04089B.

[105] A. Uddin and H. Yi, “Progress and Challenges of SnO_2 Electron Transport Layer for Perovskite Solar Cells: A Critical Review,” *Sol. RRL*, vol. 6, no. 6, p. 2100983, June 2022, doi: 10.1002/solr.202100983.

[106] A. N. Guerreiro, I. B. Costa, A. B. Vale, and M. H. Braga, “Distinctive Electric Properties of Group 14 Oxides: SiO2, SiO, and SnO2,” *Int. J. Mol. Sci.*, vol. 24, no. 21, p. 15985, Nov. 2023, doi: 10.3390/ijms242115985.

[107] A. N. Guerreiro, M. C. Baptista, B. A. Maia, and M. H. Braga, “Interfacial Chemistry with ZnO: *In Operando* Work Functions in Heterocells,” *ACS Appl. Energy Mater.*, vol. 5, no. 8, pp. 9811–9822, Aug. 2022, doi: 10.1021/acsaem.2c01503.

[108] S. B. Tekin *et al.*, “Electron affinity of metal oxide thin films of TiO2, ZnO, and NiO and their applicability in 28.3 THz rectenna devices,” *J. Appl. Phys.*, vol. 134, no. 8, p. 084503, Aug. 2023, doi: 10.1063/5.0157726.

[109] H. B. Michaelson, “The work function of the elements and its periodicity,” *J. Appl. Phys.*, vol. 48, no. 11, pp. 4729–4733, Nov. 1977, doi: 10.1063/1.323539.

[110] A. Agresti, F. Di Giacomo, S. Pescetelli, and A. Di Carlo, “Scalable deposition techniques for large-area perovskite photovoltaic technology: A multi-perspective review,” *Nano Energy*, vol. 122, p. 109317, Apr. 2024, doi: 10.1016/j.nanoen.2024.109317.

[111] A. Valencia, F. Liu, X. Zhang, X. Bo, W. Li, and W. A. Daoud, “Auto-generating a database on the fabrication details of perovskite solar devices,” *Sci. Data*, vol. 12, no. 1, p. 270, Feb. 2025, doi: 10.1038/s41597-025-04566-z.

[112] L. Qiu, S. He, L. K. Ono, S. Liu, and Y. Qi, “Scalable Fabrication of Metal Halide Perovskite Solar Cells and Modules,” *ACS Energy Lett.*, vol. 4, no. 9, pp. 2147–2167, Sept. 2019, doi: 10.1021/acsenergylett.9b01396.

[113] L. Chao *et al.*, “Solvent Engineering of the Precursor Solution toward Large-Area Production of Perovskite Solar Cells,” *Adv. Mater.*, vol. 33, no. 14, p. 2005410, Apr. 2021, doi: 10.1002/adma.202005410.

[114] J. C. Hamill, J. Schwartz, and Y.-L. Loo, “Influence of Solvent Coordination on Hybrid Organic–Inorganic Perovskite Formation,” *ACS Energy Lett.*, vol. 3, no. 1, pp. 92–97, Jan. 2018, doi: 10.1021/acsenergylett.7b01057.

[115] D. E. Bornside, C. W. Macosko, and L. E. Scriven, “Spin coating: One-dimensional model,” *J. Appl. Phys.*, vol. 66, no. 11, pp. 5185–5193, Dec. 1989, doi: 10.1063/1.343754.

[116] R. Szostak *et al.*, “Exploring the formation of formamidinium-based hybrid perovskites by antisolvent methods: *in situ* GIWAXS measurements during spin coating,” *Sustain. Energy Fuels*, vol. 3, no. 9, pp. 2287–2297, 2019, doi: 10.1039/C9SE00306A.

[117] N. J. Jeon, J. H. Noh, Y. C. Kim, W. S. Yang, S. Ryu, and S. I. Seok, “Solvent engineering for high-performance inorganic–organic hybrid perovskite solar cells,” *Nat. Mater.*, vol. 13, no. 9, pp. 897–903, Sept. 2014, doi: 10.1038/nmat4014.

[118] M. Konstantakou, D. Perganti, P. Falaras, and T. Stergiopoulos, “Anti-Solvent Crystallization Strategies for Highly Efficient Perovskite Solar Cells,” *Crystals*, vol. 7, no. 10, p. 291, Sept. 2017, doi: 10.3390/cryst7100291.

[119] Y. Gou, S. Tang, C. Yuan, P. Zhao, J. Chen, and H. Yu, “Research progress of green antisolvent for perovskite solar cells,” *Mater. Horiz.*, vol. 11, no. 15, pp. 3465–3481, 2024, doi: 10.1039/D4MH00290C.

[120] Q. An *et al.*, “Effect of Antisolvent Application Rate on Film Formation and Photovoltaic Performance of Methylammonium-Free Perovskite Solar Cells,” *Adv. Energy Sustain. Res.*, vol. 2, no. 11, p. 2100061, Nov. 2021, doi: 10.1002/aesr.202100061.

[121] M. K. A. Mohammed *et al.*, “Improving the potential of ethyl acetate green anti-solvent to fabricate efficient and stable perovskite solar cells,” *RSC Adv.*, vol. 12, no. 50, pp. 32611–32618, 2022, doi: 10.1039/D2RA05454J.

[122] C. Zervos, M. Tountas, K. Chatzimanolis, C. Polyzoidis, and E. Kymakis, “Evaluating the role of phenethylamine iodide as a novel anti-solvent for enhancing performance of inverted planar perovskite solar cells,” *J. Mater. Chem. C*, vol. 8, no. 21, pp. 7143–7148, 2020, doi: 10.1039/D0TC01244K.

[123] L. Wang *et al.*, “Annealing Engineering in the Growth of Perovskite Grains,” *Crystals*, vol. 12, no. 7, p. 894, June 2022, doi: 10.3390/cryst12070894.

[124] Z. Xiao, Q. Dong, C. Bi, Y. Shao, Y. Yuan, and J. Huang, “Solvent Annealing of Perovskite-Induced Crystal Growth for Photovoltaic-Device Efficiency Enhancement,” *Adv. Mater.*, vol. 26, no. 37, pp. 6503–6509, Oct. 2014, doi: 10.1002/adma.201401685.

[125] H. Yu *et al.*, “Room-temperature mixed-solvent-vapor annealing for high performance perovskite solar cells,” *J. Mater. Chem. A*, vol. 4, no. 1, pp. 321–326, 2016, doi: 10.1039/C5TA08565A.

[126] M. Han, J. Byeon, J. Jang, C. Hur, G. Seo, and M. Choi, “Hot Gas-Blowing Assisted Crystallinity Management of Bar-Coated Perovskite Solar Cells and Modules,” *Small Sci.*, vol. 3, no. 9, p. 2300069, Sept. 2023, doi: 10.1002/smsc.202300069.

[127] W. Nie *et al.*, “High-efficiency solution-processed perovskite solar cells with millimeter-scale grains,” *Science*, vol. 347, no. 6221, pp. 522–525, Jan. 2015, doi: 10.1126/science.aaa0472.

[128] S. Sánchez *et al.*, “Flash Infrared Pulse Time Control of Perovskite Crystal Nucleation and Growth from Solution,” *Cryst. Growth Des.*, vol. 20, no. 2, pp. 670–679, Feb. 2020, doi: 10.1021/acs.cgd.9b01083.

[129] S. Sidhik *et al.*, “Deterministic fabrication of 3D/2D perovskite bilayer stacks for durable and efficient solar cells,” *Science*, vol. 377, no. 6613, pp. 1425–1430, Sept. 2022, doi: 10.1126/science.abq7652.

[130] C. Yang *et al.*, “Achievements, challenges, and future prospects for industrialization of perovskite solar cells,” *Light Sci. Appl.*, vol. 13, no. 1, p. 227, Sept. 2024, doi: 10.1038/s41377-024-01461-x.

[131] Y. Kato, L. K. Ono, M. V. Lee, S. Wang, S. R. Raga, and Y. Qi, “Silver Iodide Formation in Methyl Ammonium Lead Iodide Perovskite Solar Cells with Silver Top Electrodes,” *Adv. Mater. Interfaces*, vol. 2, no. 13, p. 1500195, Sept. 2015, doi: 10.1002/admi.201500195.

[132] J. Thiesbrummel *et al.*, “Ion-induced field screening as a dominant factor in perovskite solar cell operational stability,” *Nat. Energy*, vol. 9, no. 6, pp. 664–676, Mar. 2024, doi: 10.1038/s41560-024-01487-w.

[133] N. Aristidou *et al.*, “The Role of Oxygen in the Degradation of Methylammonium Lead Trihalide Perovskite Photoactive Layers,” *Angew. Chem. Int. Ed.*, vol. 54, no. 28, pp. 8208–8212, July 2015, doi: 10.1002/anie.201503153.

[134] J. A. Christians *et al.*, “Tailored interfaces of unencapsulated perovskite solar cells for >1,000 hour operational stability,” *Nat. Energy*, vol. 3, no. 1, pp. 68–74, Jan. 2018, doi: 10.1038/s41560-017-0067-y.

[135] Md. H. Miah *et al.*, “Key degradation mechanisms of perovskite solar cells and strategies for enhanced stability: issues and prospects,” *RSC Adv.*, vol. 15, no. 1, pp. 628–654, 2025, doi: 10.1039/D4RA07942F.

[136] E. Kobayashi, R. Tsuji, D. Martineau, A. Hinsch, and S. Ito, “Light-induced performance increase of carbon-based perovskite solar module for 20-year stability,” *Cell Rep. Phys. Sci.*, vol. 2, no. 12, p. 100648, Dec. 2021, doi: 10.1016/j.xcrp.2021.100648.

[137] T. Wang *et al.*, “Room temperature nondestructive encapsulation via self-crosslinked fluorosilicone polymer enables damp heat-stable sustainable perovskite

solar cells," *Nat. Commun.*, vol. 14, no. 1, p. 1342, Mar. 2023, doi: 10.1038/s41467-023-36918-x.

[138] D. C. Jordan, S. R. Kurtz, K. VanSant, and J. Newmiller, "Compendium of photovoltaic degradation rates," *Prog. Photovolt. Res. Appl.*, vol. 24, no. 7, pp. 978–989, July 2016, doi: 10.1002/pip.2744.

[139] B. Dou *et al.*, "Roll-to-Roll Printing of Perovskite Solar Cells," *ACS Energy Lett.*, vol. 3, no. 10, pp. 2558–2565, Oct. 2018, doi: 10.1021/acsenergylett.8b01556.

[140] J. Li *et al.*, "Ink Design Enabling Slot-Die Coated Perovskite Solar Cells with >22% Power Conversion Efficiency, Micro-Modules, and 1 Year of Outdoor Performance Evaluation," *Adv. Energy Mater.*, vol. 13, no. 33, p. 2203898, Sept. 2023, doi: 10.1002/aenm.202203898.

[141] J. Han, R. H. Kim, S. Huang, J. Kim, and J. S. Yun, "Green Solution Processing of Halide Perovskite Solar Cells: Status and Future Directions," *Sol. RRL*, vol. 8, no. 22, p. 2400262, Nov. 2024, doi: 10.1002/solr.202400262.

[142] H. C. Weerasinghe *et al.*, "The first demonstration of entirely roll-to-roll fabricated perovskite solar cell modules under ambient room conditions," *Nat. Commun.*, vol. 15, no. 1, p. 1656, Mar. 2024, doi: 10.1038/s41467-024-46016-1.

[143] L. Vesce *et al.*, "Perovskite solar cell technology scaling-up: Eco-efficient and industrially compatible sub-module manufacturing by fully ambient air slot-die/blade meniscus coating," *Prog. Photovolt. Res. Appl.*, vol. 32, no. 2, pp. 115–129, Feb. 2024, doi: 10.1002/pip.3741.

[144] B. Yan *et al.*, "3D laminar flow–assisted crystallization of perovskites for square meter–sized solar modules," *Science*, vol. 388, no. 6749, p. eadt5001, May 2025, doi: 10.1126/science.adt5001.

[145] N. Li *et al.*, "Super-three-dimensional lithiophilic Cu-based current collector for anode-free lithium metal battery," *Mater. Today Energy*, vol. 36, p. 101341, Aug. 2023, doi: 10.1016/j.mtener.2023.101341.

[146] X. Xiao *et al.*, "Lead-adsorbing ionogel-based encapsulation for impact-resistant, stable, and lead-safe perovskite modules," *Sci. Adv.*, vol. 7, no. 44, p. eabi8249, Oct. 2021, doi: 10.1126/sciadv.abi8249.

[147] X. Xiao *et al.*, "Aqueous-based recycling of perovskite photovoltaics," *Nature*, vol. 638, no. 8051, pp. 670–675, Feb. 2025, doi: 10.1038/s41586-024-08408-7.

[148] N/A, "DIRECTIVE 2011/65/EU OF THE EUROPEAN PARLIAMENT AND OF THE COUNCIL." June 08, 2011. [Online]. Available: http://data.europa.eu/eli/dir/2011/65/2025-01-01

[149] G. Nasti and A. Abate, "Tin Halide Perovskite ($ASnX_3$) Solar Cells: A Comprehensive Guide toward the Highest Power Conversion Efficiency," *Adv. Energy Mater.*, vol. 10, no. 13, p. 1902467, Apr. 2020, doi: 10.1002/aenm.201902467.

[150] M. Konstantakou and T. Stergiopoulos, "A critical review on tin halide perovskite solar cells," *J. Mater. Chem. A*, vol. 5, no. 23, pp. 11518–11549, 2017, doi: 10.1039/C7TA00929A.

[151] J. Cao and F. Yan, "Recent progress in tin-based perovskite solar cells," *Energy Environ. Sci.*, vol. 14, no. 3, pp. 1286–1325, 2021, doi: 10.1039/D0EE04007J.

[152] J. Pascual *et al.*, "Origin of Sn(II) oxidation in tin halide perovskites," *Mater. Adv.*, vol. 1, no. 5, pp. 1066–1070, 2020, doi: 10.1039/D0MA00245C.

[153] P. Xu, S. Chen, H.-J. Xiang, X.-G. Gong, and S.-H. Wei, "Influence of Defects and Synthesis Conditions on the Photovoltaic Performance of Perovskite Semiconductor $CsSnI_3$," *Chem. Mater.*, vol. 26, no. 20, pp. 6068–6072, Oct. 2014, doi: 10.1021/cm503122j.

[154] L. Lanzetta *et al.*, "Degradation mechanism of hybrid tin-based perovskite solar cells and the critical role of tin (IV) iodide," *Nat. Commun.*, vol. 12, no. 1, p. 2853, May 2021, doi: 10.1038/s41467-021-22864-z.

[155] J. Hardy, H. Fiedler, and J. Kennedy, “A review on the current status and chemistry of tin halide perovskite films for photovoltaics,” *Prog. Mater. Sci.*, vol. 151, p. 101446, May 2025, doi: 10.1016/j.pmatsci.2025.101446.

[156] J. Zillner *et al.*, “The Role of SnF_2 Additive on Interface Formation in All Lead-Free $FASnI_3$ Perovskite Solar Cells,” *Adv. Funct. Mater.*, vol. 32, no. 28, p. 2109649, July 2022, doi: 10.1002/adfm.202109649.

[157] E. Jokar, C.-H. Chien, A. Fathi, M. Rameez, Y.-H. Chang, and E. W.-G. Diau, “Slow surface passivation and crystal relaxation with additives to improve device performance and durability for tin-based perovskite solar cells,” *Energy Environ. Sci.*, vol. 11, no. 9, pp. 2353–2362, 2018, doi: 10.1039/C8EE00956B.

[158] Q. Tai *et al.*, “Antioxidant Grain Passivation for Air-Stable Tin-Based Perovskite Solar Cells,” *Angew. Chem. Int. Ed.*, vol. 58, no. 3, pp. 806–810, Jan. 2019, doi: 10.1002/anie.201811539.

[159] X. Meng *et al.*, “Surface-Controlled Oriented Growth of FASnI3 Crystals for Efficient Lead-free Perovskite Solar Cells,” *Joule*, vol. 4, no. 4, pp. 902–912, Apr. 2020, doi: 10.1016/j.joule.2020.03.007.

[160] X. Liu *et al.*, “Templated growth of $FASnI_3$ crystals for efficient tin perovskite solar cells,” *Energy Environ. Sci.*, vol. 13, no. 9, pp. 2896–2902, 2020, doi: 10.1039/D0EE01845G.

[161] Z. Zhu, X. Jiang, D. Yu, N. Yu, Z. Ning, and Q. Mi, “Smooth and Compact $FASnI_3$ Films for Lead-Free Perovskite Solar Cells with over 14% Efficiency,” *ACS Energy Lett.*, vol. 7, no. 6, pp. 2079–2083, June 2022, doi: 10.1021/acsenergylett.2c00776.

[162] X. Liu, T. Wu, C. Zhang, Y. Zhang, H. Segawa, and L. Han, “Interface Energy-Level Management toward Efficient Tin Perovskite Solar Cells with Hole-Transport-Layer-Free Structure,” *Adv. Funct. Mater.*, vol. 31, no. 50, p. 2106560, Dec. 2021, doi: 10.1002/adfm.202106560.

[163] T. Wu *et al.*, “Heterogeneous FASnI3 Absorber with Enhanced Electric Field for High-Performance Lead-Free Perovskite Solar Cells,” *Nano-Micro Lett.*, vol. 14, no. 1, p. 99, Dec. 2022, doi: 10.1007/s40820-022-00842-4.

[164] T. Ye *et al.*, “Localized Electron Density Engineering for Stabilized B-γ $CsSnI_3$ - Based Perovskite Solar Cells with Efficiencies >10%,” *ACS Energy Lett.*, pp. 1480–1489, Mar. 2021, doi: 10.1021/acsenergylett.1c00342.

[165] Z. Zhang *et al.*, “Over 12% efficient CsSnI3 perovskite solar cells enabled by surface post-treatment with bi-functional polar molecules,” *Chem. Eng. J.*, vol. 490, p. 151561, June 2024, doi: 10.1016/j.cej.2024.151561.

[166] B. Li *et al.*, “Efficient Passivation Strategy on Sn Related Defects for High Performance All-Inorganic $CsSnI_3$ Perovskite Solar Cells,” *Adv. Funct. Mater.*, vol. 31, no. 11, p. 2007447, Mar. 2021, doi: 10.1002/adfm.202007447.

[167] G. Zeng *et al.*, “Enhancing the performance of tin-based perovskite solar cells through solvent purification of tin iodide,” *J. Mater. Chem. A*, vol. 11, no. 21, pp. 11245–11253, 2023, doi: 10.1039/D3TA01197F.

[168] V. M. Kiyek *et al.*, “Single-Source, Solvent-Free, Room Temperature Deposition of Black γ-$CsSnI_3$ Films,” *Adv. Mater. Interfaces*, vol. 7, no. 11, p. 2000162, June 2020, doi: 10.1002/admi.202000162.

[169] E. W.-G. Diau, E. Jokar, and M. Rameez, “Strategies To Improve Performance and Stability for Tin-Based Perovskite Solar Cells,” *ACS Energy Lett.*, vol. 4, no. 8, pp. 1930–1937, Aug. 2019, doi: 10.1021/acsenergylett.9b01179.

[170] M. Chen *et al.*, “Highly stable and efficient all-inorganic lead-free perovskite solar cells with native-oxide passivation,” *Nat. Commun.*, vol. 10, no. 1, p. 16, Jan. 2019, doi: 10.1038/s41467-018-07951-y.

[171] F. Gu *et al.*, “Improving Performance of Lead-Free Formamidinium Tin Triiodide Perovskite Solar Cells by Tin Source Purification,” *Sol. RRL*, vol. 2, no. 10, p. 1800136, Oct. 2018, doi: 10.1002/solr.201800136.

[172] S. Gražulis *et al.*, “Crystallography Open Database – an open-access collection of crystal structures,” *J. Appl. Crystallogr.*, vol. 42, no. 4, pp. 726–729, Aug. 2009, doi: 10.1107/S0021889809016690.

[173] H. Wang, A. Tal, T. Bischoff, P. Gono, and A. Pasquarello, “Accurate and efficient band-gap predictions for metal halide perovskites at finite temperature: corresponding atomic structures at the certain temperature.” Materials Cloud, p. 89201233, Mar. 04, 2022. doi: 10.24435/MATERIALSCLOUD:B2-BJ.

[174] H. Dong *et al.*, “Crystallization Dynamics of Sn-Based Perovskite Thin Films: Toward Efficient and Stable Photovoltaic Devices,” *Adv. Energy Mater.*, vol. 12, no. 1, p. 2102213, Jan. 2022, doi: 10.1002/aenm.202102213.

[175] S. Sánchez, L. Pfeifer, N. Vlachopoulos, and A. Hagfeldt, “Rapid hybrid perovskite film crystallization from solution,” *Chem. Soc. Rev.*, vol. 50, no. 12, pp. 7108–7131, 2021, doi: 10.1039/D0CS01272F.

[176] Q. Zhou *et al.*, “Scaffold-directed growth of metal halide perovskite hopper crystals,” *CrystEngComm*, vol. 26, no. 9, pp. 1261–1267, 2024, doi: 10.1039/D3CE01153D.

[177] X. Jiang *et al.*, “One-Step Synthesis of $SnI_2 \cdot (DMSO)_x$ Adducts for High-Performance Tin Perovskite Solar Cells,” *J. Am. Chem. Soc.*, vol. 143, no. 29, pp. 10970–10976, July 2021, doi: 10.1021/jacs.1c03032.

[178] J. Pascual *et al.*, “Lights and Shadows of DMSO as Solvent for Tin Halide Perovskites,” *Chem. – Eur. J.*, vol. 28, no. 12, p. e202103919, Feb. 2022, doi: 10.1002/chem.202103919.

[179] M. Yin, H. Yao, H. Qiu, C. Wu, M. Zhang, and F. Hao, “A Revisit of Crystallization in Tin Halide Perovskite Thin Films: From Nucleation, Intermediate to Crystal Growth,” *Adv. Funct. Mater.*, vol. 34, no. 39, p. 2404792, Sept. 2024, doi: 10.1002/adfm.202404792.

[180] Ł. Haryński, A. Olejnik, K. Grochowska, and K. Siuzdak, “A facile method for Tauc exponent and corresponding electronic transitions determination in semiconductors directly from UV–Vis spectroscopy data,” *Opt. Mater.*, vol. 127, p. 112205, May 2022, doi: 10.1016/j.optmat.2022.112205.

[181] A. N. V. J. and D. K. Govindan, “Shaping the Band Structure of n-type Cs_2 SnI_6 Thin Films Using Electron Spectroscopy,” in *2023 IEEE 13th International Conference Nanomaterials: Applications & Properties (NAP)*, Bratislava, Slovakia: IEEE, Sept. 2023, pp. MTFC04-1-MTFC04-4. doi: 10.1109/NAP59739.2023.10310702.

[182] S. N. Khan, Y. 燕 Wang 王, L. 李祥 Zhong 钟, H. 会力 Liang 梁, X. 小龙 Du 杜, and Z. 增霞 Mei 梅, “Effect of Lewis acid-base additive on lead-free Cs_2 SnI_6 thin film prepared by direct solution coating process,” *Chin. Phys. B*, vol. 33, no. 8, p. 087201, July 2024, doi: 10.1088/1674-1056/ad4a39.

[183] A. Liu *et al.*, “Modulation of vacancy-ordered double perovskite Cs2SnI6 for air-stable thin-film transistors,” *Cell Rep. Phys. Sci.*, vol. 3, no. 4, p. 100812, Apr. 2022, doi: 10.1016/j.xcrp.2022.100812.

[184] X. Qiu *et al.*, “From unstable CsSnI3 to air-stable Cs2SnI6: A lead-free perovskite solar cell light absorber with bandgap of 1.48 eV and high absorption coefficient,” *Sol. Energy Mater. Sol. Cells*, vol. 159, pp. 227–234, Jan. 2017, doi: 10.1016/j.solmat.2016.09.022.

[185] B. Saparov *et al.*, “Thin-Film Deposition and Characterization of a Sn-Deficient Perovskite Derivative Cs_2 SnI_6,” *Chem. Mater.*, vol. 28, no. 7, pp. 2315–2322, Apr. 2016, doi: 10.1021/acs.chemmater.6b00433.

[186] V. J. Anjana Nair and K. G. Deepa, “Defect tolerant Cs2SnI6 double perovskite thin films with ultrahigh carrier lifetime for high efficiency solar cells,” *Mater. Chem. Phys.*, vol. 301, p. 127632, June 2023, doi: 10.1016/j.matchemphys.2023.127632.

[187] F. M. Rombach *et al.*, “Disentangling degradation pathways of narrow bandgap lead-tin perovskite material and photovoltaic devices,” *Nat. Commun.*, vol. 16, no. 1, p. 5450, July 2025, doi: 10.1038/s41467-025-58489-9.
[188] I. Poli *et al.*, “Role of the monovalent cation in the self-doping of tin halide perovskites,” *EES Sol.*, vol. 1, no. 3, pp. 287–294, 2025, doi: 10.1039/D5EL00010F.
[189] P. Sebastia-Luna, U. Pokharel, B. A. H. Huisman, L. J. A. Koster, F. Palazon, and H. J. Bolink, “Vacuum-Deposited Cesium Tin Iodide Thin Films with Tunable Thermoelectric Properties,” *ACS Appl. Energy Mater.*, vol. 5, no. 8, pp. 10216–10223, Aug. 2022, doi: 10.1021/acsaem.2c01936.
[190] L. M. Herz, “Charge-Carrier Mobilities in Metal Halide Perovskites: Fundamental Mechanisms and Limits,” *ACS Energy Lett.*, vol. 2, no. 7, pp. 1539–1548, July 2017, doi: 10.1021/acsenergylett.7b00276.
[191] A. Senocrate and J. Maier, “Solid-State Ionics of Hybrid Halide Perovskites,” *J. Am. Chem. Soc.*, vol. 141, no. 21, pp. 8382–8396, May 2019, doi: 10.1021/jacs.8b13594.
[192] K. Song *et al.*, “SKPM study on organic-inorganic perovskite materials,” *AIP Adv.*, vol. 8, no. 3, p. 035114, Mar. 2018, doi: 10.1063/1.5021755.
[193] Z. Hu *et al.*, “The Impact of Atmosphere on Energetics of Lead Halide Perovskites,” *Adv. Energy Mater.*, vol. 10, no. 24, p. 2000908, June 2020, doi: 10.1002/aenm.202000908.
[194] S. Xiong *et al.*, “Reducing nonradiative recombination for highly efficient inverted perovskite solar cells via a synergistic bimolecular interface,” *Nat. Commun.*, vol. 15, no. 1, p. 5607, July 2024, doi: 10.1038/s41467-024-50019-3.
[195] A. Intaniwet, C. A. Mills, P. J. Sellin, M. Shkunov, and J. L. Keddie, “Achieving a Stable Time Response in Polymeric Radiation Sensors under Charge Injection by X-rays,” *ACS Appl. Mater. Interfaces*, vol. 2, no. 6, pp. 1692–1699, June 2010, doi: 10.1021/am100220y.
[196] K. P. Marshall, M. Walker, R. I. Walton, and R. A. Hatton, “Enhanced stability and efficiency in hole-transport-layer-free CsSnI3 perovskite photovoltaics,” *Nat. Energy*, vol. 1, no. 12, p. 16178, Nov. 2016, doi: 10.1038/nenergy.2016.178.
[197] J. Euvrard, Y. Yan, and D. B. Mitzi, “Electrical doping in halide perovskites,” *Nat. Rev. Mater.*, vol. 6, no. 6, pp. 531–549, Mar. 2021, doi: 10.1038/s41578-021-00286-z.
[198] J. Maibach, E. Mankel, T. Mayer, and W. Jaegermann, “The band energy diagram of PCBM–DH6T bulk heterojunction solar cells: synchrotron-induced photoelectron spectroscopy on solution processed DH6T:PCBM blends and in situ prepared PCBM/DH6T interfaces,” *J. Mater. Chem. C*, vol. 1, no. 45, p. 7635, 2013, doi: 10.1039/c3tc31745e.
[199] Q. Bao, X. Liu, S. Braun, and M. Fahlman, “Oxygen- and Water-Based Degradation in [6,6]-Phenyl-C_{61} -Butyric Acid Methyl Ester (PCBM) Films,” *Adv. Energy Mater.*, vol. 4, no. 6, p. 1301272, Apr. 2014, doi: 10.1002/aenm.201301272.
[200] V. Blazinic, L. K. E. Ericsson, I. Levine, R. Hansson, A. Opitz, and E. Moons, “Impact of intentional photo-oxidation of a donor polymer and PC_{70} BM on solar cell performance,” *Phys. Chem. Chem. Phys.*, vol. 21, no. 40, pp. 22259–22271, 2019, doi: 10.1039/C9CP04384E.
[201] O. M. Ottinger, C. Melzer, and H. Von Seggern, “Pitfalls in Kelvin probe measurements,” *J. Appl. Phys.*, vol. 106, no. 2, p. 023704, July 2009, doi: 10.1063/1.3174443.
[202] W. Ke, C. C. Stoumpos, and M. G. Kanatzidis, “‘Unleaded’ Perovskites: Status Quo and Future Prospects of Tin-Based Perovskite Solar Cells,” *Adv. Mater.*, vol. 31, no. 47, p. 1803230, Nov. 2019, doi: 10.1002/adma.201803230.
[203] H. Hu, S. Birkhold, M. Sultan, A. Fakharuddin, S. Koch, and L. Schmidt-Mende, “Surface Band Bending Influences the Open-Circuit Voltage of Perovskite Solar

Cells," *ACS Appl. Energy Mater.*, vol. 2, no. 6, pp. 4045–4052, June 2019, doi: 10.1021/acsaem.9b00060.
[204] M. G. Helander, M. T. Greiner, Z. B. Wang, W. M. Tang, and Z. H. Lu, "Work function of fluorine doped tin oxide," *J. Vac. Sci. Technol. Vac. Surf. Films*, vol. 29, no. 1, p. 011019, Jan. 2011, doi: 10.1116/1.3525641.
[205] K. P. Marshall, R. I. Walton, and R. A. Hatton, "Tin perovskite/fullerene planar layer photovoltaics: improving the efficiency and stability of lead-free devices," *J. Mater. Chem. A*, vol. 3, no. 21, pp. 11631–11640, 2015, doi: 10.1039/C5TA02950C.
[206] G. N. Derry, M. E. Kern, and E. H. Worth, "Recommended values of clean metal surface work functions," *J. Vac. Sci. Technol. Vac. Surf. Films*, vol. 33, no. 6, p. 060801, Nov. 2015, doi: 10.1116/1.4934685.
[207] J. Desarnaud, H. Derluyn, J. Carmeliet, D. Bonn, and N. Shahidzadeh, "Hopper Growth of Salt Crystals," *J. Phys. Chem. Lett.*, vol. 9, no. 11, pp. 2961–2966, June 2018, doi: 10.1021/acs.jpclett.8b01082.
[208] P. C. Bollada, P. K. Jimack, and A. M. Mullis, "Phase field modelling of hopper crystal growth in alloys," *Sci. Rep.*, vol. 13, no. 1, p. 12637, Aug. 2023, doi: 10.1038/s41598-023-38741-2.
[209] X. Li, F. Zhang, H. He, J. J. Berry, K. Zhu, and T. Xu, "On-device lead sequestration for perovskite solar cells," *Nature*, vol. 578, no. 7796, pp. 555–558, Feb. 2020, doi: 10.1038/s41586-020-2001-x.
[210] Y. Li *et al.*, "In Situ Investigation of the Growth of Methylammonium Lead Halide ($MAPbI_{3-x}Br_x$) Perovskite from Microdroplets," *Cryst. Growth Des.*, vol. 18, no. 6, pp. 3458–3464, June 2018, doi: 10.1021/acs.cgd.8b00181.
[211] L. A. Muscarella *et al.*, "Crystal Orientation and Grain Size: Do They Determine Optoelectronic Properties of $MAPbI_3$ Perovskite?," *J. Phys. Chem. Lett.*, vol. 10, no. 20, pp. 6010–6018, Oct. 2019, doi: 10.1021/acs.jpclett.9b02757.
[212] I. Petrovai, O. Todor-Boer, L. David, and I. Botiz, "Growth of Hybrid Perovskite Crystals from CH3NH3PbI3–xClx Solutions Subjected to Constant Solvent Evaporation Rates," *Materials*, vol. 16, no. 7, p. 2625, Mar. 2023, doi: 10.3390/ma16072625.
[213] L. Ji *et al.*, "Realizing Full Coverage of Stable Perovskite Film by Modified Anti-Solvent Process," *Nanoscale Res. Lett.*, vol. 12, no. 1, p. 367, Dec. 2017, doi: 10.1186/s11671-017-2117-6.
[214] N. Khan *et al.*, "Bromide Incorporation Enhances Vertical Orientation of Triple Organic Cation Tin-Halide Perovskites for High-Performance Lead-Free Solar Cells," *Sol. RRL*, vol. 6, no. 11, p. 2200631, Nov. 2022, doi: 10.1002/solr.202200631.
[215] S. Shao *et al.*, "Highly Reproducible Sn-Based Hybrid Perovskite Solar Cells with 9% Efficiency," *Adv. Energy Mater.*, vol. 8, no. 4, p. 1702019, Feb. 2018, doi: 10.1002/aenm.201702019.
[216] J. Pascual *et al.*, "Fluoride Chemistry in Tin Halide Perovskites," *Angew. Chem. Int. Ed.*, vol. 60, no. 39, pp. 21583–21591, Sept. 2021, doi: 10.1002/anie.202107599.
[217] M. Zhang *et al.*, "Strategies for Optimizing the Morphology of CsSnI3 Perovskite Solar Cells," *Crystals*, vol. 13, no. 3, p. 410, Feb. 2023, doi: 10.3390/cryst13030410.
[218] H. Ban *et al.*, "Over 8% efficient $CsSnI_3$ -based mesoporous perovskite solar cells enabled by two-step thermal annealing and surface cationic coordination dual treatment," *J. Mater. Chem. A*, vol. 10, no. 7, pp. 3642–3649, 2022, doi: 10.1039/D1TA09811J.
[219] M. Chen *et al.*, "Low-temperature sequential deposition for efficient inverted perovskite solar cells," *Nat. Commun.*, vol. 16, no. 1, p. 5746, July 2025, doi: 10.1038/s41467-025-61144-y.
[220] M. H. Braga, N. S. Grundish, A. J. Murchison, and J. B. Goodenough, "Thermodynamic considerations of same-metal electrodes in an asymmetric cell," *Mater. Theory*, vol. 3, no. 1, p. 1, Dec. 2019, doi: 10.1186/s41313-018-0014-8.

[221] B. M. Gomes, J. F. Ribeiro Moutinho, and M. H. Braga, "A perspective on the building blocks of a solid-state battery: from solid electrolytes to quantum power harvesting and storage," *J. Mater. Chem. A*, vol. 12, no. 2, pp. 690–722, 2024, doi: 10.1039/D3TA04228F.

[222] D. Lin, Y. Liu, and Y. Cui, "Reviving the lithium metal anode for high-energy batteries," *Nat. Nanotechnol.*, vol. 12, no. 3, pp. 194–206, Mar. 2017, doi: 10.1038/nnano.2017.16.

[223] R. C. Massé, C. Liu, Y. Li, L. Mai, and G. Cao, "Energy storage through intercalation reactions: electrodes for rechargeable batteries," *Natl. Sci. Rev.*, vol. 4, no. 1, pp. 26–53, Jan. 2017, doi: 10.1093/nsr/nww093.

[224] K. Xu, "Electrolytes and Interphases in Li-Ion Batteries and Beyond," *Chem. Rev.*, vol. 114, no. 23, pp. 11503–11618, Dec. 2014, doi: 10.1021/cr500003w.

[225] J. Janek and W. G. Zeier, "A solid future for battery development," *Nat. Energy*, vol. 1, no. 9, p. 16141, Sept. 2016, doi: 10.1038/nenergy.2016.141.

[226] S. Lou *et al.*, "Interface Issues and Challenges in All-Solid-State Batteries: Lithium, Sodium, and Beyond," *Adv. Mater.*, vol. 33, no. 6, p. 2000721, Feb. 2021, doi: 10.1002/adma.202000721.

[227] M. P. Fertig, K. Skadell, M. Schulz, C. Dirksen, P. Adelhelm, and M. Stelter, "From High- to Low-Temperature: The Revival of Sodium-Beta Alumina for Sodium Solid-State Batteries," *Batter. Supercaps*, vol. 5, no. 1, p. e202100131, Jan. 2022, doi: 10.1002/batt.202100131.

[228] K. Funke, "Solid State Ionics: from Michael Faraday to green energy—the European dimension," *Sci. Technol. Adv. Mater.*, vol. 14, no. 4, p. 043502, Mar. 2013, doi: 10.1088/1468-6996/14/4/043502.

[229] A. Mauger and C. M. Julien, "Solid Polymer Electrolytes for Lithium Batteries: A Tribute to Michel Armand," *Inorganics*, vol. 10, no. 8, p. 110, July 2022, doi: 10.3390/inorganics10080110.

[230] V. Lacivita, Y. Wang, S.-H. Bo, and G. Ceder, "*Ab initio* investigation of the stability of electrolyte/electrode interfaces in all-solid-state Na batteries," *J. Mater. Chem. A*, vol. 7, no. 14, pp. 8144–8155, 2019, doi: 10.1039/C8TA10498K.

[231] J. Wang *et al.*, "Design principles for NASICON super-ionic conductors," *Nat. Commun.*, vol. 14, no. 1, p. 5210, Aug. 2023, doi: 10.1038/s41467-023-40669-0.

[232] A. C. Radjendirane *et al.*, "Overview of Inorganic Electrolytes for All-Solid-State Sodium Batteries," *Langmuir*, vol. 40, no. 32, pp. 16690–16712, Aug. 2024, doi: 10.1021/acs.langmuir.4c01845.

[233] I.-H. Chu *et al.*, "Room-Temperature All-solid-state Rechargeable Sodium-ion Batteries with a Cl-doped Na3PS4 Superionic Conductor," *Sci. Rep.*, vol. 6, no. 1, p. 33733, Sept. 2016, doi: 10.1038/srep33733.

[234] H. Nguyen *et al.*, "Single-step synthesis of highly conductive Na3PS4 solid electrolyte for sodium all solid-state batteries," *J. Power Sources*, vol. 435, p. 126623, Sept. 2019, doi: 10.1016/j.jpowsour.2019.05.031.

[235] A. Hayashi *et al.*, "A sodium-ion sulfide solid electrolyte with unprecedented conductivity at room temperature," *Nat. Commun.*, vol. 10, no. 1, p. 5266, Nov. 2019, doi: 10.1038/s41467-019-13178-2.

[236] C. Fu *et al.*, "LaCl3-based sodium halide solid electrolytes with high ionic conductivity for all-solid-state batteries," *Nat. Commun.*, vol. 15, no. 1, p. 4315, May 2024, doi: 10.1038/s41467-024-48712-4.

[237] Y. Hu *et al.*, "Superionic amorphous NaTaCl6 halide electrolyte for highly reversible all-solid-state Na-ion batteries," *Matter*, vol. 7, no. 3, pp. 1018–1034, Mar. 2024, doi: 10.1016/j.matt.2023.12.017.

[238] Z. Huang, S. Yoshida, H. Akamatsu, K. Hayashi, and S. Ohno, "Na M Cl_6 (M = Nb and Ta): A New Class of Sodium-Conducting Halide-Based Solid Electrolytes," *ACS Mater. Lett.*, vol. 6, no. 5, pp. 1732–1738, May 2024, doi: 10.1021/acsmaterialslett.4c00315.

[239] L. Stolz, S. Hochstädt, S. Röser, M. R. Hansen, M. Winter, and J. Kasnatscheew, "Single-Ion *versus* Dual-Ion Conducting Electrolytes: The Relevance of Concentration Polarization in Solid-State Batteries," *ACS Appl. Mater. Interfaces*, vol. 14, no. 9, pp. 11559–11566, Mar. 2022, doi: 10.1021/acsami.2c00084.
[240] Z. Li *et al.*, "Ionic Conduction in Polymer-Based Solid Electrolytes," *Adv. Sci.*, vol. 10, no. 10, p. 2201718, Apr. 2023, doi: 10.1002/advs.202201718.
[241] Y. Xiao, Y. Wang, S.-H. Bo, J. C. Kim, L. J. Miara, and G. Ceder, "Understanding interface stability in solid-state batteries," *Nat. Rev. Mater.*, vol. 5, no. 2, pp. 105–126, Dec. 2019, doi: 10.1038/s41578-019-0157-5.
[242] S. Yang *et al.*, "Imaging dendrite growth in solid-state sodium batteries using fluorescence tomography technology," *Sci. Adv.*, vol. 10, no. 47, p. eadr0676, Nov. 2024, doi: 10.1126/sciadv.adr0676.
[243] J. Janek and W. G. Zeier, "Challenges in speeding up solid-state battery development," *Nat. Energy*, vol. 8, no. 3, pp. 230–240, Feb. 2023, doi: 10.1038/s41560-023-01208-9.
[244] A. Lasia, *Electrochemical Impedance Spectroscopy and its Applications*. New York, NY: Springer New York, 2014. doi: 10.1007/978-1-4614-8933-7.
[245] M. Kurniawan and S. Ivanov, "Electrochemically Structured Copper Current Collectors for Application in Energy Conversion and Storage: A Review," *Energies*, vol. 16, no. 13, p. 4933, June 2023, doi: 10.3390/en16134933.
[246] J. K. Eckhardt, T. Fuchs, S. Burkhardt, P. J. Klar, J. Janek, and C. Heiliger, "3D Impedance Modeling of Metal Anodes in Solid-State Batteries–Incompatibility of Pore Formation and Constriction Effect in Physical-Based 1D Circuit Models," *ACS Appl. Mater. Interfaces*, vol. 14, no. 37, pp. 42757–42769, Sept. 2022, doi: 10.1021/acsami.2c12991.
[247] J. K. Eckhardt, P. J. Klar, J. Janek, and C. Heiliger, "Interplay of Dynamic Constriction and Interface Morphology between Reversible Metal Anode and Solid Electrolyte in Solid State Batteries," *ACS Appl. Mater. Interfaces*, vol. 14, no. 31, pp. 35545–35554, Aug. 2022, doi: 10.1021/acsami.2c07077.
[248] H. Sun *et al.*, "Hierarchical 3D electrodes for electrochemical energy storage," *Nat. Rev. Mater.*, vol. 4, no. 1, pp. 45–60, Dec. 2018, doi: 10.1038/s41578-018-0069-9.
[249] Y. Yue and H. Liang, "Hierarchical micro-architectures of electrodes for energy storage," *J. Power Sources*, vol. 284, pp. 435–445, June 2015, doi: 10.1016/j.jpowsour.2015.03.069.
[250] L. Zhou *et al.*, "Recent Developments on and Prospects for Electrode Materials with Hierarchical Structures for Lithium-Ion Batteries," *Adv. Energy Mater.*, vol. 8, no. 6, p. 1701415, Feb. 2018, doi: 10.1002/aenm.201701415.
[251] M. Doyle, T. F. Fuller, and J. Newman, "Modeling of Galvanostatic Charge and Discharge of the Lithium/Polymer/Insertion Cell," *J. Electrochem. Soc.*, vol. 140, no. 6, pp. 1526–1533, June 1993, doi: 10.1149/1.2221597.
[252] T.-T. Nguyen, A. Demortière, B. Fleutot, B. Delobel, C. Delacourt, and S. J. Cooper, "The electrode tortuosity factor: why the conventional tortuosity factor is not well suited for quantifying transport in porous Li-ion battery electrodes and what to use instead," *Npj Comput. Mater.*, vol. 6, no. 1, p. 123, Aug. 2020, doi: 10.1038/s41524-020-00386-4.
[253] B. Tjaden, D. J. L. Brett, and P. R. Shearing, "Tortuosity in electrochemical devices: a review of calculation approaches," *Int. Mater. Rev.*, vol. 63, no. 2, pp. 47–67, Feb. 2018, doi: 10.1080/09506608.2016.1249995.
[254] L. Chen, M. Wang, A. Lv, W. Hu, and S. Jiao, "Self-Supporting Dendritic Copper Porous Film Inducing the Lateral Growth of Metallic Lithium for Highly Stable Li Metal Battery," *J. Electrochem. Soc.*, vol. 166, no. 16, pp. A4073–A4079, 2019, doi: 10.1149/2.0371916jes.

[255] H. Lee, T. Kwak, W. Lee, J. Song, and D. Kim, “Effect of surface topography on dendritic growth in lithium metal batteries,” *J. Power Sources*, vol. 552, p. 232264, Dec. 2022, doi: 10.1016/j.jpowsour.2022.232264.

[256] W. Dong *et al.*, “Regulating Lithium Electrodeposition with Laser-Structured Current Collectors for Stable Lithium Metal Batteries,” *ACS Appl. Mater. Interfaces*, vol. 13, no. 7, pp. 8417–8425, Feb. 2021, doi: 10.1021/acsami.0c21301.

[257] C. K. Chan *et al.*, “High-performance lithium battery anodes using silicon nanowires,” *Nat. Nanotechnol.*, vol. 3, no. 1, pp. 31–35, Jan. 2008, doi: 10.1038/nnano.2007.411.

[258] S. Kalnaus, N. J. Dudney, A. S. Westover, E. Herbert, and S. Hackney, “Solid-state batteries: The critical role of mechanics,” *Science*, vol. 381, no. 6664, p. eabg5998, Sept. 2023, doi: 10.1126/science.abg5998.

[259] E. Ravesio, A. H. A. Lutey, D. Versaci, L. Romoli, and S. Bodoardo, “Nanosecond pulsed laser texturing of Li-ion battery electrode current collectors: Electrochemical characterisation of cathode half-cells,” *Sustain. Mater. Technol.*, vol. 38, p. e00751, Dec. 2023, doi: 10.1016/j.susmat.2023.e00751.

[260] W. Pfleging, “Recent progress in laser texturing of battery materials: a review of tuning electrochemical performances, related material development, and prospects for large-scale manufacturing,” *Int. J. Extreme Manuf.*, vol. 3, no. 1, p. 012002, Dec. 2020, doi: 10.1088/2631-7990/abca84.

[261] J. Keilhofer *et al.*, “Mechanical Structuring of Lithium-Ion Battery Electrodes Using an Embossing Roller,” *Energy Technol.*, vol. 11, no. 5, p. 2200869, May 2023, doi: 10.1002/ente.202200869.

[262] P. Scherzl, M. Kaupp, W. El Mofid, and T. Sörgel, “Electroforming as a Novel One-Step Manufacturing Method of Structured Aluminum Foil Current Collectors for Lithium-Ion Batteries,” *Batteries*, vol. 9, no. 8, p. 422, Aug. 2023, doi: 10.3390/batteries9080422.

[263] P. Sun, X. Li, J. Shao, and P. V. Braun, “High-Performance Packaged 3D Lithium-Ion Microbatteries Fabricated Using Imprint Lithography,” *Adv. Mater.*, vol. 33, no. 1, p. 2006229, Jan. 2021, doi: 10.1002/adma.202006229.

[264] C. Luan, L. Chen, B. Li, L. Zhu, and W. Li, “Electrochemical Dealloying-Enabled 3D Hierarchical Porous Cu Current Collector of Lithium Metal Anodes for Dendrite Growth Inhibition,” *ACS Appl. Energy Mater.*, vol. 4, no. 12, pp. 13903–13911, Dec. 2021, doi: 10.1021/acsaem.1c02696.

[265] Y. Ma *et al.*, “Electrochemically Dealloyed 3D Porous Copper Nanostructure as Anode Current Collector of Li-Metal Batteries,” *Small*, vol. 19, no. 28, p. 2301731, July 2023, doi: 10.1002/smll.202301731.

[266] S. M. Jeong *et al.*, “A 3D Porous Inverse Opal Ni Structure on a Cu Current Collector for Stable Lithium-Metal Batteries,” *Batter. Supercaps*, vol. 5, no. 3, p. e202100257, Mar. 2022, doi: 10.1002/batt.202100257.

[267] Y. Li, G. Duan, G. Liu, and W. Cai, “Physical processes-aided periodic micro/nanostructured arrays by colloidal template technique: fabrication and applications,” *Chem. Soc. Rev.*, vol. 42, no. 8, p. 3614, 2013, doi: 10.1039/c3cs35482b.

[268] I. Doberdò *et al.*, “Enabling aqueous binders for lithium battery cathodes – Carbon coating of aluminum current collector,” *J. Power Sources*, vol. 248, pp. 1000–1006, Feb. 2014, doi: 10.1016/j.jpowsour.2013.10.039.

[269] K. Wang *et al.*, “Super-aligned carbon nanotube films with a thin metal coating as highly conductive and ultralight current collectors for lithium-ion batteries,” *J. Power Sources*, vol. 351, pp. 160–168, May 2017, doi: 10.1016/j.jpowsour.2017.03.081.

[270] A. A. Leonardi, M. J. L. Faro, and A. Irrera, “Silicon Nanowires Synthesis by Metal-Assisted Chemical Etching: A Review,” *Nanomaterials*, vol. 11, no. 2, p. 383, Feb. 2021, doi: 10.3390/nano11020383.

[271] R. Correia *et al.*, "Biocompatible Parylene-C Laser-Induced Graphene Electrodes for Microsupercapacitor Applications," *ACS Appl. Mater. Interfaces*, vol. 14, no. 41, pp. 46427–46438, Oct. 2022, doi: 10.1021/acsami.2c09667.
[272] I. M. Santos *et al.*, "Optically-Boosted Planar IBC Solar Cells with Electrically-Harmless Photonic Nanocoatings," *Adv. Opt. Mater.*, vol. 11, no. 15, p. 2300276, Aug. 2023, doi: 10.1002/adom.202300276.
[273] M. Gaberšček, "Understanding Li-based battery materials via electrochemical impedance spectroscopy," *Nat. Commun.*, vol. 12, no. 1, p. 6513, Nov. 2021, doi: 10.1038/s41467-021-26894-5.
[274] A. Ch. Lazanas and M. I. Prodromidis, "Electrochemical Impedance Spectroscopy—A Tutorial," *ACS Meas. Sci. Au*, vol. 3, no. 3, pp. 162–193, June 2023, doi: 10.1021/acsmeasuresciau.2c00070.
[275] P. T. Kissinger and W. R. Heineman, "Cyclic voltammetry," *J. Chem. Educ.*, vol. 60, no. 9, p. 702, Sept. 1983, doi: 10.1021/ed060p702.
[276] F. S. Oliveira, R. B. Cipriano, F. T. Da Silva, E. C. Romão, and C. A. M. Dos Santos, "Simple analytical method for determining electrical resistivity and sheet resistance using the van der Pauw procedure," *Sci. Rep.*, vol. 10, no. 1, p. 16379, Oct. 2020, doi: 10.1038/s41598-020-72097-1.
[277] E. N. Kaufmann, Ed., *Characterization of materials*. Hoboken, NJ: Wiley, 2003.
[278] J. Jung *et al.*, "Insights on the work function of the current collector surface in anode-free lithium metal batteries," *J. Mater. Chem. A*, vol. 10, no. 39, pp. 20984–20992, 2022, doi: 10.1039/D2TA04078F.
[279] "CRC Handbook of Chemistry and Physics, 88th ed Editor-in-Chief: David R. Lide (National Institute of Standards and Technology) CRC Press/Taylor & Francis Group: Boca Raton, FL. 2007. 2640 pp. $139.95. ISBN 0-8493-0488-1.," *J. Am. Chem. Soc.*, vol. 130, no. 1, pp. 382–382, Jan. 2008, doi: 10.1021/ja077011d.
[280] X. Cui, D. A. Hutt, and P. P. Conway, "Evolution of microstructure and electrical conductivity of electroless copper deposits on a glass substrate," *Thin Solid Films*, vol. 520, no. 19, pp. 6095–6099, July 2012, doi: 10.1016/j.tsf.2012.05.068.
[281] D. Allassem *et al.*, "Study of Copper Thin Films Resistivity by Using Van der Pauw Method at Low Frequencies," *Open J. Appl. Sci.*, vol. 12, no. 11, pp. 1944–1953, 2022, doi: 10.4236/ojapps.2022.1211135.
[282] P. P. Edwards, A. Porch, M. O. Jones, D. V. Morgan, and R. M. Perks, "Basic materials physics of transparent conducting oxides," *Dalton Trans.*, no. 19, p. 2995, 2004, doi: 10.1039/b408864f.
[283] J. M. Camacho and A. I. Oliva, "Surface and grain boundary contributions in the electrical resistivity of metallic nanofilms," *Thin Solid Films*, vol. 515, no. 4, pp. 1881–1885, Dec. 2006, doi: 10.1016/j.tsf.2006.07.024.
[284] P. P. Edwards, A. Porch, M. O. Jones, D. V. Morgan, and R. M. Perks, "Basic materials physics of transparent conducting oxides," *Dalton Trans.*, no. 19, p. 2995, 2004, doi: 10.1039/b408864f.
[285] P. Vadhva *et al.*, "Electrochemical Impedance Spectroscopy for All-Solid-State Batteries: Theory, Methods and Future Outlook," *ChemElectroChem*, vol. 8, no. 11, pp. 1930–1947, June 2021, doi: 10.1002/celc.202100108.
[286] L. Zhang *et al.*, "Recent advances in electrochemical impedance spectroscopy for solid-state batteries," *Energy Storage Mater.*, vol. 69, p. 103378, May 2024, doi: 10.1016/j.ensm.2024.103378.
[287] M. H. Braga, "Coherence in the Ferroelectric A3ClO (A = Li, Na) Family of Electrolytes," *Materials*, vol. 14, no. 9, p. 2398, May 2021, doi: 10.3390/ma14092398.
[288] M. H. Braga, "Energy harnessing and storage from surface switching with a ferroelectric electrolyte," *Chem. Commun.*, vol. 60, no. 41, pp. 5395–5398, 2024, doi: 10.1039/D4CC00414K.

Attachments

Appendix A.1

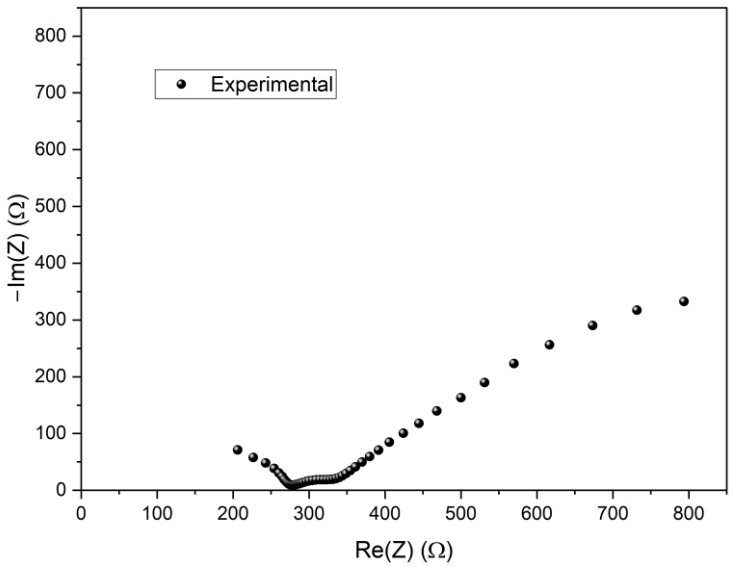


Figure A1 – PEIS for cycle 3 for the Zn/$Na_{2.99}Ba_{0.005}OCl$/Cu-sheet (⌀0.125 mm) pouch cell assembled in batch 1.

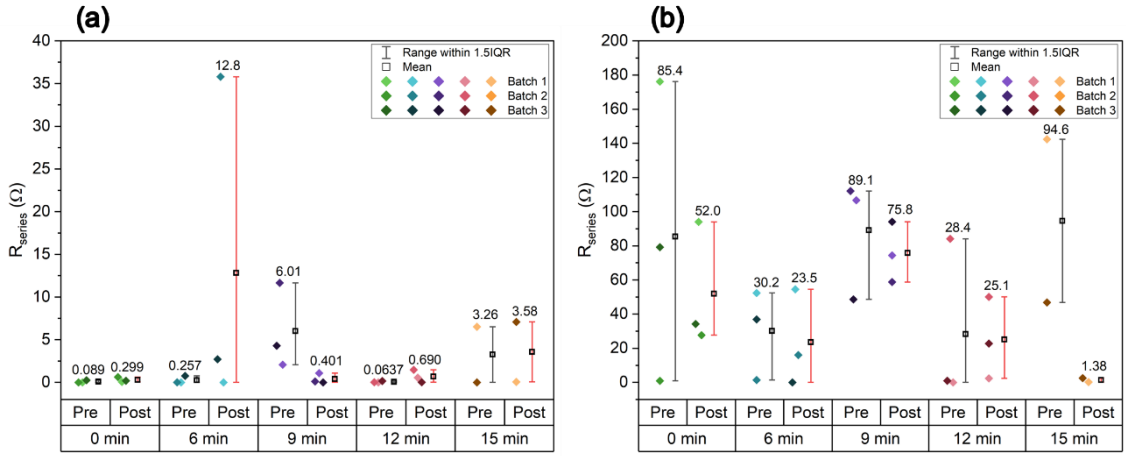


Figure A2 – Resistance in series obtained from fit of PEIS performed at (a) RT (b) 40 °C. Values on top of dispersion bars represent the mean value.

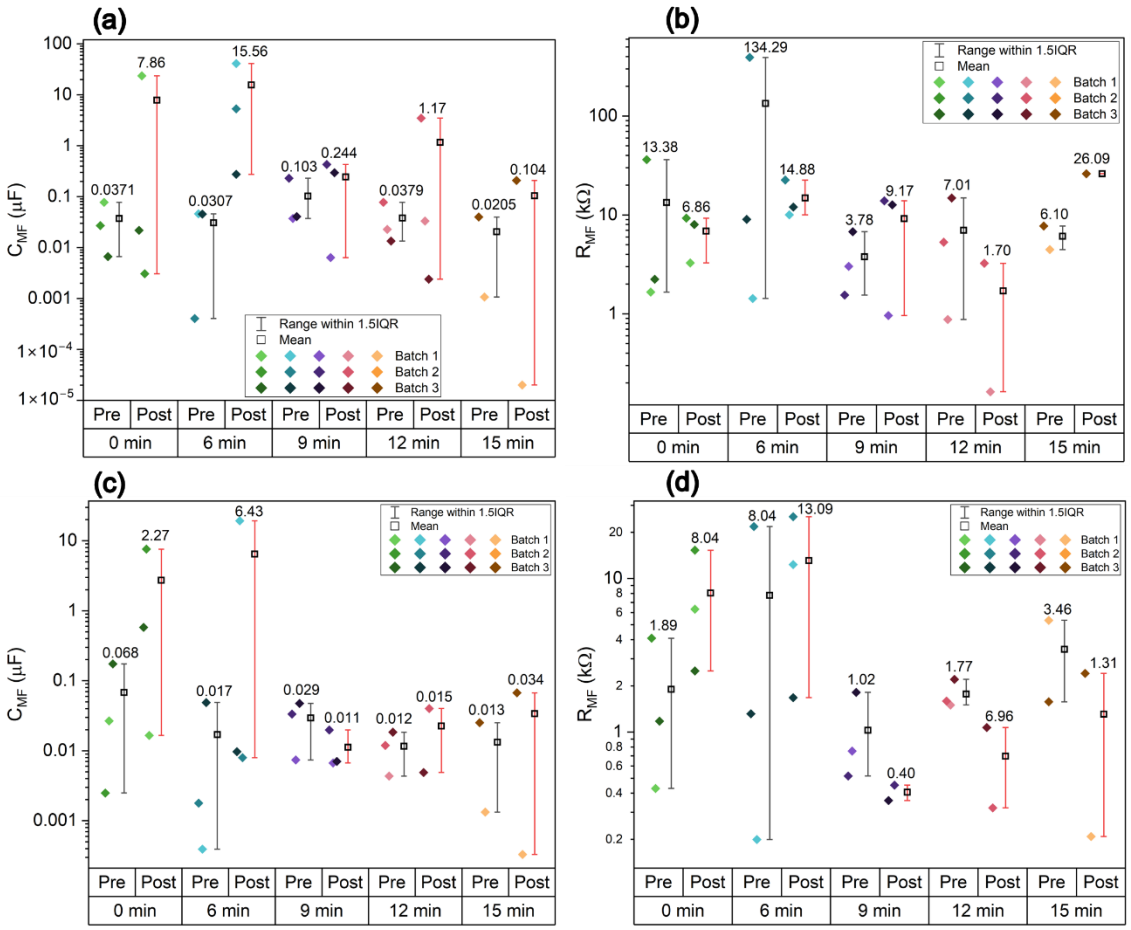


Figure A3 – Fit parameters obtained for PEIS: (a) mid frequency capacitance at RT; (b) mid frequency resistance at RT; (c) mid frequency capacitance at 40 °C; (d) mid frequency resistance at 40 °C. Values presented in logarithmic scale for better visualization. Some data points were excluded due to unreasonably low resistance or capacitance values, which indicate that the MF semicircle was not present.

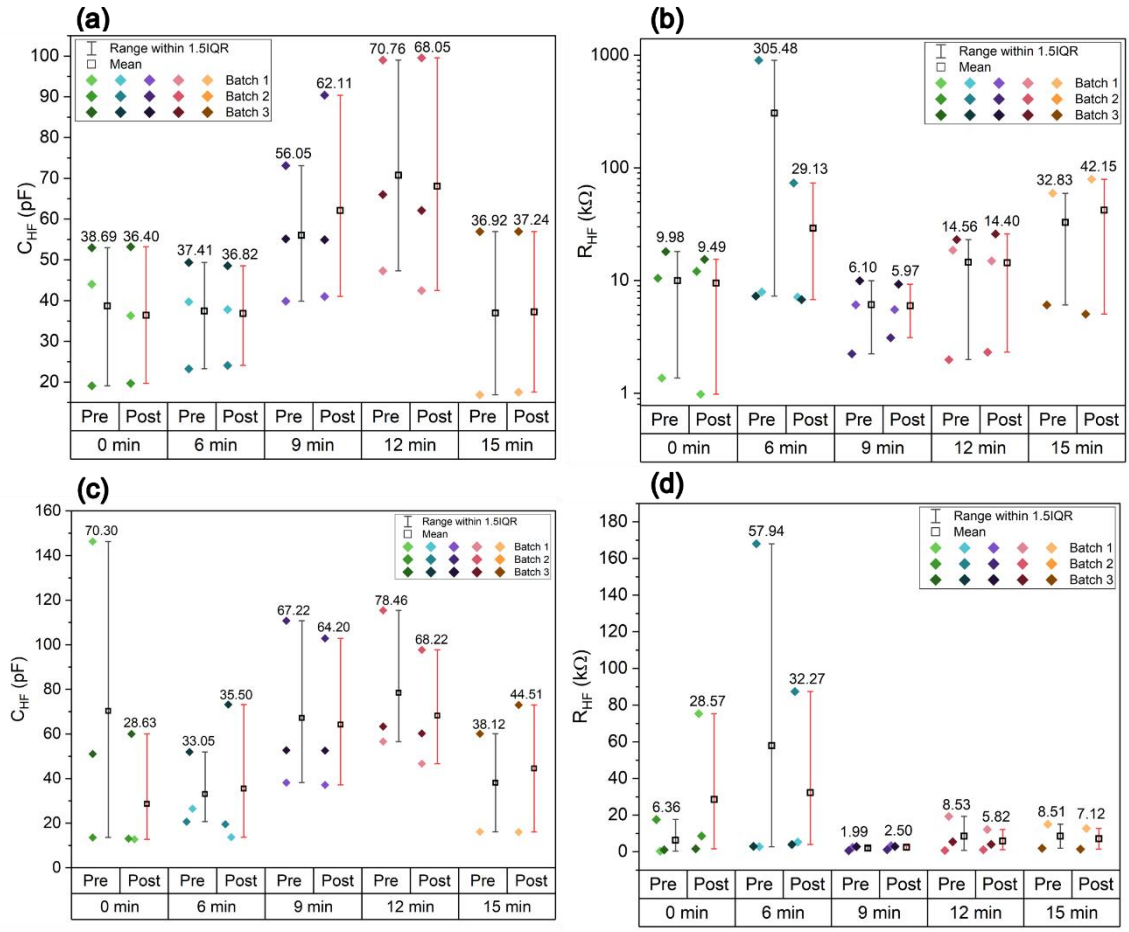


Figure A4 – Fit parameters obtained for PEIS: (a) High frequency capacitance at RT (b) Log scale High frequency resistance at RT (c) High frequency capacitance at 40 °C (d) High frequency resistance at 40 °C. Inset plots highlight zones with lower capacitance/resistance for better visualization.

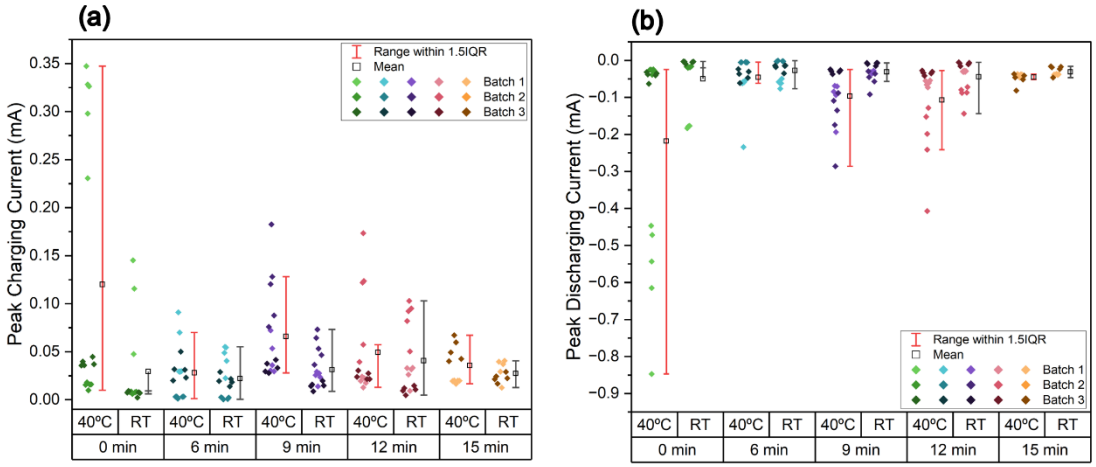


Figure A5 – Currents at: (a) anodic (charging) peak and (b) cathodic (discharging) peak function of collector type and temperature.

Appendix A.2

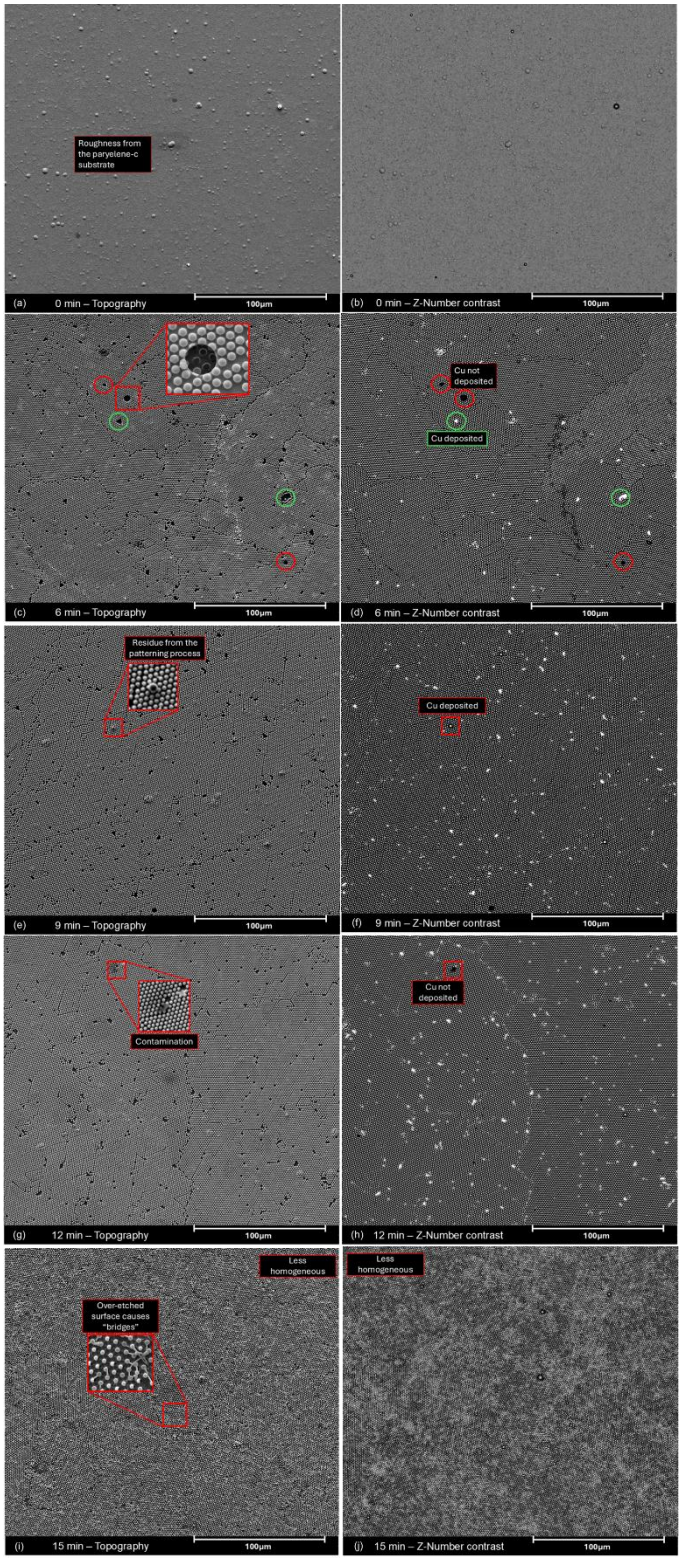


Figure A6 – Scanning electron microscope images of the microstructured current collectors for each etching duration. (a,b) 0 min, (c,d) 6 min, (e,f) 9 min, (g,h) 12 min, (i,j) 15 min. Left side column shows images obtained with secondary electrons (topography sensitive), right side columns show images obtained with backscattered electrons (atomic number sensitive).

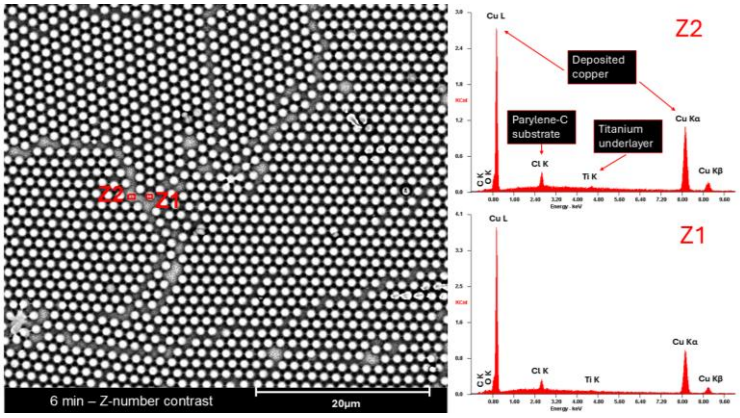


Figure A7 – Scanning electron microscope image of the microstructured copper sample etched for 6 min. Z1 and Z2 identify the spots for Energy-Dispersive X-Ray Spectroscopy analysis. On the right side are the obtained EDS spectra for each zone.

Appendix A.3

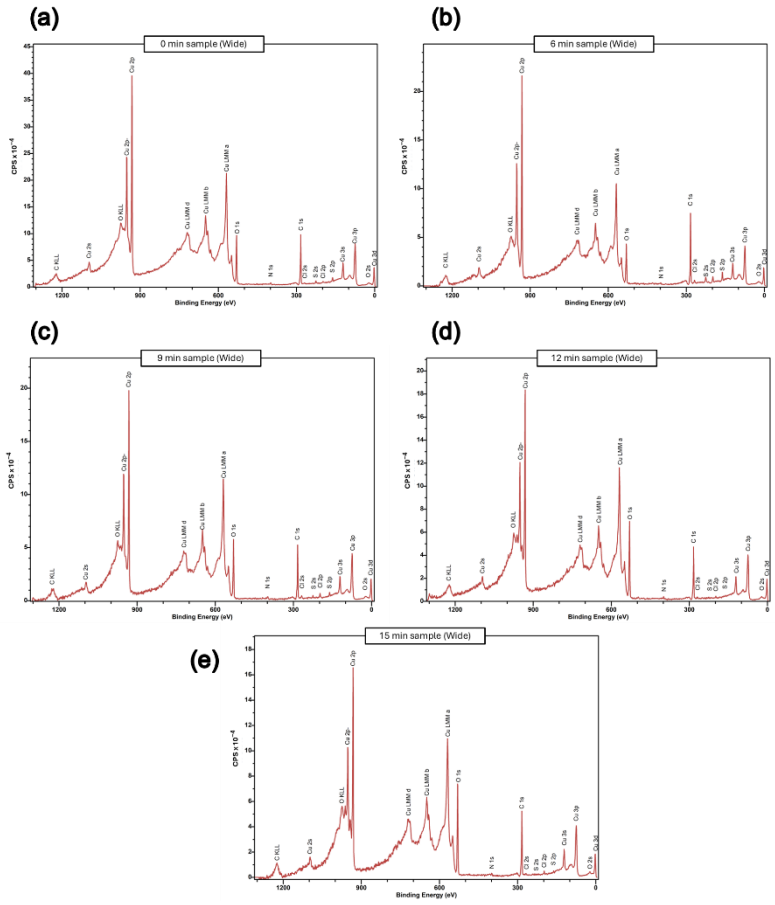


Figure A8 – Wide XPS spectra of the microstructured copper samples for each etching duration. (a) 0 min, (b) 6 min, (c) 9 min, (d) 12 min, (e) 15 min.

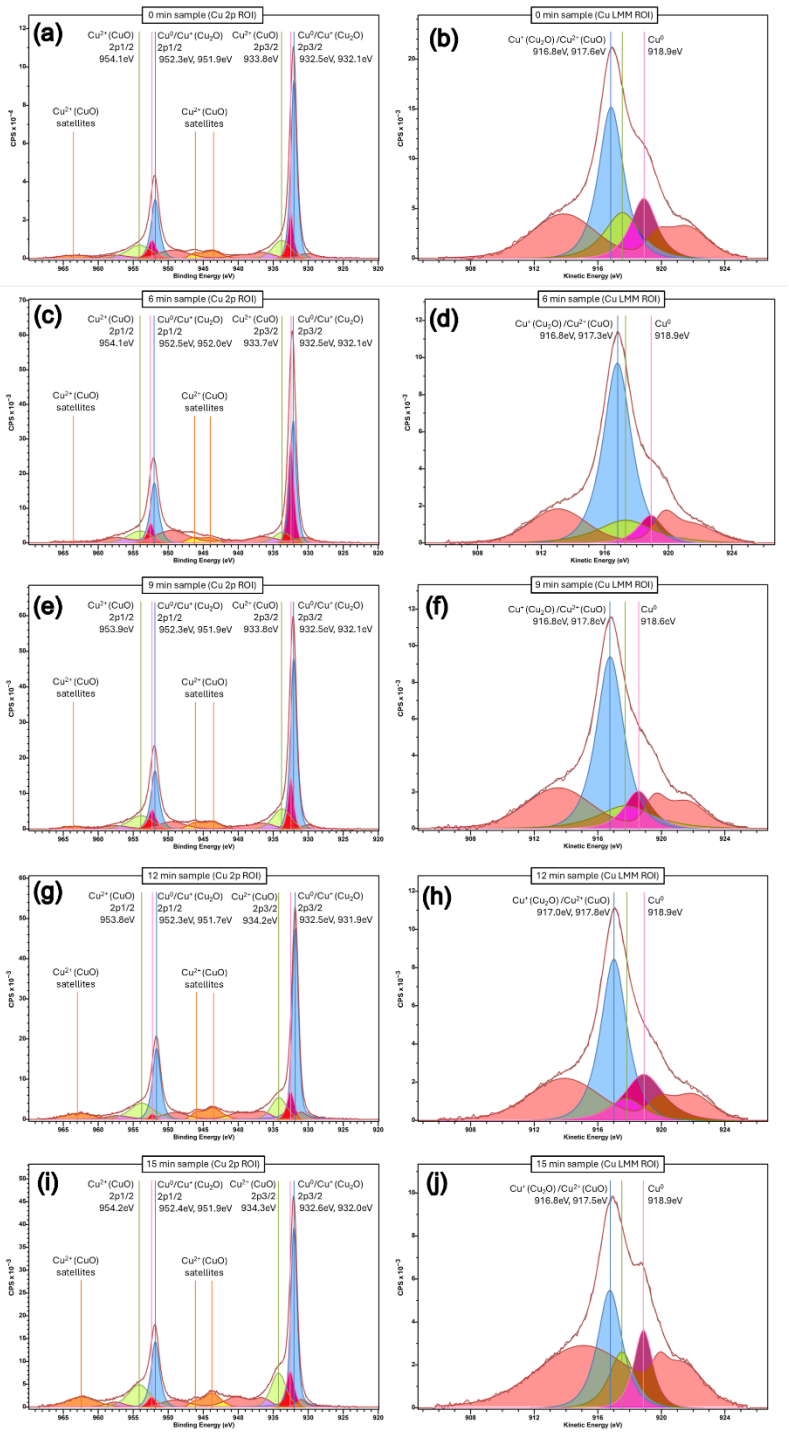


Figure A9 – Localized XPS spectra of the microstructured copper samples for each etching duration. (a,b) 0 min, (c,d) 6 min, (e,f) 9 min, (g,h) 12 min, (i,j) 15 min. Cu 2p ROI spectra, used to distinguish Cu+/Cu0 from Cu2+, on the left side column. Cu LMM (L3M4,5M4,5) Auger ROI spectra, used to distinguish Cu+ from Cu0, on the right side column. Vertical lines and adjacent labels indicate the lo-cation of identified Cu peaks, labeled according to NIST X-ray Photoelectron Spectroscopy Database. Cu+ peaks colored in blue, Cu0 peaks colored in rose, Cu2+ peaks colored in green and loss features colored in red.

Appendix A.4

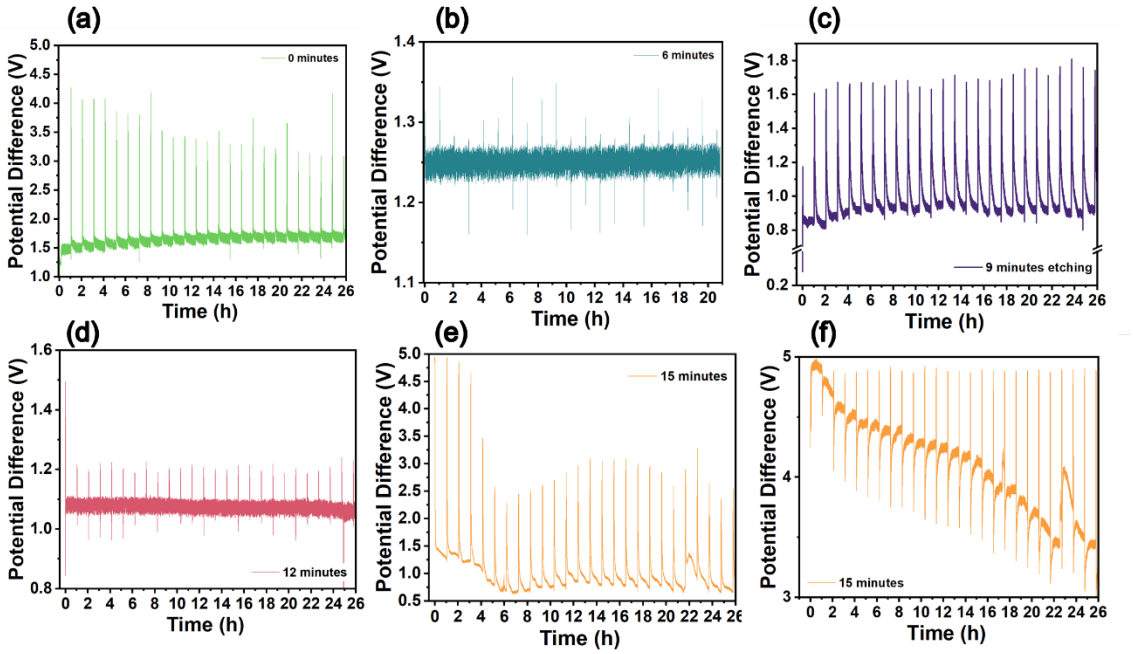


Figure A10 – GITT performance of selected Zn/Na2.99Ba0.005OCl/Microstructured-Cu cells with different etching durations for the first 20/26 h. (a) 0 min, (b) 6 min (charging current 50 μA), (c) 9 min, (d) 12 min, (e) 15 min batch 3, (f) 15 min batch 1.